Gold and Copper Based Nanomaterials for Potential Theranostic Applications

A Dissertation Submitted to the
Indian Institute of Technology Guwahati
as Partial Fulfillment of the Degree of

DOCTOR of PHILOSOPHY

by

Rama Ghosh

Roll No: 10612209

Department of Chemistry

Indian Institute of Technology Guwahati

Guwahati – 781039, Assam, India

September 2015

STATEMENT

I hereby declare that the scientific matter embodied in this thesis entitled, "**Gold and Copper Based Nanomaterials for Potential Theranostic Applications**" is the outcome of research work carried out by me under the supervision of Dr. Anumita Paul, Professor, at the Department of Chemistry, Indian Institute of Technology Guwahati, Guwahati, Assam, India, for the award of the degree of Doctor of Philosophy. To the best of my knowledge, the work delineated on this thesis is original and has not been submitted elsewhere for any degree of any other Institute or University.

IIT Guwahati
September 2015

Rama Ghosh
Candidate

Prof. Anumita Paul
Professor, Department of Chemistry
Indian Institute of Technology Guwahati
Guwahati – 781039, Assam, India
Tel: +91- 361 2582308; Fax: +91 - 361 2582349
Email: anumita@iitg.ernet.in

CERTIFICATE

It is certified that the work contained in this thesis, entitled "**Gold and Copper Based Nanomaterials for Potential Theranostic Applications**", has been carried out by Ms. Rama Ghosh, a student of the Department of Chemistry, Indian Institute of Technology Guwahati, for the award of the degree of Doctor of Philosophy under my supervision. This work has not been submitted elsewhere for any degree.

IIT Guwahati
September 2015

Anumita Paul
Thesis supervisor
Department of Chemistry
Indian Institute of Technology Guwahati
Guwahati – 781039, Assam, India

Dedicated to My Parents

Late Gurupada Ghosh

& Mrs. Niro Bala Ghosh

ACKNOWLEDGEMENTS

My endeavour of complete five years of PhD would not have been so easy without the kindness, grace, attention, encouragement, and support of those who have helped me along the way. Today, while bringing it to the end, I would like to scratch the surface in terms of the amount of people I can name to accolade for making this thesis a reality with a lot of enduring memories.

My thesis supervisor, Prof. Anumita Paul and Prof. Arun Chattopadhyay have contributed a great deal to my development as a researcher and person. Being a PhD student of Prof. Paul and Prof. Chattopadhyay placed me in an advantageous position from day one. Their insatiable curiosity, desire to produce excellent science, work ethic, and willingness to help put me in the perfect environment to succeed. I thank them for taking me into their group and helping to improve my ability to design and carry out research projects independently, along with the ability to present my ideas in a better way. The freedom they gave me in project design during the stay at laboratory allowed me to own the successes and failures that always provided me self-confidence and persistence necessary to produce a good work, in whatever field. I am grateful to Prof. Paul and Prof. Chattopadhyay for their sincere effort to create an atmosphere in the lab that promotes cordiality, team-work, presentations, and scientific discussions. Apart from the academics, they were always been nice to me in their own way and guided me in right directions. Whenever I was being ecstatic or upset, their good sense of humour always could read my mind. It's been 5 years I worked with them, still I find it hard to open up during our conversations, not because of my anxiousness but because of all the respect. Thank you madam and Sir for continually being a path shower in my life.

I thank my doctoral committee members Dr. Kalyanasis Sahu, Dr. Subhas Chandra Pan and Prof. Aiyagari Ramesh for the perceptive advices and invaluable suggestions through timely assessments during the PhD course. I am grateful to the faculty and staff at the Department of Chemistry, IIT Guwahati for providing a delightful working environment during this period.

The guidance of Prof. Siddhartha Sankar Ghosh during collaborations with him is held at high esteem. I am so grateful to him for his time and patience during my discussion about my work and problems. In particular, I would like to thank him for the suggestion he made for my work.

No words can ever be adequate to express my heartiest thank to all the lab mates to support, encourage, and help me in work, and to maintain a pleasant working environment throughput my PhD tenure. I thank my seniors Dr. Jashmini Deka, Dr. Subhojit Das, Dr. Sadhucharan Mallick, Dr. Raihana Begum for graciously taking so much of time to make me acclimatize to the lab environment, procedures, instrumentation, along with providing encouragement through the

early stages of my research career. Special thank is due to my junior Anushree for timely help, scientific conversations, and wonderful time we shared in last three years. I thank my present labmates Dr. Rumi Khandelia, Palash, Satya, Uday, Kafeel Sabyasachi, Ayan and Srestha whose presence made my stay in lab joyful and memorable, especially their indelible help, motivation and encouragement. The company of Dr. Nirmala Devi, Dr. Pallab Sanpui and especially Dr. Madhulekha Gogoi was also pretty heartening.

I thank my other lab mates from Centre for Nanotechnology, Dr. Shilpa Sarma, Dr. Amit Jaiswal, Dr. Amaresh Kumar Sahoo, Sunil, Upashi, Bandhan, and Deepanjoli for companionship and enjoyable moments. I also thank other group members Subhomoy, Archita, Asif, Sharmila and Neha and all my friends at IITG for making the time spent in the laboratory and outside pleasant and memorable. Special thanks to Amaresh and Upashi for their collaborations.

I am lucky to have Sushanta, Kishor, Pupun, Jintu da, Tulsi, Namami and Rupak da as my friends. I would like to express my sincere gratitude to these wonderful people whose care and love allowed me to express all the ups and downs of my life.

I would like to thank Indrajit Da, Dr. Babulal Das, Madhurjya Borah, Dr. Kula K. Senapati and Kesho Singh for their help to analyze samples in need. I am thankful to all the operators at the Department of Chemistry and Central Instruments Facility (CIF), IITG for their time and help in characterizing all the materials.

The research scholarship support from IIT Guwahati is acknowledged.

Finally, my PhD would not have been completed without the eternal love, care, bless, support and encouragement of my mother, and my brothers, When I was unsure of an issue or struggling to overcome an obstacle, their useful advices and optimism helped to provide me a solution to the problem. My mother is the main soul and inspiration for each and every step that I have achieved in my life. I also thank all my family members to provide me encouragement and fun times during family get-togethers.

Rama

TABLE OF CONTENTS

Chapter 1

Introduction and Literature Review

This chapter describes the importance and utility of nanotechnology in various biomedical fields. A brief description of the importance of protein–nanoparticle interaction along with their properties and application of fluorescent metal nanomaterials in theranostic has been studied.

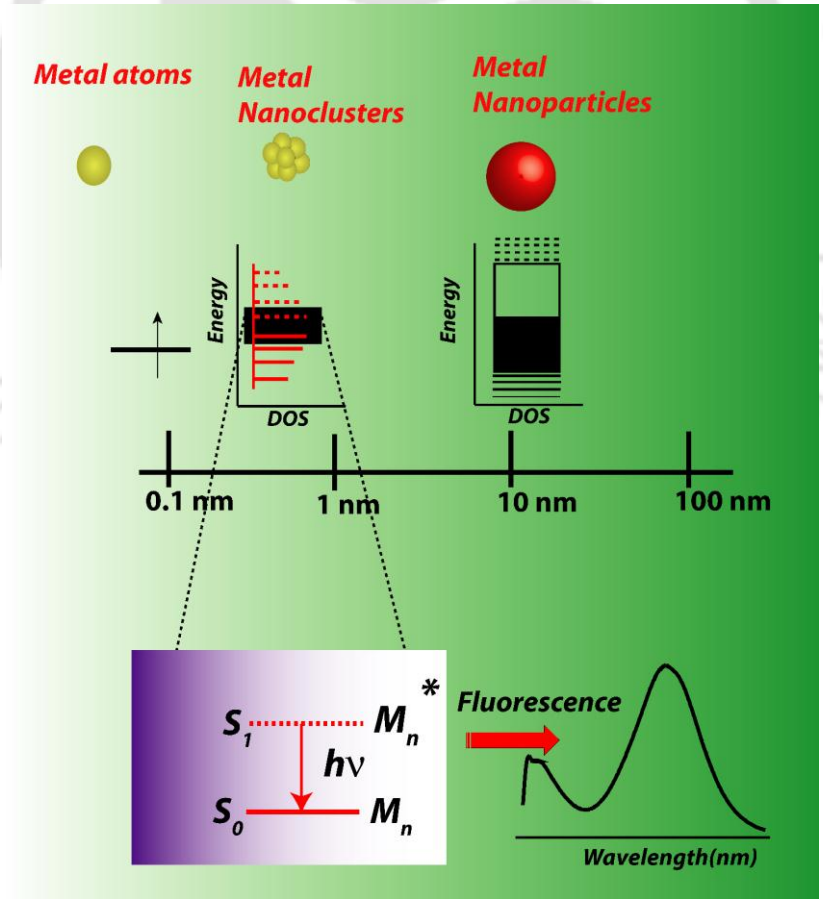

1.1. INTRODUCTION

Nanotechnology, a branch of technology that deals with matters at the nanoscale (i.e., between 1 and 100 nm), arises due to the unique properties of materials in this dimension, allowing innovative applications in varied fields. At the nanoscale level, the properties of materials behave differently from bulk materials as well as their molecular and atomic counterparts. Nanotechnology involves manipulation of matter in this length scale with application in diverse fields such as imaging, sensing and molecular simulation along with ballistic electron devices. This length scale is important as an attractive probe candidate for biological systems. Therefore, the field of biology and nanomaterial have merged in the last few decades to grow into new field called nanobiosciences and nanobiotechnology.

1.2. Metal Nanoparticles

Noble metal nanoparticles (NPs), in nanoscience and nanotechnology, have drawn enormous scientific interest due to their surface plasmon resonance (SPR) along with the other optical properties.[1-4] In addition to photonic properties such as local surface plasmon resonance (LSPR),[5] surface-enhanced fluorescence (SEF),[6] and surface-enhanced Raman scattering (SERS)[7], these NPs possess novel electrical, magnetic and catalytic properties.[8] Such intrinsic properties of NPs are exploited in a variety of applications, spanning from optoelectronics[9] to biological applications.[10-13] In this regard, coinage metals (Au, Ag, and Cu) have received greatest interest starting from exploring various synthetic protocols to studying their varied properties with potent biological applications.[14-17]

1.3. Gold Nanoparticles (Au NPs)

Gold has an interesting chemistry arising from its low reactivity. For example, among all oxidation states, only three, i.e., Au(0), Au(I) and Au(III) are stable in aqueous medium, in *vivo* all three are found to co-exist in equilibrium with each other. On the other hand, Au (0) is more stable in comparison to Au(I) and Au(III) and does not get oxidized in presence of heat, alkali or acid.[18] Interestingly, the human body is composed of a number of elements including Au in trace amounts (0.35 μg of Au–per gram of dry tissue weight). It has been reported that Au plays an important role to maintain the health of joints as well as to transmit electrical signals throughout the body. [18]

On the basis of chemistry of Au *in vivo*, it has been recognized as a promising candidate in medicine by Chinese and Egyptians since 2500 BC. In 1980, Robert Koch, a German bacteriologist, discovered that gold cyanide, *in vitro*, can be bacteriostatic to the tubercle bacillus, and such treatment lasted up to the 20th century. Au has also been used as a

therapeutic agent for the treatment of psoriatic arthritis, juvenile arthritis, and discoid lupus erythematosus.[19] In 1857, Michael Faraday first synthesized Au colloids by reduction of chloroaurate ($AuCl_4^-$) solution using phosphorus in CS_2 in a two-phase system.[20] Later on, in 20th century, various synthetic routes have been developed to obtain Au NPs with diverse properties. Among them, the most common method is the chemical and electrochemical reduction of $AuCl_4^-$ solution. In 1951, Turkevich introduced the synthesis of spherical shaped Au NPs in aqueous medium by the citrate reduction of $AuCl_4^-$ solution.[21] In 1973, Frens has further modified this reduction procedure to synthesize Au NPs of different size, by changing the ratio of the concentration of citrate/$AuCl_4^-$ solution.[22-23] As synthesized Au NPs can be characterized by the SPR band, which normally appears in the visible region ~520–540 nm. Additionally, the shape and size of Au NPs can be modulated to bring the SPR band in the range of 700–800 nm, which is ideal for biomedical applications.[23] Along with size- and shape-dependent optical properties, Au NPs possess other interesting properties (**Figure 1.1**)[24] that make them extremely attractive nanobiomaterials for biological applications.[24,25]

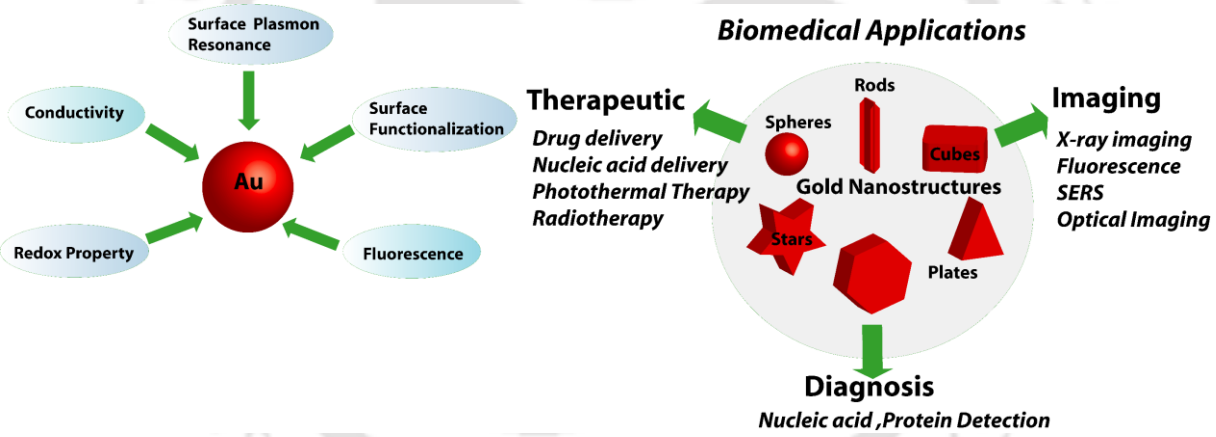

Figure 1.1 Different physical properties of Au NPs which make them an important biomaterial for medical applications due to its different sizes and shapes. Reprinted and reproduced with permission from ref 24, 25. Copyright 2012, 2013 American Chemical Society.

1.4. Protein–Metal Nanoparticles Interactions

The interaction between proteins and NPs can influence the physical and biological properties of NPs**.** Similarly, NPs can influence the conformation of the proteins (**Figure 1.2**).[26] Changes in conformation exposes new epitopes on the protein surface which inhibit the normal functioning of the protein.[27] The increase in surface area of NPs induce increasing avidity effects as a result of close spatial repetition of the same protein. Importantly the protein NPs interactions induce cooperative effect, which either inhibit or promote protein fibrillation or agglomeration of NPs.[28] Therefore, the interaction between Au NPs and protein

is dependent on a number of factors,[29,30] such as (1) composition and surface chemistry of NPs, (2) size and shape of NPs, (3) surface charge of NPs, (4) effects of hydrophobicity/hydrophilicity, and (5) Protein/NP ratio.

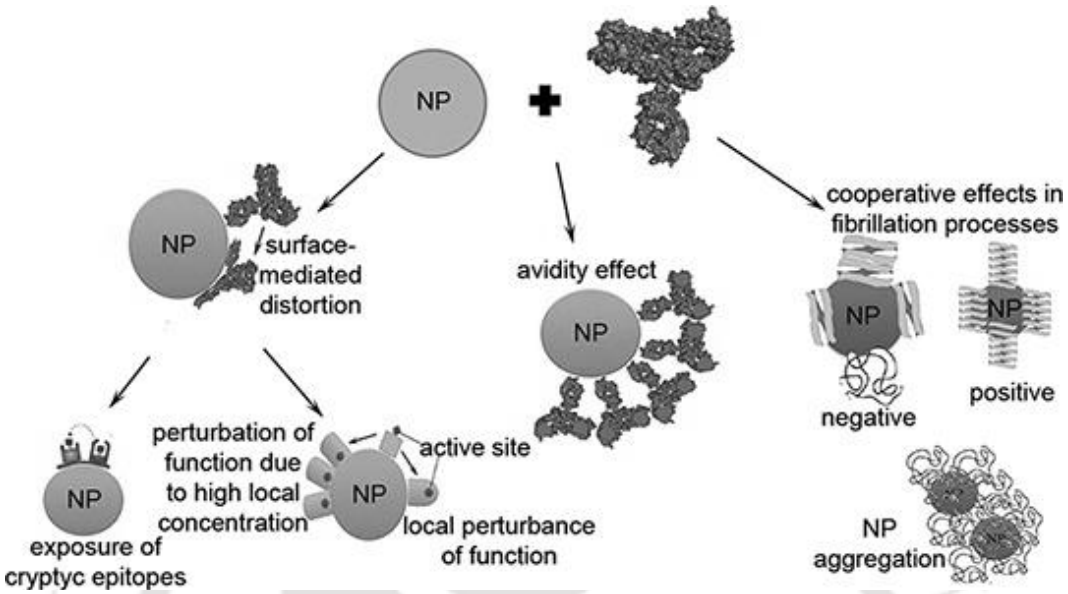

Figure 1.2 Effects of interactions of protein with NPs which altered the protein conformation to exposure the epitopes as well as protein induces NPs agglomeration. Reprinted and reproduced with permission from ref 28. Copyright 2012, American Chemical Society.

1.4.1. Protein–Gold Nanoparticles Interactions

Gold NPs are well studied for the conjugation with proteins due to their unusual optical properties, size dependent electrochemistry, chemical stability, modified surface chemistry, biocompatibility, and a high capacity of protein loading.[31] The interaction of Au NPs with different proteins induces the agglomeration of NPs depending upon size,[32] concentration, conformation,[33,34] and isoelectric point of the respective protein.[35] The protein induced Au NPs agglomeration is also dependent upon size, shape and surface functionality of Au NPs.[29,30]

1.4.2. Outcome of Protein–Nanoparticles Interactions

The interaction of NPs with protein gives a better understanding of the application of proteins/NPs in biological and medical science. Interestingly, the interaction of proteins with the surface of NP determines how a living system, which interacts with NPs, modifies its cellular responses to these NPs. Further, the adsorption of protein onto NPs gives information about the toxicity at cellular levels. Therefore, there is a scope to design nanomaterials of

different safety levels via predetermined nature and conformation of the protein that is adsorbed onto the surface of NPs for different biomedical applications (**Figure 1.3**).

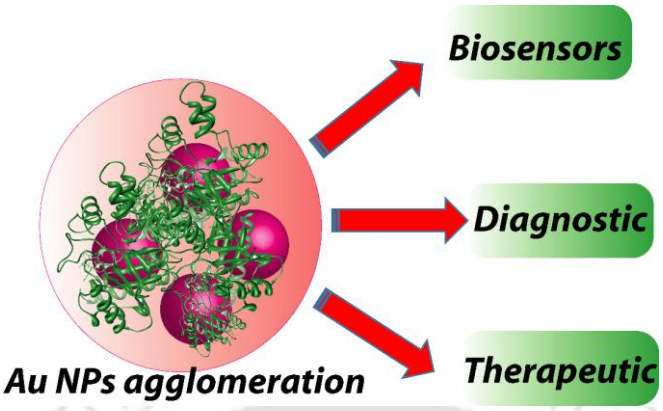

Figure 1.3 Biomedical applications due to the protein- NPs interactions.

The potential application of nanomaterials in biomedical field include improvement in diagnostic therapy, *i.e.*, theranostic. In recent years, multifunctional systems have been developed by combining drugs, molecular targeting and imaging agents into a single system.[36-39] The combined properties like imaging and therapeutic capabilities of such systems (carrier) improve the therapeutic outcome of drug delivery.[40,41] In addition, spectroscopic technique, e.g., fluorescence is also an important tool needed for the bioanalysis and imaging.[42] One of the advantages of these multifunctional systems is that they can be used to monitor the delivery of drugs with fluorescent labelling agent. In this regard, fluorescent nanomaterials such as quantum dots (Q-dots)[43-46] and metal nanoclusters (NCs)[47,48] are more superior over the conventional organic fluorophores because of their low photo bleaching ability. Interestingly, nowadays, metal NCs have been widely used as an imaging agent due to their low toxicity, chemical stability, excitation wavelength tuneability, pH dependent emissive properties, and lower toxicity than the Q-dots.[49,50]

1.5. Fluorescent Metal Nanoclusters (NCs)

Recent developments in nanotechnology have given tremendous boost to generate different new fluorophoric labels. Among them, metal NCs are found to be the most popular choice due to their unusual electronic structures along with their distinct physicochemical properties. Interestingly, metal NCs with a dimension <2 nm gets comparable to the Fermi wavelength of an electron.[51] Thus in this size regime, the continuous energy levels of NCs break down into discrete and size tunable energy levels, imparting molecular properties to the NCs as seen by quantum confinement effects,[52-54] optical (emission,[55,56] two-photon absorption,[57] and

other optical phenomena[58,59]), electrical and the chemical properties, similar to those seen in molecules.[60] Another fascinating role of these NCs is that they can be considered as the missing link between atoms and nanoparticles. Furthermore, their properties also differ significantly from the nanoparticles and bulk counterparts (**Figure 1.4**).[51,61,62] The comparable small size, high chemical stability, enduring photostability, low cytotoxicity, and high luminescence quantum yield (QY) of the metal NCs build a robust platform for their use in different biological applications. In the last few years, metal NCs have been widely used for sensing, biolabeling, bio imaging, drug delivery, and chemical catalysis.

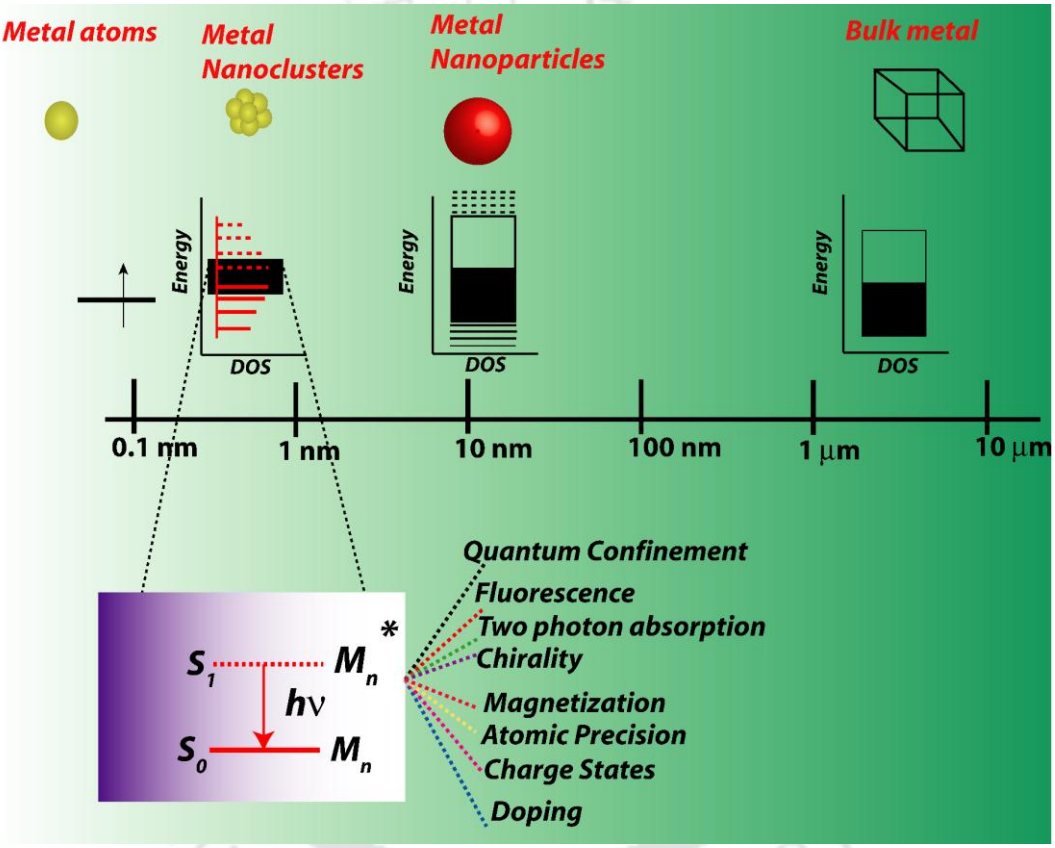

Figure 1.4. Effects of size on the properties of metals. Metal NCs are forming a bridges between the atom and NPs. Due to the discrete energy levels, NCs show various physicochemical properties. Reprinted and reproduced with permission from ref 62. Copyright 2014, Elsevier.

1.6. Methods for Synthesis of Fluorescent Metal NCs

Synthesis of NCs with high QY is the most critical factor that governs their potential use in different biological applications. In order to obtain high QY of the NCs, a few key parameters should be taken under consideration,[62] which are

(1) Metal–ligand interaction should be strong.

(2) Strong reducing agent and longer sonication time should be used.

(3) Longer time periods for the reactions.

Notably, bare NCs are unstable in aqueous medium and hence templates such as, thiolates, phosphines, dendrimers, polymers or biomolecules (protein, DNA, RNA peptides) are required to protect them. Recently, researchers have developed a vast number of synthetic methods to synthesize metal NCs. Depending on the types of stabilizers employed for the synthesis of fluorescent metal NCs, a few synthetic strategies are discussed below.

1.6.1. Synthesis of Thiol Protected Metal NCs

Thiol (–SH) containing small organic molecules are normally used to synthesize metal NCs *via* the reduction of metal ions using reducing agents. Recent years have witnessed the viable use of different –SH containing ligands like glutathione (GSH),[62-66] tiopronin,[67] phenylethylthiolate,[68] thiolate α-cyclodextrin,[69] 3-mercaptopropionic acid,[70] dihydrolipoic acid (DHLA),[71] and D-penicillamine (DPA),[72] *etc*.[73,74] for the synthesis of highly fluorescent metal NCs with high QY in aqueous medium. On the other hand, thiolates are also used to synthesize monolayer protected metal NCs by etching metal NPs with excess thiol.[48,75-77]

1.6.2. Synthesis of Dendrimers Protected Metal NCs

Dendrimers are basically branched molecules having different sizes and small cavities in their molecular framework. These cavities are used to synthesize metal NCs. For example, poly(amidoamine) dendrimers (PAMAM) are commonly used to synthesize size and emission specific Au/Ag NCs with two digit QY.[78-80]

1.6.3. Synthesis of Polymer Protected Metal NCs

Polymers have lavish functional groups such as, carboxylic, hydroxyl, epoxy, amine, *etc.*, which give the opportunity to bind with metal ion to stabilize the metal NCs. Many polymer molecules that have been used to synthesize highly fluorescent metal NCs with high QY using different synthetic method such as sonochemical,[81] microwave assisted[82] and photoreduction.[83,84] Paradigms include the use of polymers such as, poly(N-isopropyl acrylamide-acrylic acid-2-hydroxyethyl acrylate),[83] polyglycerol-block-poly(acrylic acid), poly(methacrylic acid),[81–86] polyethylenimine,[87] chitosan,[88]and poly(N-vinylpyrrolidone),[89] especially in the synthesis of Au and Ag NCs in aqueous medium.

1.6.4. Synthesis of Biomolecule Protected (template) Metal NCs

Proteins have been used as the first biomolecule to synthesize metal NCs with high colloidal stability in aqueous medium with longer shelf time. Biomolecules such as, protein, peptide

and DNA have been used for last few years to synthesize NCs due to the following key factors.[90]

(1) Biomolecules are rich in chemistry. They have a number of functional groups that can easily coordinate with metal ions and help in the controlled formation of metal NCs.
(2) Biomolecule protected NCs can be synthesized in aqueous medium at room temperature.
(3) Biomolecules can act as reducing as well as protecting agents for synthesis of NCs in aqueous medium.

Interestingly, biomolecules act as template, etching agent and also provide a number of functional groups for the synthesis of metal NCs, as schematically illustrated in **Figure 1.5**. Nowadays, a variety of proteins are being used as efficient templates which direct the formation of metal NCs. For example, Xie *et al.* have developed an efficient method to synthesis Au NCs by using Bovine serum albumin (BSA) with a QY of ~6%,[91] where BSA act as a reducing as well as a protecting agent.[92,93] Later on, by adopting a similar method, researchers have synthesized metal NCs by using lactoferrin (Lf),[94,95] transferrin (Tf),[96] and lysozyme (Lyz)[97,98] as templates. Similarly, enzymes such as, pepsin,[99] insulin[100] and horseradish peroxidase (HRP),[101] can be used for the synthesis of metal NCs with high quality. In recent years, researchers have modified the synthetic method by using a reducing agent for the synthesis of NCs in presence of protein as a template.[102-105] The synthesis efficacy of NCs has been increased by using some input energy through sonochemical and microwave assisted method.[106,107]

Like proteins, peptides, containing significant amino acids, are also greatly responsible for the synthesis of metal NCs. It is well known that cysteine, histidine, and methionine are the amino acids that are capable of forming complexes with metal ions, whereas arginine, tyrosine, and tryptophan are present in proteins or peptides and are good reducing groups. In the last few years, it has been observed that –SH containing amino acid (cysteine) favors the formation of metal NCs due to the possible formation of a strong metal−sulfur bond.[108] In this regard, cysteine containing peptide such as glutathione (GSH) has been extensively used for the synthesis of different types of metal NCs in presence of reducing agents.[65,66,109-112] Recently, some synthetic peptides (Asp-Cys-Asp, Glu-Cys-Glu, Ser-Cys-Ser, Lys-Cys-Lys, and CCYTAT) have also been used for the synthesis of fluorescent metal NCs.[113-115]

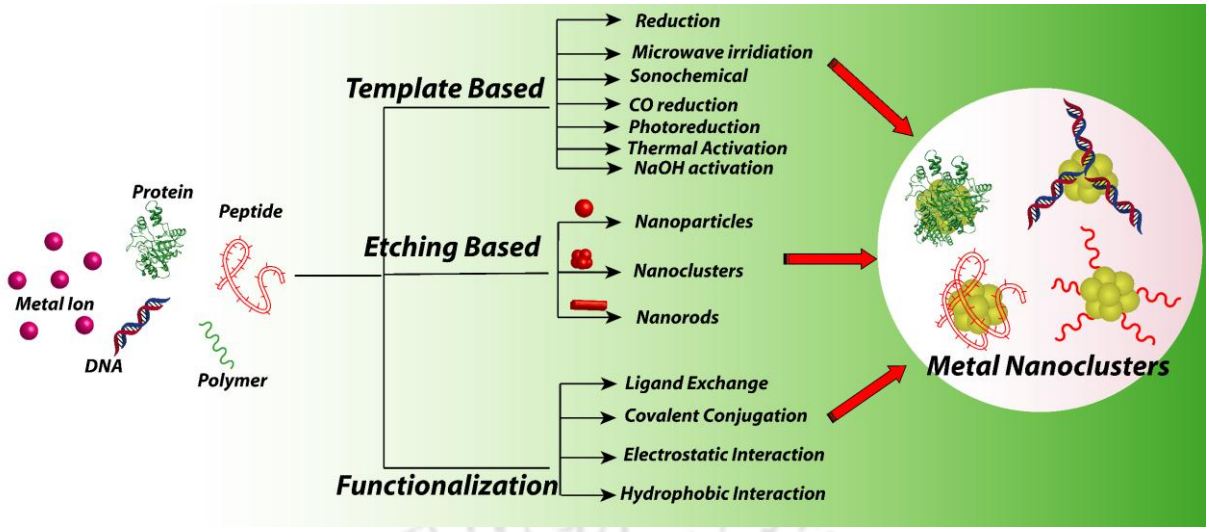

Figure 1.5 Different process of synthesis of metal NCs in presence of biomolecules and the role of biomolecules as a template, etchant and various method for functionalization.

It is fascinating to know that well-known interactions between the metal ions and deoxyribonucleic acid (DNA) have led to the formation of DNA based metal NCs. [116-121] In 2004, Dickson *et al.* have first introduced the synthesis of Ag NCs using DNA.[116] Interestingly, both single- and double-stranded DNA have been used for the synthesis of different light emitting (red, blue, and green) fluorescent metal NCs by modifying the method of synthesis e.g., use of mild reducing agents.[122-123]

Biomolecules are not only used as the template, but also act as an etchant (etching ligand) for the synthesis of metal NCs starting from NPs. Whetten *et al.* have first introduced thiolate as an etchant for the synthesis of NCs.[124] Biomolecules which are rich in –SH containing ligand (such as GSH) have been successfully used as etchants to facilitate the formation of metal NCs having different sizes in solution.[66,75,76,125-127] Similarly, protein (BSA), peptide, and amino acid have also been used as the etchants for the synthesis of metal NCs.[128]

1.7. Applications of Metal NCs

Metal NCs have taken up broad interest in biological applications due to their attractive and fascinating physicochemical and physiological properties, including size-dependent fluorescence, high photostability, large Stokes shift, biocompatibility *etc*. All these inherent properties of NCs make them an excellent platform for all types of applications, spanning from optoelectronics to biomedical fields. Interestingly, the major application of metal NCs focuses on the field of biology and are discussed in details below (**Figure 1.6**).

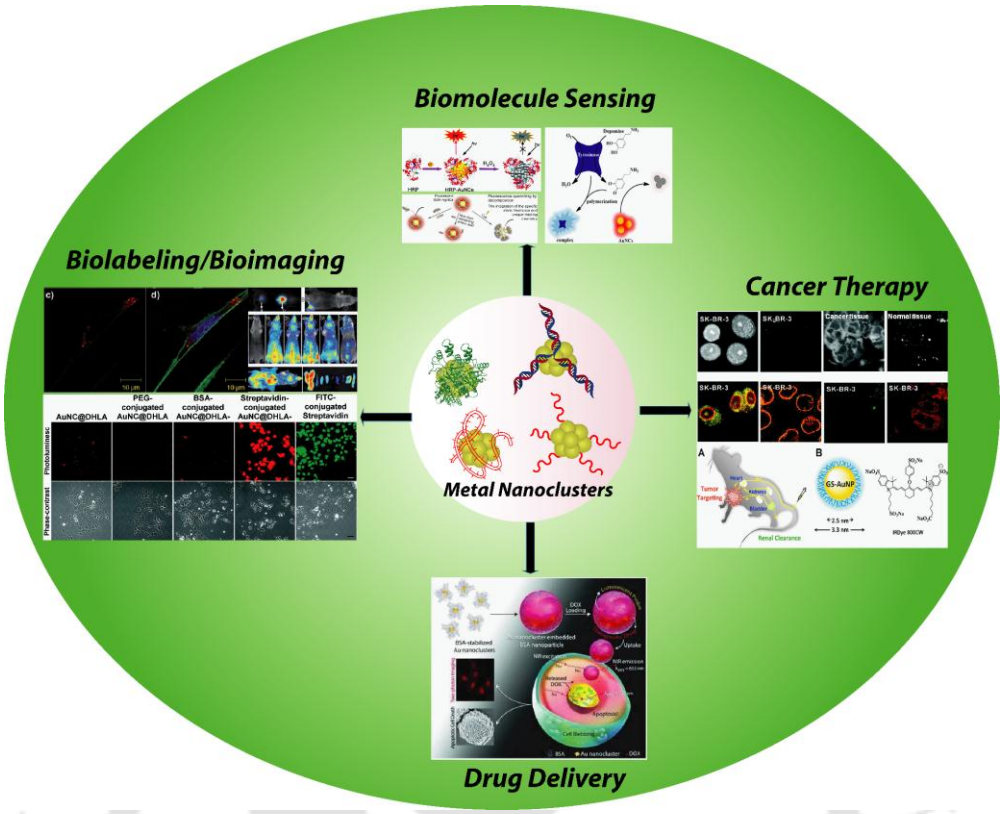

Figure 1.6 Applications of Metal NCs especially in biomedical applications. Reprinted and reproduced with permission from ref 48, 109, 138, 140, 148, 151 and 100, 146, 149. Copyright 2009, 2011, 2013, 2015, American Chemical Society, Copyright 2011, 2015, John Wiley and Sons and Copyright 2010, Royal Society of Chemistry.

1.7.1. Biomolecules Sensing

Biomolecules sensing and reactive oxygen species (ROS) sensing are the two most important areas of diagnosis that provide information about the different phases of diseases including cancer.[129] Past two decades have witnessed the extensive use of metal NCs for the detection of biothiols (Cysteine; Cys), GSH, homocysteine (Hcy), nucleic acid, protein, amino acid and DNA along with ROS such as, hydrogen peroxide (H_2O_2) by making use of quenching of fluorescent properties of NCs. In particular, biothiols (Cys, GSH and Hcy) play important maintenance roles in biological systems *via* processes like detoxification and metabolism. The alterations in concentration levels of biothiols in human body can lead to different diseases including leucocyte loss, psoriasis, liver damage, cancer, and AIDS.[130,131] Hence, the detection of biothiols has become key for the treatment of such diseases. For example, poly(methacrylic acid) stabilized Ag NCs have been used to detect Cys over and above other amino acids by a simple fluorescence method.[132] Based on similar fluorimetric methods, single stranded DNA-Ag NCs,[133,134] GSH-Ag NCs[109] and Lyz-Au NCs have also been used to detect Cys, GSH and Hcy in plasma samples with high sensitivity and selectivity due to the favorable formation of non-fluorescent complexes of Ag/Au with different thiol.

Similarly, Au NCs have widely been used for the detection of glucose,[135,136] trypsin,[137] dopamine,[138,139] and H_2O_2 [140] in solution by the quenching of fluorescence property of NCs.

Along with the detection of biothiols and small molecules, metal NCs have also been extensively used for the detection of proteins and nucleic acids. For example, Au NCs have been conjugated with receptor such as, anti-human IgG antibody to detect IgG.[141] Similarly, a large number of proteins like glutathione S-transferase (GST)-tagged proteins,[142] BSA, thrombin [143]*etc*. have been detected by Au and Ag NCs. Recently, Zhang *et al*. have reported the selective detection of DNA and ATP molecules by photoinduced electron transfer (PET) between luminescent DNA-Ag NCs and G-quadruplex/hemin complexes.[144] Interestingly, detection of microRNA (miRNA) is another important application of NCs because miRNA detection alone can act as a biomarker for disease detection. For example, DNA-Ag NCs have been designed in different ways to detect miRNA and miRNA sequence as a probe/an electrochemical probe.[145]

1.7.2. Bioimaging and Biolabeling Agent

The physical and chemical properties such as, small size, biocompatibility, brightness, and high QY, low toxicity and photostability of noble metal NCs make them an ideal fluorescence probe for bioimaging and biolabeling application over other conventional organic dyes and Q-dots. Importantly, NCs can be used as optical probes since their fluorescent properties are near infrared (NIR) region, due to which the interference from emission in the range 400–600 nm in biological media is avoided.[146]

In 2005, Baskakov *et al*. for the first time, demonstrated the use of Ag NCs (in combination with thioflavin T) in bioimaging wherein they used fluorescence microscopy to detect stained amyloid fibrils having green fluorescent emission.[147] In recent studies, metal NCs have been extensively used for bioimaging of cells in conjugation with biologically active molecules to target specific locations. The efficiency of easy functionalization of NCs is a boon for biolabeling imaging and cancer cell detection. For example, conjugation of BSA-Au with Herceptin and folic acid receptors have been used for targeting nuclear localization of ErbB2 in over-expressing cancer cells.[148] Similarly, a wide variety of Au and Ag NCs has been conjugated with polyethylene glycol (PEG), BSA, avidin, and streptavidin *via* EDC coupling to the use in bio imaging applications.[48] Interestingly, some protein stabilized metal NCs (such as, insulin, and transferrin) can be directly used to target transferrin receptor overexpressed cells[96] and insulin receptor overexpressed cells.[100] Moreover, recent studies have revealed the use of metal NCs for intracellular labeling and imaging in conjugation with cell penetrating peptide, transfecting agent or simple

endocytosis. Therefore, metal NCs have been used as an imaging probe *in vitro*, whereas their high solubility, low cytotoxicity and high penetration capability make them ideal candidate to use in live animal cell imaging. For example, Au NCs (BSA, GSH stabilized) have been applied to *in vivo* imaging, including biodistribution, renal clearance, pharmacokinetics, and tumor accumulation.[47,149-151] Two photon imaging technique is advantageous because of its high penetration depth as well as high spatial resolution in imaging with minimum auto fluorescence and background scattering. In recent studies, especially Au NCs have been extensively used in live cell imaging by using two photon excitation confocal microscopy with an excitation laser of 800–810 nm.[146]

1.7.3. Cancer Therapy

Cancer is a worldwide threat for mortal sickness and has become a major public concern. Early, detection and identification of cancer is the first and foremost step of a successful treatment plan. The development of new techniques to diagnose cancer should therefore be easy, rapid, and sensitive. Recent advances in nanotechnology have provided the standard to develop nanoscale NIR fluorescent probes which have low toxicity, bright fluorescent, smaller size for tumor imaging, and therapy. One of the reported examples is the use of folic acid (FA)-conjugated red luminescent BSA-Au NCs to detect and target cancer cells with over-expressed folate receptors through receptor-mediated endocytosis.[152, 153] Similarly, monoclonal antibody such as Herceptin can be used to detect breast cancer. Herceptin conjugated Au NCs have also been used to detect and target HER2 breast cancer cells with over-expressed Erb2 and tumor tissues.[148] Especially impressive can be seen in latest development, where metal NCs used to detect and treat cancer in a variety of ways. For example, Wang *et al*. have constructed Au NCs-GO composite where Doxorubicin is transported across HepG2 hepatocarcinoma cell membranes and thus establish the inhibitory mechanism on cancer cells.[154]

On the other hand, Au NCs can also be covalently grafted with gadolinium complex of diethylenetriaminepentacetic acid (DTPA) and used as a bimodal magnetic resonance imaging, MRI/optical nanoprobes. This nanoprobe shows higher relaxivity in comparison to clinical Gd-DTPA with intake fluorescence emission.[155] Similarly, Kong *et al*. have reported a multimodal imaging probe Gd^{3+} with Au NCs for use of its fluorescence/magnetic resonance properties.[156] Like MRI, insulin stabilized Au NCs have been used for X-ray computed tomography (CT) imaging that shows dose dependent enhancement in contrast to C2C12 myoblast cells.[100] Once cancer is detected, immediate important issue is to treat cancerous cells for cure. One of the developed prospects of treatment of cancer is

radiotherapy, which is applied to reduce tumor using high energy X-ray. With the advance of nanotechnology, a variety of nanomaterials has been developed and widely used for cancer therapy. One of the practical examples is the use of Au NPs as a radiosensitizer for the treatment of cancer due to their high absorption and high efficiency to generate radiation.[157] A good sensitizer should have some key features such as, good accumulation in tumor for sufficient enhancement in radiotherapy, tumor targeting good capability, biocompatibility, and a good renal clearance to minimize the side effects. In addition, it is found that GSH-Au NCs and BSA-Au NCs have increased tumor uptake by passive targeting specificity *via* enhanced permeability and retention (EPR) effect due to the biocompatible GSH and BSA shell on the NCs. On the other hand, identical Au NCs have 10 to 100 times more renal clearance through kidney filtration and hence stabilizes the luminescent Au NCs during blood circulation. Thus, GSH-Au NCs and BSA-Au NCs have been used as effective radiosensitizers that can feasibly enhance the safety and efficacy of radiotherapy.[150, 151, 157-159]

1.8. Copper Nanoclusters (Cu NCs)

Copper (Cu) is an essential trace nutrient, which is required throughout one's life time starting from the growth to survival. It is essential for the formation of blood vessels, healthy heart, collagen formation, brain development as well as for healthy bone and teeth. According to the World Health Organization (WHO), 1.33mg/day Cu is required to maintain metabolic requirements in a human body. On the other hand, deficiency of Cu causes osteoporosis, rheumatoid arthritis, and cardiovascular diseases.[160] The earliest mention of medical use of Cu is found in 2600 and 2200 B.C, by Smith Papyrus, an Egyptian medical text author, where he writes the use of Cu to sterilize chest wounds and drinking water. Later on, in 19th century, Cu has been used for immunization against cholera in Paris and France. In 19th and 20th century, the utilization of Cu has been widespread for the treatment of chronic adenitis, eczema, impetigo, scrofulosis, tubercular infections, lupus, syphilis, anemia, chorea, and facial neuralgia. The possible reasons for this are, the antimicrobial nature of Cu and its role as an antifungal agent in contact killing.[161] In this context, Cu NPs have been used as antimicrobial and antifungal agent since the last few decades. The antimicrobial action of Cu NPs has been extensively used for several purposes such as, textiles and cosmetics, food processing, water treatment, and so on.[162] Interestingly, the efficiency of antimicrobial activity of Cu can be further enhanced by changing its size from the bulk to nano, e.g., Cu NPs. Sincere efforts are therefore being made to reduce the dimension of Cu NPs up to <3 nm i.e. Cu NCs. However, unlike Ag and Au, it is a challenging task due to its reactive oxidation state. In essence, the ease of oxidation of Cu (E_0, 0.34 V), in contrast to that of Ag

(E_0, 0.80 V) and Au (E_0, 1.50 V), is the real bottleneck in developing new synthetic methods, especially in aqueous medium.

1.8.1. Synthesis

Synthesis of small and fluorescent Cu NCs is still limited as they are prone to oxidation on exposure to air in comparison to the Ag and Au counterparts. The preparation of ultra small, fluorescent Cu NCs thus remains as an ardent technical challenge and hence a limited number of reports focusing on the synthesis of Cu NCs were found. A few of the promising synthetic methods are demonstrated and summarized in **Figure 1.7**.[163] In 2009, Vazquez-Vazquez *et al.* have synthesized Cu NCs using a microemulsion technique and revealed the possibility to control their size and fluorescent property by tuning the concentration of reducing agent (**Figure 1.8**).[164] Serra *et al.* have also synthesized Cu NCs (Cu_N, $N \leq 14$), stabilized with tetrabutylammonium nitrate, using a simple electrochemical technique and reported a high QY of ~13 %.[165] Further, Cu NCs have been synthesized by (i) microwave assisted polyol method without adding any external protective and reducing agent[166] and (ii) photoreduction method by poly(methacrylic acid) functionalized with pentaerythritol tetrakis 3-mercaptopropionate.[167] Similarly, Cu NCs have been synthesised by a one pot wet chemical reduction using 2-mercapto-5-n-propylpyrimidine,[168] D-penicillamine (DPA),[169] BSA,[170,171] as a stabilizing ligand with high QY. On the other hand, DNA can also be used as a template for the formation of Cu NCs.[172, 173]

Apart from the top up approaches, Cu NCs have also been synthesized by top down methods such as, etching method. Paradigms include the synthesis of highly fluorescent Cu NCs using size-focused etching process in the presence of excess of thiolate (GSH) ligands. Interestingly, such Cu NCs show aggregation induced emission enhanced effect.[174]

1.8.2. Application

Similar to Au and Ag NCs, Cu NCs also possess photophysical and photochemical properties such as, high QY, biocompatibility, water-dispersibility, high fluorescence, and surface bioactivity and small size *etc*. These properties make them a potent platform for different applications, especially in cellular labeling and catalysis.[170] In the recent few years, Cu NCs have been used for the detection of metal ion like Pb(II) in water up to the ppm concentration. The detection was associated with the quenching of fluorescence of NCs through the complex formation between Pb(II) and BSA, leading to aggregations.[171] Similarly, Cu NCs are also used for the detection of glucose and H_2O_2. Apart from detection, Cu NCs have shown catalytic activity for the reduction of O_2 and methylene blue (MB).[169]

Interestingly, Cu NCs have been used to detect match and mismatch sequences with 15-mer probe DNA in solution. The fluorescence property of NCs have used as a fluorimetric indicator of the DNA hybridization event.[172]

Moreover, strong fluorescent property and low toxicity of Cu NCs enable them to be used as a bioimaging probe for labeling the cancerous cells. For example, Lyz and BSA stabilized Cu NCs have been used to label cervical (HeLa) cells and CAL-27 cells, respectively.[170]

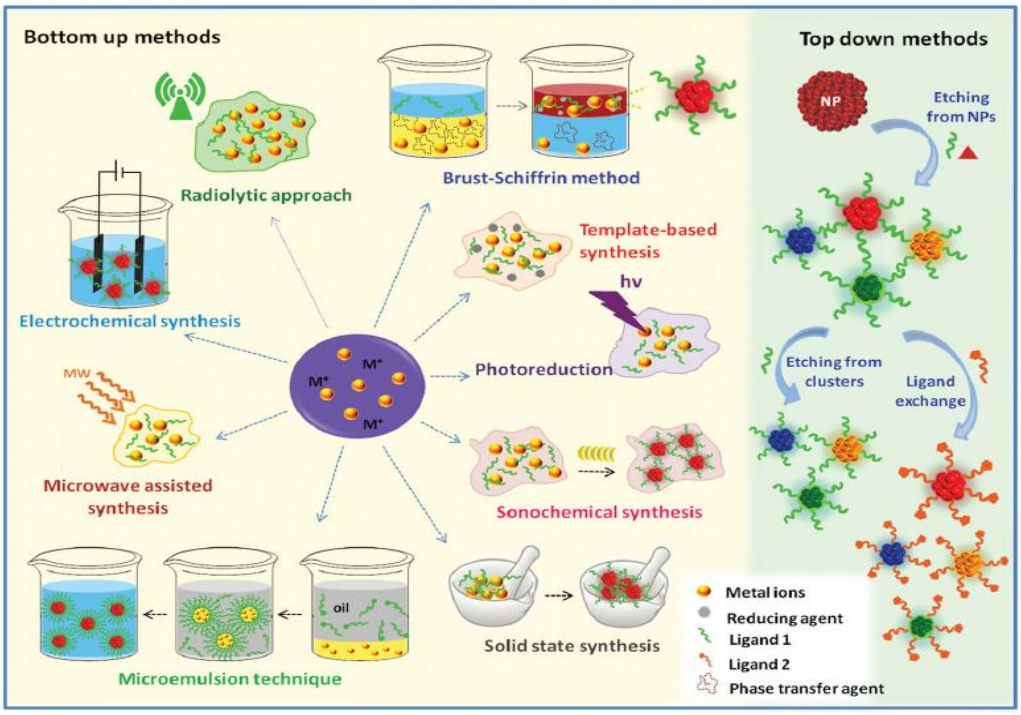

Figure 1.7 Various synthetic routes of metal NCs. Reprinted and reproduced with permission from ref 163. Copyright 2014, John Wiley and Sons.

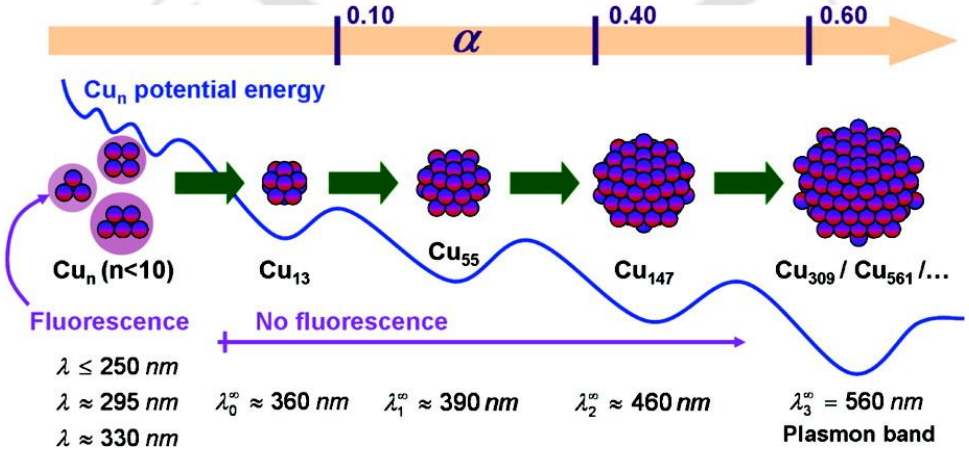

Figure 1.8 The increase size of Cu NCs with the increase in concentrations of $NaBH_4$ by microemulsion technique. Reprinted and reproduced with permission from ref 164. Copyright 2009, American Chemical Society.

1.9. Key Areas and Scopes

Based on the literature review, the potential application and scopes of research of nanomaterials (Gold and Copper) in theranostic are summarized below.

- Investigating the interaction of nanomaterials with protein to determine how NPs interact with living systems and thus modify their cellular response to NPs. There is a potential scope to design a nanomaterial by predetermining the nature of the conformation of protein that adsorbs on to the surface of NPs for different theranostic application.
- Synthesis of fluorescent metal NCs, especially Cu NCs, which is a challenging task due to its reactive oxidation and easy prone to oxidation on exposure to air.
- Investigating the mechanistic origin of antibacterial activity of fluorescent Cu NCs.
- Synthesis of biocompatible Cu NCs with high QY for their potential use in biolabeling for cervical cancer cells.
- Design and development of theranostic multifunctional nanocomposite based on Cu NCs for cancer therapy.

1.10. Outline of the Thesis

This thesis is divided into 6 parts. **Chapter 1** focus on the general introduction and a review of literatures of current position of nanotechnology in biomedical applications, especially relevant those topics and works contained in the thesis. The remaining five chapters are described as follows.

Chapter 2 describes the effect of a chemical denaturant on the agglomeration behavior of a citrate stabilized Au NP–protein composite. The agglomeration behavior has been studied by UV–Vis and Fourier transform infrared (FTIR) spectroscopy, circular dichroism (CD), dynamic light scattering (DLS) based particle size analyses, fluorescence studies, zeta potential measurements, and transmission electron microscopy (TEM). Our studies indicated that when α-amylase was added to a cit–Au NP dispersion, agglomerated structures were formed whose sizes increased with time. On the other hand, when urea was also added, the agglomerated structures did not grow further indicating that the agglomeration process was arrested. In addition, urea was found to permeate to the surface of Au NPs in the agglomerated units, as seen by changes in the UV–Vis spectra, zeta potential measurements, FTIR and fluorescence measurements. Results of CD and FTIR spectroscopy studies are indicative of the cit–Au NP induced conformational changes of α-amylase leading to its

agglomeration. The activity of the proteins present in the agglomerated structures was still retained. Interestingly, addition of chemically denatured protein (urea treated α-amylase) to the cit–Au NP–protein composite did not result in further agglomeration of the composite. The observations reported herein indicated that the interaction between the cit–Au NP and protein leading to agglomeration is dependent on the conformation of protein. Urea induced unfolding of the free proteins and the presence of ions in the medium stopped the growth of the agglomerated structures.

Chapter 3 presents the excellent bactericidal activity of Cu NCs with particular focus on understanding their possible mechanism of antibacterial action. The minimum inhibitory concentration (MIC) and minimum bactericidal concentration (MBC) values of Cu NCs against *E. coli* bacteria were found to be 13.2 ± 0.46 μg/mL and 16.1 ± 0.8 μg/mL (in terms of the concentration of Cu being present in Cu NCs), respectively, which was much less than all the reported literature values for Cu-based NPs till date. Field Emission scanning electron microscopy (EDS-FESEM) revealed that Cu NCs were present to the bacterial surface through electrostatic interaction leading to the changes in the bacterial membrane integrity. It was also found that smaller sized Cu NCs generated significant amount of intracellular ROS. The enhanced transportation of Cu NCs through the bacterial membrane, due to their ultra-small size, caused an increase in cell permeability leading to cell death. The growth curves and atomic absorption spectroscopy (AAS) studies indicated that the antibacterial activity was governed by Cu NCs rather than by Cu^{2+} leached out from the NCs. Moreover, it was found that the Cu NCs had limited toxicity towards mammalian cells.

Chapter 4 demonstrates the synthesis of highly fluorescent Cu NCs using single step reduction of copper sulphate by hydrazine, in the presence of lysozyme is reported. The fluorescence QY was measured to be as high as 18%. The emission was also found to be dependent on the excitation wavelength. Mass spectrometric analyses indicated the presence of species corresponding to Cu_2 to Cu_9. TEM analyses indicated the formation of agglomerated particles with average diameters of 2.3 nm, which were constituted of smaller particles of average diameter of 0.96 nm. They were found to be stable between pH 4–10 and in addition to having excellent chemical stability. The NCs showed high photoluminescence QY, excitation tuneable fluorescence, high photostability and colloidal stability. They could be used for labeling HeLa cells. In conjunction with the photoluminescence properties, their low cytotoxicity would make them an ideal choice for biological and biomedical applications. The composite is comprised of Cu and lysozyme, where Cu is an essential trace

element present in body and lysozyme, an anti-microbial enzyme, is substantially present in a number of secretions, such as tears and saliva. Thus the composite might be considered as biocompatible. The observed stability of the composite, coupled with the retention of fluorescence at physiological pH, is important for applications *in vitro* as well as *in vivo*.

Chapter 5 describes the synthesis of red fluorescent monodispersed Cu NCs in aqueous medium by using dihydrolipoic acid, in combination with biocompatible polymer polyvinylpyrrolidone (PVP) as a stabilizer. The fluorescence of the composite was found to be sensitive to the pH of the medium and the emission could be tuned reversibly according to the pH. Also, the polymer NC composite could easily be synthesized in the form of hydrogel nanocarrier, by using PVA as the cross linker, which is favorable for cellular uptake. The hydrogel could then be turned into a powder, which showed stable luminescence, owing to the NCs, for more than a month. Further, the emission due to the NCs was useful for imaging mammalian cells by optical microscopy and more importantly to probe the cells by commercial flow cytometer, without having to use any other dye. Cu NC containing hydrogel could encapsulate cisplatin for effective delivery to cancer cells, which was probed by using the emission properties of the NCs. Interestingly, it was found that Cu NCs generated reactive oxygen species in the cancer cells and hence enhanced the efficacy of cisplatin in killing the cells thus providing a synergy of action. In addition, optical imaging of the uptake of stable red fluorescent Cu NCs may find use in theranostic applications, owing to their high luminescence.

Chapter 6 presents a summary of the works reported in the thesis

1.11. REFERENCES

1. Kelly, K. L.; Coronado, E.; Zhao, L.L.; Schatz, G.C. *J. Phys. Chem. B* **2003**, *107*, 668–677.
2. Emory, S. R.; Nie, S. *J. Phys. Chem. B* **1998**, *102*, 493–497.
3. Ferrando, R.; Jellinek, J.; Johnston, R. L. *Chem. Rev*. **2008**, *108*, 846–910.
4. Cortie, M.B.; McDonagh, A. M. *Chem. Rev*. **2011**, *111*, 3713–3735.
5. Endo, T.; Kerman, K.; Nagatani, N.; et al. *J Phys: Condens Matter*, **2007**, *19* 215–201.
6. Rosi N L, Giljohann D A, Thaxton C S, et al. *Science*, **2006**, *312*, 1027–1030.
7. Zhang, X. Y.; Young, M. A.; Lyandres, O.; et al *J. Am. Chem. Soc.*, **2005**, *127*, 4484–4489.
8. Kim, B.H.; Hackett, M.J.; Park, J.; Hyeon, J. *Chem. Mater*. **2014**, *26*, 59−71.
9. Talapin, D. M.; Lee, J-S.; Kovalenko, M.V.; Shevchenko, E. V. *Chem. Rev*. **2010**, *110*, 389–458.
10. Jain, P. K.; Huang, X.; El-Sayed, I. H.; El-Sayed, M. A. *Acc. Chem. Res*. **2008**, *41*, 1578–1586.
11. Stewart, M. E.; Anderton, C. R.; Thompson, L. B.; Maria, J.; Gray, S. K.; Rogers, J. A.; Nuzzo, R. G. *Chem. Rev*. **2008**, *108*, 494–521.
12. El-Sayed I H, Huang I X, El-Sayed M A. *Cancer Lett*, **2006**, *239*, 129–135
13. El-Sayed I H, Huang X H, El-Sayed M. A. *Nano Lett*, **2005**, *5*, 829–834.
14. Sperling, R.A.; Gil, P.R.; Zhang, F.; Zanella, M.; Parak, W. J. *Chem. Soc. Rev*., **2008**, *37*, 1896–1908.
15. Nam, J.; La, W-G.; Hwang et.al. *ACS Nano,* **2013**, *7*, 3388–3402.
16. Brown, P. K.; Qureshi, A. T.; Moll, A. M.; Hayes, D. J.; Monroe, W. T. *ACS Nano,* **2013**, *7*, 2948–2959.
17. Kaweeteerawat et al. *ACS Nano*, **2015**, *9*, 7215–7225.
18. Merchant, B. *Biologicals* **1998**, *26*, 49–59.
19. Thakor, A. S.; Jokerst, J.; Zavaleta, C.; Massoud, T. F.; Gambhir, S. S. *Nano Lett*. **2011**, *11*, 4029–4036.
20. Faraday, M. *Philos. Trans. R. Soc. London* **1857**, *147*, 145.
21. Turkevich, J.; Stevenson, P. C.; Hillier, *J. Discuss. Faraday Soc.*, **1951**, *11*, 55–75.
22. Frens, G. *Nature: Phys. Sci* **1973**, *241*, 20–22.
23. Hu, M.; Chen, J.; Li, Z. Y.; Au, L.; Hartland, G. V.; Li, X.; Marquez, M.; Xia, Y. *Chem. Soc. Rev.* **2006**, *35*, 1084–1094.
24. Saha, K.; Agasti, S. S.; Kim, C.; Li, X.; Rotello, V. M. *Chem. Rev*. **2012**, *112*, 2739−2779.
25. Mieszawska, A. J.; Mulder, W. J. M.; Fayad, Z. A.; Cormode, D. P. *Mol. Pharmaceutics* **2013**, *10*, 831−847.
26. Deng, Z. J.; Liang, M.; Toth, I.; Monteiro, M. J.; Minchin, R. F. *ACS Nano* **2012**, *6*, 8962–8969.
27. Lynch, I.; Dawson, K. A.; Linse, S. *Sci. STKE* **2006,** *327*,p4.
28. Shemetov, A. A.; Nabiev, I.; Sukhanova, A. *ACS Nano*, **2012**, *6*, 4585–4602.
29. Cedervall, T.; Lynch, I.; Lindman, S.; Berggard, T.; Thulin, E.; Nilsson, H.; Dawson, K. A.; Linse, S. *Proc. Nat. Acad. Sci. U.S.A.* **2007,** *104*, 2050−2055.
30. Mahmoudi, M.; Lynch, I.; Ejtehadi, M. R.; Monopoli, M. P.; Bombelli, F. B.; Laurent, S. *Chem. Rev*. **2011**, *111*, 5610–5637.
31. Liu, F.; Wang, L.; Wang, H.; Yuan, L.; Li, J.; Brash, J. L.; Chen, H. *ACS Appl. Mater. Interfaces* **2015**, *7*, 3717−3724.
32. De, M.; Miranda, O. R.; Rana, S.; Rotello, V. M. *Chem. Commun*., **2009**, 2157–2159.

33. Deka, J.; Paul, A.; Chattopadhyay, A. *Nanoscale*, **2010**, *2*, 1405–1412.
34. Deka, J.; Paul, A.; Chattopadhyay, A. *J. Phys. Chem. C*, **2009**, *113*, 6936–6947.
35. De, M.; You, C-C.; Srivastava, S.; Rotello, V. M. *J Am Chem Soc* **2007,** *129*, 10747–10753.
36. Liong, M.; Lu, J.; Kovochich, M.; Xia, T.; Ruehm, S. G.; Nel, A. E.; Tamanoi, F.; Zink, J. I. *ACS Nano* **2008**, *2*, 889–896.
37. Chen, W-H.; Lei, Q.; Luo, G-F.; Jia, H-Z.; Hong, S.; Liu, Y-X.; Cheng, Y-J.; Zhang, X-Z. *ACS Appl. Mater. Interfaces* **2015,** DOI: 10.1021/acsami.5b04031.
38. Kim, J.; Kim, H. S.; Lee, N.; Kim, T.; Kim, H.; Yu, T.; Song, I. C.; Moon, W. K.; Hyeon, T. *Angew. Chem. Int. Ed*. **2008**, *47*, 8438–8441.
39. Argyo, C.; Weiss, V.; Bräuchle, C.; Bein, T. *Chem. Mater*. **2014**, *26*, 435−451.
40. De, M.; Ghosh, P. S.; Rotello, V. M. *Adv. Mater.* **2008**, *20*, 4225–4241.
41. Dhar, S.; Daniel, W. L.; Giljohann, D. A.; Mirkin, C. A.; Lippard, S. J. *J. Am. Chem. Soc*. **2009**, *131*, 14652–14653.
42. Giepmans, B. N. G.; Adams, S. R.; Ellisman, M. H.; Tsien, R. Y. *Science* **2006**, *312*, 217–224.
43. So, M.-K.; Xu, C.; Loening, A. M.; Gambhir, S. S.; Rao, J. *Nat. Biotechnol*. **2006**, *24*, 339–343.
44. Wang, Y.; Hu, R.; Lin, G.; Roy, I.; Yong, K-T. *ACS Appl. Mater. Interfaces* **2013**, *5*, 2786−2799.
45. Diagaradjane, P.; Deorukhkar, A.; Gelovani, J. G.; Maru, D. M.; Krishnan, S. *ACS Nano*, **2010**, *4*, 4131–4141.
46. Saurabh, S.; Beck, L. E.; Maji, S.; Baty, C. J.; Wang, Y.; Yan, Q.; Watkins, S. C.; Bruchez, M. P. *ACS Nano* **2014**, *8*, 11138–11146.
47. Wu, X.; He, X.; Wang, K.; Xie, C.; Zhou, B.; Qing, Z. *Nanoscale* **2010**, *2*, 2244−2249.
48. Lin, C.-A. J.; Yang, T.-Y.; Lee, C.-H.; Huang, S. H.; Sperling, R.A.; Zanella, M.; Li, J. K.; Shen, J.-L.; Wang, H.-H.; Yeh, H.-I.; Parak, W. J.; Chang, W. H. *ACS Nano* **2009**, *3*, 395−401.
49. Yu, J.; Choi, S.; Dickson, R. M. *Angew. Chem., Int. Ed*. **2009**, *48*, 318−320.
50. Tanaka, S.-I.; Miyazaki, J.; Tiwari, D. K.; Jin, T.; Inouye, Y. *Angew. Chem., Int. Ed*. **2011**, *50*, 431−435.
51. Zheng, J.; Nicovich, P. R.; Dickson, R. M. *Ann. Rev. Phys. Chem*. **2007**, *58* 409-431.
52. Chen, S. *Science* **1998**, *280*, 2098–2101.
53. Jin, R. *Nanoscale* **2010**, *2*, 343–362.
54. Schaaff, T. G.; Shafigullin, M. N.; Khoury, J. T.; Vezmar, I.; Whetten, R. L.; Cullen, W. G.; First, P. N.; Gutieerrez-Wing, C.; Ascensio, J.; Jose-Yacamman, M. J. *J. Phys. Chem. B* **1997**, *101*, 7885–7891.
55. Yau, S. H.; Varnavski, O.; Gilbertson, J. D.; Chandler, B.; Ramakrishna, G.; Goodson, T. *J. Phys. Chem. C* **2010**, *114*, 15979–15985.
56. Wang, G.; Huang, T.; Murray, R. W.; Menard, L.; Nuzzo, R. G. *J. Am. Chem. Soc*. **2005**, *127*, 812–813.
57. Ramakrishna, G.; Varnavski, O.; Kim, J.; Lee, D.; Goodson, T. *J. Am. Chem. Soc*. 2008, 130, 5032–5033.
58. Zhu, M.; Aikens, C. M.; Hollander, F. J.; Schatz, G. C.; Jin, R. *J. Am. Chem. Soc.* **2008**, *130*, 5883–5885.

59. Devadas, M. S.; Bairu, S.; Qian, H.; Sinn, E.; Jin, R.; Ramakrishna, G. *J. Phys. Chem. Lett*. **2011**, *2*, 2752–2758.
60. Qian, H.; Zhu, M.; Wu, Z.; Jin, R. *Acc. Chem. Res*., **2012**, *45*, 1470–1479.
61. Jin, R. Nanoscale, 2010, 2, 343–362. *Nanoscale*, **2010**, *2*, 343-362.
62. Zhanga, L.; Wanga, E. *Nano Today*, **2014**, *9*, 132–157.
63. Jin, R. *Nanoscale* **2010**, *2*, 343–362.
64. Link, S.; Beeby, A.; FitzGerald, S.; El-Sayed, M.; Schaaff, T.; Whetten, R. *J. Phys. Chem. B* **2002**, *106*, 3410–3415.
65. Negishi, Y.; Nobusada, K.; Tsukuda, T. *J. Am. Chem. Soc*. **2005**, *127*, 5261–5270.
66. Negishi, Y.; Takasugi, Y.; Sato, S.; Yao, H.; Kimura, K.; Tsukuda, T. *J. Am. Chem. Soc*. **2004**, *126*, 6518–6519.
67. Huang, T.; Murray, R. J. *Phys. Chem. B* **2001**, *105* 12498–12502.
68. Lee, D.; Donkers, R. L.; Wang, G.; Harper, A. S.; Murray, R.W. *J. Am. Chem. Soc*. **2004**, *126*, 6193–6199.
69. Paau, M.; Lo, C.; Yang, X.; Choi, M. *J. Phys. Chem. C* **2010**, *114*, 15995–16003.
70. Wang, Z.; Cai, W.; Sui, J. *ChemPhysChem* **2009**, *10*, 2012–2015.
71. Adhikari, B.; Banerjee, A. *Chem. Mater*. **2010,** *22*, 4364–4371.
72. Shang, L.; Dörlich, R.M.; Brandholt, S.; Schneider, R.; Trouillet, V.; Bruns, M.; Gerthsen, D.; Nienhaus, G.U. *Nanoscale* **2011**, *3*, 2009–2014.
73. Huang, C.-C.; Yang, Z.; Lee, K.-H.; Chang, H.-T. *Angew. Chem. Int. Ed*. **2007**, *46*, 6824−6828.
74. Huang, C.-C.; Liao, H.-Y.; Shiang, Y.-C.; Lin, Z.-H.; Yang, Z.; Chang, H.-T. *J. Mater. Chem*. **2009**, *19*, 755−759.
75. Muhammed, M. A. H.; Ramesh, S.; Sinha, S. S.; Pal, S. K.; Pradeep, T. *Nano Res*. **2008**, *1*, 333−340.
76. Muhammed, M.; Verma, P.; Pal, S.; Kumar, R. C. Arun.; Paul, S.; Omkumar, R.; Pradeep, T. *Chem. Eur. J*., **2009**, *15*, 10110–10120.
77. Udaya Bhaskara Rao, T.; Pradeep, T. *Angew. Chem. Int. Ed.* **2010,** *49***,** 3925–3929.
78. Zheng, J.; Dickson, R. M.; *J. Am. Chem. Soc*. **2002**, *124*, 13982–13983.
79. Zheng, J.; Petty, J. T.; Dickson, R. M. *J. Am. Chem. Soc*. **2003**, *125*, 7780–7781.
80. Bao, Y.P.; Zhong, C.; Vu, D.M.; Temirov, J.P.; Dyer, R.B.; Martinez, J.S. *J. Phys. Chem. C* **2007**, *111* 12194–12198.
81. Xu, H.; Suslick, K. S. *ACS Nano* **2010**, *4* 3209–3214.
82. Liu, S.; Lu, F.; Zhu, J.-J. *Chem. Commun*. **2011**, *47*, 2661–2663.
83. Zhang, J. G.; Xu, S. Q.; Kumacheva, E. *Adv. Mater*. **2005**, *17*, 2336–2340.
84. Shang, L.; Dong, S. J. *Chem. Commun* **2008,** 1088–1090
85. Shen, Z.; Duan, H.W.; Frey, H. *Adv. Mater*. **2007**, *19*, 349–352.
86. Díez, I.; Pusa, M.; Kulmala, S.; Jiang, H.; Walther, A.; Goldmann, A.S.; Muller, A.H.E.; Ikkala, O.;. Ras, R.H.A. *Angew. Chem. Int. Ed*. **2009**, *48*, 2122–2125.
87. Duan, H.; Nie, S. *J. Am. Chem. Soc*. **2007**, *129*, 2412–2413.
88. Sahoo, A. K.; Banerjee, S.; Ghosh, S.S.; Chattopadhyay, A. *ACS Appl. Mater. Interfaces*, **2014**, *6*, 712–724.
89. González, B. S.; Rodríguez, M. J.; Blanco, C.; Rivas, J.;.Lòpez-Quintela, M.A.; Martinho, J.M.G. *Nano Lett*. **2010**, *10*, 4217−4221.
90. Goswami, N.; Zheng, K.; Xie, J. *Nanoscale*, **2014**, *6*, 13328−13347.
91. Xie, J.; Zheng, Y.;Ying, J. Y. *J. Am. Chem. Soc.*, **2009**, *131*, 888–889.

92. Guével, X. L.; Hötzer, B.; Jung, G.; Hollemeyer, K.; Trouillet, V.; Schneider, M. *J. Phys. Chem. C* **2011**, *115*, 10955−10963.
93. Mathew, A.; Sajanlal, P. R.; Pradeep, T. *J. Mater. Chem.* **2011**, *21*, 11205−11212.
94. Chaudhari, K.; Xavier, P. L.; Pradeep, T. *ACS Nano* **2011**, *5*, 8816−882.
95. Xavier, P. L.; Chaudhari, K.; Verma, P. K.; Pal, S. K.; Pradeep, T. *Nanoscale*, **2010**, *2*, 2769−2776.
96. Le Guevel, X.; Daum, N.; Schneider, M. *Nanotechnology*, **2011**, *22*, 275103
97. Lin, Y.-H.; Tseng, W.-L. *Anal. Chem.* **2010**, *82*, 9194−9200.
98. Zhou, T.; Haunq, Y.; Li, W.; Cai, Z.; Luo, F.; Yanq, J. C.; Chen, X. *Nanoscale* **2012**, *4*, 5312−5315.
99. Kawasaki, H.; Hamaguchi, K.; Osaka, I.; Arakawa, R. *Adv. Funct. Mater*. **2011**, *21*, 3508−3515.
100. Liu, C.-L.; Wu, H.-T.; Hsiao, Y.-H.; Lai, C.-W.; Shih, C.-W.; Peng, Y.-K.; Tang, K.-C.; Chang, H.-W.; Chien, Y.-C.; Hsiao, J.-K.; Cheng, J.-T.; Chou, P.-T. *Angew. Chem., Int. Ed.* **2011**, *50*, 7056−7060.
101. Wen, F.; Dong, Y.; Feng, L.; Wang, S.; Zhang, S.; Zhang, X. *Anal. Chem.* **2011**, *83*, 1193−1196.
102. Narayanan, S. S.; Pal, S. K. *J. Phys. Chem. C*, **2008**, *112*, 4874−4879.
103. Mathew, A.; Sajanlal, P. R.; Pradeep, T. *J. Mater. Chem*., **2011**, *21*, 11205–11212.
104. Lu, D.; Zhang, C.; Fan, L.; Wu, H.; Shuang, H.; Dong, C. *Anal. Methods*, **2013**, *5*, 5522–5527.
105. Anand, U.; Ghosh, S.; Mukherjee, S. *J. Phys. Chem. Lett*., **2012**, *3*, 3605–3609.
106. Yan, L.; Cai, Y. Zheng, B.;Yuan, H.; Guo, Y.; Xiao, D.; Choi, M. M. F. *J. Mater. Chem.*, **2012**, *22*, 1000–1005.
107. Liu, H.; Zhang, X.; Wu, X.; Jiang, L.; Burda, C.; Zhu, J-J. *Chem. Commun*., **2011**, *47*, 4237–4239.
108. Häkkinen, H. *Nat. Chem*., **2012**, *4*, 443–455.
109. Yuan, X.; Tay, Y.; Dou, X.; Luo, Z.; Leong, D. T.; J. Xie, J. *Anal. Chem*., **2012**, *85*, 1913–1919.
110. Yu, Y.; Luo, Z.;Chevrier, D. M.; Leong, D. T.; Zhang, P.; Jiang, D.-E.; Xie, J. *J. Am. Chem. Soc*., **2014**, *136*, 1246–1249.
111. Yuan, X.; Setyawati, M. I.; Tan, A.; Ong, C. N.; Leong, D. T.; Xie, J. *NPG Asia Mater.*, **2013**, *5*, e39.
112. Yuan, X.; Yao, Q.; Yu, Y.; Luo, Z.; Dou, X.; Xie, J. *J. Phys. Chem. Lett*. **2013**, *4*, 1811−1815.
113. Cui, Y.; Wang, Y.; Liu, R.; Sun, Z.; Wei, Y.; Zhao, Y.; Gao, X. *ACS Nano*, **2011**, *5*, 8684−8689.
114. Wang, Y.; Cui, Y.; Zhao, Y.; Liu, R.; Sun, Z.; Li, W.; Gao, X. *Chem. Commun*., **2012,** *48*, 871−873.
115. Song, W.; Liang, R.-P.; Wang, Y.; Zhang, L.; Qiu, J. –D. *Chem. Commun*., **2015**, *51*, 10006.
116. Petty, J. T.; Zheng, J.; Hud, N. V.; Dickson, R. M. *J. Am. Chem. Soc*. **2004**, *126*, 5207−5212.
117. Richards, C. I.; Choi, S.; Hsiang, J.-C.; Antoku, Y.; Vosch, T.; Bongiorno, A.; Tzeng, Y.-L.; Dickson, R. M. *J. Am. Chem. Soc*. **2008**, *130*, 5038−5039.

118. Ritchie, C. M.; Johnsen, K. R.; Kiser, J. R.; Antoku, Y.; Dickson R. M.; Petty, J. T. *J. Phys. Chem. C*, **2006**, *111*, 175−181.
119. Petty, J. T.; Story, S. P.; Hsiang J.-C.; Dickson, R. M. *J. Phys. Chem. Lett*., **2013,** *4*, 1148−1155.
120. Copp, S. M.; Schultz, D.; Swasey, S.; Pavlovich, J.; Debord, M.; Chiu, A.; Olsson, K.; Gwinn, E. *J. Phys. Chem. Lett.*, **2014**, *5*, 959−963.
121. Schultz, D.; Copp, S. M.; Markešević, N.; Gardner, K.; Oemrawsingh, S. S. R.; Bouwmeester, D.; Gwinn, E. *ACS Nano*, **2013**, *7*, 9798−9807.
122. Kennedy, T. A. C.; MacLean, J. L.; Liu, J. *Chem.Commun.*, **2012**, *48*, 6845−6847.
123. Liu, G.; Shao, Y.; Ma, K.; Cui, Q.; Wu, F.; Xu, S. *Gold Bull.*, **2012**, *45*, 69−74.
124. Schaaff T. G.; Whetten, R. L. *J. Phys. Chem. B***, 1999**,*103*, 9394−9396.
125. Kumar, S.; Bolan M. D.; Bigioni, T. P. *J. Am. Chem. Soc.*, **2010**, *132*, 13141−13143
126. Shichibu, Y.; Negishi, Y.; Tsunoyama, H.; Kanehara, M.; Teranishi, T.; Tsukuda, T. *Small*, **2007**, *3*, 835−839.
127. Shichibu, Y.; Negishi, Y.; Tsukuda, T.; Teranishi, T. *J. Am. Chem. Soc*., **2005**, *127*, 13464−13465.
128. Zhou, R.; Shi, M.; Chen, X.; Wang, M.; Chen, H. *Chem. –Eur. J*., **2009**, *15*, 4944−4951.
129. Chen, X.; Zhou, Y.; Peng, X.; Yoon, J. *Chem. Soc. Rev*. **2010**, *39*, 2120−2135.
130. Townsend, D. M.; Tew, K. D.; Tapiero, H. *Biomed. Pharmacother*., **2003**, *57*, 145−155.
131. Herzenberg, L. A.; De Rosa, S. C.; Dubs, J. G.; Roederer, M.; Anderson, M. T.; Ela, S. W.; Deresinski, S. C.; Herzenberg, L. A. *Proc. Natl. Acad. Sci. U. S. A.*, **1997**, *94*, 1967−1972.
132. Shang, L.; Dong, S. *Biosens. Bioelectron.* **2009**, *24*, 1569−73.
133. Han, B.; Wang, E. *Biosens. Bioelectron*. **2011**, *26*, 2585−9.
134. Huang, Z.; Pu, F.; Lin, Y.; Ren, J.; Qu, X. *Chem. Commun*. **2011,** *47*, 3487−3489.
135. Jin, L.; Shang, L.; Guo, S.; Fang, Y.; Wen, D.; Wang, L.; Yin, J.; Dong, S. *Biosens. Bioelectron*. **2011**, *26*, 1965−1969.
136. Shiang, Y-C.; Huang, C-C.; Chang, H-Y. *Chem. Commun.*, **2009**, 3437−3439.
137. Hua, L.; Hana, S.; Parveena, S.; Yuana, Y.; Zhanga, L.; Xua, G. *Biosens. Bioelectron*. **2012**, *32*, 297−299.
138. Li, L.; Liu, H.; Shen, Y.; Zhang, J.; Zhu, J-J. *Anal. Chem.* **2011**, *83*, 661−665.
139. Teng, Y.; Jia, X.; Li, J.; Wang, E. *Anal. Chem*. **2015**, *87*, 4897−4902.
140. Wen, F.; Dong, Y.; Feng, L.; Wang, S.; Zhang, S.; Zhang, X. *Anal. Chem*. **2011**, *83*, 1193−1196.
141. Triulzi, R. C.; Micic, M.; Giordani, S., Serry, M.; Chiou, W.-A.; Leblanc, R. M. *Chem. Commun*. **2006**, 5068−5070.
142. Chen, C.-T.; Chen, W.-J.; Liu, C.-Z.; Chang, L.-Y.; Chen, Y.-C. *Chem.Commun*. **2009**, *48*, 7515−7.
143. Sharma, J.; Yeh, H.-C.; Yoo, H.; Werner, J. H.; Martinez, J. S. *Chem.Commun.* **2011**, *47*, 2294–2296.
144. Zhang, L.; Zhu, J.; Guo, S.; Li, T.; Li, J.; Wang, E. *J. Am. Chem. Soc.* **2013**, *135*, 2403−2406.
145. Yang, C.; Shi, K.; Dou, B.; Xiang, Y. Chai, Y.; Yuan, R. *ACS Appl. Mater. Interfaces* **2015**, *7*, 1188−1193.
146. Khandelia, R.; Bhandari, S.; Pan, U. N.; Ghosh, S. S.; Chattopadhyay, A. **2015**, *11*, 4075−4081.
147. Makarava, N.; Parfenov, A.; Baskakov, I. V. *J.* **2005**, *89*, 572−580.

148. Wang, Y.; Chen, J.; Irudayaraj, J. *ACS Nano* **2011**, *5*, 9718−9725.
149. Wu, X.; He, X. X.; Wang, K.; Xie, C.; Zhou, B.; Qing, Z. *Nanoscale* **2010**, *2*, 2244−2249.
150. Zhou, C.; Long, M.; Qin, Y.; Sun, X.; Zheng, J. *Angew. Chem. Int. Ed.* **2011**, *50*, 3168−3172.
151. Liu, J.; Yu, M.; Zhou, C.; Yang, S.; Ning, X.; Zheng, J. *J. Am. Chem. Soc*. **2013**, *135*, 4978−4981.
152. Archana, R.; Sonali, S.; Deepthy, M.; Prasanth, R.; Habeeb, M.; Thalappil , P.; Shantikumar, N.; Manzoor, K. *Nanotechnology* **2010** ,*21* , 055103.
153. Hu, D.; Sheng, Z.; Fang, S.; Wang, Y.; Gao, D.; Zhang, P.; Gong, P.; Ma, Y.; Cai, L. *Theranostics* **2014,** *4*, 142−153.
154. Wang, C.; Li, J.; Amatore, C.; Chen, Y.; Jiang, H.; Wang, X.-M. *Angew. Chem. Int. Ed.* **2011**, *50*, 11644–11648.
155. Sun, G.; Zhou, L.; Liu, Y.; Zhao, Z. *New J. Chem.* **2013**, *37*, 1028−1035.
156. Liang, G.; Ye, D.; Zhang, X.; Dong, F.; Chen, H.; Zhang S.; Li, J.; Shen, X.; Kong, J. *J. Mater. Chem. B* **2013**, *1*, 3545−3552.
157. Zhang, X.-D.; Wua, D.; Shen, X. Chen, J.; Sun, Y.-M.; Liu, P.-X.; Liang, X.-J. *Biomaterials* **2012,** *33*, 6408–6419.
158. Zhang, X.-D.; Luo, Z.; Chen, J.; Shen, X.; Song, S.; Sun, Y.; Saijun F.; Fan, F.; Leong, D. T.; Xie. J. *Adv. Mater*. **2014**, *26*, 4565−4568.
159. Zhang, X.-D.; Chen, J.; Chen, J.; Wu, D.; Shen, X.; Song, S.-S.; Sun, Y.-M.; Liu, P.-Y.; Zhao, J.; Huo, S.; Fan, S.; Fan, F.; Liang, X.-J.; Xie, J. *Adv. Healthcare Mater*. **2014**, *3*, 133–141.
160. Keen, C. L.; McArdle, H. J.; Ward, E. M. International Copper Association Ltd. **2003**.
161. Grass, G.; Rensing, C.; Solioz, M. *Appl. Environ. Microbiol.* **2011**, *77*, 1541–1547.
162. Mallick, S.; Sharma, S.; Banerjee, M.; Ghosh, S. S.; Chattopadhyay, A.; Paul, A. *ACS Appl. Mater. Interfaces* **2012**, *4*, 1313−1323.
163. Mathew, A.; Pradeep, T. *Part. Part. Syst. Charact.* **2014**, *31*, 1017–1053
164. Vazquez-Vazquez, C.; Banobre-Lopez, M.; Mitra, A.; Lopez-Quintela, M.A.; Rivas, J. *Langmuir* **2009,** *25*, 8208−8216.
165. Vilar-Vidal, N.; Blanco, M.C.; Lopez-Quintela, M.A.; Rivas, J.; Serra, C. *J. Phys. Chem. C* **2010,** *114*, 15924−15930.
166. Kawasaki, H.; Kosaka, Y.; Myoujin, Y.; Narushima, T.; Yonezawa, T.; Arakawa, R. *Chem. Commun.* **2011**, *47*, 7740−7742.
167. Zhang, H.; Huang, X.; Li, L.; Zhang, G.; Hussain, I.; Li, Z.; Tan, B. *Chem. Commun.*, **2012**, *48*, 567–569
168. Wei, W.; Lu, Y.; Chen, W.; Chen, S. *J. Am. Chem. Soc*. **2011**, *133*, 2060−2063.
169. Jia, X.;Yang, X.; Li, J.; Li, D.; Wang, E. *Chem. Commun.*, **2014**, *50*, 237−239.
170. Wang, C.; Wang, C.; Xu, L. Cheng, H. Lin, Q.; Zhang, C. *Nanoscale*, **2014**, *6*, 1775–1781.
171. Goswami, N.; Giri, A.; Bootharaju, M. S., Xavier, P. L.; Pradeep, T.; Pal, S. K. *Anal. Chem.* **2011**, *83*, 9676–9680.
172. Jia, X.; Li, J.; Han, L.; Ren, J.; Yang, X.; Wang, E. *ACS Nano* **2012**, *6*, 3311−3317.
173. Qing, Z.; He, X.; He, D.; Wang, K.; Xu, F.; Qing, T.; Yang, X. *Angew. Chem., Int. Ed*. **2013**, *52*, 9719−9722.
174. Jia, Z.; Li, J.; Wang, E. *Small* **2013**, *9*, 3873−38.

Chapter 2

Conformation Aspect in α-Amylase Induced Agglomeration of Citrate-Stabilized Gold Nanoparticles*

This chapter describes the effect of a chemical denaturant on agglomeration behaviour of citrate stabilized gold nanoparticles–protein composite. The interaction between the citrate stabilized gold nanoparticles and protein leading to agglomeration is dependent on the conformation of protein, and that while native protein was involved in the agglomeration process. Urea (denaturant) induced unfolding of free proteins as well as presence of ions in the medium stopped or stalled the growth of agglomerated structures.

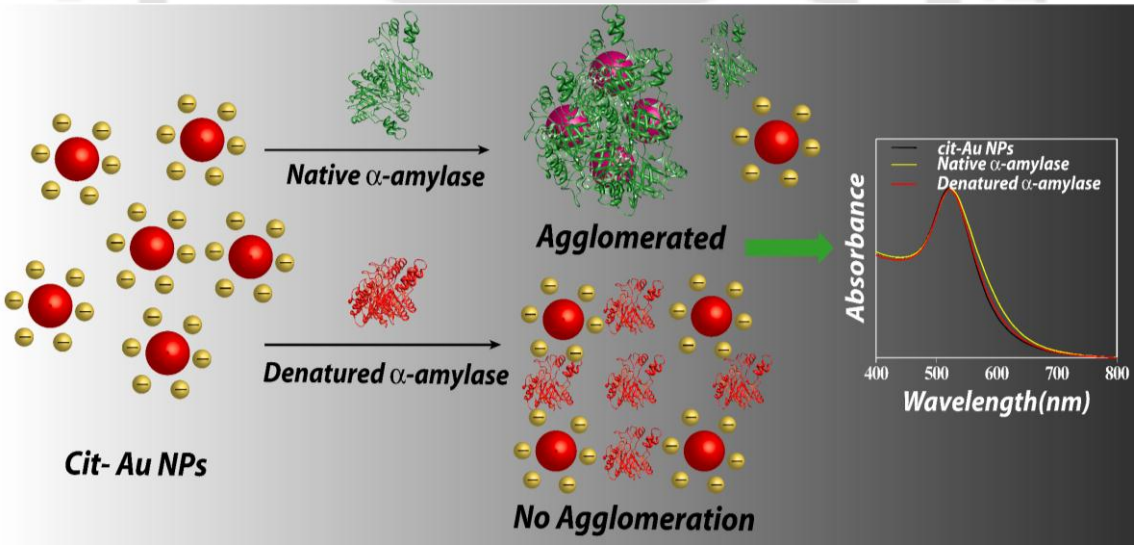

*Ghosh, R.; Deka, J.; Chattopadhyay, A.; Paul, A. *RSC Adv*. **2013,** *3*, 23015–23027. Reproduced with permission from *RSC Adv*. Copyright 2013, Royal Society of Chemistry.

2.1. INTRODUCTION

Rapid progress in nanoscale science and technology is increasingly finding nanomaterials being used for a wide range of applications starting from food and clothing to diagnostics and therapeutics.[1-5] Interaction of nanoparticle with protein has been found to alter the conformation of proteins, which in turn could potentially activate unwanted biochemical reactions that may lead to toxicity and disease.[6] Among the nanomaterials, gold nanoparticles (Au NPs) and Nano rods (NRs) have been proposed to have large-scale applications especially in healthcare. For example, functionalized Au NPs have been used, among others, for hyperthermia treatment of cancer cells,[7] for estimation of pathogens,[8] for assay of proteins,[9-15] for DNA sensing,[16-18] for enzymatic activity assays[19,20] and for probing selective cellular functions.[21] Further, Au NPs when functionalized with proteins, have been used for immunoassays,[22,23] light controlled released of drug[24] and for glucose sensing.[25] Recently protein functionalized Au NPs have been used for killing cancer cells.[26] Also, interactions of Au NP with enzyme has led to its activity enhancement.[27,28] Anticipating increasing role of properties of Au NPs and their interactions with proteins in applications related to nanobiotechnology, it deserves attention on a more fundamental level especially understanding the factors which lead to property modifications of either one or both of them.

Recent investigations of interactions of Au NP dispersions and proteins indicate that when the NPs are stabilized through electrostatic interaction with the stabilizing molecules they tend to form agglomerates in presence of proteins.[13] The nature and extent of agglomeration depends on the protein and its conformation and also on its concentration in the medium.[29] For example, when citrate-stabilized Au NPs were treated with proteins, the extinction spectrum of the NPs changed systematically with the concentration of the proteins and their conformations.[30] These changes have been associated with agglomeration of the NPs and proteins, the extent of which depended on the above mentioned parameters. Studies also indicated specificity of interactions involving a binary mixture of proteins and Au NPs.[31] Interestingly, although the agglomeration behaviour have been studied with substantial details along with the consequence on the properties of the NPs there is still a lack of systematic studies on the fate of the proteins, especially in regard to their conformation and activity. Our laboratory has recently demonstrated that the agglomeration is associated with the modulation of activity of the enzyme (in this case α-amylase). Further, the modulation has been proposed to be due to oriented attachment of the proteins on the NPs at lower concentrations giving rise to enhanced activity.[28] At higher concentrations of protein, the agglomeration leads to non-availability of the protein for enhanced catalysis. However, there are still many questions about the fate of the conformation of the attached protein. Recent

studies indicated possible partial unfolding of the protein upon attachment to the NP.[13,31] In addition, a pertinent question could be raised on the origin of agglomeration. In this respect, it would be important to probe the fate of the agglomerates in the presence of a chemical denaturant of protein, as this may provide at least some answers on the mechanism of agglomeration of a mixture of protein and cit–Au NP. Further, it can be anticipated that knowledge arising out of these studies would facilitate further understanding of the consequences of introducing Au NPs in living systems.

Herein we report the agglomeration behaviour of a mixture of citrate-stabilized Au NPs and a protein (α–amylase) in presence of urea, which is a chemical denaturant of the protein. The protein α–amylase is an endo acting enzyme, which belongs to the glycosidic hydrolase 13(GH13) family. The molecular weight of α–amylase is 55 kDa, which consists of three domains (**Scheme 2.1**). The larger, the N−terminal part, consists of 330 amino acid residues. The central domain has the typical parallel-stranded alpha beta barrel structure. The C–terminal domain forms a distinct globular unit where the chain folds into an eight-stranded antiparallel αβ−barrel. The amino acid sequence contains 12 cysteine, 5 disulfide bonds and two exposed free thiol groups (cys 103, cys 119), which are spatially close to each other. [32] The attachment of Au NP to one free thiol group would facilitate binding with the neighboring –SH group. It is possible that many α–amylase molecules could bind simultaneously with Au NPs forming an aggregate.[33] Earlier investigations from our laboratory indicated both concentration and conformation dependent changes occurring in a mixture of native or denatured protein and Au NPs.[29,30] However, what we have probed here is influence of a denaturing agent on the agglomeration of a mixture of protein and Au NPs. UV–Visible spectroscopy, transmission electron microscopy (TEM), dynamic light scattering (DLS) based particle size analysis, zeta potential measurement, UV- circular dichroism (CD) measurement, Fluorescence spectroscopy and Fourier transform infrared (FTIR) spectroscopy have been used to establish the potential origin of agglomeration of Au NPs in presence of the protein. The results indicated that the interaction between the NPs and the native protein in aqueous medium is conformation dependent and this interaction led to the agglomeration of Au NPs and the protein molecules. Initially, smaller agglomerated structures formed between the NPs and protein. However, the sizes of these structures grew with time by incorporating additional proteins and NPs. On the other hand, in presence of urea further growth of the structures was arrested. Urea not only denatured the proteins in the medium and partly those present on the surface of the agglomerates, but also stabilized the structures. Interestingly, the proteins present in the agglomerates retained enzymatic activity in presence of urea, in comparison to those present freely in the medium.

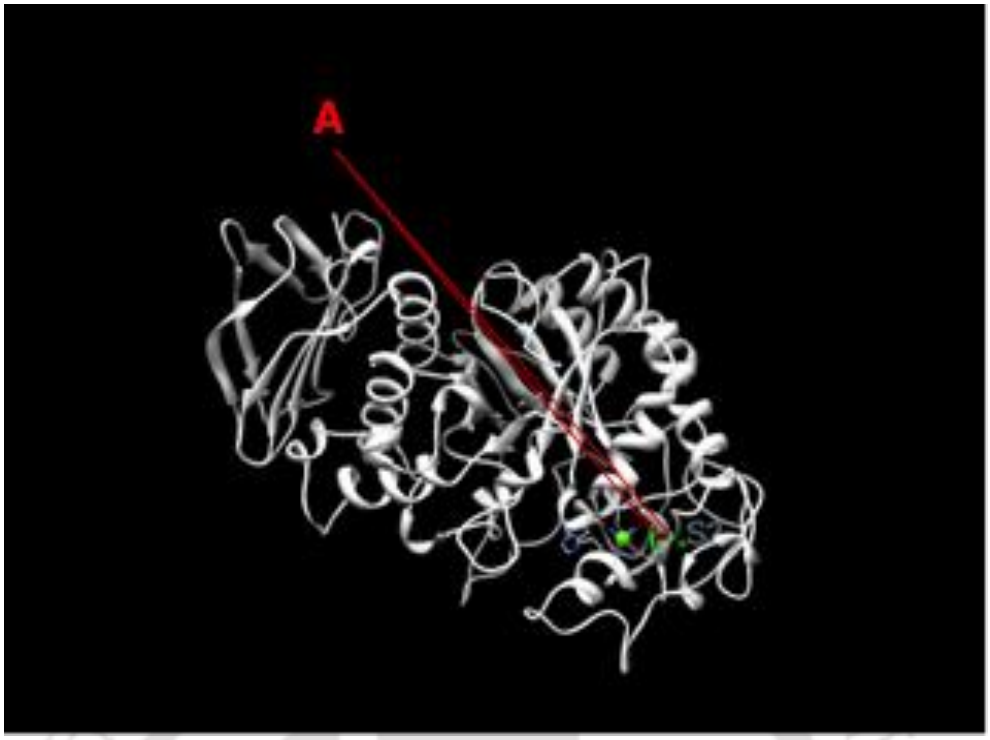

Scheme 2.1 Three-dimensional structure of α–amylase showing the respective locations of (**A**) Au NP binding site containing free thiol groups. The protein data base (PDB) number is 1SMD.

2.2. EXPERIMENTAL SECTION

2.2.1. Materials

α–amylase from hog pancreas (43.6 U/mg activity) and hydrogen tetrachloroaurate trihydrate were purchased from Sigma Aldrich Chemical Co., Trisodium citrate dehydrate purified and urea extra pure were purchased from Merck Specialities Private Limited, India. Milli-Q grade water (18.2MΩcm) was used for all the experiments. Isoelectric point of α–amylase is 6.5.

2.2.2. Preparation of cit–Au NP dispersion

Citrate stabilized Au NPs were synthesized by following procedure: A mixture of 0.750 mL of 1.73×10^{-2} M of $HAuCl_4$ and 30.0 mL of Milli-Q grade water was taken in a round bottom flask and then heated to boiling under reflux condition. When the mixture started to boiling, 1.0 mL of 0.857 M of trisodium citrate 2-hydrate solution was added to the above solution all at once, under constant stirring. The solution first turned to faint blue and then changed to deep wine red, indicating the formation of cit–Au NP dispersion. The solution was boiled and stirred continuously for another 30 min to ensure the complete reduction of $HAuCl_4$. The formation of cit–Au NPs was confirmed by UV–Vis spectroscopy and TEM analysis. The pH of cit–Au NP was 5.5. The dispersion of cit–Au NPs was diluted 2 times with phosphate buffer (0.01 M, pH = 7.0) with overall pH of 6.9, before performing experiments. The concentration of cit–Au NP was found to be 44.6 nM from the particle size of TEM analysis.

2.2.3. Preparation of protein

1.0 mg/mL α–amylase was used in these experiments. 1.0 mg/mL of α–amylase was prepared by dissolving α–amylase protein in 0.01 M phosphate buffer. It was found that α–amylase was sparingly soluble in buffer and hence, it was stirred for 15 min in a magnetic stirrer at room temperature for proper mixing. Then, it was centrifuged at 5000 rpm for another 15 minutes. The supernatant was collected and used for further experiments. The actual protein content was determined using the Bradford test for 1.0 mg/mL solution. The concentration of stock α–amylase solution is 1270 nM. α–amylase solution was diluted 10 times with phosphate buffer solution to obtain 127 nM. The calibration and actual concentration of α–amylase was calculated by our group.[29] The molar concentrations of protein used in UV−Visible experiments, DLS and zeta potential measurements, TEM analysis and FTIR spectroscopy measurements were 0.84 nM to 2.5 nM. But for CD analysis and enzymatic activity studies the concentration of protein used was 24.9 nM. The ratio of protein and cit–Au NP used in different experiments were varied from 1: 0.19 to 1: 0.56.

2.2.4. Preparation of urea solutions

4 M, 6 M and 8 M urea stock solutions were prepared by dissolving respective amounts of urea in phosphate buffer.

2.2.5. Preparation of Denatured α–amylase solution

8 M of urea solution was added to a 1.5 mL portion of 1270 nM of α–amylase solution and kept at 4 ºC (4 h) in refrigerator. This was then brought to room temperature for experiments.

2.2.6. Enzymatic Activity of α–amylase

2.2.6.1. Preparation of Au NP-α-amylase composite.

A 60.0 mL dispersion of cit–Au NPs was taken in a 250 mL conical flask. To this 0.06 mL of 1270 nM of α–amylase (10 times more than the UV−Vis study) was added which was then shaken well and kept for 15 min. The final concentration of α–amylase was found to be 24.5 nM. The Au NP–protein composite was then centrifuged at 25,000 rpm and 4°C for 30 min to remove excess α–amylase and free Au NPs. The supernatant was discarded, and the pellet was re-suspended in phosphate buffer (pH 7.0). Similarly, to 60.0 mL of cit–Au NPs and 0.06 mL of 1270 nM of protein composite, 1.5 mL of 8 M stock urea solution was added, shaken well and kept for 15 min. The Au NP–protein–urea composite was then by centrifuged at 25,000 rpm for 30 min and 4°C to remove excess amounts of Au NPs, urea and protein.

2.3. ANALYTICAL MEASUREMENTS

UV–Vis spectroscopic measurements were carried out by Hitachi U–2900 spectrophotometer in the range 400−800 nm. FTIR spectroscopic measurements were performed by using a Spectrum One, Perkin Elmer spectrophotometer in the range 400−4000 cm^{-1}. TEM measurements were made using a JEOL JEM 2100 TEM operating at a maximum accelerating voltage of 200 kV. CD spectrum was recorded by using a JASCO J–815 machine. The instrument was calibrated with camphor sulfonic acid. All CD spectra were recorded at 25 ºC using thermostatically controlled cell holder with path length of cell being 10 mm. DLS and zeta potential measurements for samples were carried out by using Malvern zeta size Nano–ZS90 instrument at instrument temperature 25 ºC and Viscosity 0.8872 mPaS. Fluorescence measurements were performed at 280 nm excitation and a slit width of 5 nm using a Fluromax 4-spectroflurometer equipped with a Xe lamp.

2.4. UV–Vis measurements

2.4.1. Successive addition of urea to the cit–Au NP–protein composite

These were performed in three sets. For Set I, a mixture of cit–Au NPs, protein and urea the following procedure was followed: 3.0 mL of cit–Au NPs dispersion was taken in a plastic cuvette and the UV–Vis spectrum of the same was recorded. A 0.02 mL of 127 nM of α–amylase solution was added to it, shaken well for 5 min and the UV–Vis spectrum was recorded thereafter. The final concentration of α–amylase in the mixture was found to be 0.84 nM. A 0.01 mL of 8 M of stock urea solution was added drop wise to the Au NP–protein composite, shaken well, kept for another 5 min and the UV–Vis spectrum was recorded. The final concentration of urea in the mixture was found to be 0.026 M. This was followed by the addition of 0.02 mL of 8 M stock urea solution to the mixture and recorded the UV–Vis spectrum. In this manner, successive addition of urea solution was done, followed by the UV–Vis spectra recording. The addition of urea and recording of spectrum was continued till there was no change in the UV–Vis spectra. For every set of experiments the protein concentration was kept constant in the plastic cuvette before adding the urea solution to it. Similar experiments were carried out for 0.04 mL and 0.06 mL of α–amylase with 8 M of stock urea solution. The final concentration of α–amylase for 0.04 mL and 0.06 mL was found to be 1.7 nM and 2.5 nM, respectively. This completes the set I experiments. For sets II, identical experiments were carried out with 4 M of stock urea solution and for set III, similar experiments were carried out with 6 M of stock urea solution. The UV–Vis spectra were reported in the **Figure. 2A.1** and **Figure. 2A.2** in **appendix.**

2.4.2. Calculations of the average area under the UV–Vis spectrum

The area under the UV–Vis extinction curve is performed by using the software which is automatically associated with the operating software of the spectrophotometer. The average area under the extinction curve was calculated by selecting the two wavelengths under the extinction spectrum. For calculating the average area, the extreme wavelengths were set at 405 and 650 nm.

2.4.3. Enzymatic starch digestion studies.

For the starch digestion kinetic studies, a stock solution of starch was prepared in phosphate buffer (pH 7.0) with a concentration of 0.5 mg/mL. 2.0 mL of Au NP–protein composite was added to the 30.0 mL of above starch solution and was incubated at 37ºC. Similarly, an equivalent amount of Au NP–protein containing urea was taken to compare the digestion of starch. Aliquots (3.0 mL) from each of the reaction mixtures were withdrawn at regular interval of time, 0.2 mL of iodine solution (Gram's iodine, Himedia) was added and the UV−Vis spectra recorded. For kinetics, the area under the curves was plotted as a function of time.

2.5. Sample preparations for TEM analysis

Eight sample solutions were prepared for TEM analysis. They were a solution containing cit–Au NPs (without α–amylase), a solution containing 0.04 mL α–amylase of 127 nM with 3.0 mL of cit–Au NPs dispersion, a mixture of 3.0 mL of cit–Au NPs containing 0.04 mL of 127 nM α–amylase with 0.01 mL of 8 M urea, a mixture of 3.0 mL of cit–Au NPs containing 0.04 mL 127 nM α–amylase with 0.05 mL of urea and a mixture of 3.0 mL of cit–Au NPs containing 0.04 mL of 127 nM α–amylase with 0.12 mL of 8 M urea solutions, respectively. The final concentration of α–amylase in the mixture was found to be 1.7 nM. Similarly, the final concentrations of urea in the mixtures were found to be 0.026 M, 0.129 M and 0.304 M, respectively. TEM samples for control experiments were made from 3.0 mL of cit–Au NPs in the presence of corresponding volume of 8 M stock urea solution as mentioned above. The above solutions were drop casted on the carbon-coated copper TEM grids (5 min after addition of protein/urea to the cit–Au NPs dispersions) and then kept for drying overnight at room temperature. These grids were analyzed by a Jeol JEM 2100 TEM operating at a maximum accelerating voltage of 200 kV.

2.6. Sample preparations for FTIR measurements

The solutions of cit–Au NPs containing 2.5 nM of α–amylase and 0.2 mL of urea (8 M) stock solutions were centrifuged at 25,000 rpm and 4°C for 30 min and dried at room temperature for recording the FTIR spectra. FTIR spectra of native α–amylase, urea, and above centrifuged pellets were recorded by forming disc with KBr. The scan was performed in the range of 400–4000 cm^{-1} in transmittance mode.

2.7. Particle size analysis by DLS method

3.0 mL of cit–Au NPs dispersion was taken in a quartz cuvette for which particle size distribution was measured using a Malvern zeta size instrument. 0.04 mL of 127 nM of α–amylase solution was added to the above solution of cit–Au NPs and shaken well before recording the particle size distribution. To this solution, 0.01 mL of 8 M urea solution was added, shaken well and its particle size distribution was recorded. The final concentration of urea solutions in the mixture was found to be 0.026 M. In this way urea was continually added till addition of 0.05 mL and then 0.120 mL with final concentration of urea as 0.129 M and 0.304 M was achieved. The mixtures were shaken well and particle size distributions were recorded. All the samples were kept for 5 min before recording the particle size distribution.

2.7.1. Zeta potential determinations by DLS method

3.0 mL of cit–Au NPs dispersion was taken in a quartz cuvette for which zeta potential was measured using a Malvern zeta size instrument. To this, 0.04 mL of 127 nM of α–amylase solution was added and shaken well before recording the zeta potential distribution. The final concentration of α–amylase in the mixture was found to be 1.7 nM. To this 0.01 mL of 8 M urea solution was added and shaken well before recording the zeta potential. The final concentration of urea in the mixture was found to be 0.026 M. This analysis continued till an addition of 0.05 mL and then 0.12 mL of 8 M urea to the above solution was attained, in which the final concentration of urea was found to be 0.129 M and 0.304 M respectively. All the samples were kept for 5 min before recording the zeta potential. Zeta potential was also recorded for a mixture containing 3.0 mL of cit–Au NPs with 0.01 mL, 0.05 mL and 0.120 mL of 8 M stock urea solution with final concentrations 0.027 M, 0.131 M and 0.307 M, respectively, by following the above mentioned procedure.

2.8. Samples preparations for Circular Dichroism

For CD measurements, we have used 24.5 nM of α–amylase which was 10 times more than other studies. This was necessary for achieving enough sensitivity for the measurements. 0.06 mL of 1270 nM of α–amylase was added to 3.0 mL of cit–Au NPs and incubated for 5 min and the CD spectrum was then recorded. The final concentration of cit–Au NPs in the mixture was found to be 24.5 nM. Similarly, 0.4 mL of 8 M urea solution was added to the above protein NP composite and kept for another 5 min and the spectrum was monitored. The final concentration of urea in the mixture was found to be 0.92 M. UV−CD spectra were also recorded after 30 min incubations of the samples.

2.9. Samples preparation for Fluorescence measurements

Fluorescence measurements were carried out in three different mode of addition: In set I, 3.0 mL of sodium phosphate buffer was taken in a fluorescence cuvette and it 0.06 mL of 1270 nM of α–amylase was added and its emission spectra was recorded by using Fluromax 4-spectrometer with Xe lamp. The concentration of α–amylase in solution was found to be 24.9 nM. 0.4 mL of 8 M urea solution was added drop wise to the above solution and mixed well and kept for 5 min before recording the emission spectra. Similarly, the emission spectrum of the maintained mixture of α–amylase and urea in presence of 3.0 mL of cit–Au NPs was recorded, the protein and urea mixture was added drop wise to cit–Au NPs. Before recording the spectrum, the sample was mixed well and kept for another 5 min.

In set II, 3.0mL of cit–Au NPs was taken in a fluorescence cuvette and it 0.06 mL of 1270 nM of α–amylase was added and its emission spectrum was recorded. The above mentioned protein was added drop wise to 3.0 mL of cit–Au NPs dispersion and the time-dependent fluorescence measurement was made. Spectra were recorded after 5, 10, 15, 20, 25 and 30 min from the time of addition of proteins to cit–Au NPs dispersion. After 30 min, 0.4 mL of 8 M urea solution was added to the maintained mixture, mixed well and kept for 5 min and recorded the emission spectrum. The concentration of urea in the solution was found to be 0.92 M.

In set III, 3.0mL of cit–Au NPs was taken in a fluorescence cuvette and to it 0.06 mL of 1270 nM of α–amylase was added and the emission spectrum was recorded. Similarly, 0.4 mL of 8 M urea solution was added simultaneously the above mixture and shaken well and recorded the emission spectra of α–amylase. Before recording the spectra, the samples were kept for 5 min.

2.10. RESULTS AND DISCUSSION

Cit–Au NPs dispersions, prepared by the trisodium citrate 2-hydrate reduction of $HAuCl_4$ appeared wine red in colour. When 0.02–0.06 mL of 127 nM of α–amylase was added to 3.0 mL of cit–Au NPs dispersion, the wine red colour slowly changed to deep purple. This is in accordance with the observations made earlier.[29] Further, when urea was added to this dispersion, intensity of purple colour increased marginally. The above observations in colour changes were corroborated by detailed UV–Vis spectroscopic studies described below.

UV–Vis spectrum of the cit–Au NPs dispersion showed a single band with a peak at 521 nm (**Figure 2.1A**) due to the surface Plasmon resonance (SPR) peak of the Au NPs. When urea was added to the dispersion, there was a small yet systematic decrease in peak intensity at 521 nm accompanied by slight broadening of the peak, with increasing volume (from 0.01 mL to 0.250 mL) of 8 M solution of urea. On the other hand, the effect of addition of α–amylase to cit–Au NPs is known to broaden the SPR band due to the agglomeration of the Au NPs upon adsorption of the native protein to the surface of the NPs.[29,30] In this study too we observed increasing amounts of α–amylase (0.02–0.06 mL of 127 nM) to cit–Au NPs (3.0 mL), led to considerable broadening of the SPR peak accompanied by a small but consistent red shift (521 to 524 nm) in the peak maximum (**Figure 2.1A** inset, and **Figure 2.3B**). More importantly though, the observation that increasing amounts of α–amylase did not cause significant decrease in the SPR peak intensity at 521 nm (**Figure 2.1A** inset), an observation which differed from that obtained by the addition of urea to cit–Au NPs (i.e. **Figur**e **2.1A**) where the peak intensity at 521 nm decreased with increasing urea concentration. Thus the slight decrease in peak intensity at 521 nm in case of urea addition to cit–Au NPs, in **Figure 2.1A,** is probably related to dilution of the sample.

Urea is known to denature free protein.[34] However, when α–amylase is bound to cit–Au NPs, the effect of added urea showed some interesting behaviour, both as a function of concentration and as a function of time. **Figure 2.1(B−D)** shows the effect of added urea concentrations on the SPR band of cit–Au NPs dispersion containing α–amylase. To delineate the time effects from concentration effects, the concentration spectra in **Figure 2.1(B−D)** were recorded with a constant delay of 5 min between additions of any reagent. It was found that when 0.01 mL of 8 M urea solution was added to 3.0 ml of cit–Au NPs solution containing specific amount of α–amylase (range in 0.02-0.06 mL of 127 nM), the absorption maximum shifted from 523 nm to 525 nm with increasing amount of urea. In other words, successive additions of urea (up to 0.2 mL) led to increasing broadening of the SPR peak towards longer wavelengths. But additions beyond 0.150 mL of 8 M stock urea solution resulted in no further change in the UV−Vis spectrum (**Figure 2.1B**, **2.1C** and **2.1D**)

indicating that a saturation concentration of urea was reached. The final concentration ranges of urea and α–amylase in these solutions were 0.026 – 0.378 M and 1.7 nM – 2.5 nM respectively corresponding to **Figures 2.1B–2.1D**. Similar UV–Vis results for studies carried out with 4 M and 6 M stock solutions of urea are given in the Appendix (**Figures 2A.1** and **2A.2**, in **appendix**), which demonstrate reproducibility of the results even at lower concentrations of urea.

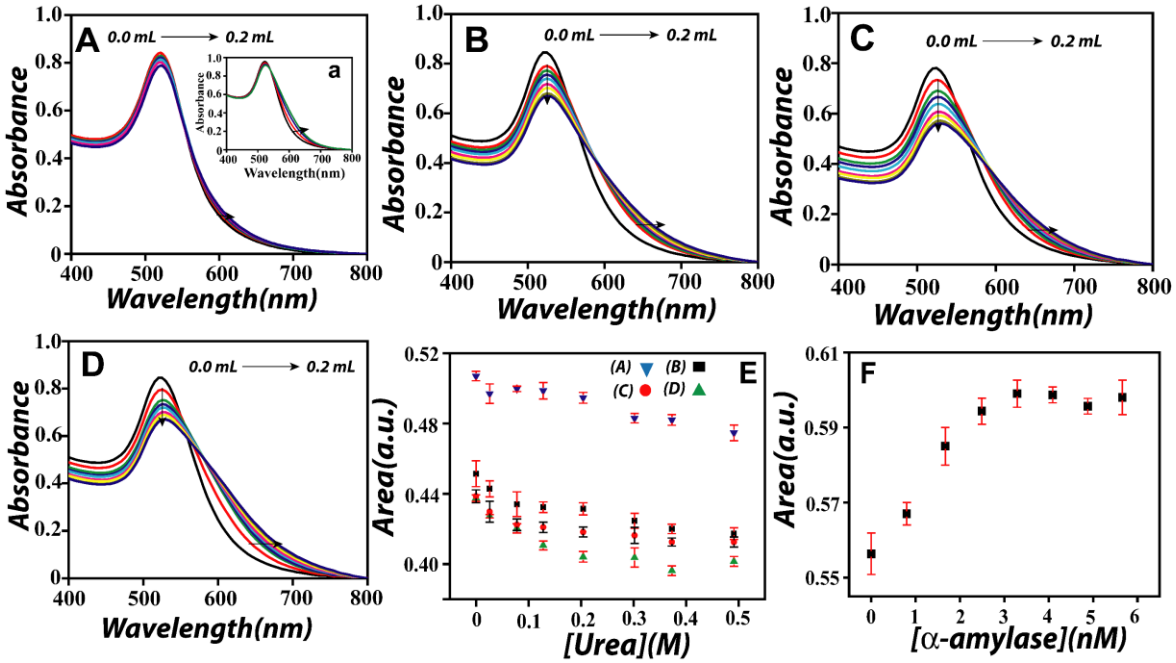

Figure 2.1 UV–Vis spectra of 3.0 mL of cit–Au NPs solution on successive addition (from 0.01 mL to 0.2 mL) of 8 M stock urea solution, already containing (**A**) 0.00 mL (**B**) 0.02 mL (**C**) 0.04 mL and (**D**) 0.06 mL of α–amylase The stock concentration of α–amylase was 127 nM. All the UV–Vis spectra were recorded after 5 min incubation. cit–Au NPs mixture with α–amylase was kept for 5 min, urea added to the composite, kept further for 5 min and then the spectra were recorded. (**E**) Area under the curves in A, B, C, D versus corresponding urea concentration. (**F**) Area under the curves versus corresponding concentrations of α–amylase to cit–Au NPs. Inset: (**a**) UV-Vis spectra of 3.0 mL of cit–Au NPs solution on addition of 0.02-0.06 mL of 127 nM α–amylase. The error bar were calculated from three sets of experiments.

A better representation of the twin effects of peak broadening and SPR peak intensity changes in **Figures 2.1A−2.1D** is obtained by plotting the area under these spectra (between 405−650 nm) against the concentration of urea for each α–amylase containing cit–Au NPs solution as shown in **Figure 2.1E**. It was found that in presence of α–amylase, the SPR peak area decreased exponentially with increasing concentration of urea and the effect was more pronounced for cit–Au NPs containing larger amounts of α–amylase (**Figure 2.1E**). It may be noted that a similar plot of area under the SPR peak of cit–Au NPs plotted against concentration of α–amylase in absence of urea (**Figure 2.1F**) yielded a graph whose area increased linearly with the concentration of the protein and then reached saturation level,

consistent with our earlier findings.[30] Thus while the addition of α–amylase increased the area under the curve as well as broadened the SPR peak, addition of urea in presence of the protein had the effect of more broadening but accompanied with a systematic decrease in peak area. The latter was due to a significant decrease in SPR peak intensity. Combined results in **Figure 2.1**, suggest that the agglomeration process of cit–Au NPs with α–amylase is not necessarily driven by denaturation of the protein.

Previous time-dependent UV–Vis spectroscopic studies of cit–Au NPs in presence of α–amylase indicated that the broadening of SPR peak in the presence of α–amylase gradually increased with time and reached a saturation level, beyond which, further broadening was not observed.[29] In the present study, when 0.06 mL of 127 nM of α–amylase was added to 3 mL of cit–Au NPs solution and the UV–Vis spectrum, recorded at 5 min intervals was found to evolve slowly with time (**Figure 2.2A**). Further, with time the changes became less and less apparent and after about 40 min the changes were hardly noticeable. In other words, the spectrum reached a 'saturation point' in time. Thereafter, 0.01−0.2 mL of 8 M stock urea was added and the evolution of UV–Vis spectrum was recorded at increasing concentration of urea, the results of which are displayed in **Figure 2.2B**. The addition of urea to the 'time saturated' cit–Au NPs –protein composite resulted in a slight decrease in the peak absorbance at 522 nm accompanied by a slight red shift to 524 nm. Apart from this, the 'time saturated' spectra of cit–Au NPs protein composite was not much affected upon addition of urea. Small changes that are observed in **Figure 2.2B** are similar to the control experiments of addition of urea to cit–Au NPs (**Figure 2.1A**) and may be attributed to dilution effects. We conclude from here that once protein agglomeration with cit–Au NPs is complete, urea had minimal effect on the UV–Vis spectrum. In another experiment, 0.06 mL of 127 nM α–amylase was added to 3.0 mL of cit–Au NPs dispersion. After 5 min, 0.12 mL of 8M urea solution was added and the UV-Vis spectra were recorded at 5 min intervals. In the presence of urea, the UV–Vis spectrum of cit–Au NPs and α–amylase mixture was found to evolve with time accompanied by a substantial decrease in peak absorbance at 522 nm. Further, a shoulder at 600 nm became prominent and there appeared to be an isosbestic point at 575 nm (**Figure 2.2E**). Interestingly, we find that the isosbestic point is sharper when the concentration of urea was higher for the same concentration of protein (**Figure 2A.3,** in **appendix**). Since the agglomeration of cit–Au NPs in presence of protein does not lead to an isosbestic point (**Figure 2.2A**), the origin of isosbestic point must be attributed to presence of urea in the system during the agglomeration process of α–amylase and cit–Au NPs seen in **Figure 2.2E**. Further, this system also reached saturation point in time beyond which no further change in the spectrum was observed (**Figure 2.2E**). A comparison of the time saturated spectrum in

Figure 2.2A and **Figure 2.2E** is given in **Figure 2.2G** and which shows that in presence of urea, the extinction spectrum of the cit–Au NPs–protein composite broadened more with time than in absence of urea. The combined results in **Figure**s **2.2A**, **2.2E** and **2.2G** suggests that the conformation of proteins around cit–Au NPs in the two agglomerated systems, i.e. α–amylase in presence of urea and α–amylase in absence of urea, are different.

A comparison of plots of area under the UV–Vis spectra with time and concentration of urea for the two cases: **Figure 2.2C** for cit–Au NPs in presence of only α–amylase up to saturation point and Figure **2.2D** for cit–Au NPs in presence of α–amylase after reaching the saturation point and then addition of urea, shows that in absence of urea the peak area increased up to saturation point. Further, addition of increasing amount of urea to cit–Au NPs–protein composite at 'saturation point' caused the area to decrease (**Figure 2.2D**). Similarly the area under SPR band of cit–Au NPs in presence of freshly added α–amylase and a constant amount of urea also decreased with time (**Figure 2.2F**). Thus here again we find the spectral behaviour of cit–Au NPs are different in presence of α–amylase only, on one hand, and in presence of α–amylase plus urea.

An estimate of the rates of the two processes can be obtained from **Figure 2.2C** and **Figure 2.2F**. Both the processes are first order but the former showed an exponential growth while the latter an exponential decay in the area under their respective extinction spectra with time. The rate constant for the growth in the peak area of cit–Au NPs spectrum in the presence of α–amylase was 0.064 min^{-1}, while the first order decay in the peak area of cit–Au NP spectrum in presence of urea and α–amylase occurred with a rate constant of 0.032 min^{-1}. Thus the conformation changes of α–amylase in presence of urea (leading possibly to denaturation) proceeded more slowly than the conformational changes occurring in absence of urea when cit–Au NPs was present in the system. As a result, at higher concentrations of urea the rate of denaturation of protein can effectively compete with the agglomeration process possibly explaining the more pronounced isosbestic point in the UV−Vis spectra of cit–Au NPs (**Figures 2A.3,** in **appendix)**. Also, the difference in rates of the two processes suggests that the conformational changes of α–amylase associated with cit–Au NPs are probably distinct and different that those occur in presence of denaturant urea. The overall observations, so far thus, seem to suggest that the changes in the optical behaviour of cit–Au NPs in presence of a denaturant added after the addition of α–amylase is distinctly different from the optical behaviour of cit–Au NPs containing only α–amylase.

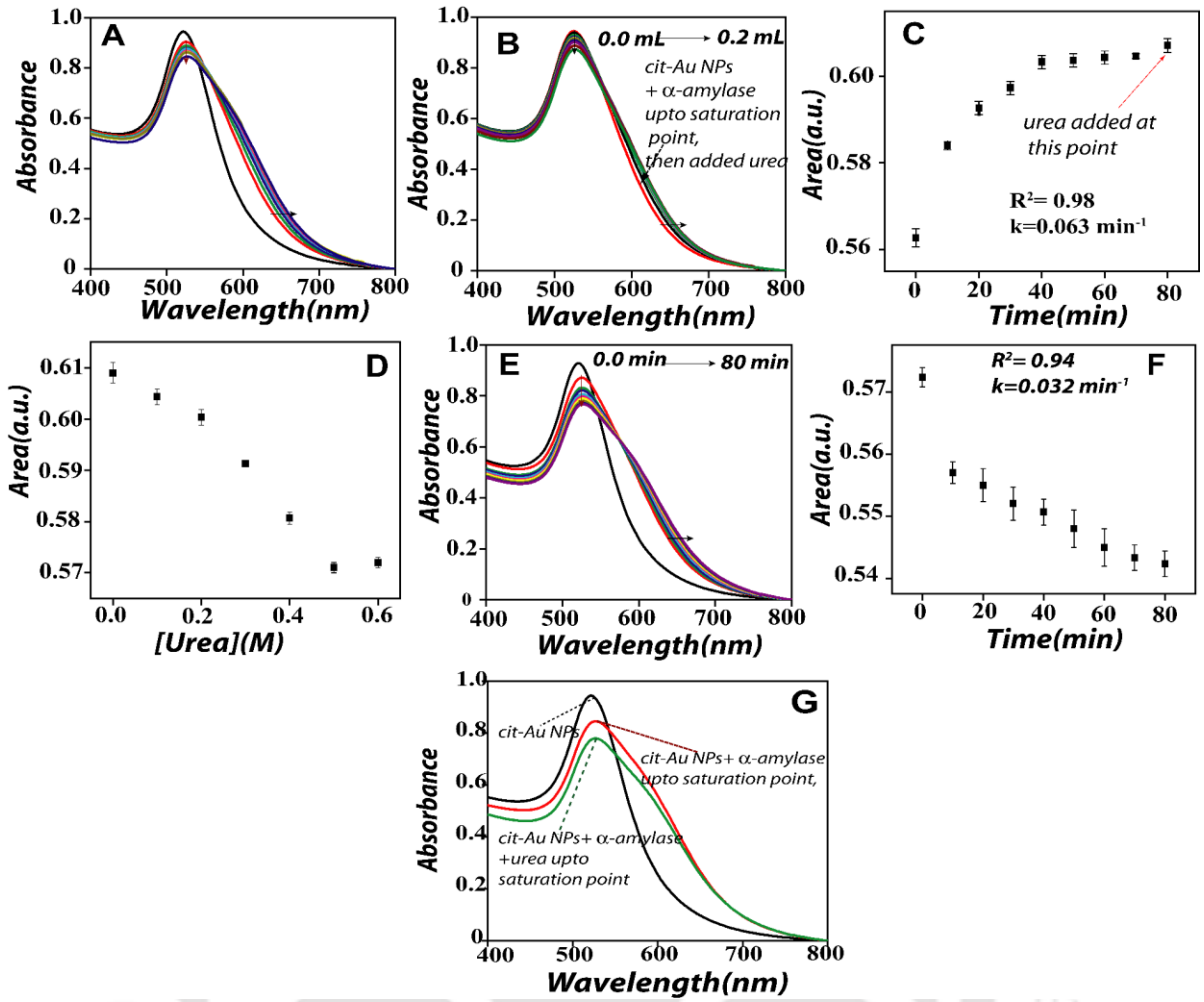

Figure 2.2 (**A**) Time Dependent UV–Vis spectra of 3.0 mL of cit–Au NPs in presence of 0.06 mL of α–amylase (0–80 min). (**B**) Time Dependent UV–Vis extinction spectra of 3.0 mL of cit–Au NPs in presence of 0.06 mL of α–amylase after reaching saturation point and addition of successive amounts of 8 M urea solution(0.01-0.2mL).(**C**) Area under the curves in A versus corresponding time. (**D**) Area under the curves in presence of 0.06 mL of α–amylase after reaching saturation point and then added the successive amounts of 8 M of stock urea solution (**E**) Time dependent UV–Vis extinction spectra of 3.0 mL of cit–Au NPs in presence of 0.06 mL of α–amylase and 0.12 mL urea solutions (0–80 min). cit– Au NPs–protein composite are kept for 5 min and then urea solution was added to it and the extinction spectra were recorded. **(F)** Area under the curves in (**E**) versus corresponding time. (**G**) Comparative broadening up to saturation point of 3.0 mL cit–Au NPs in presence of 0.06 mL of α–amylase and of 3.0 mL of cit-Au NPs in presence of 0.06 mL of α–amylase and 0.12 mL urea solution. The stock concentration of α–amylase and urea were 127 nM and 8 M, respectively. The error bar were calculated from three set of experiments.

The large drop in the area under the extinction spectrum of cit–Au NPs–protein composite on addition of urea (**Figure 2.2F**) probably reflects conformational changes in α–amylase, which affects the next stage of interaction of the protein with Au NPs. It is obvious that the UV–Vis spectrum of cit–Au NPs broadened in presence of protein only (**Figure 2.2A**) till the 'saturation point'. Further, when urea was added after the saturation point, the spectrum changed marginally (**Figure 2.2B**). It is reported that the denatured form of α–amylase broadens the extinction curve of cit–Au NPs less than that of the native form of protein α–amylase.[29] Therefore the marginal changes in **Figure 2.2B** suggests that urea is

unable to affect the conformation of the protein once it is agglomerated in the cit–Au NPs–protein composite. However, if urea is added early on, during the course of the agglomeration process of α–amylase with cit–Au NPs, the denaturation process may effectively compete and change the course of the agglomeration process. The large changes in the spectral characteristics shown in **Figure 2.2E** and the drastic drop in area under the SPR band in **Figure 2.2F**, are indicative of interplay of such competing processes. Therefore, when urea is present while the agglomeration process is taking place, simultaneous changes in the conformation of α–amylase [30] must be responsible behind the greater broadening of the SPR peak of Au NPs. Moreover, when time dependent UV–Vis spectrum was recorded for cit–Au NPs containing constant amount of α–amylase, but different concentration of urea, it was found that for higher concentrations of urea the SPR peak broadened more (**Figure 2A.3**, in **appendix*).*** The first order rate constants extracted from the exponential decay in the peak area under these SPR bands showed that peak broadening was faster for higher concentrations of urea (**Figure 2A.3F** in **appendix**). This is consistent with the more pronounced isosbestic point in the UV–Vis spectra of cit–Au NPs α–amylase system at higher concentrations of urea (**Figure 2A.3** in **appendix**). This indicated that in the presence of α–amylase only, cit–Au NPs agglomerated more easily whereas in the presence of urea the extent of agglomeration was less.

We have observed that when 0.02 mL of native α–amylase was added to 3.0 mL of cit–Au NPs, the absorption maximum shifted from 521 nm to 523 nm (**Figure 2.3A** and inset to **Figure 2.1A**). The changes in spectral characteristics continued to occur with more addition of protein till a volume of 0.08 mL was reached when the protein concentration was 3.29 nM, indicating a saturation of the process (**Figure 2.3D**). Similar experiments carried out in presence of 0.08 mL of 127 nM chemically denatured α–amylase showed nominal changes in the spectral characteristics (**Figure 2.3B**) which saturated at a concentration of 4.09 nM as seen on a plot of area vs concentration (**Figure 2.3D**). A clear comparison of the two saturated spectra, seen in **Figure 2.3C**, shows greater SPR peak broadening of cit–Au NPs in presence of native α–amylase than in presence of chemically denatured α–amylase. A comparison of plots of area under the UV–Vis spectra with the concentration of the native and denatured protein in **Figure 2.3D** show that the area increases in both cases, it does so less in presence of denatured protein than in case of native protein. The above results indicate that the agglomeration of cit–Au NPs and protein not only depended on the concentration of protein but also on its conformational state.

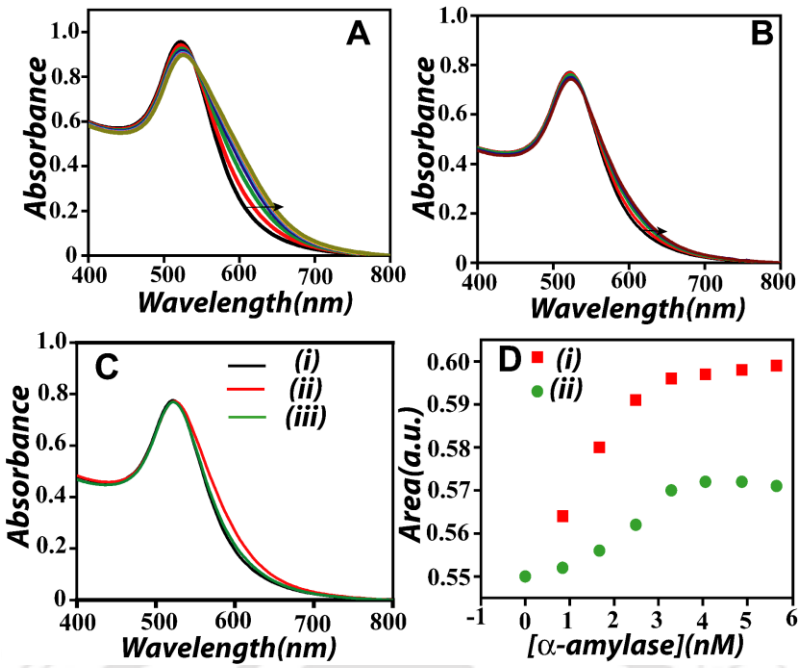

Figure 2.3 UV–Vis spectra of 3.0 mL of Cit-Au NPs in presence of: (**A**) various amount of native α–amylase of 127 nM with final concentration from 0.84–5.66 nM added successively, (**B**) various amount of chemically denatured α–amylase (0.02–0.08 mL of 127 nM with final concentration from 0.84–5.66 nM added successively, (**C**) Comparative analysis in presence of only cit-Au NPs (**i**), native α–amylase {0.04 mL as final concentration 1.7 nM,}(**ii**) and denatured α–amylase {0.04 mL as final concentration 1.7 nM} (**iii**), (**D**) Comparison of normalised area under the extinction curves of (**i**) (0.84-5.66 nM) of native α–amylase and **(ii)** denatured α–amylase 0.84−5.66 nM).

To ascertain the origin of broadening in the UV–Vis spectra, further investigations were carried out with TEM measurements. **Figure 2.4A** shows the image of cit–Au NPs dispersions produced by the present method in absence of protein. The average size of cit–Au NPs was found to be 10.0 ± 2.2 nm. The Au NPs produced were nearly mono dispersed and spherical in shape. Addition of 0.04 mL of α–amylase to 3.0 mL of cit–Au NPs dispersions led to the agglomeration without affecting the individual size of the NPs (**Figure 2.4B**). When 0.01 mL of 8 M urea solution was added to the above solution (**Figure 2.4C**), the size of agglomeration was similar to the cit–Au NPs–protein composite in **Figure 2.4B**. It is noteworthy that **Figure 2.4C** also shows the presence of a significant number of Au NPs that were not aggregated. Further addition of increasing amounts of 0.05–0.12 mL 8 M urea to the cit–Au NPs–protein composite did not result in significant increase in the extent of agglomeration of the NPs as is evident from **Figures 2.4(C–E)**. Thus, the TEM results showed that cit–Au NPs in presence of native form of α–amylase were agglomerated. Further agglomeration was not observed when urea was added to the composite. The slight increase in extent of agglomeration that was seen could be induced by evaporation of the samples on TEM grid.

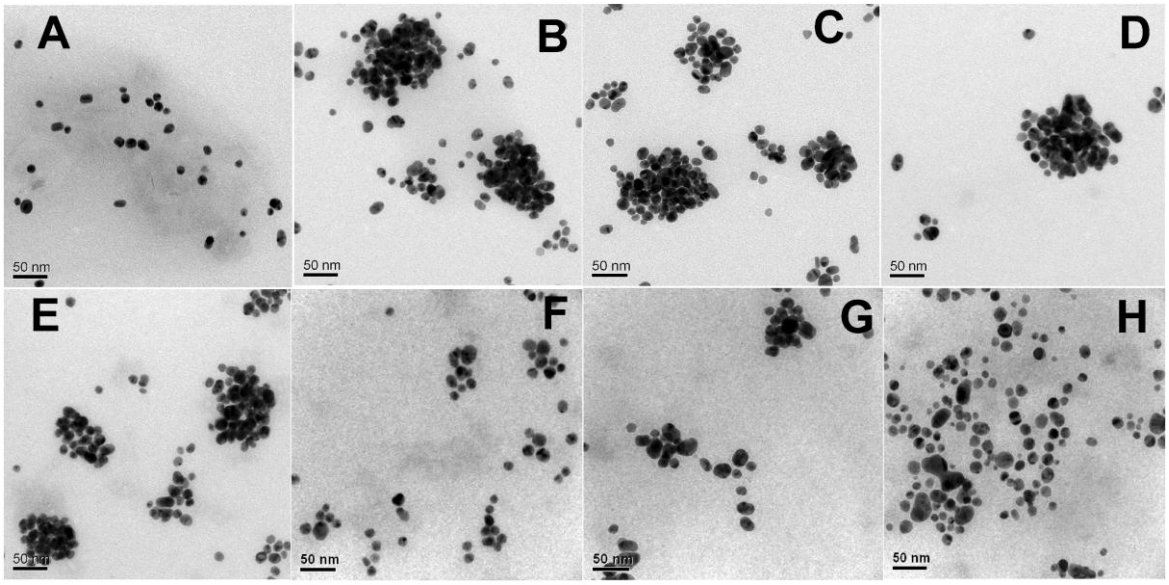

Figure 2.4 TEM images (scale bar 50 nm) of 3.0 mL of cit–Au NPs dispersions in presence of (**A**) 0.00 mL α–amylase (**B**) 0.04 mL of α–amylase (**C**) 0.04 mL α–amylase + 0.01 mL urea solution (**D**) 0.04 mL of α–amylase + 0.05 mL urea solution (**E**) 0.04 mL α–amylase + 0.12 mL urea solution (**F**) 0.01 mL (**G**) 0.05 mL (**H**) 0.12 mL of 8 M urea solution only. The stock concentration of α–amylase and urea were of 127 nM and 8 M, respectively.

The agglomeration of cit–Au NPs in presence of proteins has been studied earlier by our laboratory.[29] It was found that cit–Au NPs underwent agglomeration with increasing concentration of α–amylase.[29] Such agglomeration behaviour of NPs in presence of proteins has helped deciphering its conformation also. Our findings here suggest that when a solution of urea was added to cit–Au NPs dispersion in presence of α–amylase the on-going agglomeration process gets affected. This indicates that adding a chemical denaturant does not necessarily promote agglomeration of the cit–Au NPs α–amylase composite. Similarly, TEM images of samples consisting of 3.0 mL of cit–Au NPs in the presence of either of 0.01 mL, 0.05 mL and 0.12 mL of 8 M stock urea solutions were also carried out and the results are reported in **Figure 2.4F, G,** and **H**. These images also indicate negligible agglomeration in absence of protein. This is consistent with our observations that upon addition of urea to the Au NP dispersions in absence of α–amylase, little change was observed in the absorption spectra of cit–Au NPs (**Figure 2.1A**).

Further investigations on agglomeration of NPs were carried out by DLS-based measurement of particle size distribution (**Figure 2.5**). These DLS studies also substantiate the formation of agglomerated NPs in the presence of protein consistent with TEM and UV–Vis spectroscopic results. The agglomerated state was found to remain unchanged upon addition of urea to a solution of cit–Au NPs containing α–amylase. DLS based particle size

analysis indicated that for cit–Au NPs only, the hydrodynamic diameter of the particle was 19 nm and the maximum of the particle size distribution was found to be at 37 nm. The hydrodynamic diameter and the maximum distribution of particle sizes are shown in **Table 2.1**. In the presence of 0.04 mL of 127 nM of α–amylase the hydrodynamic diameter was found to increase to 38 nm and the maximum was found to shift to 77 nm. To this solution (3.0 mL cit–Au NPs containing 0.04 mL of 127 nM of α–amylase) when increasing amounts of urea (0.01 ml to 0.12 ml of 8M) were added, the hydrodynamic diameter was found to increase slightly from 40 to 41 nm and the maximum of distribution shifted from 80 to 86 nm (**Table 2.1** and **Figure 2.5A**). Any further addition of urea (see 0.2 ml of 8M, **Table 2.1**) did not affect the distribution of the agglomerated state.

However, our UV–Vis data showed increased broadening upon addition of urea. To reconcile our DLS and TEM findings with UV–Vis results, it is proposed that the size of the agglomerated units remained the same upon addition of urea and changes in dielectric constant of the local environment resulted in the observed broadening of UV–Vis spectra. DLS studies with 4 M and 6 M of stock urea solutions were also carried out resulting in similar observations (**Figure 2A.4, Table 2A.1**, **Table 2A.2, Table 2A.3, Table 2A.4** in **appendix**). It is noteworthy that in absence of α–amylase there was no significant change in the size distribution of cit–Au NPs upon addition of urea (**Figure 2.5B**).

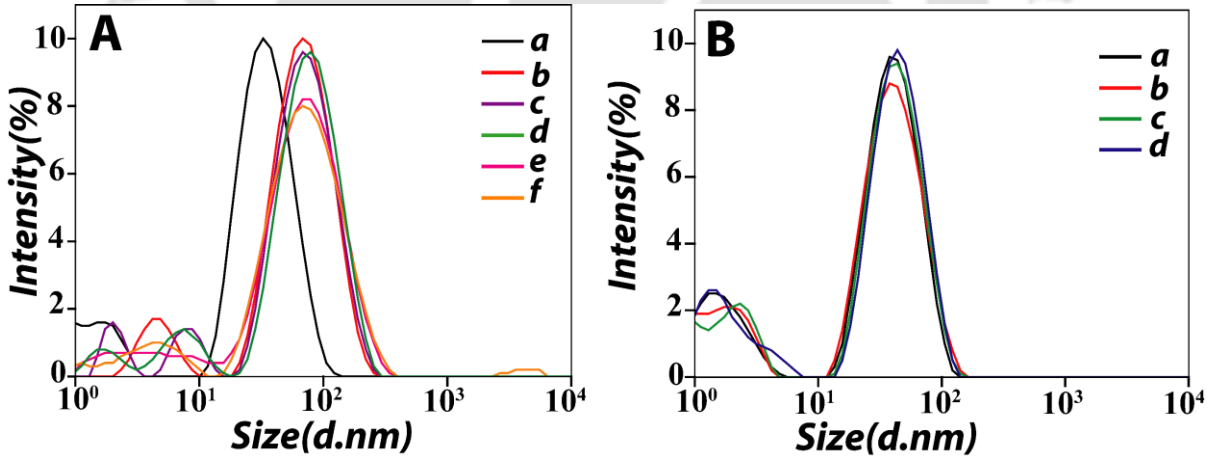

Figure 2.5 Particle size distribution curves of 3.0 mL of cit–Au NPs dispersion in presence of (**A**) (a) 0.00 mL α–amylase (b) 0.04 mL α–amylase (c) 0.04mL of α–amylase + 0.01 mL of urea solution (d) 0.04mL α–amylase + 0.05 mL urea solution (e) 0.04mL α–amylase + 0.12 mL urea solution (f) 0.04mL α–amylase + 0.2 mL urea solution (the stock concentration of α–amylase and urea were of 127 nM and 8 M, respectively) (**B**) 3.0 mL of cit–Au NPs dispersion in presence of (a) 0.00 mL (b) 0.01 mL (c) 0.05 mL (d) 0.12 mL urea solution. (The stock concentration of urea was 8 M). All the samples were kept for 5 min before recording the particle size distribution.

Table 2.1 Particle size distribution by DLS measurements using 8 M urea stock solution. All the samples were kept for 5 min prior to record the size. Urea was added to cit–Au NPs–α–amylase composite at 5 min interval.

Sample	Size (d.nm)	Peak 1		Peak 2	
		Size (d.nm)	Area (%)	Size (d.nm)	Area (%)
3.0mL cit–Au NPs	19	37	82.4	1.7	9.7
3.0mL cit–Au NPs + 0.04 mL of nM α–amylase	38	77	90.4	4.7	9.6
3.0mL cit–Au NPs + 0.04 mL of 127 nM α–amylase + 0.01 mL0f 8 M urea solution	40	80	87.3	8.2	6.8
3.0mL cit–Au NPs + 0.04 mL of 127 nM α–amylase + 0.05 mL of 8 M urea solution	41	85	89.1	4.6	10.9
3.0mL cit–Au NPs + 0.04 mL of 127 nM α–amylase + 0.120 mL of 8 M urea solution	41	86	88.4	4.4	8.9
3.0mL cit–Au NPs + 0.04 mL of 127 nM α–amylase + 0.2 mL of 8 M urea solution	41	86	87	7.7	8.8

Collective observations made from UV–Vis studies, DLS measurements, TEM analysis suggested the likelihood that the presence of α–amylase led to the agglomeration of Au NPs, which remains unchanged due to the further addition of urea, and that the broadening of the SPR peak on adding urea to the Au NP–protein composite might be due to other effects such as changes in dielectric constant of the medium.[35] The peptide chain of α–amylase contains 12 cysteine groups of which two –SH groups are exposed to the aqueous medium.[33] These –SH groups have a strong affinity to bind with the surface of Au NPs. That the α–amylase was adsorbed on cit–Au NPs was confirmed by zeta-potential measurements, where addition of 0.04 mL of 127 nM α–amylase to 3.0 mL cit–Au NPs caused the negative surface charge to drop from -50.6 to -47.7 mV. If we correlate the findings, the addition of α–amylase to a solution of cit–Au NPs showed a red-shift in the SPR band (**Figure 2.1**) together with an increase in hydrodynamic diameter (**Table 2.1**) and a drop in negative surface charge from (**Table 2.2**), they indicate a substantial coverage of protein on the surface of cit–Au NPs.[15]

At pH ~7, α–amylase is slightly negative charged /nearly neutral (isoelectric point = 6.5). Whereas the Au NPs, synthesised in presence of excess citrate ions and are fully deprotonated at pH 7.0, are stable due to the electrostatic repulsion between the negatively charged citrate capped Au NPs. Upon addition of α–amylase to cit–Au NPs, the surface charge of -47.7 mV is still sufficiently negative to stabilize the Au NPs. Thus the origin of the agglomeration of Au NPs in presence of α–amylase is unlikely to be electrostatically driven. It is probable that at the initial stages, the nearly neutral α–amylase is driven towards the negatively charged cit–Au NPs by local electrostatic interactions involving functional

groups such as the quaternary amine groups with the citrate capping agent of the Au NPs. Once the proteins and the NPs are close enough –SH group interact with Au to form Au–S bond. This could happen at the expense of some of the citrate molecules which are replaced from the surface of the Au NPs to make room for the incoming protein molecules. This could explain the reduced negative surface charge density observed in zeta potential measurements. Further, the adsorption of the α–amylase may lead to conformational changes in the protein which then could drive the observed agglomeration process. Also, the presence of excess proteins may lead to larger-scale agglomeration where additional proteins may remain as such without being directly attached to the Au NPs. Addition of 0.01 mL of 8 M stock urea solution to the Au NPs– α–amylase dispersion showed a red shift in the SPR band from 523 nm to 525 nm (**Figure 2.1**) accompanied by an increase in size from 38 nm to 40 nm and a slight decrease in the negative surface charge from −47.7 mV to −47.0 mV. Addition of increasing amounts of 8 M of stock urea (from 0.01 mL to 0.12 mL) to the Au NP– α–amylase dispersion showed decreasing peak intensity at 523 nm accompanied by increasing broadening of the SPR band (**Figure 2.1**) together with marginal increase in size from 40 nm to 41 nm and a decrease in the surface charge from −47.0 mV to −44.4 mV (**Table 2.2**). This means that the presence of urea did not destabilize the Au NPs by changing the overall electrostatic interactions in any major way. The above observations suggests that while electrostatic effects have minor role to play in agglomeration of Au NPs in protein, urea still is able to affect surface charge of Au NPs, which presumably are embedded inside the agglomerated unit. Thus urea can possibly permeate inside the agglomerated structure. These trends in zeta potential measurements and sizes are consistent with the negligible enhancement in agglomeration of the protein conjugated Au NPs in presence of urea, which were also substantiated by the TEM and UV–Vis measurements that were shown in **Figures 2.4** and **2.1**, respectively. Further increase in the added volume of 8 M stock urea of (0.05 mL and 0.12 mL) to cit–Au NPs resulted in further decrease in measured zeta potential (−45.8 mV and −44.1 mV) without any accompanying change in the hydrodynamic diameter (**Table 2A.5** , **Table 2A.6** in **appendix**). The decreasing trend of zeta potential indicated that the overall negative charge on Au NPs decreased which may be due the direct interaction of urea with the cit−Au NPs. It is noteworthy that the addition of 0.01 mL of 8 M urea stock solution to cit−Au NPs resulted in decrease in the negative surface charge from –49.7 mV to –47.9 mV without the concomitant increase in the hydrodynamic diameter. The latter was also substantiated from UV–Vis results (**Figure 2.1D**) where no significant agglomeration of cit−Au NPs was detected upon addition of urea.

Table 2.2 Results of zeta potentials of cit−Au NPs in presence of 127 nM of α–amylase and 8 M urea solutions.

Samples	Zeta potential (mV)
3.0 mL cit−Au NPs	– 50.6
3.0 mL cit−Au NPs + 0.04 mL of 127 nM α–amylase	– 47.7
3.0 mL cit−Au NPs + 0.04 mL of 127 nM of α–amylase + 0.01 mL of 8 M urea solution	– 47.0
3.0 mL cit−Au NPs + 0.04 mL of 127 nM of α–amylase + 0.05 mL of 8 M urea solution	– 46.6
3.0 mL cit−Au NPs + 0.04 mL of 127 nM of α–amylase + 0.120 mL of 8 M urea solution	– 44.4

IR spectroscopy is also an important technique to study the interaction between biomolecules and NPs.[36] Conformational changes of protein adsorbed on Au NPs has been studied by IR spectroscopy.[37] In IR spectrum, proteins show three different amide bands: amide I, amide II and amide III ,which provide important characteristic information for different type of secondary structures of protein. Among all the amide bands, amide I band is found in the region of 1700–1600 cm^{-1} and is the most important in exploring the secondary structure of proteins.[38] We have recorded the FTIR spectra of native α–amylase and its conjugates with cit−Au NPs in presence and absence of urea at pH 7.0. Pure native α–amylase showed an FTIR band in the region 1625–1700 cm^{-1} corresponding to the amide I linkage (**Figure 2.6A**), whereas cit−Au NP showed a sharp FTIR band at around 1589 cm^{-1} which is due to ν(C=O) vibration of citrate on its surface (**Figure 2.6B**).[39] When 1.7 nM of α–amylase was added to 3.0 mL of cit−Au NPs the FTIR spectrum showed a broad band at 1598 cm^{-1} corresponding to the cit−Au NPs –protein composite (**Figure 2.6B**). Further, several sharp peaks become prominent (**Figure 2.6B**) such as the one at 1327 cm^{-1} which corresponds to the ν(COO^{-}) vibration and at 920 cm^{-1} corresponding to νCH_2 of citrate group (**Figure 2.6B**). Since these features were not prominent in the FTIR spectrum of citrate capped Au NPs (**Figure 2.6A**) we conclude that upon addition of α–amylase a change in the environment around citrate ions occurs. It is possible that some of the Au NP surface bound citrate ions are released into polar regions of the protein which is consistent from our zeta potential measurements. When 0.301 M urea solution was added to the Au NP–α–amylase composite, the FTIR band of amide I red shifted indicating possible deformation of protein structure in presence of urea (**Figure 2.6B**). FTIR studies support that the conformational changes in α–amylase by cit–Au NPs are distinct from the conformational changes induced by urea. Hence, while the former leads to agglomeration in the cit–Au NPs–α–amylase system the introduction of the latter (urea) in the system stalls the agglomeration process.

The stability of the NPs was further investigated by studying agglomeration of Au NP–protein composite in an aqueous solution over a range of NaCl concentrations. It is well

known that electrolyte induced agglomeration occurs when the equilibrium between electrostatic repulsion forces and van der Waals attractive forces is disturbed due to changes in the thickness of the double layer.[40] Thus, for example, it is reported that cit−Au NPs undergo agglomeration in presence of electrolyte such as NaCl at high concentrations.[41] We have found that addition of increasing amounts (0.05–0.5 mL) of 50 mM of NaCl to the cit–Au NPs –protein composite at pH 7.0 broadens the 522 nm SPR band towards longer wavelengths (**Figure 2.7A**). This broadening is similar to that observed in case of addition of urea to cit–Au NPs–protein composite (**Figure 2.2B**). As the SPR broadening is not accompanied by agglomeration as corroborated by DLS measurements, it is probably a result of changes in dielectric constant of the medium surrounding the protein layer on the surface of Au NPs, in both the cases. This is consistent with control experiments in absence of α–amylase, which showed that when 50 mM of NaCl was added to cit-Au NPs, the UV–Vis spectra broadened slightly (**Figure 2.7B**); which was similar to the results obtained upon addition of urea to cit−Au NPs (Figure **2.1A**). In this regard it is interesting to note that plots of area under the UV–Vis spectra and particle size distribution (**Figure 2.7D** and **Figure 2A.5** and **Tables 2A.7**, **2A.8** in **appendix**) with protein–Au NP composite containing NaCl and the area under the UV–Vis spectra decreased in presence of the electrolyte.

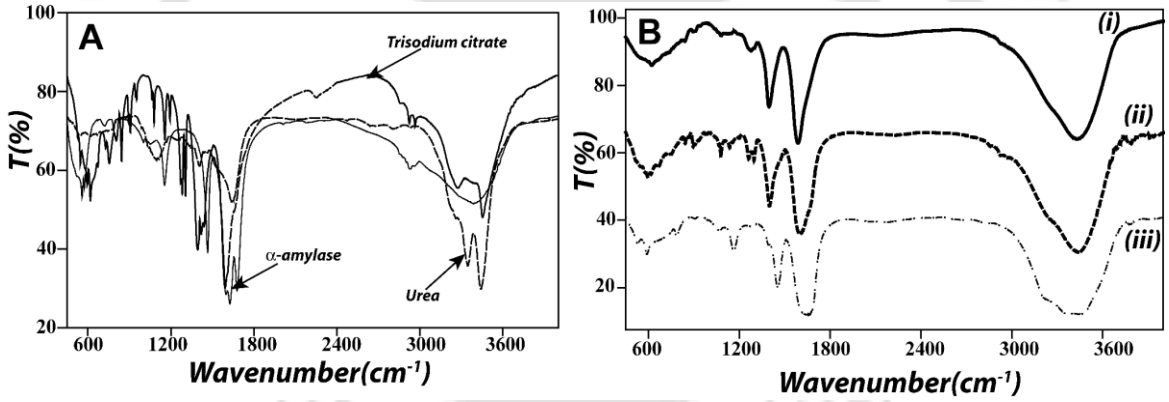

Figure 2.6 FTIR spectra of (**A**) α–amylase, citrate and urea only (**B**) cit–Au NPs in presence of (**i**) 0.00 mL of α–amylase, (**ii**) 0.04 mL α–amylase and (**iii**) 0.04 mL of α–amylase + 0.2 mL of 8 M urea.

CD spectroscopy is a powerful tool for studying the protein conformations either when in solution or when adsorbed on the surface.[42] **Figure 2.8** shows far–UV CD spectra of native α–amylase, Au NP–α–amylase and Au NP–α–amylase in presence of urea at pH 7.0. The CD spectra of native α–amylase at pH 7.0 showed two negative minima in the ultraviolet region occurring at 208 nm and 222 nm, which are the significant peaks for α–helical conformations of protein.[42] Tabulated results, obtained from the UV−CD spectra are given in **Table 2.3**, which show that the conformation of native α–amylase consists of 86% α–helix

and 6% β–sheets. In presence of cit–Au NPs after 5 min, conformational changes occur in the protein wherein some α–helix is converted to β–sheets, but 74% α–helix content is still retained (**Table 2.3**). These conformational changes in adsorbed α–amylase presumably result in agglomeration of the cit–Au NP–protein composites. Further when urea was added, conformational changes proceeded slowly, so that after 5 min 70% of α–helix and after 30 min about 30% α– helix content still remained (**Figure 2.8B** and **Table 2.3**). Interestingly though, control experiments upon addition of urea to α–amylase shows that conformational changes are faster such that after 30 min only 10% α–helix content remains (**Figure 2A.6** and **Table 2A.9** in **appendix**). This suggests that cit–Au NPs protein agglomerates are more resistant to chemical unfolding of the protein by urea than free protein.[34] It is plausible that in presence of cit–Au NPs the conformational changes directly increases the stability of the alpha helix structures of the adsorbed protein molecules making them less susceptible to attack by urea than that the free protein molecules. The results of CD, FTIR and DLS all are consistent with this view. The reduced enzyme activity of the cit–Au NPs protein composite and further reduction of this activity by urea (**Figure 2A.7** in **appendix**) is also consistent with this model.

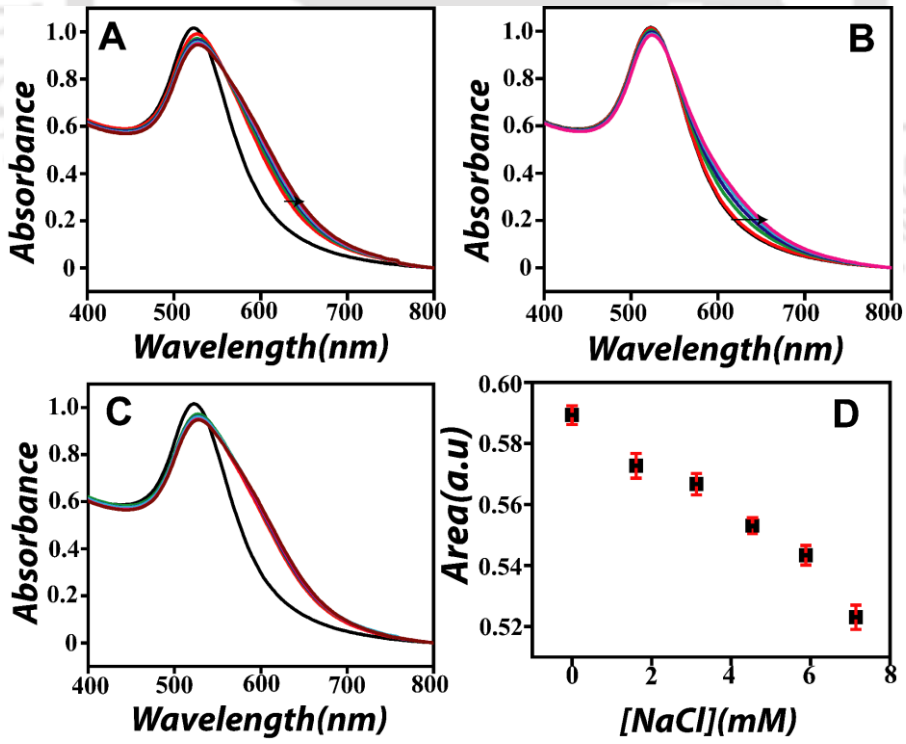

Figure 2.7 UV–Vis spectra of 3.0 mL cit–Au NPs in presence of (**A**) 0.06 mL α–amylase + 0.05–0.5 mL of 50 mM NaCl at pH 7.0. All the samples were kept for 5 min before recording the spectra. (**B**) 0.05–0.5 mL of 50 mM NaCl. (**C**) Time dependent UV–Vis spectra of 3.0 mL of cit–Au NPs in presence of 0.06 mL of 127 nM of α–amylase and 0.2 mL of 50 mM NaCl. NaCl is added after reaching saturation point of Au NPs –protein composite (0–60 min) (**D**) Area under the curve of (**A**) between (405–650 nm). The error bar were calculated from three individual experiments.

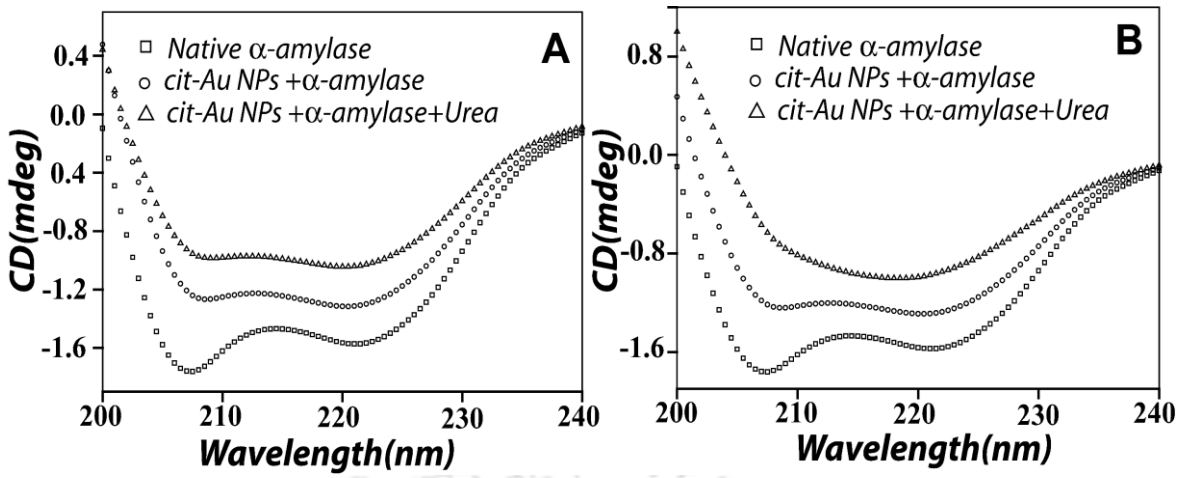

Figure 2.8 CD spectra of 0.06 mL of α–amylase (square), 3.0 mL of cit–Au NPs and 0.06 mL of α–amylase (circle) and 3.0 mL of cit–Au NPs and 0.06 mL of α–amylase with 0.4 mL of urea (Cube) (**A**) After 5 min (**B**) After 30 min Spectra were recorded in the wavelength region 200–240nm. A stock concentration of 1270 nM and 8 M were used for α–amylase and urea, respectively.

Table 2.3 Helicity of protein α–amylase obtained from UV–CD spectroscopy.

Samples	5 min		30 min	
	α–helix	β–sheet	α–helix	β–sheet
3.0 mL of α–amylase	82	6	82	6
3.0 mL of cit–Au NPs+ 0.06 mL of 1270 nM of α–amylase	74	26	70	26
3.0 mL of cit–Au NPs+ 0.06 mL of 1270 nM of α–amylase + 0.4 mL of 8M of stock urea solution	70	29	32	67

Fluorescence studies are used to monitor the environment around the tryptophan units in a protein, shedding light on its conformation state.[43] In α–amylase at pH 7, the tryptophan units which are close to the surface of the protein and exposed to the aqueous medium fluoresce with a peak at 350 nm (**Figure 2.9A**). When urea (0.92 M) was added to native α–amylase the fluorescence yield went down by ~50% but the peak position remained unchanged (**Figure 2.9A**). This shows that unfolding was not significant at these concentrations of urea, as complete unfolding would have exposed the hydrophobic pockets, decreasing the effective dielectric constant of the medium around tryptophan, and hence blue shifting the fluorescence. Probably the small changes associated with urea addition (such as polarity) are responsible for decreased fluorescence in α–amylase in **Figure 2.9A**. When to 0.46 mL of this solution 3.0 mL of cit–Au NP dispersion was added the fluorescence was found to be completely quenched (**Figure 2.9A**). This indicates that that urea treated protein binds to the surface of cit–Au NPs, probably close to the tryptophan units, such that their fluorescence is completely quenched.

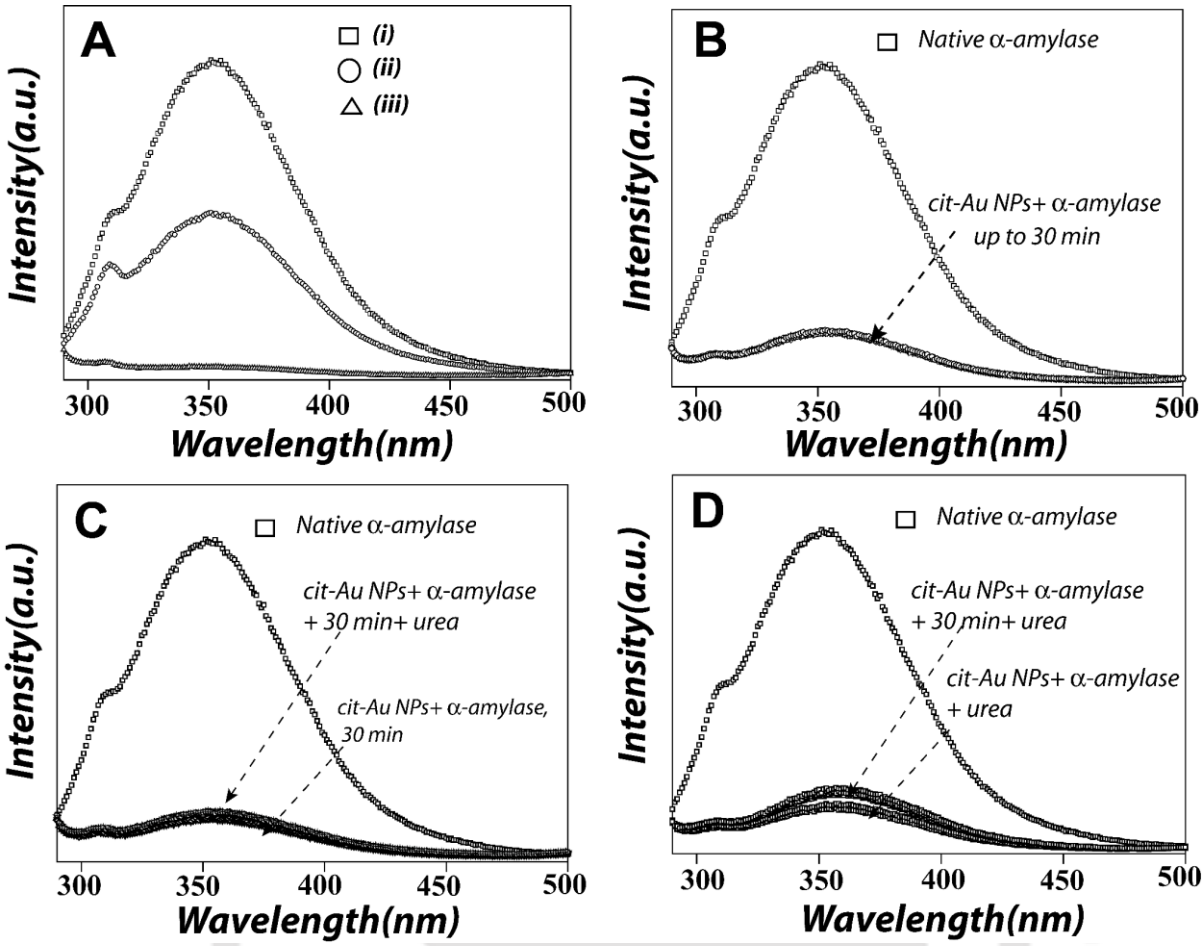

Figure 2.9 (**A**) Fluorescence spectra of native α–amylase (**i**), α–amylase + 0.4mL of urea (**ii**) and α–amylase + 0.4 mL urea + 3.0 mL of cit–Au NPs (**iii**). **(B)**Time dependent Fluorescence spectra of α–amylase in presence of 3.0 mL cit–Au NPs (0-30 min). (**C**) Addition of 0.4mL of urea to the mixture containing 0.06 mL of α–amylase and 3.0 mL of cit–Au NPs after 30 min. (**D**) Simultaneous addition of 0.06 mL α–amylase and 0.4 mL of urea to 3.0mL of cit–Au NPs. Spectra were recorded after 5 min. The stock concentration of urea and α–amylase were 8 M and 127 nM, respectively.

Interestingly when the order of addition of reagents is changed the results observed are different. To cit–Au NPs when native α–amylase is added, fluorescence yield goes down by 95% rapidly (within 5 min) and does not change further with time (**Figure 2.9B**). This indicates that α–amylase is bound to cit–Au NPs and probably close to tryptophan groups, such that it reduces the fluorescence nearly completely. The slight red shift (about 4 nm in 30 min) could be due to salt/electrostatic effect of citrate ions. We conclude that unfolding of α–amylase did not occur as blue shift was not observed in this case. After 30 minutes when urea was added to this solution a small fluorescence yield (about 2%) is recovered, however more red shift was observed (by about 4 nm in additional 30 min) (**Figure 2.9C**). This means urea has some effect on fluorescence, meaning that the cit–Au NP-amylase aggregate is not completely impenetrable by urea and that the red shift could be associated with electrostatic effects induced by urea. This fact was also substantiated from our FTIR studies and zeta potential measurements.

In another experiment, to cit–Au NPs when native α–amylase and urea were added in quick sequence, fluorescence yield also dropped by ~ 95% almost immediately and then regained by about 5% after ~30 min (**Figure 2.9D**). There was a constant red shift (while fluorescence yield dropped by ~ 95%), which red shifted further when fluorescence was partly recovered (about 5%) after 30 min. Note that 5% regain is greater than 2% regain in the above experiments of **Figure 2.9C**. So urea penetrates more into the aggregated structure in this case (**Figure 2.9D**) than that in the above case (**Figure 2.9C**), as would be expected, because the aggregated structures grow slowly (in minutes) with time.

All experimental evidences indicated that the conformational changes accompanying the addition of urea to cit–Au NPs treated α–amylase is certainly different than when added to free α–amylase. This was also substantiated from detailed enzymatic activity studies of the digestion of starch in absence of, and in presence of the α–amylase–Au NP composite, as well as urea treated α–amylase–Au NP composite (**Figure 2A.7** in **appendix*)***. We found that the rate was highest when native α–amylase was used ($k = 0.099\ min^{-1}$) and that rate dropped marginally for cit–Au NPs –α–amylase composite ($k = 0.097\ min^{-1}$). However, in presence of 1.5 mL of 8M urea the rate constant of the cit–Au NPs–α–amylase composite lowered drastically ($k = 0.05\ min^{-1}$ vs. $0.097\ min^{-1}$, respectively). Similar experiments were carried out in presence of 6 M and 4 M of urea stock solutions containing α–amylase and Au NPs, and from these we conclude that in presence of 8 M urea stock solution the rate for the digestion of starch was lower than for 6 M or 4 M of urea stock solutions (**Figure 2A.7** in **appendix**) The marginal reduction in the enzymatic activity of cit–Au NP–protein composite from the native protein in this study could be a reflection of the agglomerated state of some of the protein, whereby the embedded protein molecules are inaccessible for catalytic activity. The presence of large number of free proteins accounts for a considerable enzyme activity in the system ($k = 0.0973\ min^{-1}$). Upon addition of urea, however enzyme activity is reduced considerably as free protein molecules are readily denatured.

Overall, from the results reported herein it is clear that when α–amylase was added to cit–Au NPs dispersion, agglomeration took place leading to the formation of composite between the NPs and the protein. With time the size of the composite increased, which was reflected in the UV–Vis spectral broadening and supported by DLS and TEM studies. However, the agglomeration reached a limit with time beyond which their sizes did not increase. Moreover, addition of urea to the cit–Au NP–protein composite did not lead to further agglomeration of the composite. Rather agglomeration of cit–Au NP–α–amylase got stalled upon addition of urea. Further, FITR, zeta potential and fluorescence results indicated that the cit–Au NP–protein in agglomerated structures are relatively permeable to urea.

In essence, the conformational changes in α–amylase induced by cit–Au NPs are slow and the NPs appear to stabilize the alpha helix of the protein. Thus if urea is added early to the system, the cit–Au NPs do not have enough time to change the conformation of the α–amylase, making it more susceptible to attack by urea, whereby it undergoes conformational changes associated with denaturation of the protein which halts the agglomeration process. However, if urea is added much later, then cit–Au NPs have enough time to change and lock the conformation of the α–amylase which leads to formation of agglomerated structures, as well as making it less susceptible to attack by urea. A schematic representation of the process of agglomeration between cit–Au NPs and α–amylase with time and its fate upon addition of urea shown in **Scheme 2.2**. The rate of conformational changes induced by cit–Au NPs appears to be slightly faster to the rate at which urea induces conformational changes, at the present experimental conditions. The origin of agglomeration between cit–Au NPs and α–amylase is due to conformation changes that occur upon adsorption of the protein on the surface of Au NPs. These conformation changes are distinct from those induced by the chemical denaturing agent, which is a new finding of this study.

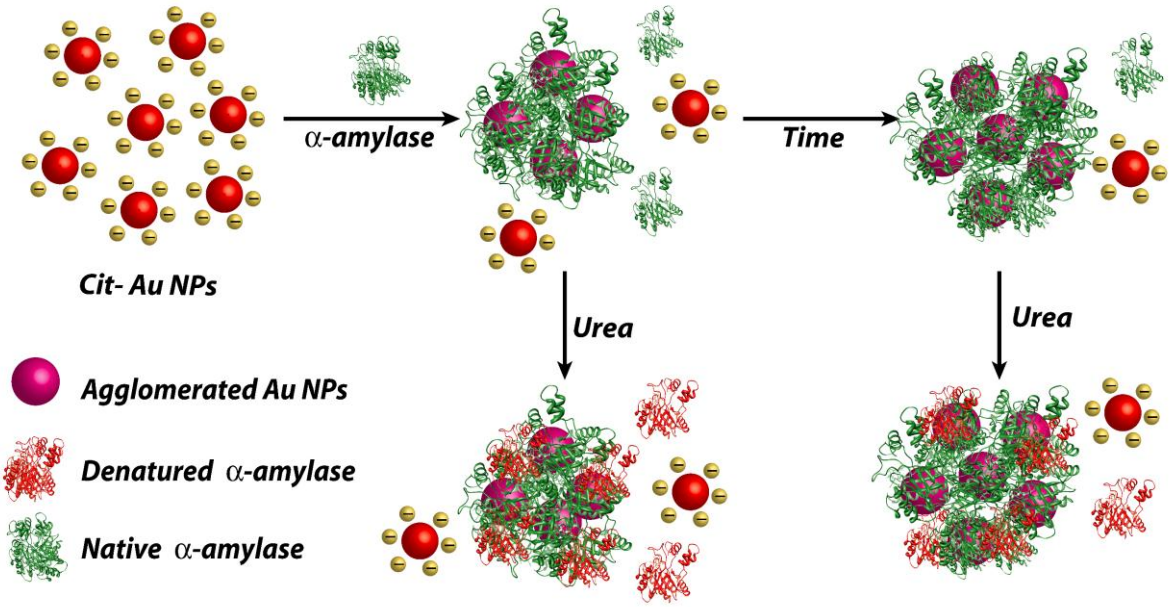

Scheme 2.2 A schematic representations of the agglomeration process of Au NPs in presence of α–amylase and urea.

2.11. CONCLUSION

In conclusion, we have been able to establish a better understanding of the agglomeration process of Au NPs and a protein. It has been observed that conformation changes in the protein upon adsorption on the surface of cit–Au NPs dominated the agglomeration process, which occurs in time scales of minutes. When urea was added to this system, unfolding of free protein molecules in the solution took place. On the other hand, although urea permeates the cit–Au NP protein agglomerated structures, the protein molecules embedded deep within these structures are more resistant to attack by urea. However we cannot rule out some partial unfolding of the proteins attached on the periphery of the agglomerates. Unfolding of free protein molecules by urea appear to prevents further agglomeration in the system. The activity of the protein is retained partially even in presence of urea, which indicates the retention of native structures for at least some of the proteins in the system. Overall, our results suggest that agglomeration of NPs takes place in presence of a protein due to specific conformation changes, however these changes neither lead to unfolding of the protein towards denaturation nor does denaturation of protein favour agglomeration of Au NPs. The evidences put forth in this study indicate newer, and more specific interactions between biomolecules and NPs, which is relevant for future applications and understandings in Nano biotechnology.

2.12. REFERENCES

1. Panyam, J.; Labhasetwar, V. *Adv. Drug Delivery Rev.*, **2003**, *55*, 329–347.
2. Michalet, X. ; Pinaud, F.F.; Bentolila, L.A.; Tsay, J.M.; Doose, S.; Li, J.J.; Sundaresan, G.; Wu, A.M.; Gambhir S. S.; Weiss. S. *Science*, **2005**, *307*, 538–544.
3. Mahmoudi, M.; Kalhor, H. R.; Laurent, S.; Lynch, I. *Nanoscale*, **2013**, *5*, 2570–2588
4. Sk, M. P.; Jaiswal, A.; Paul, A.; Ghosh, S. S.; Chattopadhyay, A. *Sci. Rep.*, **2012**, *2*, 383–387.
5. 5. Perelshtein, I.; Applerot, G.; Perkas, N.; Guibert, G.; Mikhailov, S.; Gedanken, A. *Nanotechnology*, **2008**, *19*, 245705–245710.
6. Lavik, E.; Recum, H. V. *ACS Nano*, **2011**, *5*, 3419–3424.
7. Su, Y.; Wei, X.; Peng, F.; Zhong, Y.; Lu, Y.; Su, S.; Xu, T.; Lee, S.–T.; He, Y. *Nano Lett.*, **2012**, *12*, 1845–1850.
8. Gates, A. T.; Fakayode, S. O.; Lowry, M.; Ganea, G. M.; Murugeshu, A.; Robinson, J. W.; Strongin, R. M.; Warner, I. M. *Langmuir*, **2008**, *24*, 4107–4113.
9. Tsai, D.- H.; DelRio, F. W.; Keene, A. M.; Tyner, K. M.; MacCuspie, R. I.; Cho, T. J.; Zachariah, M. R.; Hackley, V. A. *Langmuir*, **2011**, *27*, 2464–2477.
10. Chen, Y.-M.; Yu, C.-J.; Cheng, T.-L.; Tseng, W.-L. *Langmuir*, **2008**, *24*, 3654–3660.
11. Zhang, D.; Neumann, O.; Wang, H.; Yuwono, V. M.; Barhoumi, A.; Perham, M.; Hartgerink, J. D.; Wittung-Stafshede P.; Halas, N. J. *Nano Lett.*, **2009**, *9*, 666–671.
12. Sen, T.; Mandal, S.; Haldar, S.; Chattopadhyay, K.; Patra, A.; *J. Phys. Chem. C*, **2011**, *115*, 24037–24044.
13. Brewer, S. H.; Glomm, W. R.; Johnson, M. C.; Knag, M. K.; Franzen, S. *Langmuir*, **2005**, *21*, 9303–9307.
14. Tessier, P. M.; Jinkoji, J.; Cheng, Y.-C.; Prentice, J. L.; Lenhoff, A. M. *J. Am. Chem. Soc.*, **2008**, *130*, 3106–3112.
15. Tsai, C.-S.; Yu, T.-B.; Chen, C.-T. *Chem. Commun.*, **2005**, *0*, 4273–4275.
16. Goodrich, G. P.; Helfrich, M. R.; Overberg, J. J.; Keating, C. D. *Langmuir*, **2004**, *20*, 10246–10251.
17. Claridge, S. A.; Liang, H. W.; Basu, S. R.; Fréchet, J. M. J. Alivisatos, A. P. *Nano Lett.*, **2008**, *8*, 1202–1206.
18. Kim, J. – Y.; Lee, J.–S. *Nano Lett.* **2009**, *9*, 4564–4569.
19. You, C.–C.; Agasti, S. S.; De, M.; Knapp, M. J.; Rotello, V. M. *J Am. Chem. Soc.*, **2006**, *128*, 14612-14618.
20. Hong, R.; Fischer, N. O.; Verma, A.; Goodman, C. M.; Emrick, T.; Rotello, V. M. *J. Am. Chem. Soc.*, **2004**, *126*, 739–743.
21. Dykman, L. A.; Khlebtsov, N. G. *Acta Nature*, **2011**, *2*, 34–53.
22. Neely, A.; Perry, C.; Varisli, B.; Singh, A. K.; Arbneshi, T.; Senapati, D.; Kalluri, J. R.; Ray, P. C. *ACS Nano*, **2009**, *3*, 2834–2840.
23. Zhou, G.; Liu, Y.; Luo, M.; Xu, Q.; Ji, X.; He, Z. *ACS Appl. Mater. Interfaces*, **2012**, *4*, 5010–5015.
24. Kah, J. C. Y.; Chen, J.; Zubieta, A.; Hamad-Schifferli, K. *ACS Nano*, **2012**, *6*, 6730–6740.
25. Aslan, K.; Lakowicz, J. R.; Geddes, C. D. *Anal. Chem.*, **2005**, *77*, 2007–2014.
26. Lee, I.-H.; Kwon, H.-K.; An, S.; Kim, D.; Kim, S.; Yu, M. K.; Lee, J.-H.; Lee, T.-S.; Im, S.-H.; Jon, S. *Angew. Chem., Int. Ed.*, **2012**, *51*, 8800–8805.

27. Wu, C.-S.; Lee, C.-C.; Wu, C.-T.; Yang, Y.-S.; Ko, F.-H. *Chem. Commun.*, **2011**, *47*, 7446–7448.
28. Deka, J.; Paul, A.; Chattopadhyay, A. *RSC Advances*, **2012**, *2*, 4736–4745.
29. Deka, J.; Paul, A.; Chattopadhyay, A. *J. Phys. Chem. C*, **2009**, *113*, 6936–6947.
30. Deka, J.; Paul, A.; Chattopadhyay, A. *Nanoscale*, **2010**, *2*, 1405–1412.
31. Khandelia, R.; Deka, J.; Paul, A.; Chattopadhyay, A. *RSC Adv.*, **2012**, *2*, 5617–5628.
32. Buisson, G.; Duee, E.; Haser, R.; Payan, F. EMBO J. 1987, 6, 3909–3916.
33. Rangnekar, A.; Sarma, T. K.; Singh, A. K.; Deka, J.; Ramesh, A.; Chattopadhyay, A. *Langmuir*, **2007**, *23*, 5700–5706.
34. Qi, X. L.; Holt, C.; Mcnulty, D.; Clarke, D. T.; Brownlow, S.; Jones, G. R. *Biochem. J*, **1997**, *324*, 341–361.
35. Mahmoud, M. A.; Chamanzar, M.; Adibi, A.; El-Sayed, M. A. *J. Am. Chem. Soc.*, **2012**, *134*, 6434−6442.
36. Shang, L.; Wang, Y.; Jiang, J.; Dong, S. *Langmuir*, **2007**, *23*, 2714–2721.
37. Deka, J.; Paul, A.; Ramesh, A.; Chattopadhyay, A. *Langmuir*, **2008**, *24*, 9945–9951.
38. Surewicz, W. K.; Mantsch, J. H.; Chapman, D. *Biochemistry*, **1993**, *32*, 389–394.
39. Ojea-Jimeńez, I.; Romero, M. F.; Bastús, G. N.; Puntes, V. *J. Phys. Chem. C*, **2010**, *114*,1800–1804.
40. Hunter, R. J. *Foundations of Colloid Science* **1992**, Clarendon Press: Oxford, U.K.
41. Wang, G.; Sun, W. *J. Phys. Chem. B*, **2006**, *110*, 20901–20905.
42. Greenfield, N. J. *Natl. Protoc*, **2006**, *6*, 2876–2890.
43. Iosin, M.; Toderas, F.; Baldeck, P. L.; Astilean, S. *J. Mol. Struct.*, **2009**, *924-926*, 196–200.

Chapter 3

Superior Antibacterial Activity of Fluorescent Copper Nanoclusters via Reactive Oxygen Species (ROS)*

This chapter describes an excellent bactericidal activity of copper nanoclusters with a particular emphasis on the understanding of possible mechanism of antibacterial action. The pronounced antibacterial activity of copper nanoclusters was due to the heightened oxidative stress fuelled by reactive oxygen species (ROS) formed by the interaction of copper nanoclusters with bacterial cell membrane through electrostatic interactions. Moreover, electron microscopy and flow cytometric studies confirmed the damage of bacterial cell membrane caused by the penetration of copper nanoclusters owing to their small size.

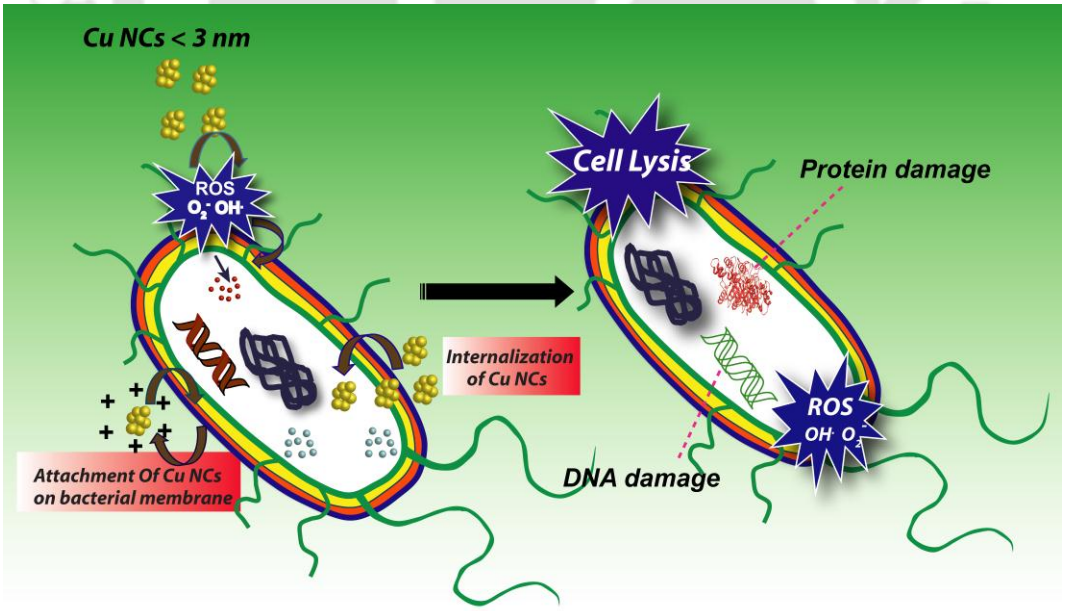

*Ghosh, R.; Goswami, U.; Sanpui, P.; Ghosh, S. S.; Chattopadhyay, A.; Paul, A. **2015,** (Manuscript to be submitted)

3.1. INTRODUCTION

The growing need and the commensurate advancement of nanotechnology have witnessed the advent of nanomaterials as emerging candidates for diverse applications especially in medicine. The enormous interest in nanomaterials is primarily due to the tuneability of their intrinsic physical and chemical properties based on size, shape and surface functionalization. For example, nanomaterials are particularly effective, owing to their small size as well as high surface-to-volume ratio, for large surface activity in making contact with microorganisms, which leads to their inactivation.[1]

Copper (Cu) is a well-known broad spectrum biocide that inhibits the growth of various microorganisms including bacteria.[2] For example, in contrast to the bulk materials, a nanoscale form (size <100 nm) of copper oxide (CuO) or other inorganic/metal oxide materials (ZnO, TiO_2) have been explored as promising antibacterial agents against both Gram positive and Gram negative bacteria.[3-7]Among all the metal oxide nanoparticles (NPs), CuO NPs are the most potent antibacterial agent and therefore are being widely used in textile industries.[8] Additionally, CuO/Cu NPs have been used in antifouling paint,[9] wood preservation,[3] gas sensing, ink, plastics lubricants and cosmetics due to the proven efficacy against different microorganisms (for examples, virus, algae, bacteria etc.).[10-12] Unlike silver, which although has been extensively studied as antibacterial agent in its bulk as well as in nano dimensions is cytotoxic, Cu is an essential trace element needed for structural and functional integrity of most living organisms. The quintessence of Cu arises due to its two oxidation states, Cu (I) (reduced) and Cu (II) (oxidized), which effectively contribute to its potential role as a catalytic cofactor in diverse biological reactions.[13] Unlike Au and Ag, a feasibility to remove excess amounts of Cu from human body by sequestration makes it an important metal in biological reactions.[14] In addition, utilizing Cu is cost-effective due to its cheaper feedstock as compared to that of Ag.

So far it has still not been possible to clearly explain the origin of bactericidal activity of CuO NPs or Cu NPs, even though several reports attribute toxicity of a few metals and their oxide NPs (CuO, ZnO and Ag NPs) to the leaching of metal ions from the corresponding NPs.[15-16] These soluble metal ions then are said to interact with the cellular membranes resulting in their observed antibacterial activity.[15-16] However, it has also been demonstrated that the NPs themselves – rather than the leached metal ions – cause the antibacterial activity, primarily due to the specificity as well as the small size of the metal NPs.[17] As in an earlier report from our group, the interaction of Cu NPs to sulphur containing proteins in the bacterial membrane, caused an increased permeability of the membrane, leading to bacterial death has.[11] Applerot *et al.* have reported that the antibacterial activity of

CuO NPs (different in size) in Escherichia coli (*E. coli*) arises from the uptake of the NPs by the bacterial cells, resulting in the oxidative stress through the production of reactive oxygen species (ROS).[18] However, the origin of bactericidal activity of Cu NPs – especially when the size is less than 3 nm – has not been clearly understood yet.

To address this challenge, herein we report the antibacterial activity of Cu nanoclusters (Cu NCs) by using green fluorescent protein (GFP) expressing recombinant *E. coli* as a model bacterium. The Cu NCs, synthesized using bovine serum albumin (BSA) as a stabilizer and hydrazine hydrate as the reducing agent, were found to be ca. 2.6 nm in size and showed bright red luminescence under UV light. The minimum inhibitory concentrations (MIC) and minimum bactericidal concentration (MBC) of the Cu NCs were found to be 13.2 ± 0.46 μg/mL and 16.1 ± 0.8 μg/mL respectively, in terms of Cu concentration in the medium. Field-emission scanning electron microscopy (FESEM) analyses and zeta potential measurements revealed the presence of the Cu NCs to the bacterial membrane, which may leading to change in bacterial surface. It was observed that the NCs induced oxidative stress in the treated bacteria, ultimately resulting in bacterial death. The ultra-small size of the BSA stabilized NCs enables them to easily cross through the bacterial membrane and subsequently generate ROS, inducing oxidative stress within the bacterial cell.

3.2. EXPERIMENTAL SECTION

3.2.1. Materials

$CuSO_4$, sodium hydroxide and hydrazine hydride (80%) were procured from Merck Specialities Pvt. Ltd., India. BSA and nitroblue tetrazolium chloride (NBT) were supplied by Sisco Research Laboratories Pvt. Ltd. and Sigma Aldrich USA, respectively. Milli-Q grade water (18.2 MΩcm) was used for all the experiments. GFP-expressing recombinant *E. coli*,[19] was cultured in Luria-Bertani (LB) medium (Sigma Aldrich, USA). All the antibacterial experiments were carried out in presence of phosphate buffered saline (PBS), pH 7.4.

3.2.2. Synthesis of BSA stabilized Cu NCs

The BSA stabilized Cu NCs were synthesized according to a literature reported method.[20] Briefly, 4.2 mM of $CuSO_4$ and 0.3 mM of BSA were mixed in 5.0 mL of water in weight ratio of 13:1. The solution was stirred for few minutes at room temperature and then 0.1 mL of 1.0 M NaOH was added to make the solution alkaline (pH~10-11). In alkaline medium, protein partially unfolded exposing the functional groups which interacted with Cu^{2+} ions. To the above solution 1.0 mL of 80% N_2H_4 was added drop wise and stirred constantly for 4-6 h

at room temperature as the colour of the solution changed from purple to pale yellow. The as synthesized Cu NCs were purified by dialysis [MW 1 kDa).

3.3. CHARACTERIZATION

UV–visible and fluorescence spectra of the Cu NCs were recorded with a Perkin-Elmer Lamda 25 spectrophotometer and Fluorolog–3 (Horiba JobinYvon, Edison, NJ, USA), respectively. The size and morphology of the Cu NCs were examined in transmission electron microscopy (TEM; JEM 2100, JEOL) at operating voltage of 200 kV. The samples were drop-cast onto carbon coated copper grids and air-dried overnight at room temperature, before recording the images. The presence of the Cu NCs were examined in Field-emission scanning electron microscopy (FESEM) analyses were carried out in a Carl Zeiss, SIGMA VP instrument. The samples were drop-cast onto aluminium foil coated glass slide and air-dried overnight at room temperature, before recording the elemental analysis. Surface charges of the Cu NCs were determined by measuring the zeta potential in a Malvern Zeta Size Nano ZS-90 instrument at 25℃ with sample viscosity of 0.8872 mPa.s.

3.4. ANTIBACTERIAL TEST

The antibacterial efficacy of the Cu NCs was tested on GFP-expressing gram negative *E. coli* bacteria. Bacterial strains were grown overnight in LB media (pH 7) containing ampicillin at 37°C under continuous shaking (220 rpm). Next morning, the bacterial cells were harvested by centrifugation. The bacterial pellet was washed with PBS and resuspended in 0.3 mL of fresh LB medium. Cu NCs were resuspended in PBS to attain the appropriate pH as well as concentrations (13.02−17.3 μg/mL). The bactericidal efficacy of Cu NCs was evaluated by adding appropriate amount of Cu NCs stock to 2.0 mL culture media containing 0.02 mL of bacterial cells (10^7 CFU/mL) and then incubating the cultures in a shaker-incubator at 220 rpm at 37 °C (12 h). The bacterial growth was monitored by recording the optical density at 595 nm. The antibacterial potency of the Cu NCs was estimated by the viability-count assay. At specific time-point, bacterial culture was diluted in PBS, spread on LB-agar plates and subsequently incubated at 37°C for 24 h. The number of viable bacterial cells was calculated by counting the bacterial colonies grown in each plate multiplied by the dilution factor and expressed as CFU/mL.[18] Each experiment was repeated three times for reproducibility.

3.4.1. Nitroblue Tetrazolium Assay for Oxidative stress in Bacterial Cells

Bacterial suspension (10^7 CFU/mL) was centrifuged at 10,000 rpm for 2 min at 4°C. The bacterial pellet was redispersed in 0.1 mL of Hanks balanced salt solution (HBSS) and

incubated with the Cu NCs at MIC (13.2±0.46 μg/mL) and MBC (16.1±0.8 μg/mL) for 5, 15, 30 45 and 60 min at 37 °C, respectively.[4] Then, 500 μL of NBT (1 mg/mL) was added to each tube and incubated for another 30 min at 37 °C in a water bath. After removing the tubes from water bath, 0.1 mL of 1.0 M of HCl was added to each tube to stop the reaction. Then, the tubes were centrifuged at 10,000 rpm for 2 min at 4°C to remove the supernatant from the bacterial cells. After removing the supernatant, the bacterial pellets were redispersed in DMSO to collect the formazan products generated from NBT. The formation of blue coloured formazan was monitored by measuring the absorbance at 575 nm using UV-visible spectrophotometer.

3.4.2. Flow-cytometric Analysis of Bacterial Cells

The viability of bacterial cells was analyzed by flow cytometer (FACS Calibur, BD Biosciences) with propidium iodide (PI) staining. PI is a membrane impermeant dye for the viable cells and intercalates between the base pairs of the double strand DNA. Bacterial suspension (10^7 CFU/mL cells) containing MIC and MBC of Cu NCs (13.2±0.46 μg/mL and 16.1±0.8 μg/mL in terms of concentration of copper ion in Cu NCs) were incubated at room temperature for 2 h respectively. After 2 h of incubation, 0.2 mM of PI and 150 mM of NaCl was mixed into each tube and the samples analyzed by illuminating with a 15 mW argon ion laser (488nm) in the flow cytometer. The fluorescence of GFP and PI was detected in green (525 ± 10 nm) and red (620 ±10 nm) channel, respectively.

3.4.3. EDS-FESEM analysis of Cu NCs on Bacteria

Bacterial suspension with Cu NCs (13.2 μg/mL) were incubated at 220 ppm at 37°C for 2h. The samples were then centrifuged, washed with PBS buffer and fixed with 2.5% of glutaraldehyde for 1 h. Next, 6.0 μL of treated bacterial suspension were drop-cast onto aluminium foil coated glass slide and air-dried overnight at room temperature, before recording the elemental analysis.

3.4.4. Cell Viability Assay

Human cervical carcinoma cells, HeLa and human embryonic kidney cells, HEK were received from National Centre for Cell Sciences (NCCS) Pune, India and maintained in Dulbecco's Modified Eagle's Medium (DMEM) accompanied with L-glutamine, penicillin, streptomycin and fetal bovine serum (10%) under humidified CO_2 (5%) atmosphere at 37 ˚C. The viability of the cells was determined by MTT [3-(4,5-dimethylthiazol-2-yl)-2,5-diphenyltetrazolium bromide] assay. About $5x10^3$ cells/well (HeLa and HEK) were seeded in

a 96-well microplate and grown overnight in DMEM. Then, Cu NCs (8.2 -24.9 μg/mL) were added to the cells and incubated for 24 h at 37 °C under 5% CO_2. After incubation, 7.0 μL of MTT was added to each well and incubated for another 2 h under same condition for the formation of formazan (purple colored) product. The formazan product was subsequently solubilised in DMSO and its absorbance recorded at 550 nm with a microplate reader (Bio-Rad model 680; Bio-Rad, CA). The number of living cells was directly proportional to the formation of formazan and, in turn, to the absorbance at 550 nm. The viability (%) was calculated by using the following formula:

$$\% \text{ viable cells} = \frac{(A_{550} - A_{690}) \text{ of NC treated cells}}{(A_{550} - A_{690}) \text{ of control cells}} \times 100$$

where, A_{550} and A_{690} were the absorbance for the formation of formazan and control medium respectively.

3.5. RESULTS AND DISCUSSION

Red luminescent and biocompatible Cu NCs were prepared in the presence of BSA by modifying a reported procedure.[20] The macromolecule BSA contains a number of functional groups such as NH_2, –COOH, and –SH to which Cu^{2+} ions were bonded and they were further reduced to Cu NCs by hydrazine hydrate in alkaline conditions. In alkaline medium, the partially unfolded BSA could expose enough number of such groups that would further assist in the strong binding of the NCs to the protein.[21] Notably, the three-dimensional structure of BSA provides enough space to attach more than one cluster to the same protein due to a number of functional groups.[22,23] Consequently, the as synthesized light yellow colored BSA-stabilized Cu NCs were stable in aqueous medium for a long time. The absorption spectrum of the NCs (**Figure 3.1A**) lacked a surface plasmon peak between 500–600 nm, indicating the lack of formation of Cu NPs. Moreover, the emission spectrum of the BSA-stabilized Cu NCs showed maxima at 640 nm when excited at 405 nm (**Figure 3.1B).** The bright and intense luminescence of the NCs under UV light is due to the d-band transition of Cu NCs.[14] The morphology and size are among the key factors of any nanomaterial for its applications in biomedical field. TEM images confirmed the formation of spherical Cu NCs with average size 2.6±0.57 nm (**Figure 3.1C, D**).

GFP-expressing *E. coli* was chosen as a model bacterium to investigate the antibacterial characteristics of Cu NCs in the present study. The MIC and MBC of the NCs for *E. coli* bacteria were determined by the turbidity test. In order to find out the MIC and MBC value, $1x10^7$ CFU/mL of GFP-expressing *E. coli* was inoculated in LB media, supplemented with various concentrations of Cu NCs, and incubated for 12 h at 37 ˚C.

Similarly, control experiments were performed with BSA and $CuSO_4$ solution The MIC and MBC values of Cu NCs for *E. coli* were found to be 13.2 ± 0.46 µg/mL and 16.1 ± 0.8 µg/mL, in terms of the concentration of copper in the medium, respectively. The values were much lower than the reported literature value for Cu NP systems (**Table 3.1**).[11]

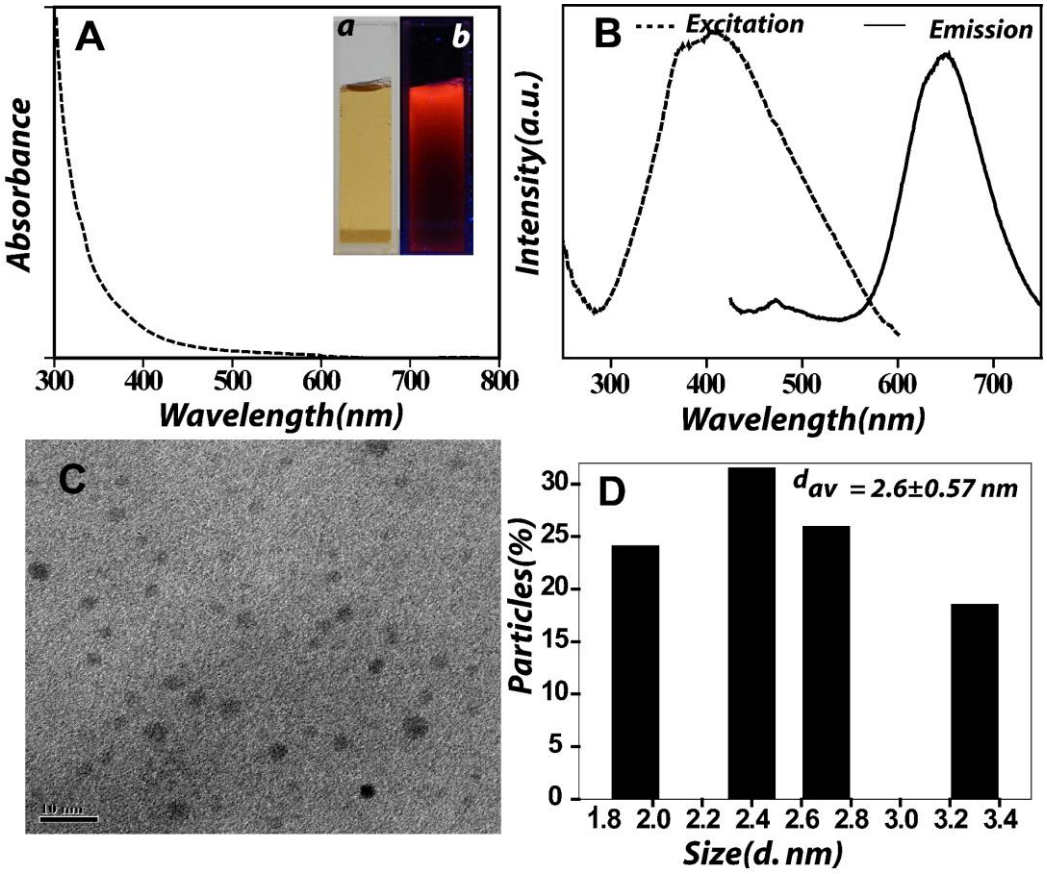

Figure 3.1 (**A)** UV-Visible spectrum of Cu NCs, inset: digital photograph of Cu NCs under (**a**) day light and (**b**) UV light λ_{ex}=405 nm). (**B**) The excitation and emission spectra of Cu NCs when excited at 405 nm (λ_{ex}) with emission maximum at 640 nm (λ_{em}) at pH 7.4. (**C**) TEM image of Cu NCs demonstrating small sizes of the NCs. (**D**) The particle size distribution of Cu NCs with average size 2.6 nm.

Table 3.1. The superior antibacterial activity of Cu NCs in comparison to other Cu-based NPs.

Nanoparticles	MIC(µg/mL)	MBC(µg/mL)	Size(nm)
CuO NPs[24]	140	160	41-82
CuO NPs[25]	Not determined	25±3	22
Cu NPs[11]	21.5	39.4	17±4
Cu NCs(present work)	13.2±0.46	16.1±0.8	2.5

The viability of GFP-expressing *E. coli* bacteria, treated with Cu NCs at MIC and MBC values for short interval of time (up to 6 h), was estimated by colony-count method (**Figure 3.2** and **3.3**) and are presented in **Table 3.2**. It was found that the bacterial viability was reduced by 50% or more after 2 h treatment with MIC and MBC values of the NCs. Moreover, when the treatment was extended up to 6 h, only 10 % of bacteria were viable at

the MIC value whereas the viability further decreased to 1.5% in case of MBC. It is clear from the Table 2 that the bacterial viability was reduced in the presence of Cu NCs in a concentration dependent manner. However, no change in viability was observed in the untreated bacterial sample during the course of the experiment. Similarly, the antibacterial activity was examined for MIC and MBC concentrations of Cu NCs by agar plate method, where it was found that the zone of inhibition increased from 1.2 cm to 1.8 cm (**Figure 3.4).**

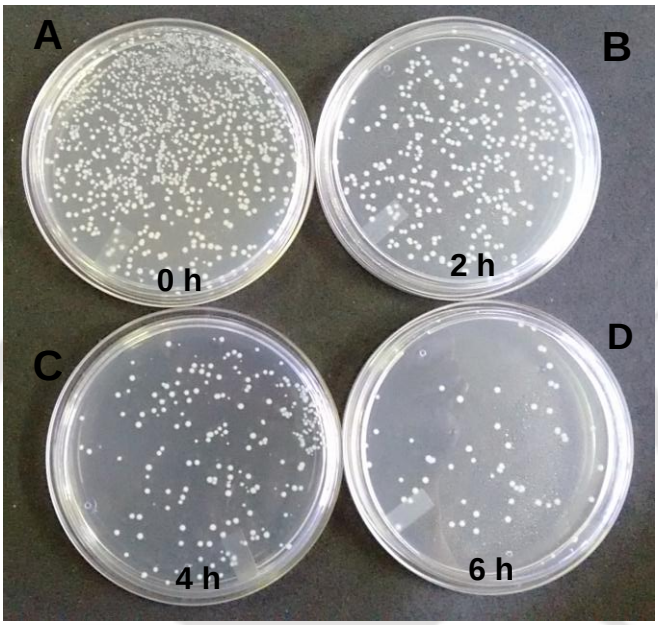

Figure 3.2 Viability of *E. coli* determined by colony count method after treatment with Cu NCs (MIC, 13.2±0.46 μg/mL) for (**A**) 0 h, (**B**) 2 h, (**C**) 4 h and (**D**) 6 h, respectively.

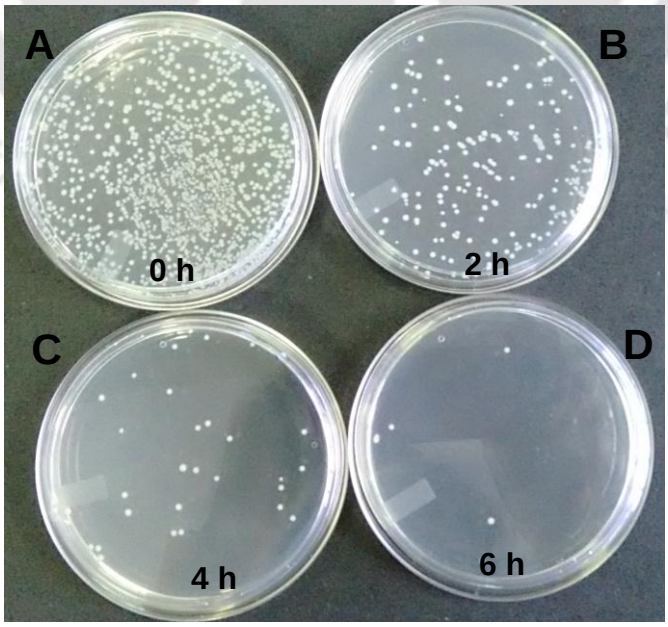

Figure 3.3 Viability of *E. coli* determined by colony count method after treatment with Cu NCs (MBC, 16.1±0.8 μg/mL) for (**A**) 0 h, (**B**) 2 h, (**C**) 4 h and (**D**) 6 h, respectively.

Table 3.2: Viability of Cu NCs treated *E. coli* at various interval of time expressed in CFU/mL.

Cu NCs (µg/mL)	Exposure time (h)	CFU (mL^{-1})	N/N_0	Non-viable bacteria (%)
MIC(13.2)	0	6.4×10^7	1	0
	2	3.1×10^7	4.8×10^{-1}	51.5
	4	1.8×10^7	2.8×10^{-1}	71.8
	6	5.8×10^6	9.0×10^{-2}	90.9
MBC(16.1)	0	6.4×10^7	1	0
	2	1.9×10^7	2.9×10^{-1}	70.3
	4	3.5×10^6	5.4×10^{-2}	94.5
	6	9×10^5	1.4×10^{-3}	98.5

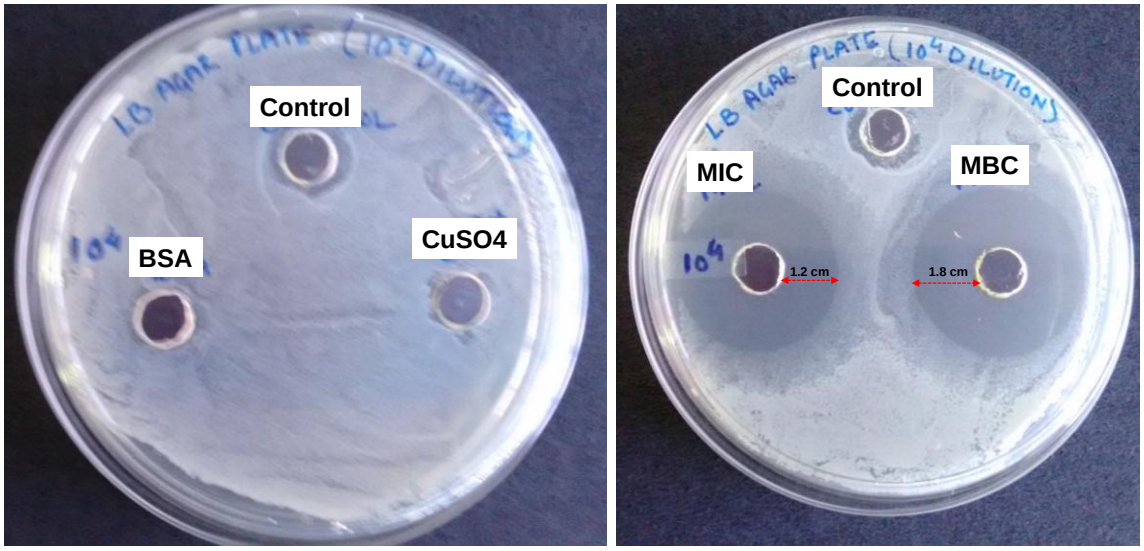

Figure 3.4 Zone of inhibition on LB-agar plate overlaid with *E. coli* in presence of BSA, $CuSO_4$ and Cu NCs (MIC and MBC), respectively.

The efficient antibacterial activity of Cu NCs could be due to their ultra-small size. The decrease in size increases the surface-to-volume ratio which, in turn, increases the degree of Cu NC-attachment on bacterial membrane. This can lead to enhanced killing of bacteria by the Cu NCs causing increased membrane damage. In addition, the small size could allow them to easily penetrate the cell membrane helping in reducing the bacterial viability further. The MIC and MBC values for *E. coli* found in case of Cu NCs were much lower than the values reported literature (of Cu concentration in NPs) as mentioned in **Table 3.2**. The time dependent bacterial growth in presence of Cu NCs at MIC and MBC, as monitored by recording the optical density at 595 nm, is shown in **Figure 3.5.** It is evident that, at MIC and MBC, no bacterial growth was observed. On the other hand, individual reactants (i.e. $CuSO_4$ and BSA) at their individual concentrations equivalent to those in the NCs, did not inhibit the bacterial growth.

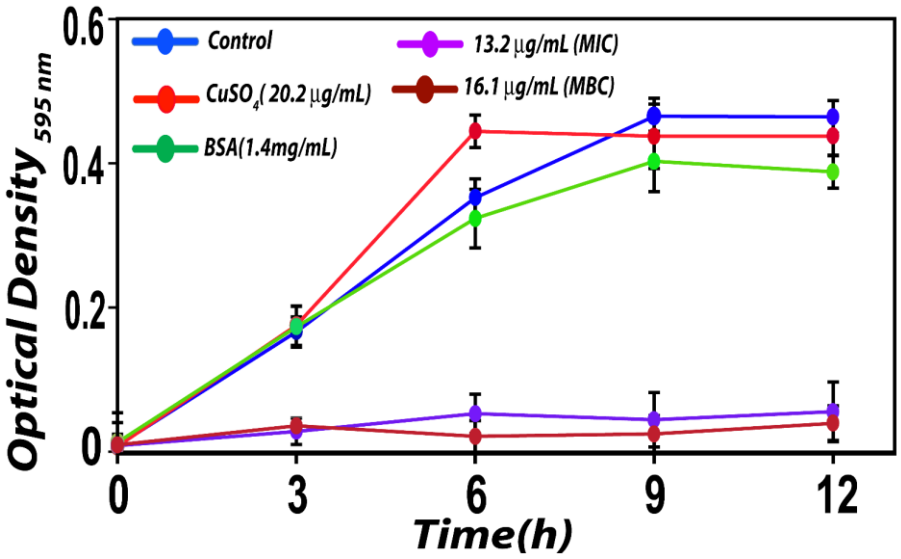

Figure 3.5 Growth curves of GFP expressing *E. coli* bacteria in presence of Cu NCs at 13.2 µg/mL (MIC) and 16.1µg/mL (MBC), $CuSO_4$(20.2 µg/mL) and BSA (1.4 mg/mL). Also shown here is the growth curve of untreated bacteria (control).

The interaction of NCs with the bacterial cell membrane and subsequent damage of the membrane integrity was further investigated by flow cytometric analysis. For this, nucleic acid binding dye PI was employed to stain the treated as well as control GFP-expressing *E. coli*. The healthy GFP-expressing *E. coli* bacteria with intact cell membrane do not allow PI to enter inside the cells and thus only fluoresce green due to GFP. However, bacteria with compromised cell membrane fluoresce green (due to GFP) as well as red due to entrance of PI and its subsequent binding with the bacterial DNA. On the other hand, in case of dead bacteria, GFP leaks out and only red fluorescence is observed. Lastly, the completely lyzed bacteria do not show any fluorescence. The change in cell membrane integrity and consequent viability in Cu NCs treated GFP expressing *E. coli* was examined, through the corresponding fluorescence indicator, in a flow cytometer (**Figure 3.6**). **Figure 3.6** reveals that the bacterial cells, treated with MIC and MBC of Cu NCs for 2 h at 37 °C, showed a gradual shift in population from living to compromised cells with negligible amount of dead and lysed cells in this time period. From the figure, it was also found that with increasing concentration of Cu NCs, only-green-fluorescent intensity decreased, indicating the loss of membrane integrity. The results of flow cytometric analysis, summarized in **Table 3.3,** demonstrated that the Cu NC-treatment at MIC and MBC for 2 h resulted in 46% and 50% increase, respectively, in the population of bacteria with damaged cell membrane.

In order to find out the presence of Cu NCs on treated bacterial sample was confirmed by energy-dispersive X-ray spectroscopy (EDS) (**Figure 3.7**). The attachment of the Cu NCs to the bacterial membrane was also investigated by zeta potential measurements. The zeta

potential of as-prepared BSA-stabilized Cu NCs at pH 12 was found to be –26.4 mV, while the value changed to + 9.80 mV at pH 7.4. Thus, the electrostatic interaction between the positively charged BSA stabilized Cu NCs and negatively charged bacterial cell membrane could explain the attachment of Cu NCs with bacteria. This could potentially increase the cell-particle interactions, resulting in increased toxicity and damage to the bacterial membrane. NCs having sizes < 3 nm size could easily cross the cell membrane and interact with the enzymes present inside the cells, causing cell death.[18]

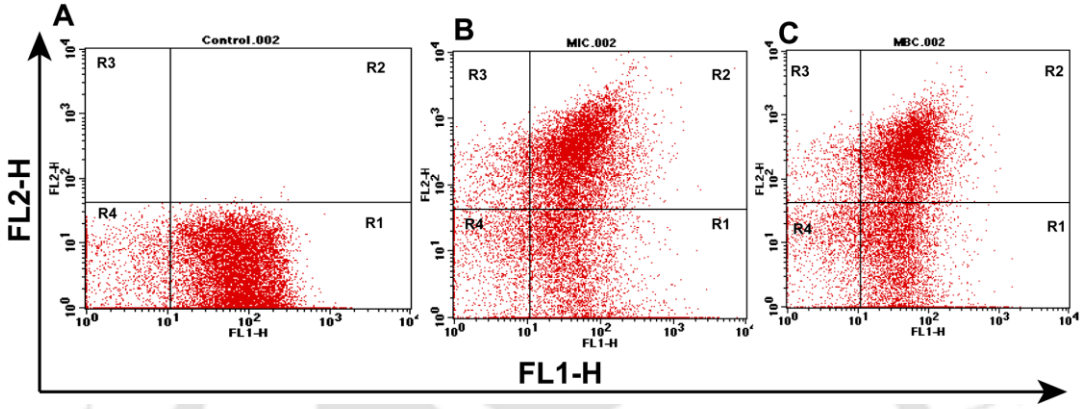

Figure 3.6 Bacterial population in various viability-stage was determined by PI staining in a flow cytometer. (**A**) Represents the non-treated bacteria while (**B**) and (**C**) show the bacterial population in presence of MIC and MBC, respectively, values of Cu NCs. The viability stages of bacterial cells are denoted as R1 (live), R2 (compromised), R3 (dead) and R4 (lyzed).

Table 3.3: Distribution of *E. coli* population into various phases after treatment with Cu NCs (at MIC and MBC) for 2 h.

Population	Control (%)	Treated (MIC, %)	Treated (MBC, %)
Live	92.9	38.10	33.64
Compromised	0.07	46.72	50.82
Dead	0.0	4.47	5.88
Lysed	7.03	10.51	9.66

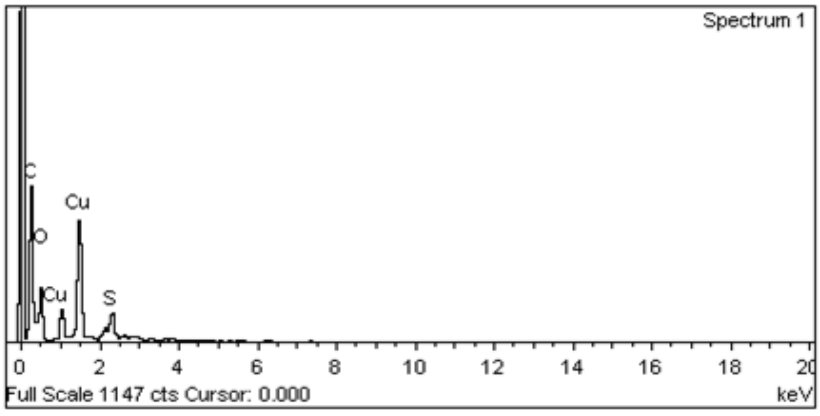

Figure 3.7. Elemental analysis of Cu NCs after treating with bacteria indicating the presence of copper by energy-dispersive X-ray spectroscopy (EDS) from Field Emission Scanning Electron Microscopy(FESEM).

Therefore, the mechanism of enhanced bactericidal activity of Cu NCs might involve a combination of both physical and chemical interactions of Cu NCs with the bacterial cell. Once the Cu NCs get attached to the bacterial membrane, they can further interact with sulphur-containing proteins of the membrane triggering greater permeability and physical damage of the membrane.[11] The Cu NCs now can pass through the damaged membrane and generate ROS. ROS are generally generated inside the cells, either intrinsically or extrinsically, and the cell has inbuilt defensive mechanism to readily detoxify them and overcome from this stress. It has been reported that metal NPs can disturb this physiological balance, resulting in oxidative stress, due to the prooxidant functional groups harboring at the NP surface and the redox characteristics of the transition metals.[26] Thus, ROS generated oxidative stress overwhelms the defense mechanism of the cell causing large scale damage to the inner membranes, DNA and protein eventually killing the bacteria. To confirm the production of ROS inside the bacterial cells to Cu NC exposure in the present study, Nitroblue Tetrazolium (NBT) assay was performed. From **Figure 3.8**, it is evident that the untreated cells generated negligible amount of ROS, whereas Cu NC treated bacterial cells generated maximum amount of ROS. The production of ROS increased inside the bacterial cells with increase in the concentration of Cu NCs. In addition, the bacterial cells when treated with individual components such as BSA and Cu^{2+} ($CuSO_4$ solution), were found to cause negligible increase in ROS production. It has been reported that Cu NPs and Cu NCs can induce oxidative stress through ROS generation.[14] The particle size and surface area, in this regard, are key factors of nanomaterials for their toxicity. The reduced size of Cu NCs (NCs < 3 nm) increases the surface area altering their electronic properties. This alteration of electronic properties produces particular surface states that can react with molecular O_2 to form $O_2^{-\bullet}$, due to their capabilities of acting as 'reactive sites' having electron donor/acceptor tendencies.[14] The result of NBT assay also supports that large amount of ROS was generated inside the *E. coli* cells from the surface defect sites of Cu NCs in the present study.

As earlier studies indicate the role of metal ions, leached from dispersed metal NPs, in their antibacterial activity,[3] we determined the release of Cu^{2+} from Cu NCs in bacterial culture media (incubated for 12 h at 37 °C) by using atomic absorption spectrophotometer (AAS) and investigated their effect on antibacterial activity in present study. From **Figure 3.9**, it is observed that the concentration of Cu^{2+} released from Cu NCs at MIC was 2.8 ppm at 3 h which increased to 4.04 pm after 12 h incubation. The antibacterial activity of Cu^{2+} was further analyzed by turbidity test using varying concentrations of $CuSO_4$ (**Figure 3.10**). It was found that there was no significant inhibition in bacterial growth, even when the

concentrations of Cu^{2+} increased from 4 ppm to 15 ppm. This indicates that Cu^{2+} ions have little antibacterial effect, if any, in this study.

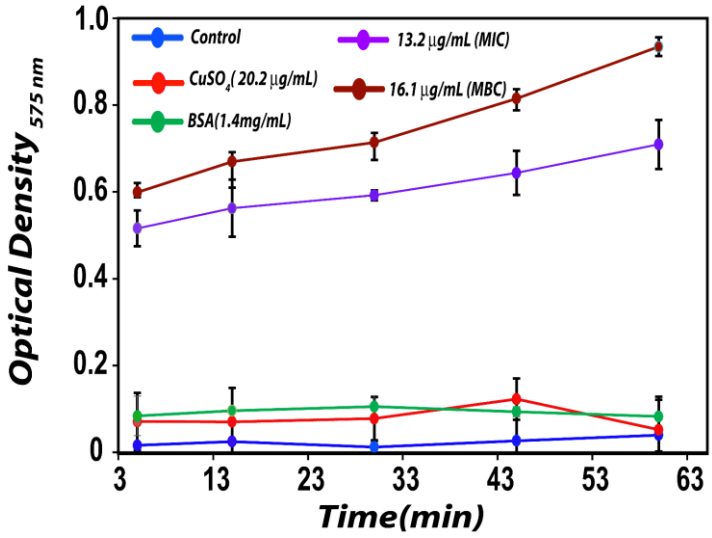

Figure 3.8 Production of ROS in the bacterial cells with the treatment of Cu NCs (at MIC and MBC), $CuSO_4$, and BSA respectively. ROS in non-treated control bacteria is also shown for comparison.

Based on the above results, we propose that the mechanism of the enhanced antibacterial activity of Cu NCs was due to the combined effect of strong electrostatic interaction of Cu NCs with bacterial membrane, and the generation of ROS within the bacterial cells due to their altered electronic properties, defect sites as well as their increased surface-to-volume ratio of the ultra-small Cu NCs (**Figure 3.11)**.The small sizes of the Cu NCs increased the probability of their transportation through the bacterial membrane leading to cell death. This mode of mechanism is dominant when the particle size is very small.

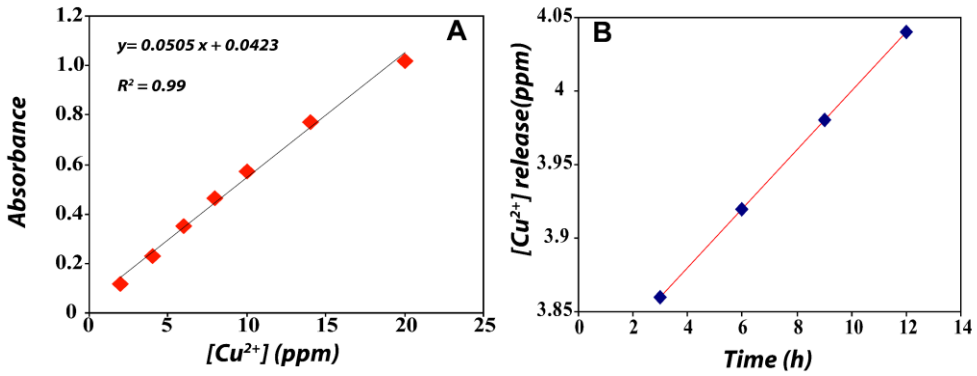

Figure 3.9 Atomic absorption spectrophotometric analysis for the release of copper ion: (**A**) calibration curve of $CuSO_4$ (**B**) Cu^{2+} released from Cu NCs with time in LB medium.

The biocompatibility of a nanomaterial is a critical parameter for its effective biomedical application. To determine the possible cytotoxicity associated with Cu NCs, we

carried out MTT-based cell viability assay on normal (HEK) as well as cancer (HeLa) cells. The effect of Cu NCs on the viability of mammalian cells are shown in **Figure 3.12**. It was found that 76% of HeLa cells and 78% of HEK cells were still viable, when incubated with 18.01 µg/mL of Cu NCs (above MBC) for 24 h. The cytotoxicity values are in good agreement with the reported value in literature for Cu NCs.[19] In other words, the cytotoxicity of Cu NCs to mammalian cells, in spite of their small size, did not exceed the toxicity level associated with bulk Cu.

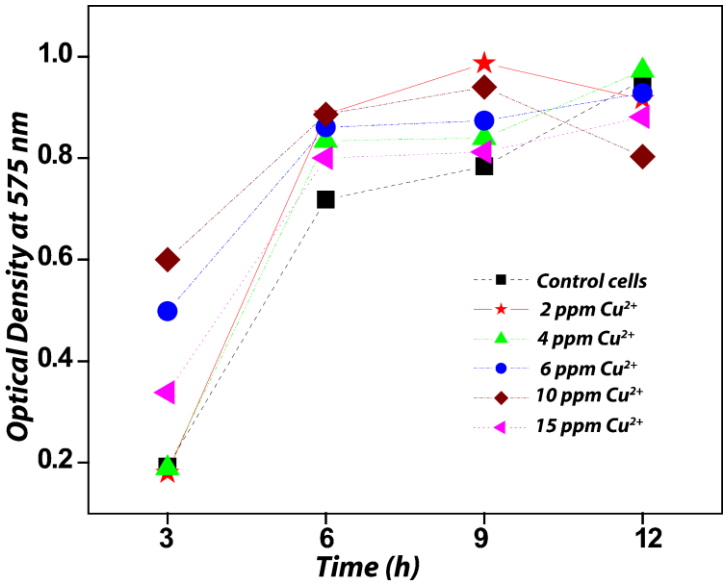

Figure 3.10 Growth curve of *E. coli* bacteria in LB media in presence of different concentrations of $CuSO_4$ to examine the role of released ion for inhibiting the growth of bacteria.

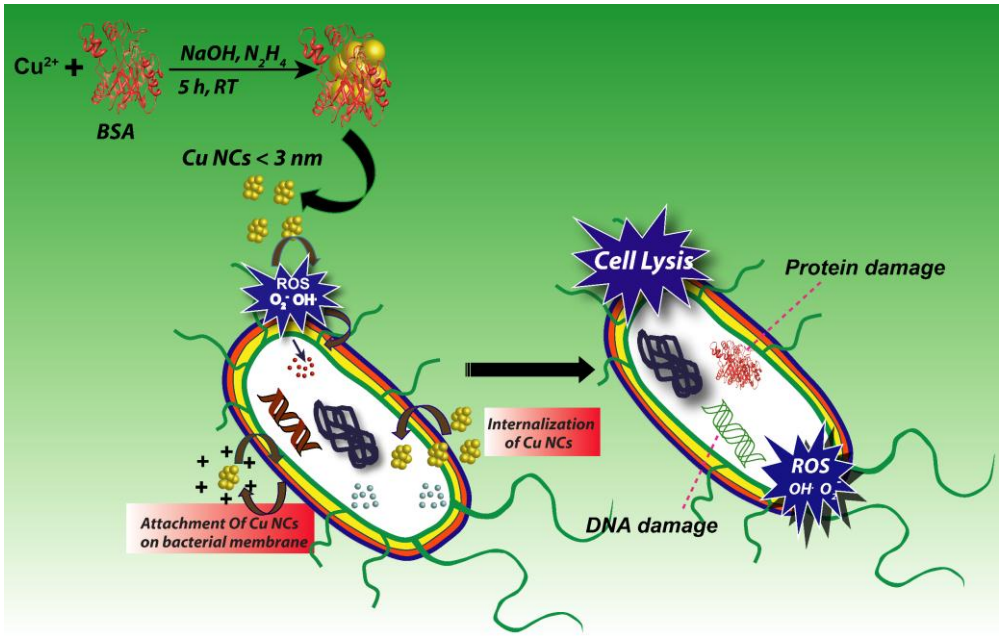

Figure 3.11. Schematic representation of possible mechanism of the antibacterial activity shown by Cu NCs.

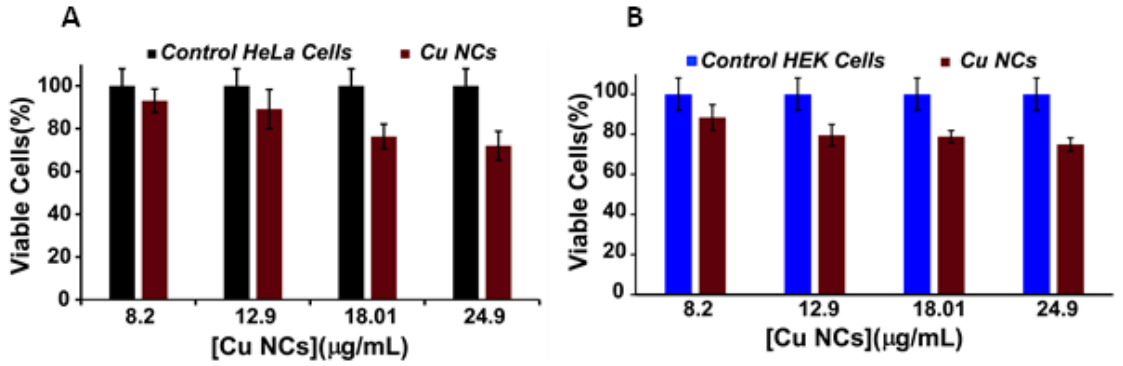

Figure 3.12 The viability of **(A)** HeLa cells **(B)** HEK cells treated with Cu NCs at different concentrations for 24 h was determined by MTT assay.

3.6. CONCLUSION

In this chapter, we have reported the excellent bactericidal activity of Cu NCs with particular focus on understanding the possible mechanism of antibacterial action. The MIC and MBC values of Cu NCs against *E. coli* bacteria were found to be 13.2±0.46 μg/mL and 16.1±0.8 μg/mL (in terms of the concentration of copper in Cu in the medium, respectively, which was much less than the reported literature values for Cu-based NPs till date. Electron microscopy (EDS-FESEM) and zeta potential measurements revealed that Cu NCs were attached to the bacterial surface possibly through electrostatic interaction leading to the changes in the bacterial membrane integrity. It was also found that smaller sized Cu NCs generated significant amount of intracellular ROS. The enhanced transportation of the Cu NCs through the bacterial membrane, due to their ultra-small size, caused an increase in cell permeability leading to cell death. The growth curves and AAS studies indicated that the antibacterial activity was governed by Cu NCs rather than Cu^{2+} leached.

3.7. REFERENCES

1. Bogdanovic, U.; Vodnik, V.; Mitric, M.; Dimitrijevic, S.; Skapin, S. D.; Zunic, V.; Budimir, M.; Stoiljkovic, M. *ACS Appl. Mater. Interfaces* **2015**, *7*, 1955−1966.
2. Jia, B.; Mei, Y.; Cheng, L.; Zhou, J.; Zhang, L. *ACS Appl. Mater. Interfaces* **2012**, *4*, 2897–2902.
3. Gunawan, C.; Teoh, W.-Y.; Marquis, C. P.; Amal, R. *ACS Nano* **2011**, ***5***, 7214–7225.
4. Ren, G.; Hu, D.; Cheng, E.W.C.; Vargas-Reus, M. A.; Reip, P.; Allaker, R. P. *Int. J. Antimicrob. Agents* **2009**, *33*, 587–590.
5. Raghupathi, K. R.; Koodali, R. T.; Manna, A. C. *Langmuir* **2011**, *27*, 4020−4028.
6. Applerot, B. G.; Lipovsky, A.; Dror, R.; Perkas, N.; Nitzan, Y.; Lubart, R.; Gedanken. A. *Adv. Funct. Mater*. **2009**, *19*, 842−852.
7. Brunet, L.; Lyon, D. Y.; Hotze, E. M.; Alvarez, P. J. J.; Wiesner, M. R. *Environ. Sci. Technol*. **2009**, *43*, 4355−4360.
8. Gabbay, J.; Borkow, G.; Mishal, J.; Magen, E.; Zatcoff, R.; Shemer-Avni, Y. *J. Ind. Textiles* **2006**, *35*, 323−335.
9. Anyaogu, K. C.; Fedorov, A. V.; Neckers, D. C. *Langmuir* **2008**, *24*, 4340−4346.
10. Hanagata, N.; Zhuang, F.; Connolly, S.; Li, J.; Ogawa, N.; Xu, M. *ACS Nano* **2012**, *5*, 9326−9338.
11. Mallick, S.; Sharma, S.; Banerjee, M.; Ghosh, S. S.; Chattopadhyay, A.; Paul, A. *ACS Appl. Mater. Interfaces* **2012, *4***, 1313−1323.
12. Cioffi, N.; Ditaranto, N.; Torsi, L.; Picca, R. A.; Sabbatini, L.; Valentini, A.; Novell, L.; Tantillo, G.; Bleve-Zacheo, T.; Zambonin, P. G. *Anal. Bioanal. Chem*. **2005**, *381*, 607−616.
13. Grass, G.; Rensing, C.; Solioz, M. *Appl Environ Microbiol.* **2011**, *77*, 1541−1547.
14. Ghosh, R.; Goswami, U.; Ghosh, S. S.; Paul, A.; Chattopadhyay, A. *ACS Appl. Mater. Interfaces* **2014**, *7*, 209−222.
15. Xia, T.; Kovochich, M.; Liong, M.; Mädler, L.; Gilbert, B.; Shi, H.; Yeh, J. I.; Zink, J. I.; Nel, A. E. *ACS Nano* **2008**, *2*, 2121−2134.
16. Gunawan, C.; Teoh, W. Y.; Marquis, C. P.; Lifia, J.; Amal, R. *Small* **2009,** *5*, 341−344.
17. Midander, K.; Cronholm, P.; Karlsson, H. L.; Elihn, K.; Moeller, L.; Leygraf, C.; Wallinder, I. O. *Small* **2009**, *5*, 389−399.
18. Applerot, G.; Lellouche, J.; Lipovsky, A.; Nitzan, Y.; Lubart, R.; Gedanken, A.; Banin, E. *Small* **2012**, *8*, 3326−3337.
19. Gogoi, S.; Gopinath, P.; Paul, A.; Ramesh, A.; Ghosh, S. S.; Chattopadhyay, A. *Langmuir* **2006**, *22*, 9322–9328
20. Wang, C.; Wang, C.; Xu, L.; Cheng, H.; Lin, Q.; Zhang, C. *Nanoscale*, **2014**, *6*, 1775−1781.
21. Ghosh; R.; Sahoo, A. K.; Ghosh, S. S.; Paul, A.; Chattopadhyay, A. *ACS Appl. Mater. Interfaces* **2014**, *6*, 3822–3828.
22. Chen, T.-H.; Tseng, W.-L. *Small* **2012**, *8*, 1912−1919.
23. Baksi, A.; Xavier, P. L.; Chaudhari, K.; Goswami, N.; Pal, S. K.; Pradeep, T. *Nanoscale* **2013**, *5*, 2009−2016.
24. Ruparelia, J. P.; Chatterjee, A. K.; Duttagupta, S. P.; Mukherji, S. *Acta Biomaterialia* **2008**, *4* 707−716.
25. Azam, A.; Ahmed, A. S.; Oves, M.; Khan, M. S.; Habib, S. S.; Memic, A. *Int J Nanomedicine*. **2012**, *7*, 6003−6009.
26. Nel, A.; Xia, T.; Mädler, L.; Li, N. *Science* **2006,** *311*, 622−627.

Chapter 4

Blue Emitting Copper Nanoclusters Synthesized in Presence of Lysozyme as Candidates for Cell Labeling*

This chapter describes the synthesis of blue fluorescent copper nanoclusters using lysozyme which exhibited excitation wavelength tuneable emission properties. The nanoclusters were found to be stable between pH 4-10 and in addition having excellent chemical and photostability. The non-cytotoxic nanoclusters were used to successfully label cervical cancer HeLa cells.

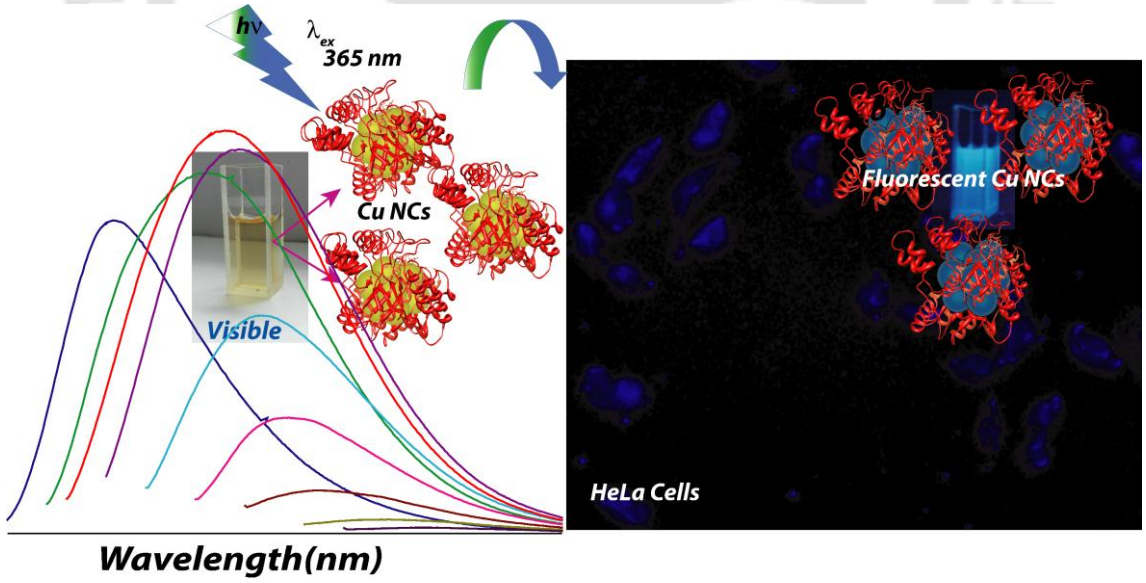

*Ghosh, R.; Sahoo, A. K.; Ghosh, S. S.; Paul, A.; Chattopadhyay, A. *ACS Appl. Mater. Interfaces* **2014**, *6*, 3822–3828**.** Reproduced with permission from *ACS Appl. Mater. Interfaces*. Copyright 2014, American Chemical Society.

4.1. INTRODUCTION

Stabilizing nanoclusters (NCs) of noble metal remains the primary challenge in their syntheses and applications. It has been proposed that these highly luminescent and photostable NCs could substitute toxic quantum dots in bioimaging and biolabeling.[1,2] In this regard, owing to their redox properties, NCs of gold (Au), and to some extent those of silver (Ag), have been stabilized with considerable success in comparison to those of copper (Cu). For example, syntheses of luminescent Au and Ag NCs using dendrimers,[3] poly(acrylic acid) polymer,[4,5] DNA,[6,7] and protein[8] as stabilizers have been reported. Among the proteins, bovine serum albumin,[8–10] lacto transferrin,[11] lysozyme,[12,13] insulin,[14] horseradish peroxidase,[15] and pepsin[16] have been preferred as stabilizers. It is worth to mention here that the proposed use of these clusters in a biological environment demands their stability in an aqueous medium. This has remained a challenge for the synthesis of NCs of Cu. The ease of oxidation of Cu (E^0, 0.34 V), in comparison to that of Ag (E^0, 0.80 V) and Au (E^0, 1.50 V), has limited progress in the development of synthetic methods, especially in an aqueous medium. A recent report indicates that Cu NCs of less than 3 nm, synthesized using a polyol method under a N_2 atmosphere, were stable following their redispersion in an aqueous medium.[17] On the other hand, the possibility of the synthesis of small Cu NCs in an aqueous medium electrochemically has also been demonstrated.[18] Interestingly, DNA-hosted Cu NCs, synthesized in the presence of ascorbic acid, have been used for the identification of single nucleotide polymorphism.[19] However, there is a need for the development of aqueous-based synthetic methods for versatile use, especially in biological applications. Cu is an important trace element, being present in the human body as an essential catalytic cofactor in redox-active enzymes such as cytochrome *c* oxidase and lysyl oxidase. The permissible intake of Cu for an adult is 0.6–1.6 mg/day.[20] The ease of sequestration of Cu by a natural bodily mechanism and the availability of commercial chelating agents also make its use relatively friendly in human subjects over those of Au and Ag, especially at low concentrations.[21,22]

Herein we report the synthesis of highly fluorescent, blue-emitting Cu NCs by chemical reduction of $CuSO_4$ in an aqueous medium, in the presence of lysozyme. Lysozyme, a 14.3 kDa protein, has 129 amino acid residues including 8 cysteine residues. The antimicrobial protein is biocompatible and has been a favorite as a stabilizer of Au NCs.[13] The so-synthesized protein-stabilized Cu NCs, with wavelength-tunable emission, were stable in an aqueous medium under ambient conditions; they could easily be isolated and used for labeling cervical cancer HeLa cells. Cell viability studies indicated their noncytotoxic nature, making the NCs ideal for biological applications. The essential steps of the synthesis are depicted in **Scheme 4.1**.

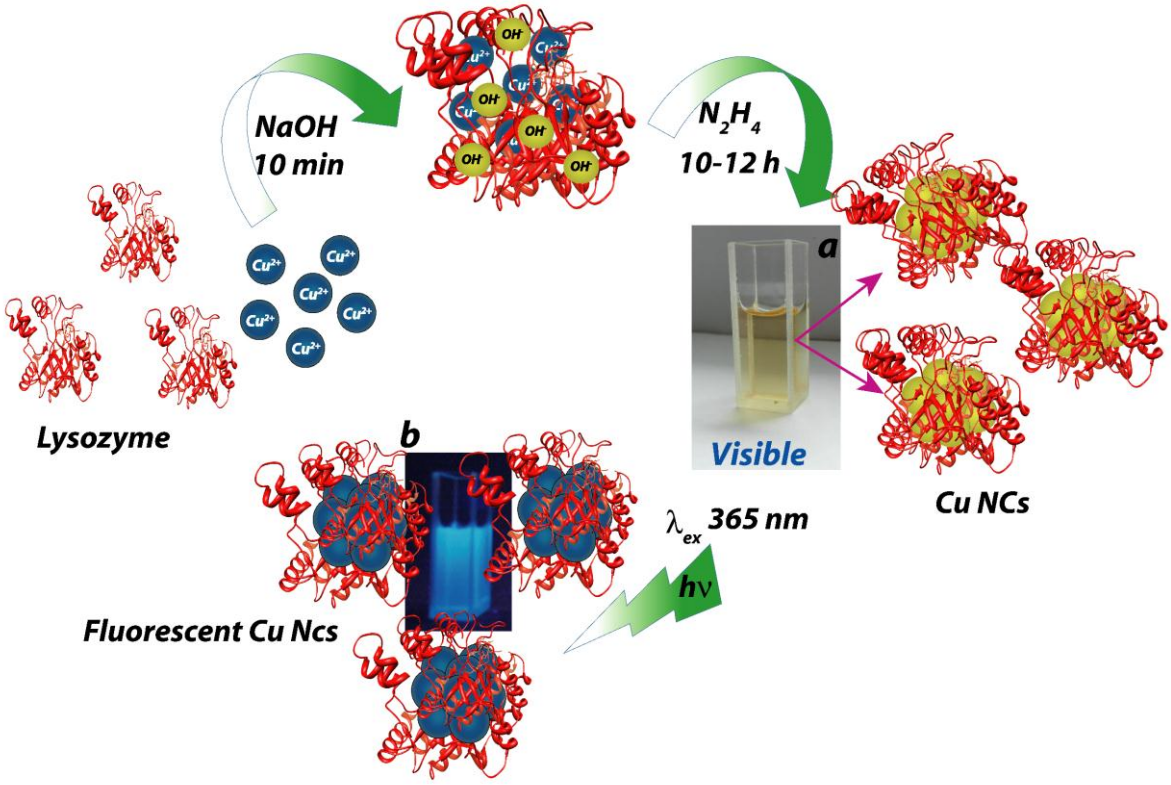

Scheme 4.1 Reaction scheme for the synthesis of Cu NCs in the presence of Lysozyme. The photographs of the products under **(a)** daylight and (**b**) UV light at 365 nm are also included.

4.2. EXPERIMENTAL SECTION

4.2.1. Materials

Copper sulfate ($CuSO_4$), sodium hydroxide (NaOH), and hydrazine hydride (80%) were purchased from Merck Specialities Private Ltd., India. Lysozyme was purchased from Sisco Research Laboratories Pvt. Ltd. 2,3-Bis(2-methoxy-4-nitro-5-sulfophenyl)-2*H*-tetrazolium 5-carboxanilide (XTT) and sinapinic acid for matrix-assisted laser desorption ionization (MALDI) analysis were purchased from Sigma-Aldrich USA. Milli-Q-grade water (18.2 MΩcm) was used for all of the experiments.

4.2.2. Synthesis of Cu NCs

$CuSO_4$ and lysozyme were mixed in water in a weight ratio of 2:1. The solution was stirred for 10 min at 45 °C, and then 0.04 mL of 1.0 M NaOH was added to adjust the pH to ~10–11 when the color changed from blue to purple. To this was added 0.01 mM 80% N_2H_4, and the resulting solution was stirred for 6–12 h. The final color change of the solution was from purple to pale yellow. The same process for the synthesis was followed for different ratios of metal-to-protein concentration such as 2:1, 4:1, 6:1, and 8:1. For cell labeling and viability assay, Cu NCs were synthesized in a phosphate buffer at pH 7.4.

4.2.3. Characterization

Transmission electron microscopy (TEM) measurements were made using a JEOL JEM 2100 transmission electron microscope operating at a maximum accelerating voltage of 200 kV. The Cu NC dispersion was drop-cast onto carbon-coated Cu TEM grids and then kept for drying overnight at room temperature. UV–visible and fluorescence spectra were recorded with a Hitachi U-2900 or Perkin Elmer Lamda 25 and a Fluoromax-4 spectrophotometer instrument, respectively. Circular dichroism (CD) spectra were recorded using a Jasco J-815 machine. The instrument was calibrated with camphor sulfonic acid. All CD spectra were recorded at 25 °C, using a thermostatically controlled cell holder with a path length of 10 mm. ζ-potential measurements for samples were carried out using a Malvern zeta size Nano-ZS90 instrument at a temperature of 25 °C and a sample viscosity of 0.8872 mPas. Fourier transform infrared (FTIR) spectroscopic measurements were performed using a Perkin-Elmer Spectrum One spectrophotometer in the range 400–4000 cm^{-1}. X-ray diffraction (XRD) measurements were made using a Bruker AXS D8 Advance X-ray diffractometer fitted with a Cu $K\alpha_1$ source. Cellular labeling studies were carried out using a Epifluorescence microscope (Nikon eclipse). For MALDI-time-of-flight (TOF) mass spectrometry (MS) analysis, an Applied Bio systems 4800 Plus MALDI TOF/TOF analyser was used with sinapinic acid as the matrix. X-ray photoelectron spectroscopy (XPS) measurements for Cu NCs were performed by using a PHI 5000 VersaProbeII scanning XPS microprobe. Samples were prepared as pellets and introduced into XPS pre chamber under ultrahigh-vacuum conditions. Time-resolved fluorescence intensity decay of the NCs was recorded using a Life Spec II spectrofluorimeter. The sample was excited by a 375 nm laser light source. The decay curves were analyzed by *FAST* software, provided by Edinburgh Instruments along with the fluorimeter. The curves were fitted into the function

$$I(t) = \sum \alpha_i \exp\left(-t / \tau_i\right) \quad (1)$$

where α_i is the initial intensity of the decay component *i*, having a lifetime of τ_i. The average lifetime of Cu NCs was calculated using the equation

$$\langle \tau \rangle = \frac{\sum_i \alpha_i \tau_i^2}{\sum_i \alpha_i \tau_i} \quad (2)$$

4.2.4. Quantum Yield Measurement of Cu NCs

Quantum yield (QY) measurement was carried out by dissolving quinine sulfate in 0.1 M H_2SO_4 (used as the reference) according to the standard protocol.[23] The Cu NC dispersion was used as such. The absorbance of the respective sample was measured on a Perkin-Elmer

LS 55 UV–visible spectrophotometer. The QY was calculated from the equation

$$Q = Q_R \frac{m_s}{m_r} \frac{n_s^2}{n_r^2} \quad (3)$$

where Q is the QY of Cu NCs, Q_R is the QY of quinine sulfate, m_s is the slope of the plot of integrated fluorescence intensity versus absorbance of Cu NCs, m_r is the slope of the plot of integrated fluorescence intensity verses absorbance of reference quinine sulfate, and n_s and n_r are the refractive indices of the sample and reference, respectively, in distilled water, which are assumed to be equal to that of water (1.33). The emission spectra for the samples were recorded at a 360 nm excitation, keeping the slit width at 2 nm.

4.2.5. Sample Preparation for MALDI-TOF MS Measurement

For MALDI-TOF MS analysis, an Applied Bio systems 4800 Plus MALDI TOF/TOF analyser was used with sinapinic acid as the matrix. Spectra were collected in the linear positive mode with mid-mass. The matrix was prepared by dissolving 10 mg of sinapinic acid in a 1:3 mixture of acetonitrile and 0.1% trifluroacetic acid, and water was used to make up the volume to 1.0 mL (i.e., 0.2 mL of acetonitrile, 0.6 mL of 0.1% trifluroacetic acid, and 0.2 mL of water). The samples were prepared at 1:1, 1:2, and 1:3 ratios with samples and a matrix. The cluster dispersion, without dilution, was mixed thoroughly with the matrix mixture, and from it, 0.8 μL of the resulting mixture was used for spotting.

4.2.6. Agarose Gel Electrophoresis

The electrophoretic stability of a lysozyme and Cu NC mixture was pursued by an agarose gel electrophoresis study. This was performed in 0.8% agarose at 5 V/cm and was visualized under a UV transilluminator (with excitation at 305 nm).

4.2.7. Cell Culture

HeLa cells (human cervical carcinoma) were acquired from the National Centre for Cell Sciences, Pune, India, and cultured in Dulbecco's modified Eagle's medium (DMEM) supplemented with 10% (v/v) fetal bovine serum obtained from PAA Laboratories, Austria, in a 5% CO_2 humidified incubator at 37 °C.

4.2.8. Cell Viability Assay

Cell viability assays were carried out as per the following. Cells (1×10^4 cells/well) were seeded in a 96-well microplate and grown in DMEM for 24 h in the presence of 5% CO_2 at 37 °C. Then various concentrations of Cu NCs (2.3–34.5 μg/mL) were added to the cells and

kept for 24 h in similar conditions, which was followed by XTT assay as per standard manufacturer protocol. For the reaction, 7.0 µL of XTT was added to each well of the microplate and kept for 2 h for the formation of formazan. The control experiment was carried out in a similar way with various amounts of lysozyme. All of the experiments were carried out in triplicate. The percentage of cell viability of the control was taken as 100%. The cell viability was calculated based on the following formula:

$$\% \text{ viable cells} = \frac{(A_{450} - A_{650}) \text{ of NC treated cells}}{(A_{450} - A_{650}) \text{ of control cells}} \times 100$$

The absorbances at 450 and 650 nm (A_{450} and A_{650}) correspond to the formation of formazan and the control medium, respectively.

4.2.9. Epifluorescence Microscopy

For cell imaging, 1×10^4 HeLa cells were seeded in a 35 mm cell culture plate and grown for 24 h. Cu NCs were added to the plate and incubated for another 2 h. The medium was then removed, and the cells were washed with phosphate-buffered saline (PBS) several times. Finally, 1 mL of PBS was added to the plate, and the cells were observed under an Epifluorescence microscope (Nikon ECLIPSE TS100, Tokyo). An excitation for UV (340–380 nm) and an emission (435–485 nm) band-pass filters were used for cellular imaging.

4.2.10. Hemolysis Assay *in Vitro*

A total of 2.0 mL of human blood was centrifuged at 3000 rpm for 10 min to obtain human red blood cells (HRBCs). After removal of the supernatant, the HRBCs were washed with PBS, which was followed by centrifugation. HRBCs so collected were suspended in deionized water. Portions of 0.1 mL of the HRBC suspension were added to 0.9 mL each of deionized water and PBS buffer, considered as positive and negative controls, respectively. Then experiments were performed in five different concentrations of a Cu NC composite. For each experiment, 0.1 mL of a stock HRBC suspension was added to 0.9 mL of a Cu NC composite with different concentrations (which varied from 0.6 to 4.5 µg/mL). All samples were incubated at 37 °C in a water bath for 3 h. After 3 h, the samples were centrifuged at 3000 rpm for 10 min, and the absorbance of the supernatants at 541 nm was recorded. The percentage of hemolysis of Cu NC suspension was calculated by using the equation

$$\% \text{ of hemolysis} = \frac{\text{O.D. of Cu NCs} - \text{O.D. of negative control}}{\text{O.D. of positive control} - \text{O.D. of negative control}} \times 100$$

Where O.D. corresponds to the absorbance values of HRBCs at 541 nm. The hemolysis assay was performed in triplicate. The ethical IBSC clearance and donor consent involved with human blood studies has been taken from hospital and Institute Biosafety Committee. The necessary documents are attached in the permission section of the thesis.

4.3. RESULTS AND DISCUSSION

Cu NCs were synthesized by treating a mixture containing a 2:1 molar ratio of $CuSO_4$ and lysozyme with N_2H_4 (0.01 mM) at pH 10–11 at 45 °C with constant stirring for 10–12 h. The medium, after reaction, appeared intense blue under a UV lamp, indicating the formation of Cu NCs (**Scheme 4.1**). UV–vis spectrum (**Figure 4.1A**) of the reaction mixture recorded after 12 h did not exhibit the presence of any discernible peak. However, a gradual increase in extinction below 475 nm could be observed. An identical experiment in the absence of N_2H_4 did not result in such a bright-blue coloration, evidencing the role of N_2H_4 in the synthesis (**Figure 4.2**) Cu NCs, as evidenced from a strong fluorescence intensity, formed readily in the presence of hydrazine with high yield, as observed from fluorescence spectra (**Figure 4.2**). They were reasonably stable in the presence of hydrazine after preparation at ambient conditions. In the absence of hydrazine, the fluorescence intensity decreased quickly with time (**Figure 4.3**), thus indicating the additional role of hydrazine in stabilizing the NCs.

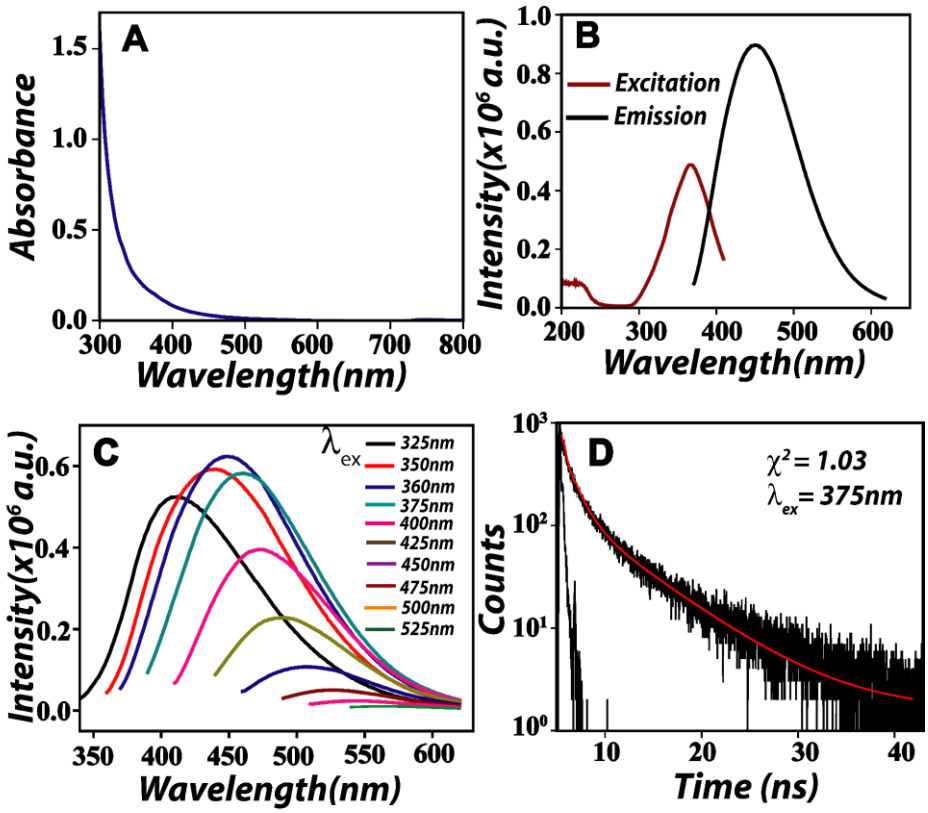

Figure 4.1 (**A**) Absorption spectrum of the product of the reaction of $CuSO_4$ and N_2H_4 in the presence of lysozyme. (**B**) Excitation and emission spectra of the product. (**C**) Excitation-dependent emission spectra of the product. (**D**) Fluorescence decay profile (λ_{ex} = 375 nm and λ_{em} = 450 nm) of the product.

On the other hand, when the concentration ratio of $CuSO_4$/lysozyme was increased to 4:1 and beyond, a clear surface plasmon resonance (SPR) peak due to Cu NPs could be observed, occurring at 550 nm (**Figure 4.4**). Thus, the studies reported in the present work

were limited to products formed from a mixture of 2:1 molar ratio of $CuSO_4$ and the protein. The fluorescence spectrum of the product consisted of a single peak with a maximum at 450 nm, when excited by 360 nm light (**Figure 4.1B**). The excitation spectrum consisted of a single peak with a maximum at 360 nm (**Figure 4.1B**). The fluorescence QY was measured as 18% (λ_{ex} = 360 nm) with reference to quinine sulfate (54%) as the standard (**Figure 4.5A**).

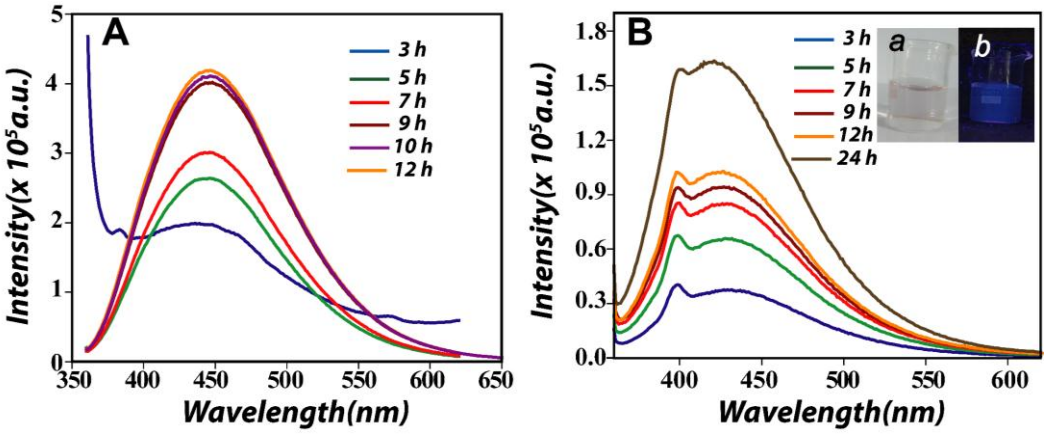

Figure 4.2 Fluorescence spectra of Cu NCs in presence of lysozyme, at different time points during their synthesis. Spectra were recorded for synthesis (**A**) in presence of N_2H_4 and (**B**) in absence of N_2H_4. Inset shows the photograph of Cu NCs prepared by lysozyme in absence of N_2H_4 under **(a)** day light and **(b)** UV light at 365 nm. The formation of Cu NCs in presence of N_2H_4 started after~ 5 h and there was no change in the intensity after 12 h.

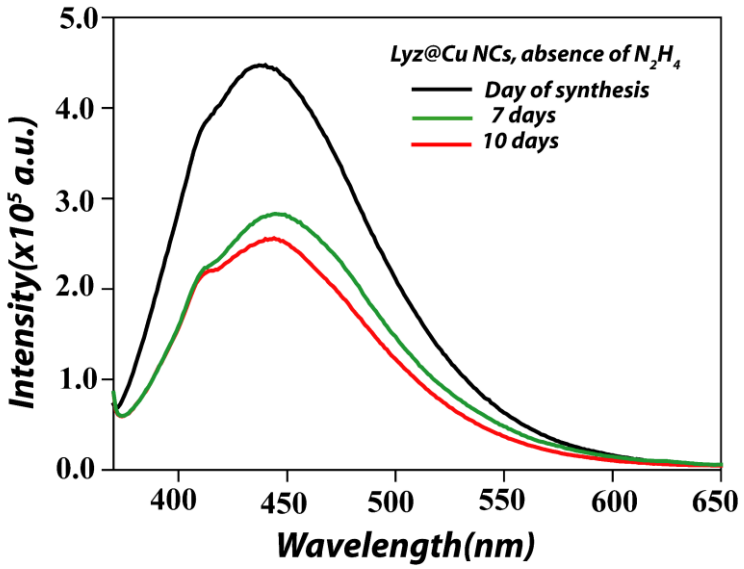

Figure 4.3 Stability of the synthesized Cu NCs (in the absence of hydrazine) as studied by fluorescence spectroscopy. The change in the fluorescence emission indicated the instability of Cu NCs.

Interestingly, the emission spectrum was found to be wavelength-tunable, with the emission maximum shifting from 410 to 575 nm, when the excitation wavelength was changed from 325 to 525 nm (**Figures 4.1C** and **4.5B**). In the absence of N_2H_4, a similar product might have been formed; however, the fluorescence intensity of the product was less

than that synthesized in the presence of N_2H_4 (**Figure 4.6A**). Also, the emission spectrum of the product formed in the absence of N_2H_4 did not exhibit clear wavelength-tunable properties like that formed in the presence of N_2H_4 (**Figures 4.6A, B**).

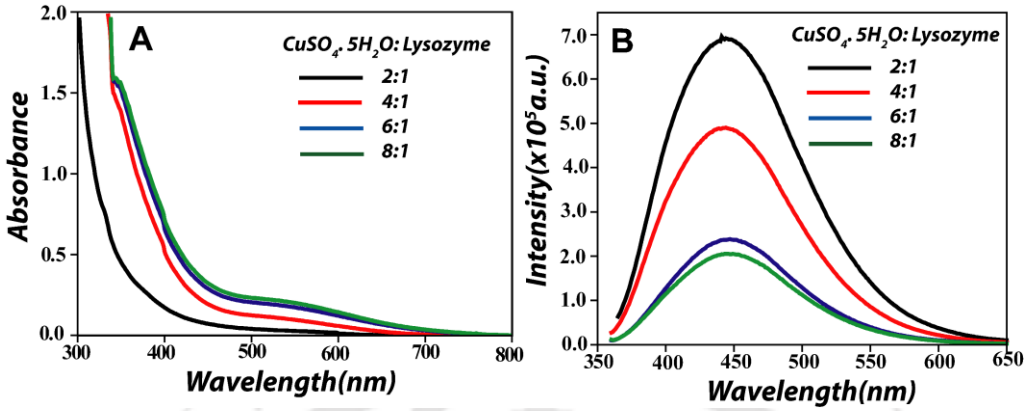

Figure 4.4 Probing the synthesis of Cu NCs in the presence of different concentrations of $CuSO_4$ as observed by recording of (**A**) UV-visible absorption and (**B**) fluorescence spectra.

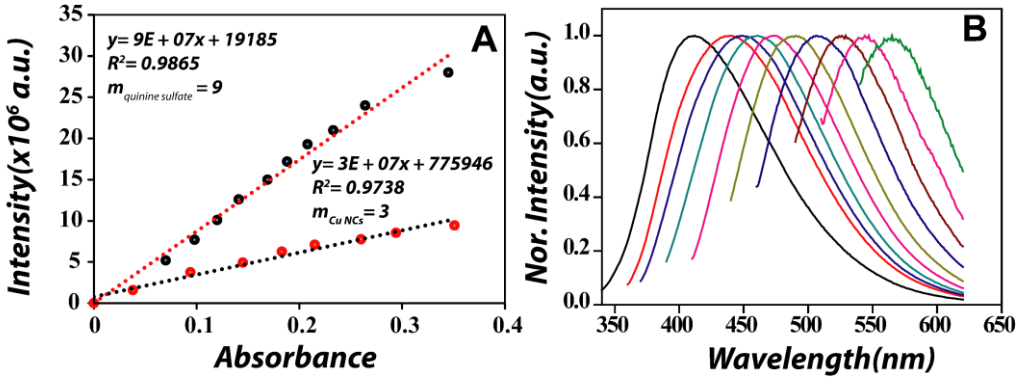

Figure 4.5 (**A**) Integrated fluorescence intensity vs absorbance plot of Cu NCs and quinine sulphate. (**B**) Excitation-tuneable normalized fluorescence spectra of Cu NC with excitation at λ_{ex}= 325–525 nm and λ_{em} = 410–575 nm.

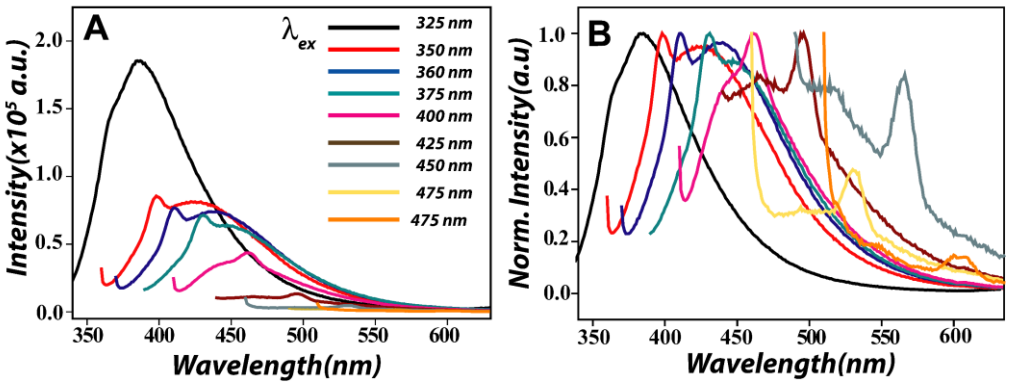

Figure 4.6 (**A**) Excitation-tuneable fluorescence spectra of product prepared with lysozyme and in absence of N_2H_4, with excitation at λ_{ex}= 325–500 nm. (**B**) Excitation-tuneable normalized fluorescence spectra of the same.

The control experiment in the absence of $CuSO_4$ also indicated the presence of fluorescent species (**Figure 4.7**); however, the intensity of fluorescence was either small or the peak occurred at shorter wavelength (**Figure 4.7**). Also, the wavelength-tunable emission was not observed. Additionally, time-resolved fluorescence measurements indicated a clear difference between the products formed in the presence and absence of $CuSO_4$. For example, the average lifetime of emission of the product obtained from $CuSO_4$ and lysozyme was measured to be 6.5 ns (**Figure 4.1D** and **Table 4.1**), whereas that in the absence of $CuSO_4$ was found to be 1.8 ns (**Figure 4.8** and **Table 4.2**). The emission characteristics of the product formed from the reaction match those reported for Cu NCs.[24] Thus, in the medium, Cu NCs were likely formed in the presence of the protein. Hydrazine acted as the reducing agent, producing Cu^0 from Cu^{2+} present in the medium. It was also observed that Cu NCs so produced (in the presence of hydrazine) were stable as the fluorescence emission did not change even after 15 days under ambient conditions (**Figure 4.9**).

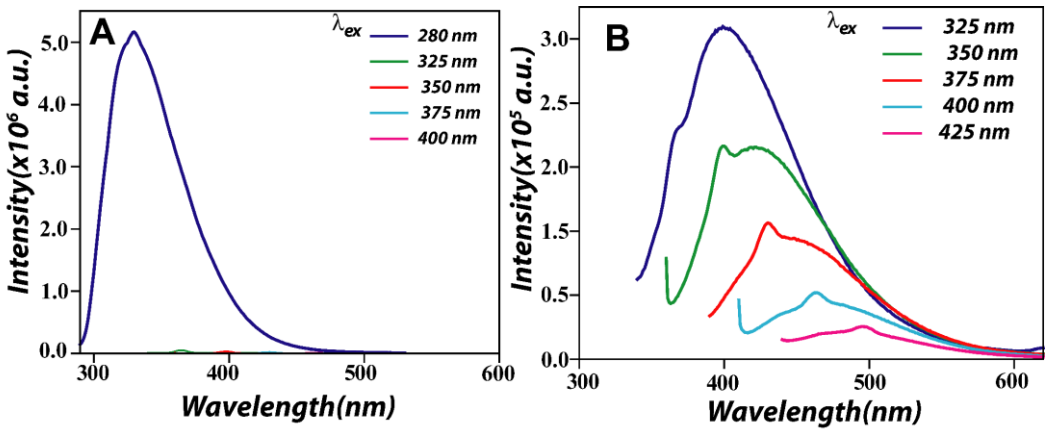

Figure 4.7 Excitation-dependent emission spectra of (**A**) lysozyme only and (**B**) presence of NaOH and N_2H_4.

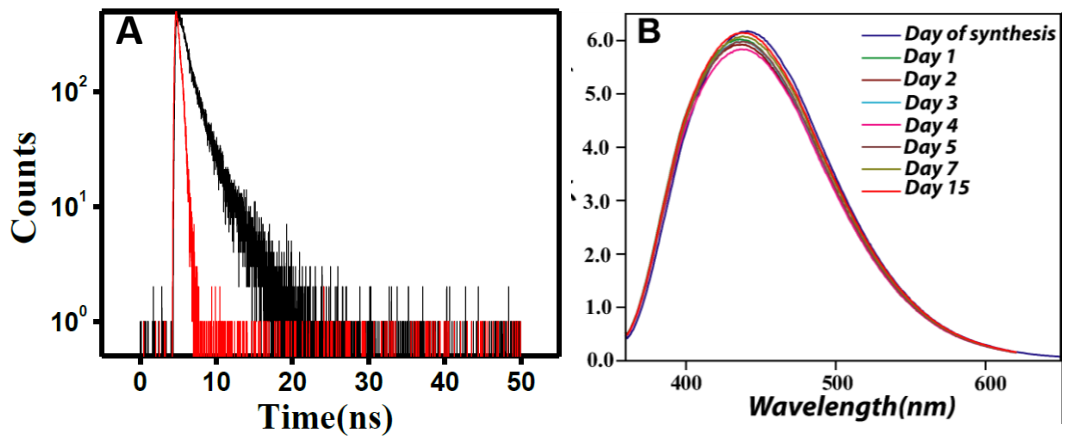

Figure 4.8 (A) Fluorescence decay profile (in black) of lysozyme (λ_{ex}= 308 nm and λ_{em}=393 nm).(**B**) Stability of the synthesized Cu NCs (in the presence of lysozyme) as studied by fluorescence spectroscopy. The little change in the fluorescence emission indicated stable Cu NCs is due to the presence of hydrazine in the medium.

Table 4.1. Life-time data obtained from tri- exponential model for the fluorescence decay profile Cu NCs.

τ_1 (ns)	τ_2 (ns)	τ_3 (ns)	α_1	α_2	α_3	χ^2	<τ> (ns)
0.473	2.4	8.5	40.3	33.4	26.2	1.03	6.5 ns

Table 4.2. Life-time data obtained from bi- exponential model for the fluorescence decay profile of Lysozyme.

τ_1 (ns)	τ_2 (ns)	α_1	α_2	χ^2	<τ> (ns)
0.181	1.89	32.20	67.80	0.99	1.8 ns

TEM measurements indicated the presence of small Cu NCs forming aggregates of average size of 2.3 ± 0.7 nm (**Figure 4.9A, B**). It is important to note here that the average particle size in **Figure 4.9B** appears to be higher than that of typical NCs. However, it is also known that when metallic NCs are generated in the absence or presence of additional capping agents, agglomerated structures are formed, leading to an apparent higher particle size and even increased luminescence.[18,24,25] In the case of lysozyme, Au NCs formed agglomerated nanosized structures larger than individual NCs.[25,26] The average size of individual Cu NCs inside the aggregates (inset to **Figure 4.9A** and **Figure 4.9C**) was calculated as 0.96 ± 0.25 nm. Further probing of the sample using high-resolution TEM (HRTEM) showed the presence of crystalline particles with a lattice spacing of 0.207 nm, corresponding to the (111) plane of Cu^0 (**Figure 4.9D**).[27] However, it may be stressed here that crystalline particles so observed might have been non emissive and may represent larger SPR-active Cu nanoparticles. On the other hand, a crystalline lattice of ultrasmall atomic clusters of Cu may not be observed in HRTEM. Additionally, the population of larger crystalline Cu nanoparticles might have been rather small in the medium and thus not to have exhibited a clear SPR peak in the UV–visible spectrum.

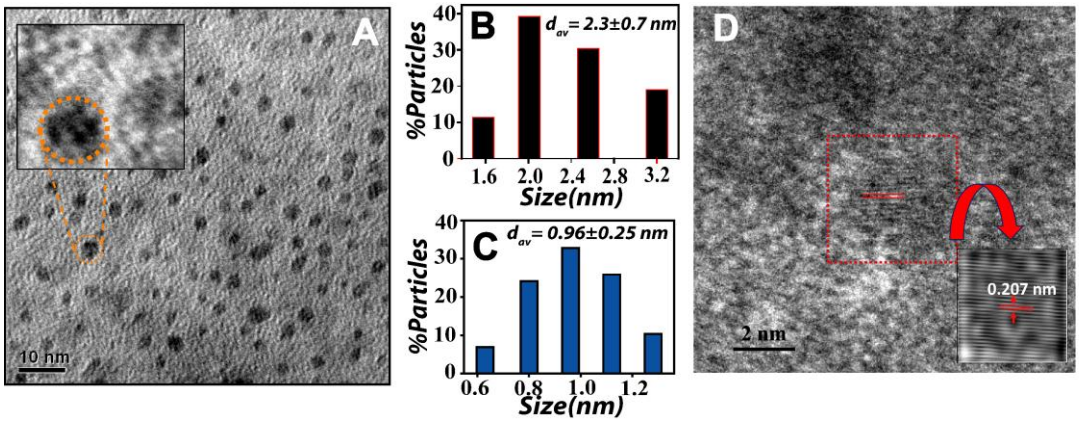

Figure 4.9 (**A**) TEM images of the product containing agglomerates of different sizes (scale bar 10 nm). Inset shows the enlarged image of one of the agglomerated particles. (**B**) Size histogram of different sizes of the particles (agglomerates). (**C**) Size histogram of individual clusters present inside the agglomerated product. (**D**) HRTEM image of Cu NCs. IFFT image of (inset) gives a lattice spacing of 0.207±0.015 nm for the (111) plane of Cu (0).

Powder XRD pattern of the composite showed a broad peak at around 22° and the absence of characteristic peaks due to Cu (**Figure 4.10A**). The results also support a lack of crystallinity of the Cu NCs so formed and the absence of a significant population of crystalline Cu nanoparticles in the sample (consistent with a larger population of small-sized NCs). FTIR spectra of lysozyme and lysozyme-stabilized Cu NCs are presented in **Figure 4.10B**. Three amide bands (amides I, II and III) due to the protein and occurring at 1600–1700, 1480–1575, and 1229–1301 cm^{-1}, respectively,[28,29] were present in the spectra. In addition, the peaks at 3400–3000 cm^{-1} due to −NH and −OH stretching vibrations were prominent in the spectra. The presence of functional groups such as $-NH_2$, −COOH, and −SH in the protein lysozyme may provide stability to the NCs. In a strongly alkaline medium, the protein might have been partially unfolded, thereby exposing a sufficient number of such groups that would facilitate attachment of the NCs to the protein.[30] It may also be true that the three-dimensional structure of the protein, with its functional groups separated spatially, provides enough room for attachment of more than one cluster to the same protein.

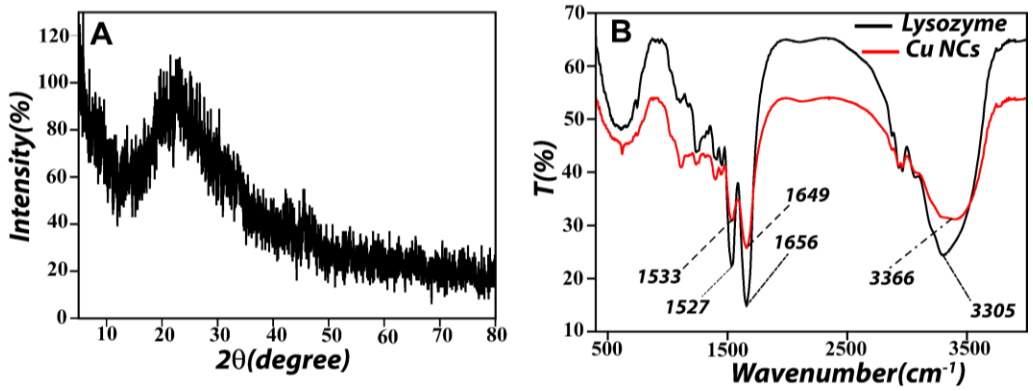

Figure 4.10 (**A**) Powder XRD pattern of lysozyme stabilized Cu NCs. The broad peaks indicated the ultra-small particles of Cu NCs. (**B**) FTIR spectra for lysozyme and lysozyme stabilized Cu NCs.

Among the three coinage metals, Cu is easily oxidized because of its low reduction potential. Therefore, it was deemed important to establish the oxidation state of Cu in the composite. For this, XPS analysis was performed for confirmation of the oxidation state of Cu in the Cu NC samples (**Figure 4.11**). Two prominent peaks, observed at 952.1 and 932.2 eV, were assigned to Cu $2p_{1/2}$ and Cu $2p_{3/2}$, which were characteristic peaks due to Cu^0. The absence of peak due to Cu^{2+} at 942 eV indicated that the Cu NCs did not contain Cu^{2+}. However, because the peak due to Cu^+ (932.3 eV) occurs at 0.1 eV apart from Cu^0, its presence cannot be ruled out. Further, the binding energy of sulfur (S) 2p observed at 162.8 eV (**Figure 4.12**) indicated the presence of chemisorbed S on the surface of Cu NCs, which is supportive of the presence of Cu and S on the sample.[31,32]

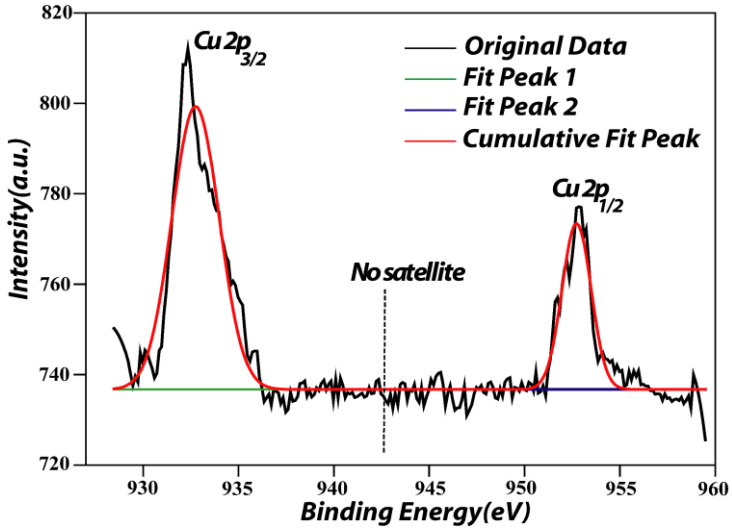

Figure 4.11 X-ray photoelectron spectrum of Cu 2p electrons in Cu NCs. The absence of satellite peaks indicated the absence of Cu^{2+} in the sample.

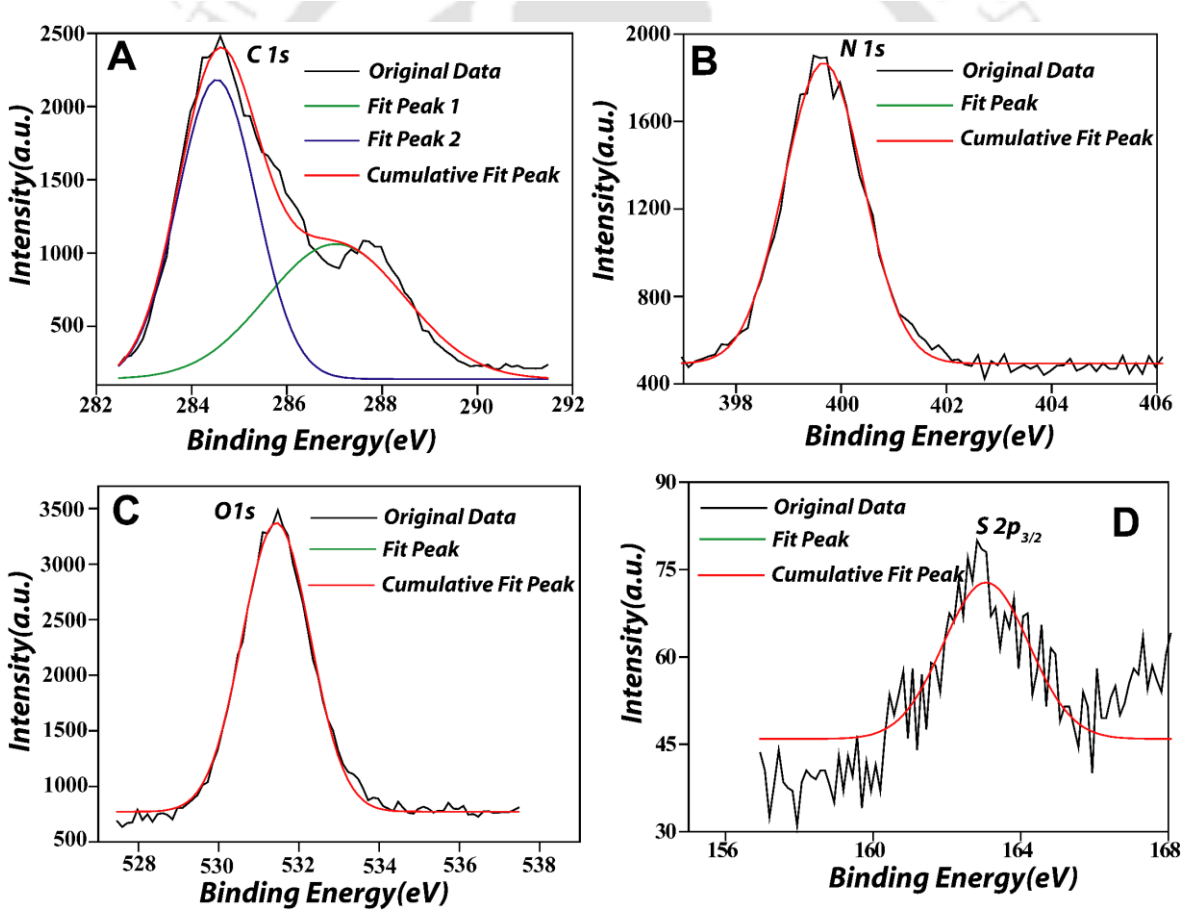

Figure 4.12 X-ray photoelectron spectra of the elements present in the composite of protein (lysozyme) and Cu NCs. (**A**) C 1s, (**B**) N 1s, (**C**) O 1s.and (**D**) S 2p

Further analysis was carried out using MALDI-TOF MS to determine the core size of the Cu NCs. The spectrum was recorded in the linear positive mode, using a sinapinic acid matrix.

The peak due to lysozyme appeared at 14300 Da (**Figures 4.13**) because of its monocation form. It is expected that the molecular weight of a lysozyme/Cu NC composite will have peaks at masses higher than 14300 Da. A series of peaks in the region of 14300–14900 Da were observed. However, four peaks were prominent that appeared at *m*/*z* 14300, 14434, 14564, and 14874 Da, as shown in **Figure 4.13B**. They can be attributed to $[Lyz]^+$, $[Lyz + Cu_2]^+$, $[Lyz + Cu_4]^+$, and $[Lyz + Cu_9]^+$, respectively. The results thus indicated the formation of Cu_2, Cu_4, and Cu_9 NCs, which were the same as those reported.[17,24,33] It is plausible that other clusters were also formed; however, they were not clearly detected in the MALDI-TOF MS spectrum.

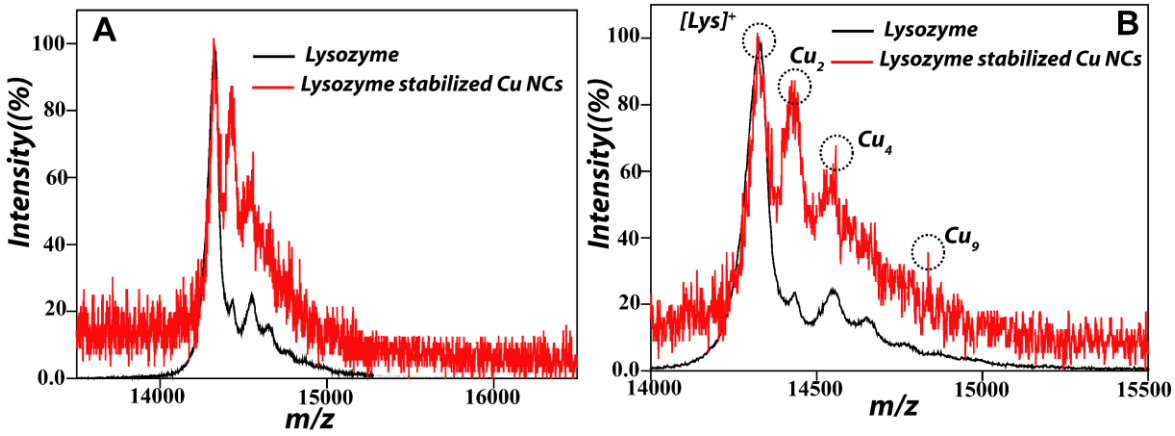

Figure 4.13 (**A**) MALDI-TOF MS spectra of lysozyme (black line) and lysozyme-stabilized product (red line) with assignment of the characteristic peaks due to Cu NCs (dotted circles) in (**B**) The expanded spectra of Figure **4.13A**.

CD measurements indicated a decrease in the α-helix content of proteins present in the product medium from 52 % to 45 % following cluster formation (**Figure 4.14A** and **Table 4.3**). Denaturation of the protein (even partially) consequent upon possible breakage of disulphide bonds,[26] or otherwise, might have led to agglomeration, accompanying the formation of Cu NCs at 45 °C. Additionally, the photostability of NCs is one of the properties that finds use in bioimaging and biolabeling applications. As shown in **Figure 4.14B**, fluorescence of the present Cu NCs remained nearly constant under continuous irradiation, with a fluorescence decrease rate of only 0.04 %/min. In comparison, fluorescence of an organic fluorophore, rhodamine 6G, decreased at a rate of 0.23 %/min with the photoirradiation time. The excellent resistance to photobleaching exhibited by the present Cu NCs, along with a considerable Stokes shift in the emission wavelength, makes a strong case for their use for cellular labeling and imaging. Additionally, an agarose gel electrophoresis study revealed the electrophoretic stability of NCs stabilized by the protein (**Figure 4.15**).

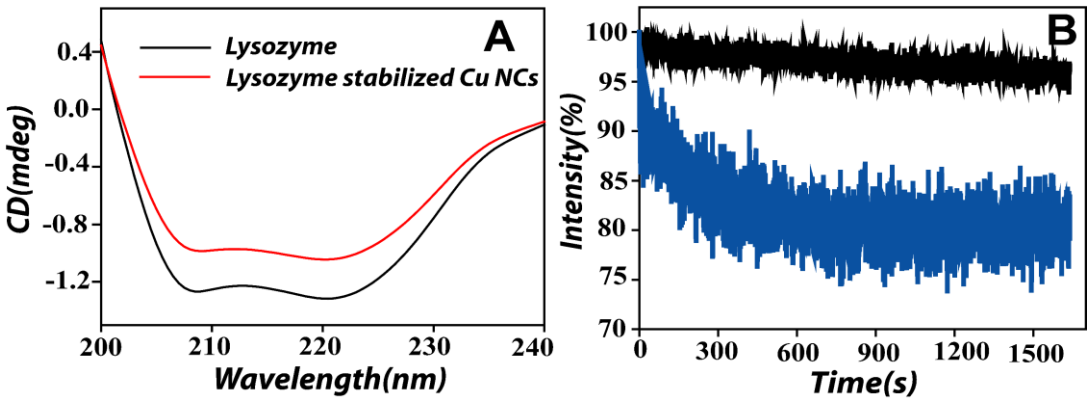

Figure 4.14 (**A**) CD spectra of lysozyme (black line) and as-synthesized Cu NCs (wine red) in the presence of lysozyme, exhibiting changes in the helicity of α-helical structure following synthesis. (**B**) Representative time trace of fluorescence emission of Cu NCs (black line) showing slower decay in comparison to organic fluorophore, rhodamine 6G (blue line), under the same conditions.

Table 4.3. Helicity of protein lysozyme obtained from UV–CD spectroscopy (corresponding to **Figure 4.14A).**

Samples	α–helix (%)	β–sheet (%)
Lysozyme	52	26
Lysozyme stabilized Cu NCs	45	30

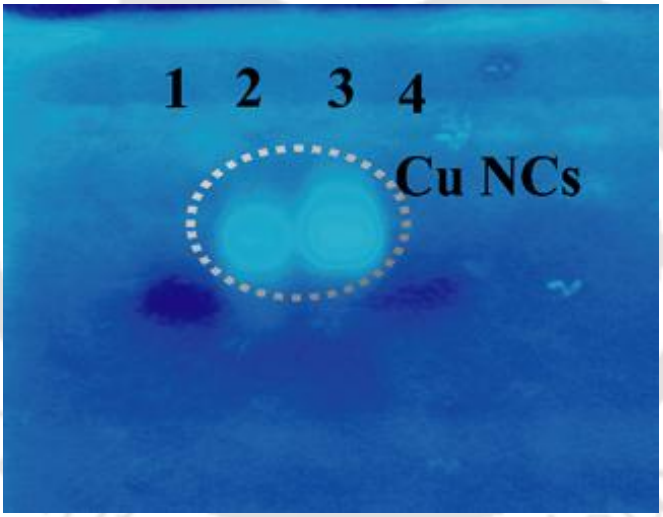

Figure 4.15. Agarose gel electrophoresis of Cu NCs (synthesized in the presence of lysozyme) along with lysozyme (only), indicating the characteristic blue fluorescence of the NCs under UV light and only lysozyme (with no clear fluorescence) under the same condition. Lane 1 and 4 correspond to lysozyme, lane 2 and 3 correspond to Cu NCs (with Cu: lysozyme at 4:1 and 2:1, respectively).

In order to probe the surface charge of the synthesized Cu NCs, ζ–potential measurements were performed (**Table 4.4**). As-synthesized composite had a ζ–potential value of −28.1 mV, indicating an overall negative charge of the composite. Further, the potentials measured at the medium pH values of 9.0 and 4.5 were found to be −32.4 and −19.3 mV, respectively. The pH dependence of the ζ–potential could be due to the contribution from the protein, in addition to that of the clusters.

Table 4.4 Zeta potential value of copper nanoclusters (Cu NCs) synthesized in the presence of lysozyme and measured at different pH values of the medium.

Samples	Zeta potential (mV)
Lysozyme	−4.38
Lysozyme stabilized Cu NCs (pH: 9.0)	−32.4
Lysozyme stabilized Cu NCs (pH: 7.4)	−28.1
Lysozyme stabilized Cu NCs (pH: 4.5)	−19.3

Further, it was deemed important to probe the effect of the pH on the fluorescence of the NCs. The NCs were synthesized at pH 11; the emission peak (at 450 nm) was found to be stable for 2 weeks. On the other hand, when the pH was made acidic, there was no change in the fluorescence, as was observed until an acidic pH of 4.3. The results are presented **Figure 4.16**. The observation of pH-independent emission of Cu NCs indicates their importance for applications over a large pH range.

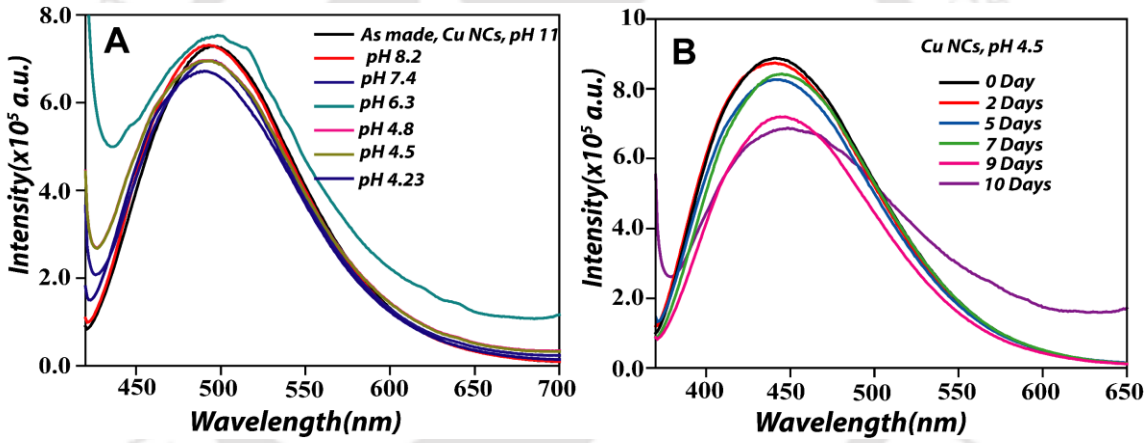

Figure 4.16 (**A**) Fluorescence spectra of Cu NCs at different pH. **(B**) Stability of Cu NCs in acidic pH at 4.3.

4.4. CELL IMAGING AND CELL VIABILITY TEST BY XTT ANALYSIS

An *in vitro* toxicity study of the NCs was examined by the XTT-based cell viability assay. XTT assay was performed to probe the cytotoxicity of the Cu NC composite by incubation in HeLa cells. The concentration of the composite used was 2.3–34.5 μg/mL. It should be mentioned here that the amount of Cu present in the composite, i.e., excluding lysozyme and hydrazine, was found to be 0.3–4.5 μg/mL. The Cu concentration is calculated based on the initial Cu salt taken for the reaction and assuming full conversion of the salt to Cu NCs. This means that the metal concentration reported here is the upper limit. The results indicated that Cu NCs had little or no cytotoxicity even at considerably higher concentration. HeLa cells (cervical cancer) in DMEM were incubated with different concentrations of Cu NCs in standard cell culture conditions. Following 24 h of incubation, the viability of the cells was

determined, and the results are shown in **Figure 4.17A**. From XTT assay, it was found that more than 98% cells were viable upon incubation with 34.5 μg/mL of the Cu NC composite. The results indicated that the Cu NCs had no toxic effect even at a considerably higher starting concentration of Cu.

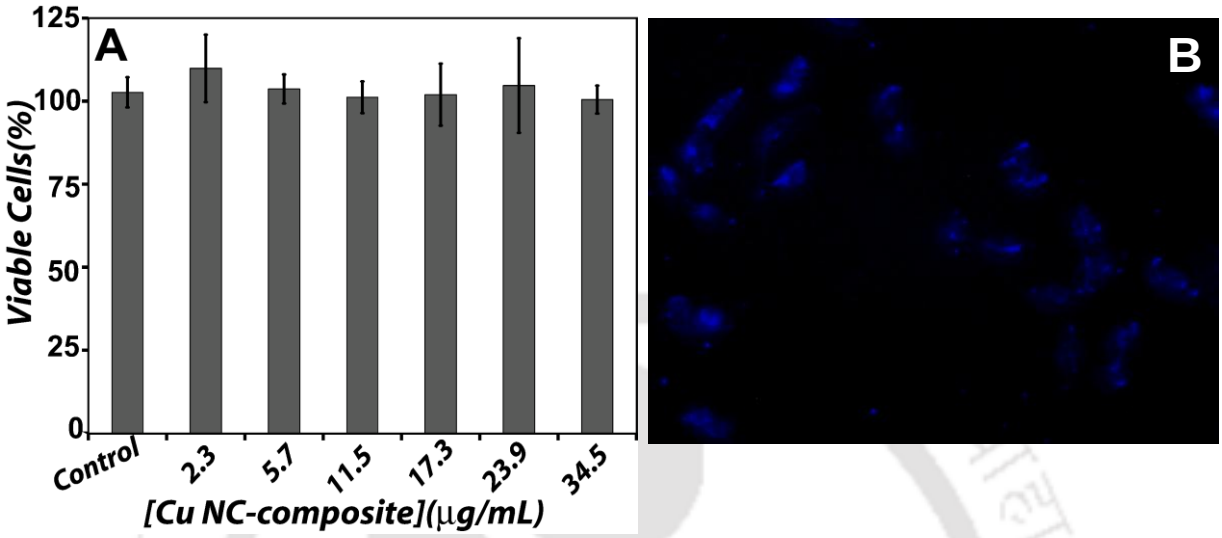

Figure 4.17. (A) Cell viability for measuring the cytotoxicity of the Cu NCs on HeLa cells as measured by XTT assay after 24 h of incubation (B) Epifluorescence microscopic images of HeLa cells under UV light. Cells were incubated with Cu NCs for 2 h (scale bar 50 μm).

The non-cytotoxicity and high fluorescence QY and photostability of the Cu NCs made it possible to test their suitability for cell labeling. This was pursued by incubating HeLa cells with Cu NCs for 2 h in DMEM. After removal of the medium, the cells were washed thoroughly with PBS (pH 7.4) to remove free unbound Cu NCs and finally were observed under a fluorescence microscope. The cells in the image (**Figure 4.17B**) could easily be observed under UV light (340–380 nm) because they appeared bright blue, which is the characteristic color of the Cu NCs. The corresponding image under a bright field and merged images are shown in **Figure 4.18**. In comparison, control cells and cells treated with lysozyme did not exhibit any such fluorescence (**Figures 4.19** and **Figure 4.20**). This clearly demonstrated the utility of the so-synthesized Cu NCs in live cell labeling.

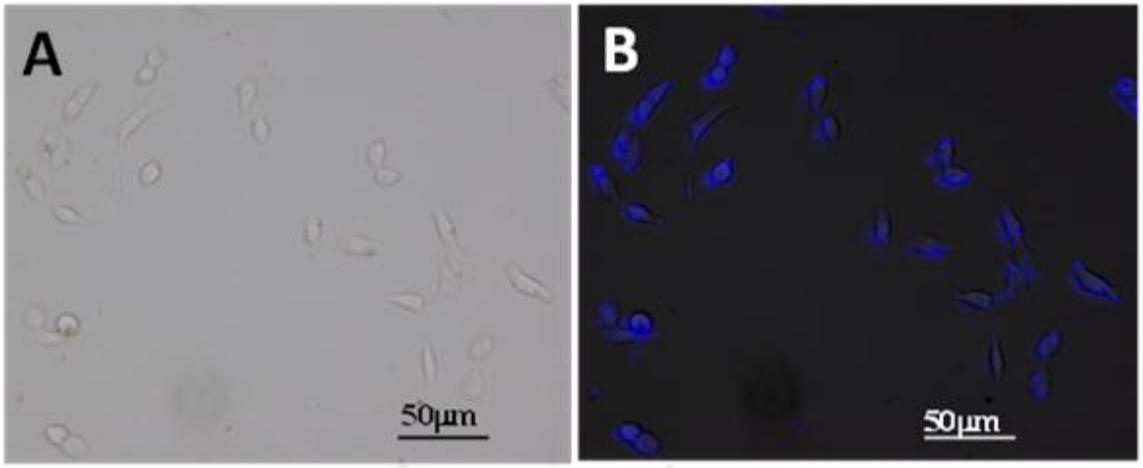

Figure 4.18. Epifluorescence microscopic image of HeLa cells treatment with Cu NCs stabilized by lysozyme (**A**) Bright field, (**B**) Merged image under UV excitation. Scale bar: 50 µm.

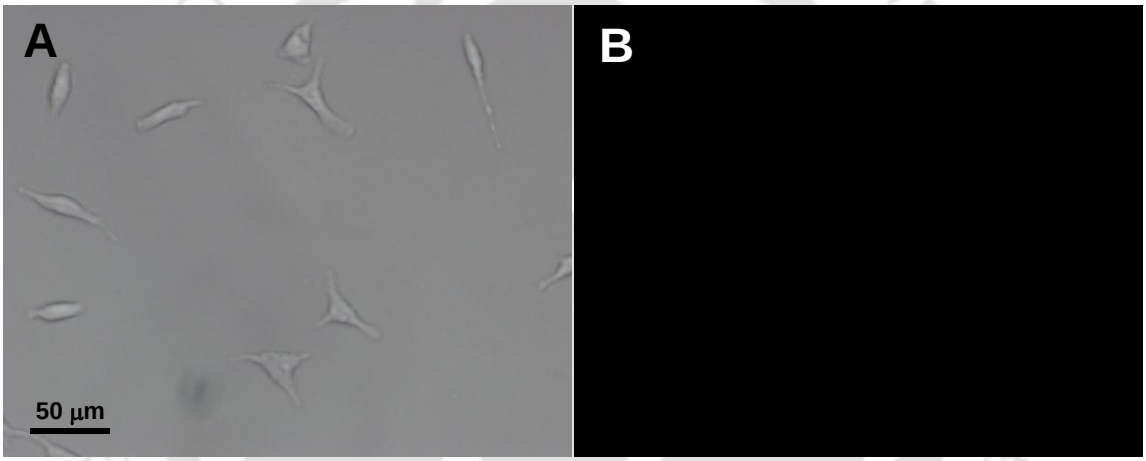

Figure 4.19. Epifluorescence microscopic image of HeLa cells without any treatment with Cu NCs stabilized by lysozyme. (**A**) Bright field and (**B**) under UV excitation images. Scale bar: 50 µm.

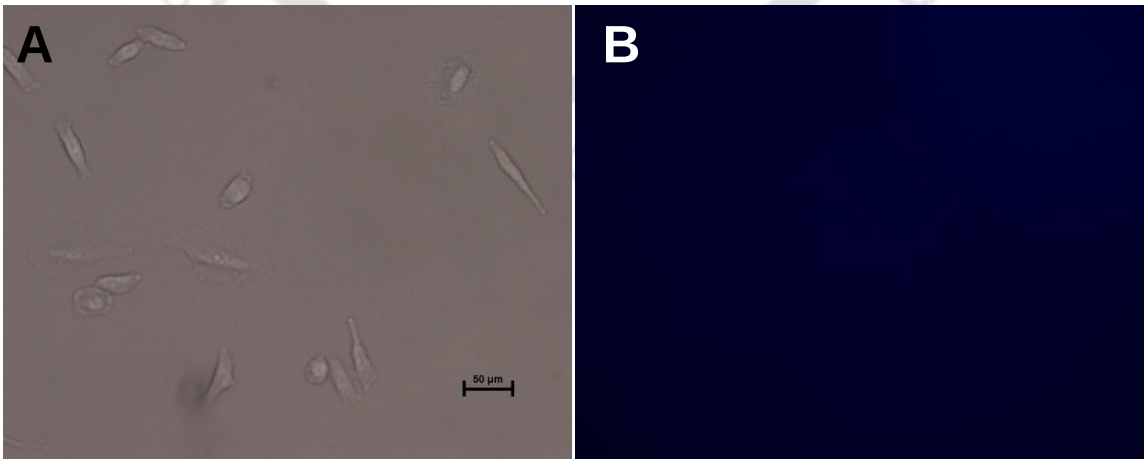

Figure 4.20. Epifluorescence microscopic image of HeLa cells recorded following treatment with lysozyme only. The images were recorded under (**A)** bright light and (**B**) under UV-excitation. Scale bar: 50 µm.

Blood compatibility assay is an essential and initial requirement for the administration of any material *in vivo* such as hemolysis.[34] For that, preliminary investigations were performed using blood serum treated with Cu NCs. There was no loss of fluorescence (**Figure 4.21**). On the other hand, there was an increase in fluorescence, which could be due to reducing the nature of the environment in the serum. The hemocompatibility of various concentrations of Cu NCs were performed by hemolysis assay. The results (**Figure 4.22**) demonstrated that Cu NCs did not cause significant hemolysis; i.e., they were hemocompatible at the concentrations used for the bioimaging and cell viability assay (0.6–4.5 μg/mL), which is comparable to previous studies.[35] Thus, blood compatibility assay supported the potential of the composites (and thus Cu NCs) for applications *in vivo*.

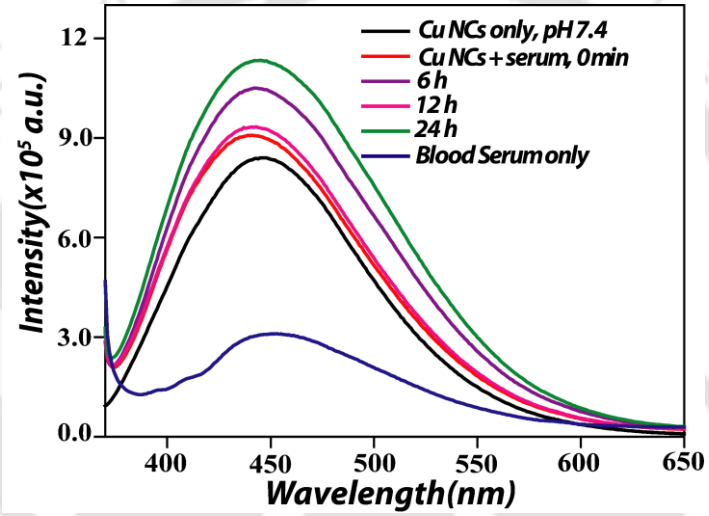

Figure 4.21. Blood compatibility study *in vitro* represented by the emission spectra of Cu NCs in phosphate buffer (pH 7.4) and incubated with blood serum in water. Fluorescence intensity gradually increased in 24 h of incubation.

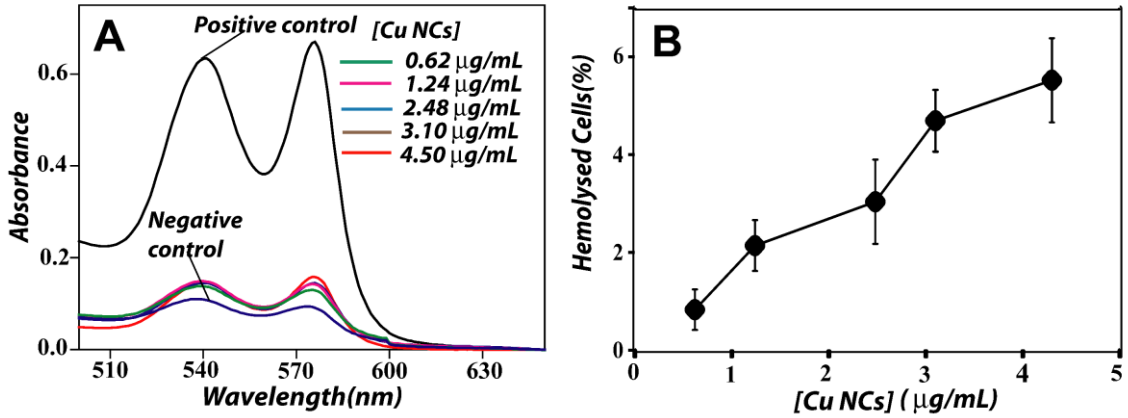

Figure 4.22. Blood compatibility studies *in vitro*: (**A**) UV-vis spectra in the supernatant of Cu NCs in PBS of experimental concentrations (0.6–4.3 μg/mL) after incubated with HRBCs using water and PBS buffer as positive and negative controls. (**B**) Hemolysis (%) of Cu NCs in PBS in experimental concentrations (0.6–4.3 μg/mL).

4.5. CONCLUSION

Bright-blue fluorescent Cu NCs have been synthesized through a simple one-step reduction of $CuSO_4$ by N_2H_4, using lysozyme as the stabilizer. The NCs showed high photoluminescence QY, excitation-tunable fluorescence, high photostability, and colloidal stability. They could be used for labeling HeLa cells. In conjunction with the photoluminescence properties, their low cytotoxicity would make them an ideal choice for biological and biomedical applications. The composite is comprised of Cu and lysozyme, where Cu is an essential trace element present in the body and lysozyme, an antimicrobial enzyme, is substantially present in a number of secretions, such as tears, saliva, etc. Thus, the composite might be considered to be biocompatible. The observed stability of the composite, coupled with the retention of fluorescence at physiological pH, is important for applications *in vitro* as well as *in vivo*.

4.6. REFERENCES

1. Wu, X.; He, X.; Wang, K.; Xie, C.; Zhou, B.; Qing, Z. *Nanoscale* **2010**, *2*, 2244–2249.
2. Lin, C.-A. J.; Yang, T.-Y.; Lee, C.-H.; Huang, S. H.; Sperling, R. A.; Zanella, M.; Li, J. K.; Shen, J.-L. ; Wang, H.-H. ; Yeh, H.-I.; Parak, W. J.; Chang, W. H. *ACS Nano* **2009**, *3*, 395–401.
3. Thompson, D.; Hermes, J. P.; Quinn, A. J.; Mayor, M. *ACS Nano* **2012**, *6*, 3007–3012.
4. Sahoo, A. K.; Banerjee, S.; Ghosh, S. S.; Chattopadhyay, A. *ACS Appl. Mater. Interfaces* **2014**, *6*, 712–724.
5. Shen, Z.; Duan, H.; Frey, H. *Adv. Mater.* **2007**, *19*, 349–352.
6. Petty, J. T.; Zheng, J.; Hud, N. V.; Dickson, R. M. *J. Am. Chem. Soc*. **2004**, *126*, 5207–5212.
7. Richards, C. I.; Choi, S.; Hsiang, J.-C.; Antoku, Y.; Vosch, T.; Bongiorno, A.; Tzeng, Y.-L.; Dickson, R. M. *J. Am. Chem. Soc*. **2008**, *130*, 5038–5039.
8. Xie, J.; Zheng, Y.; Ying, J. Y. *J. Am. Chem. Soc.* **2009**, *131*, 888–889.
9. Guével, X. L.; Hötzer, B.; Jung, G.; Hollemeyer, K.; Trouillet, V.; Schneider, M. *J. Phys. Chem. C* **2011**, *115*, 10955–10963.
10. Mathew, A.; Sajanlal, P. R.; Pradeep, T. *J. Mater. Chem.* **2011**, *21*, 11205–11212.
11. Chaudhari, K.; Xavier, P. L.; Pradeep, T. *ACS Nano* **2011**, *5*, 8816–882.
12. Lin, Y.-H.; Tseng, W.-L. *Anal. Chem*. **2010**, *82*, 9194–9200.
13. Zhou, T.; Haunq, Y.; Li, W.; Cai, Z.; Luo, F.; Yanq, J. C.; Chen, X. *Nanoscale* **2012**, *4*, 5312–5315.
14. Liu, C.-L.; Wu, H.-T.; Hsiao, Y.-H. ; Lai, C.-W. ; Shih, C.-W. ; Peng, Y.-K. ; Tang, K.-C.; Chang, H.-W.; Chien, Y.-C.; Hsiao, J.-K.; Cheng, J.-T.; Chou, P.-T. *Angew. Chem. Int. Ed.*, **2011**, *50*, 7056–7060.
15. Wen, F.; Dong, Y.; Feng, L.; Wang, S.; Zhang, S.; Zhang, X. *Anal. Chem*. **2011**, *83*, 1193–1196.
16. Kawasaki, H.; Hamaguchi, K.; Osaka, I.; Arakawa, R. *Adv. Funct. Mater*. **2011**, *21*, 3508–3515.
17. Kawasaki, H.; Kosaka, Y.; Myoujin, Y.; Narushima, T.; Yonezawa, T.; Arakawa, R. *Chem. Commun.* **2011**, *47*, 7740–7742.
18. Vilar-Vidal, N.; Blanco, M. C.; López-Quintela, M. A.; Rivas, J.; Serra, C. *J. Phys. Chem. C* **2010**, *114*, 15924–15930.
19. Jia, X.; Li, J.; Han, L.; Ren, J.; Yang, X.; Wang, E. *ACS Nano* **2012**, *6*, 3311–3317.
20. Tapiero, H., Townsend, D. M., Tew, K. D. *Biomed. Pharmacother.* **2003**, *57*, 386–398.
21. Gaggelli, E.; Kozlowski, H.; Valensin, D.; Valensin, G. *Chem. Rev*. **2006**, *106*, 1995−2044.
22. Cater, M. A.; Fontaine, S. L.; Shield, K.; Deal, Y.; Mercer, J. F. *Gastroenterology* **2006**, *130*, 493−506.
23. Lakowicz, J. R. *Principles of Fluorescence Spectroscopy*, 2nd Ed.; Kluwer Academic/Plenum Publishers: New York, **1999**.
24. Jia, Z.; Li, J.; Wang, E. *Small* **2013**, *9* 3873–3879.
25. Xu, H.; Suslick, K. S. *Adv. Mater*. **2010**, *22*, 1078–1082.

26. Baksi, A.; Xavier, P. L.; Chaudhari, K.; Goswami, N.; Pal, S. K.; Pradeep, T. *Nanoscale* **2013**, *5*, 2009–2016.
27. Qing, Z.; He, X.; He, D.; Wang, K.; Xu, F.; Qing, T.; Yang, X. *Angew. Chem. Int. Ed*. **2013**, *52*, 9719–9722.
28. Shang, L.; Wang, Y.; Jiang, J.; Dong, S. *Langmuir* **2007**, *23*, 2714–2721.
29. Surewicz, W. K.; Mantsch, J. H.; Chapman, D. *Biochemistry* **1993**, *32*, 389–394.
30. Chen, T.-H.; Tseng, W.-L. *Small* **2012,** *8***,** 1912–1919.
31. Wei, W.; Lu, Y.; Chen, W.; Chen, S. *J. Am. Chem. Soc*. **2011**, *133*, 2060–2063.
32. Bensebaa, F.; Ellis, T. H.; Kruus, E.; Voicu, R.; Zhou, Y. *Langmuir* **1998**, *14*, 6579–6587.
33. Jia, X.; Yang, X.; Li, J.; Li, D.; Wang, E. *Chem. Commun.* **2014** *50*, 237–239.
34. Wu, H. X.; Zhang, S. J.; Zhang, J. M.; Liu, G.; Shi, J. L.; Zhang, L.X.; Cui, X. Z.; Ruan, M. L.; He, Q. J.; Bu, W. B. *Adv. Funct. Mater*. **2011**, *21*, 1850−1862.
35. Chandra, V. S.; Baskar, G.; Suganthi, R. V.; Elayaraja, K.; Joshy, A. M. I.; Beaula, W. S.; Mythili, R.; Venkatraman, G.; Kalkura, S. N. *ACS. Appl. Mater. Interfaces* **2012,** *4*, 1200–1210.

Chapter 5

Synergistic Anticancer Activity of Fluorescent Copper Nanoclusters and Cisplatin Delivered Through a Hydrogel Nanocarrier*

This chapter describes the synthesis of red fluorescent copper nanoclusters using polyvinylpyrrolidone and lipoic acid which exhibited pH tuneable reversible optical properties. The nanoclusters when converted into hydrogel by cross linking with polyvinyl alcohol, delivered anticancer drug to cervical cancer (HeLa) cells, thereby induces apoptotic cell death. Red emission properties of copper nanoclusters in the hydrogel were used for optical imaging and flow cytometric probe of cellular uptake. Cell viability assay, Caspase3 assay and cell cycle analyses demonstrated that the Cu NCs present in the hydrogel composite exhibited synergy of action, along with the drug, cisplatin, against HeLa cells.

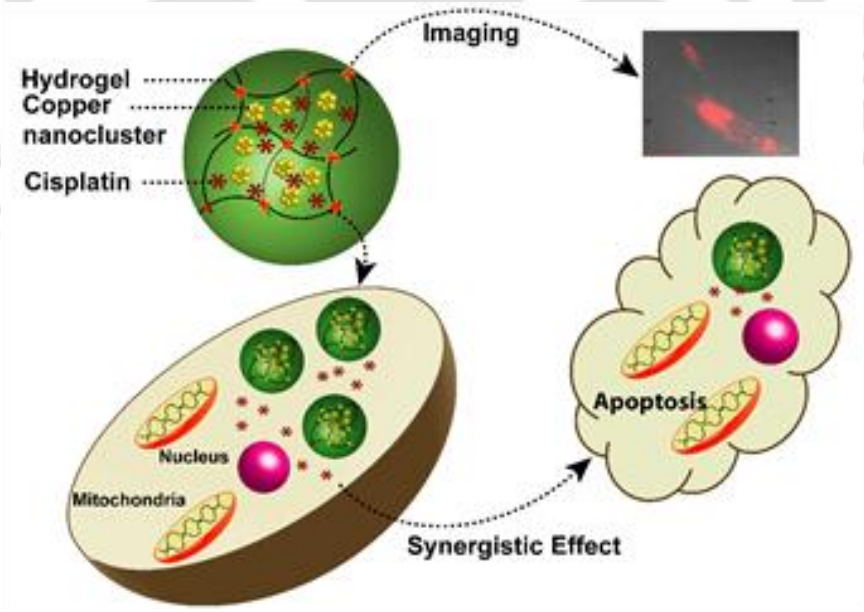

*Ghosh, R.; Sahoo, A. K.; Ghosh, S. S.; Paul, A.; Chattopadhyay, A. *ACS Appl. Mater. Interfaces* **2015**, *7*, 209–222**. DOI: 10.1021/acsami.5b08088** Reproduced with permission from *ACS Appl. Mater. Interfaces*. Copyright 2015, American Chemical Society.

5.1. INTRODUCTION

Metal nanoclusters (NC) bridge the materials gap between the atom and nanoparticle (NP). The inherent quantum behavior of the NCs makes them a promising material endowed with size, tunable optical, and the other physical properties. Smaller size, reasonable chemical stability, excellent photostability, low cytotoxicity, and high luminescence quantum yield (QY) collectively provide a better prospect for using the noble metal NCs (especially Au NCs) in biological applications, instead of semiconductor quantum dots, which are generally cytotoxic. Recent surge of reports on their use for sensing,[1–3] biolabeling, bioimaging,[4–7] and chemical catalysis[8–10] is a testimony to their growing importance.

An important parameter that decides the utility of the NCs is their stability in liquid media, especially in the milieu of chemically and biochemically active moieties. This is where the development of new methods play an important role in generating physically and environmentally responsive NCs. Among the noble metals, NCs of Au and Ag have been synthesized using templates such as polymer,[11,12] DNA,[13,14] protein,[15–17] and thiol-containing smaller molecular entities.[18] The inherent chemical stability of Au and Ag favors the synthesis of their NCs with comparative ease as opposed to those of Cu. The case of Cu NC is particularly difficult because of its instability even in mildly oxidizing condition. However, recent experiments from our laboratory[19] and others suggest that it is possible to synthesize stable Cu NCs. For example, Cu NCs have been synthesized by 2-mercapto-5-*n*-propylpyrimidine[20] and D-penicillamine[21] as protecting ligands. Also, etching of Cu NPs along with the use of glutathione (GSH) as a stabilizing ligand resulted into monodispersed fluorescent Cu NCs.[22] On the other hand, Cu NCs synthesized in the presence of DNA have been used to identify single nucleotide polymorphism.[23] Further, blue and red-emitting Cu NCs, synthesized in the presence of protein such as lysozyme[19] and BSA,[24] have been used in cell labeling applications. As mentioned above, while there are a few methods available for the synthesis of Cu NCs, there are still demands for Cu NCs with high stability and having application-specific stabilizing molecules or structures. For example, there is a need to obtain stable red-emitting Cu NCs. In addition, if the NCs could be stabilized in the form of solid composites it would be better for storage, transport, and further use. That copper is an important and essential trace element in human, that there are sequestering agents for copper,[25,26] and that excess copper could be removed from the human body in comparison to gold and silver make it an important noble metal, which could be of paramount importance for superior biomedical applications.

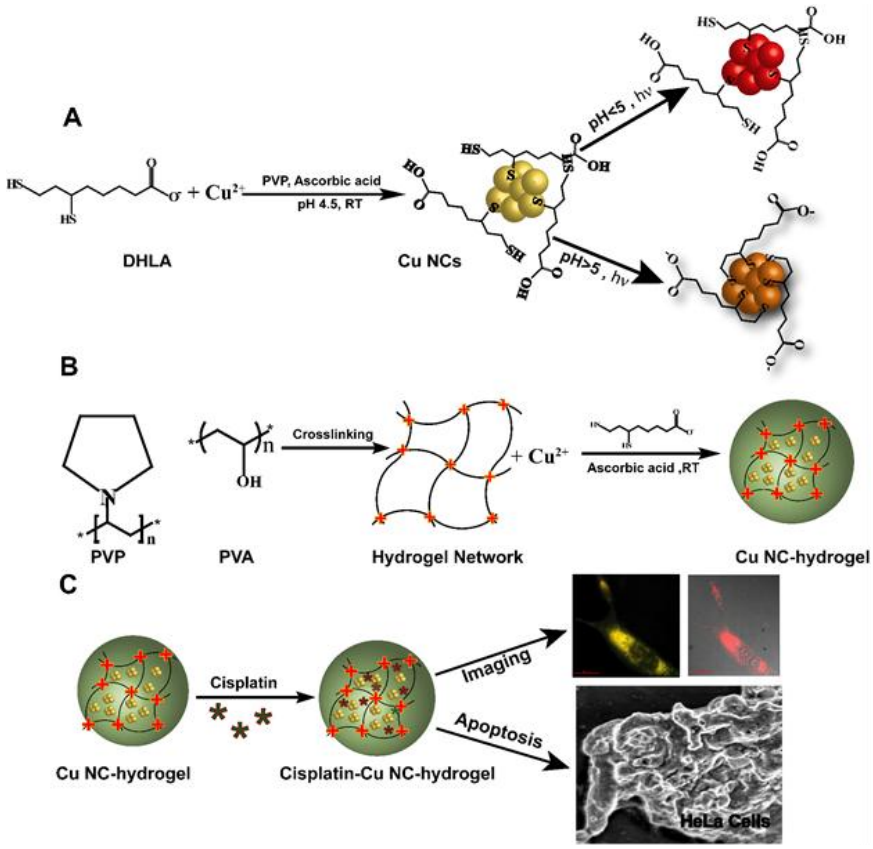

Scheme 5.1 Schematic representation of (**A**) synthesis of Cu NCs having pH-dependent fluorescence; (**B**) synthesis of Cu NC–hydrogel composite by crosslinking PVP and PVA, and (**C**) cisplatin-loaded Cu NC-hydrogel composite leading to apoptotic cell death as probed by cellular imaging.

Herein we report the synthesis of red fluorescent monodispersed Cu NCs in aqueous medium by dihydrolipoic acid, in combination with biocompatible polymer poly(vinylpyrrolidone) (PVP) as a stabilizer. The fluorescence of the composite was found to be sensitive to the pH of the medium, and the emission could be tuned reversibly according to the pH. Also, the polymer NC composite could easily be synthesized in the form of hydrogel nanocarrier, by using poly(vinyl alcohol), PVA, as the cross-linker, which is favorable for cellular uptake.[27] The hydrogel could be then turned into a powder, which showed stable fluorescence, owing to the NCs, for more than a month. Further, the emission due to the NCs was useful for imaging mammalian cells by optical microscopy and more importantly to probe the cells by commercial flow cytometer, without having to use any other dye. Cu NC-containing hydrogel could encapsulate cisplatin (CP) for effective delivery to cancer cells, which was probed by using the emission properties of the NCs. Interestingly, it was found that Cu NCs generated reactive oxygen species (ROS) in the cancer cells and hence enhanced the efficacy of CP in killing the cells, thus providing a synergy of action. The essential concept involving reaction scheme for the formation of composite of Cu NCs and PVP and its application in drug delivery as well as imaging of cells is depicted in **Scheme 5.1**.

5.2. EXPERIMENTAL SECTION

5.2.1. Materials

Copper chloride ($CuCl_2$), sodium hydroxide, sodium chloride, hydrochloric acid, and sodium bromide were purchased from Merck Specialties Private Limited, India. PVP, average molecular weight: 15 kDa, PVA, average molecular weight: 30 kDa, α-lipoic acid, (3-(4, 5-dimethylthiazolyl-2)-2,5-diphenyltetrazolium bromide) (MTT), and α-cyano-4-hydroxycinnamic acid were purchased from Sigma-Aldrich, U.S.A. Cisplatin was purchased from a commercial source. Milli-Q grade water (18.2 MΩ cm) was used for all experiments.

5.2.2. Synthesis of Copper Nanoclusters (Cu NCs)

To synthesize fluorescent Cu NCs, 10.3 mg (10 mM) of α-lipoic acid was added to 5.0 mL of milli-Q water. To this insoluble mixture, 0.92 mg (5 mM) of $NaBH_4$ was added, and the mixture was stirred until the color of the medium changed from yellow to colorless, indicating the reduction of lipoic acid to dihydrolipoic acid (DHLA). Separately, 10 mg/mL of PVP was added to 3.8 mL of saturated solution of NaCl in a 15 mL culture tube, and the mixture was stirred for 2 min. To this, 0.2 mL (25 mM) of $CuCl_2$ and 3.5 mg (4 mM) of ascorbic acid were added to reduce Cu (II) chloride to colourless Cu(I) chloride solution. This was followed by the addition of 1.0 mL (10 mM) of DHLA, and the mixture was stirred for another 5 min. The final color of the mixture changed from colorless to pale yellow. The color changed immediately after the addition of DHLA. The product was centrifuged at 10000 rpm for 10 min (at 4 °C), and the precipitate was redispersed in milli-Q water and phosphate-buffered saline (PBS; pH ≈ 7.4) for further use.

5.2.3. Preparation of PVP/PVA Hydrogel

Hydrogel was prepared by cross-linking of PVA and PVP (70:30 w/w) by freeze–thaw method. For this, PVP and PVA powders were mixed together containing 7.0 mL of PVA (10 mg/mL) and 3.0 mL of PVP (10 mg/mL), and the mixture was stirred at 90 °C for 24 h. The mixture was then kept at −20 °C for 12 h, and the frozen mixture was allowed to melt at room temperature. Freeze–thaw step was repeated for several times to induce the formation of hydrogel.

5.2.4. Synthesis of Cu NCs in Hydrogel

Cu NCs were synthesized inside hydrogel *via* an *in situ* precipitation method. For the same, 1.0 mM $CuCl_2$ solution was added to 5.0 mL of hydrogel, followed by the addition of 2.6 mL of saturated solution of NaCl. The mixture was then stirred for 10 min. After this, 4.0 mM of

ascorbic acid was added, and the mixture was stirred for 5 min. Finally, 2 mM of DHLA was added to it, leading to the formation of fluorescent red color inside the hydrogel. From atomic absorption spectrophotometric (AAS) analysis, it was found that 168.5 μg mL^{-1} of Cu was present in the clusters synthesized with 1.0 mM of Cu salt precursor.

5.2.5. Loading Efficiency of Cu NC–Hydrogel Composite for Cisplatin (CP)

To determine the amount of CP loaded into the carrier, Cu NC–hydrogel composite (2.0 mL, 0.5 mg of particles, corresponding to particle loading of 21.08 μg/mL) was taken in a 15 mL beaker; CP (0.1 mL of 19.6 μg/mL) was added to it, and the mixture was incubated for 24 h under the dark. The mixture was centrifuged at 10000 rpm for 10 min (4 °C). The supernatant was collected, and UV–vis spectrum was recorded for CP at 230 nm. To quantify the amount of CP loaded in the Cu NC–hydrogel composite, UV–vis spectrum of free CP present in the supernatant (CP_f) was recorded. This was determined by the measured absorbance at 230 nm, and the concentration so obtained was subtracted from the amount of CP initially used for encapsulation (CP_i).

$$\text{Loading efficiency (\%)} = \frac{CP_i - CP_f}{CP_i} \times 100$$

5.2.6. Analysis of Cisplatin Release from Cu NC–Hydrogel Composite

To quantify the *in vitro* release of CP from Cu NC–hydrogel composite, the release profile was studied in acetate buffer (0.01 mM, pH 4.5) and PBS (0.01 mM, pH 7.4) at constant time intervals. For this, 0.5 mL of CP-loaded Cu NC–hydrogel composite was added to 1.5 mL of acetate or PBS buffer and was incubated for 48 h at 37 °C. After each time interval, that is, at 1, 3, 6, 12, 24, 36, and 48 h, the sample was centrifuged, supernatant was collected, and the amount of CP released from Cu NC–hydrogel composite was determined. The absorbance of supernatant was recorded at 230 nm, and the released CP from Cu NC–hydrogel composite in the supernatant was calculated by using the following equation.

$$\text{Cumulative release (\%)} = \frac{\text{Cisplatin released in the supernatant}}{\text{Cisplatin released in the Cu NC—hydrogel composite}} \times 100$$

5.2.7. Characterization

UV–vis spectra were recorded by Hitachi-U2900/PerkinElmer Lamda 25 spectrophotometer. Fluorescence spectra were recorded by a spectrophotometer (Fluorolog−3, Horiba Jobin Edison, NY, USA). Photostability analyses of Cu NCs were carried out in the presence of continuous irradiation of UV light in the time interval from 0.1 s to 30 min, under the

excitation wavelength at 365 nm, with emission wavelength maximum being 650 nm. JEOL JAM 2100 transmission electron microscopy (TEM) instrument operating at a maximum voltage of 200 kV was used to analyze the size of Cu NCs. Diluted Cu NC dispersion (6.0 μL) was drop-cast on to C-coated Cu grid and was kept for drying overnight at room temperature in air, before making measurements. Zeta potential and hydrodynamic diameter measurements of the samples were performed by a Malvern Zeta Size Nano ZS-90 instrument (at 25 °C) with a sample viscosity of 0.8872 mPa·s. Fourier transform infrared spectroscopy (FTIR) measurements were carried out in the scan range of 400–4000 cm^{-1} using a PerkinElmer Spectrum One instrument. The samples were prepared by drying in vacuum and then making the pellets with KBr. Applied Bio systems 4800 Plus MALDI TOF analyzer was used with α-cyano-4-hydroxycinnamic acid as the matrix for matrix-assisted laser desorption ionization time-of–flight mass spectrometric (MALDI-TOF-MS) analysis. Mass spectra were collected in linear negative mode with low mass. To prepare the matrix, α-Cyano-4-hydroxycinnamic acid (10 mg) was dissolved in a mixture of solvents (acetonitrile/trifluroacetic acid, 1:3, v/v) and water was used to make up the volume to 1.0 mL. The samples were prepared by mixing Cu NCs with matrix in different ratios (1:1, 1:2, and 1:3); the mixtures were mixed thoroughly, and from this 0.8 μL of each sample was used for spotting. Field-emission scanning electron microscopy (FESEM) analyses were carried out in a Carl Zeiss, SIGMA VP instrument. FESEM samples were prepared by drop-casting on an Al foil coated glass slide and drying overnight in air. PHI 5000 VersaProbeII scanning microprobe was used for X-ray photoelectron spectroscopy (XPS) measurements of Cu NCs. Samples were prepared in pellet form and were introduced into the XPS prechamber under ultrahigh vacuum prior to the final measurement.

5.2.8. Quantum Yield Measurements of Cu NCs

QY of Cu NCs was measured by following a standard protocol[28] using a quinine sulfate solution in 0.1 M H_2SO_4 as the reference. QY was calculated using the following equation.

$$Q_{\text{Cu NC}} = Q_{\text{ref}} \frac{m_{\text{Cu NC}}}{m_{\text{ref}}} \frac{n_{\text{Cu NC}}^2}{n_{\text{ref}}^2}$$

Where $Q_{\text{Cu NCs}}$ and Q_{ref} are QY of Cu NCs and quinine sulfate, respectively; $m_{\text{Cu NCs}}$ and m_{ref} are the slopes of the plot of integrated fluorescence intensity *vs*. absorbance of Cu NCs and quinine sulfate, respectively;

$n_{\text{Cu NCs}}$ and n_{ref} are the refractive indices of Cu NCs and the reference, respectively, in distilled water (assumed to be equal to that of water, i.e., 1.33). Emission spectra of the samples were recorded at 365 nm excitation, keeping the slit width at 2 nm.

5.2.9. Cell Culture

HeLa cells (human cervical carcinoma) were obtained from National Centre for Cell Sciences (NCCS) Pune, India, and cultured in Dulbecco's Modified Eagle's Medium (DMEM) complemented with L-glutamine (4 mM), penicillin (50 units/mL), streptomycin (50 mg/mL) which were purchased from sigma Aldrich and 10% (v/v) fetal bovine serum (FBS, purchased from PAA Laboratories, Austria), being kept in a 5% CO_2 incubator at 37 °C.

5.2.10. FESEM and TEM Analysis for Untreated and Treated Cells

For TEM and FESEM analyses, HeLa cells were seeded in a 35 mm cell culture plate and nursed for 24 h. After that the CP-loaded Cu NC–hydrogel composite was added to the cells and kept for 3 h. For the control sample, cells were incubated in media without the composite. After 3 h of incubation, cells were washed with PBS a number of times. The cells were then trypsinized, centrifuged, and fixed in glutaraldehyde solution (2%) for 10 min. The cells were dehydrated in chilled ethanol solution and finally dispersed in absolute ethanol. To prepare TEM sample, 10 μL of the cell dispersion was drop-cast on C-coated Cu grid and dried in air. For FESEM analysis, 20 μL of the sample was drop-casted onto Al foil coated glass slide, followed by drying in air.

5.2.11. Epifluorescence Microscopy

For cell imaging, 1×10^5 HeLa cells were seeded in six-well cell culture plate and grown for 24 h. HeLa cells were incubated with Cu NC–hydrogel composite or CP-loaded Cu NC–hydrogel composite for another 2 h. After 2 h of incubation, the medium was removed and the cells were washed with PBS. Finally, 1 mL of PBS was added to the plate and the cells were analyzed under epi-fluorescence microscope (Nikon ECLIPSE TS100, Tokyo) to observe the fluorescence of NCs inside the cells. For imaging, the band-pass filters used for excitation were blue (340–380 nm) and green (540/25 nm) and that for emission were green (515–555 nm) and red (655/55 nm).

5.2.12. Cell Viability Assay

Cell viability assay was carried out to quantify the viable cells after the treatment with Cu NC–hydrogel composite and CP-loaded Cu NCs–hydrogel composite. About 1×10^4 cells/well were seeded in 96-well micro plate and were incubated in DMEM media for 24 h in presence of 5 % CO_2 at 37 °C. CP-loaded Cu NC–hydrogel composite with various concentrations (3.2–15.7 μg/mL) was then added to the cells and kept for 24 h under similar conditions. After 24 h of incubation, cell viability assay was performed which was followed by MTT

assay wherein tetrazolium salt, MTT [3-(4,5-dimethylthiazol-2-yl)-2,5-diphenyltetrazolium bromide] was reduced to purple colored formazan by respiring mitochondria present in the live cells. For the reaction, 7.0 μL of MTT was added to each well of the microplate and kept for 2 h in 5 % CO_2 at 37 °C for the formation of formazan. After 2 h of incubation, the medium was removed and 60 μL of DMSO was added to each well for the development of purple color due to the formation of formazan, which absorbs at 550 nm. The control experiments were carried out in similar ways with various amounts of CP (1.5–8.4 μg/mL) and Cu NC–hydrogel composite (3.2–15.7 μg/mL). All the experiments were carried out in triplicate. The percentage of cell viability of control was taken as 100 %. The cell viability was calculated by using the standard formula.

$$\%\ \text{viable cells} = \frac{(A_{450} - A_{650})\ \text{of NC treated cells}}{(A_{450} - A_{650})\ \text{of control cells}} \times 100$$

where A_{550} and A_{690} are the absorbance at 550 and 690 nm corresponding to the formation of formazan and control medium, respectively.

5.2.13. Fluorescence-Activated Cell Sorting Analysis for Uptake of Cu NC–Hydrogel

Cellular uptake of Cu NC–hydrogel composite was studied using a flow cytometer. For the same, 1×10^5 cells were seeded in 60 mm tissue culture plate for 24 h at 37 °C. Cu NC–hydrogel composite (8.9 μg/mL) or CP-loaded Cu NC–hydrogel composite (8.9 μg/mL) was then added to the plate and incubated for 3 h under the same condition. After incubation, the residual media were removed, and the plate was washed with PBS and trypsinized. Finally, the cells were centrifuged at 650 rcf for 5 min, and the cells were redispersed in PBS. The samples were analyzed by fluorescence-activated cell sorting (FACS) calibur (BD Biosciences), and the fluorescence of Cu NCs in the composite was recorded with the Cell Quest pro in different channels such as FL2 (band-pass filter 585/42 nm) and FL3 (low pass filter, 670 nm). For each run 15,000 cells were used.

5.2.14. FACS Analysis for Reactive Oxygen Species Generation

To analyze the generation of ROS inside the cells by Cu NC–hydrogel composite and CP-loaded Cu NC–hydrogel composite, 2′,7′-dichlorofluoreceindiacetate (DCFH-DA) staining was performed, followed by the measurement using a FACS calibur instrument. DCFH-DA is a non-fluorescent dye, and it diffuses into the cell through plasma membrane and is converted to DCFH by cellular esterase activity. Non-fluorescent DCFH is converted to green fluorescent 2′,7′-dichlorofluorecein (DCF) by intracellular oxidation, which absorbs at 488 nm and emits at 530 nm. For this, 2×10^5 HeLa cells were seeded in a six-well plate for

24 h. After 24 h of incubation, CP-loaded Cu NC–hydrogel composite (8.9 μg/mL) was added, kept for 3 h. After 3 h of incubation, the residual medium was removed, and the cells were washed with PBS several times. Finally, the cells were trypsinized, redispersed in 1.0 mL of fresh DMEM in which 5.0 μL of 1.0 mM of DCFH-DA was present, and incubated for 10 min at 37 °C. After incubation, the samples were analyzed for the fluorescence of DCF by flow cytometer using Cell Quest pro in fluorescence channel for 15000 cells for each sample. An identical procedure was repeated with HeLa cells treated with CP (4.5 μg/mL) and Cu NC–hydrogel composite (8.9 μg/mL). Experiments were carried out in triplicate.

5.3. RESULTS AND DISCUSSION

Red fluorescent Cu NCs were synthesized in aqueous medium at room temperature, by a simple and fast process, involving the reduction of Cu^{2+} ions by ascorbic acid and DHLA in presence of PVP as the stabilizer. Ascorbic acid reduced Cu^{2+} to Cu^{+} ions in presence of saturated solution of NaCl, as observed by a change in color of the medium from yellow to colorless.[29] Upon addition of DHLA the color of the solution changed from yellow to colorless accompanied by a slight precipitation. UV–vis spectrum of pale yellow reaction mixture, recorded after 30 min of mixing the reactants (**Figure 5.1A**), consisted of a featureless broad background and did not exhibit any peak in 500–600 nm region, thus excluding the formation of surface plasmon resonance (SPR) active Cu NPs. The medium appeared fluorescent red under UV lamp (**Figure 5.1B**), indicating the formation of Cu NCs. Fluorescence spectrum of the yellow product in water exhibited two emission peaks centered at 435 and 650 nm, when excited at either 365 or 405 nm (**Figure 5.1B**). The low-energy excitation peak (at 405 nm) of Cu NCs might originate from the ligand-to-metal charge transfer (LMCT), while the high-energy excitation peak (at 365 nm) might be originated from DHLA ligand through intraligand as well as metal-perturbed intraligand transition.[30,31] On the other hand, dual emission peaks of metal NCs (stabilized by the ligand) may arise either from the interband electronic transition or intraband transition.[20] However, according to Yam *et al.*, high-energy emission peak appears due to the metal-perturbed intraligand phosphorescence, whereas the low-energy emission peak may be due to the LMCT.[30,31] Also, it is known that the emission properties are dependent on size of clusters.[19] The dual emission of Cu NCs is originated either from the same-sized clusters as described above or from the different sizes of clusters. As our results indicate that two emissions are independent of the excitation wavelength, emissions may be coming from the same-sized cluster. To examine whether LMCT from the triplet excited state of Cu NCs was occurring in our system, we carried out time-correlated single photon counting fluorescent experiments. A long radiative

lifetime of 0.8 μs in these experiments (**Figure 5.1C**) supported that the emission had its origin in the excited triplet state of a ligand and through the charge transfer to metal.[20,23,30,31]

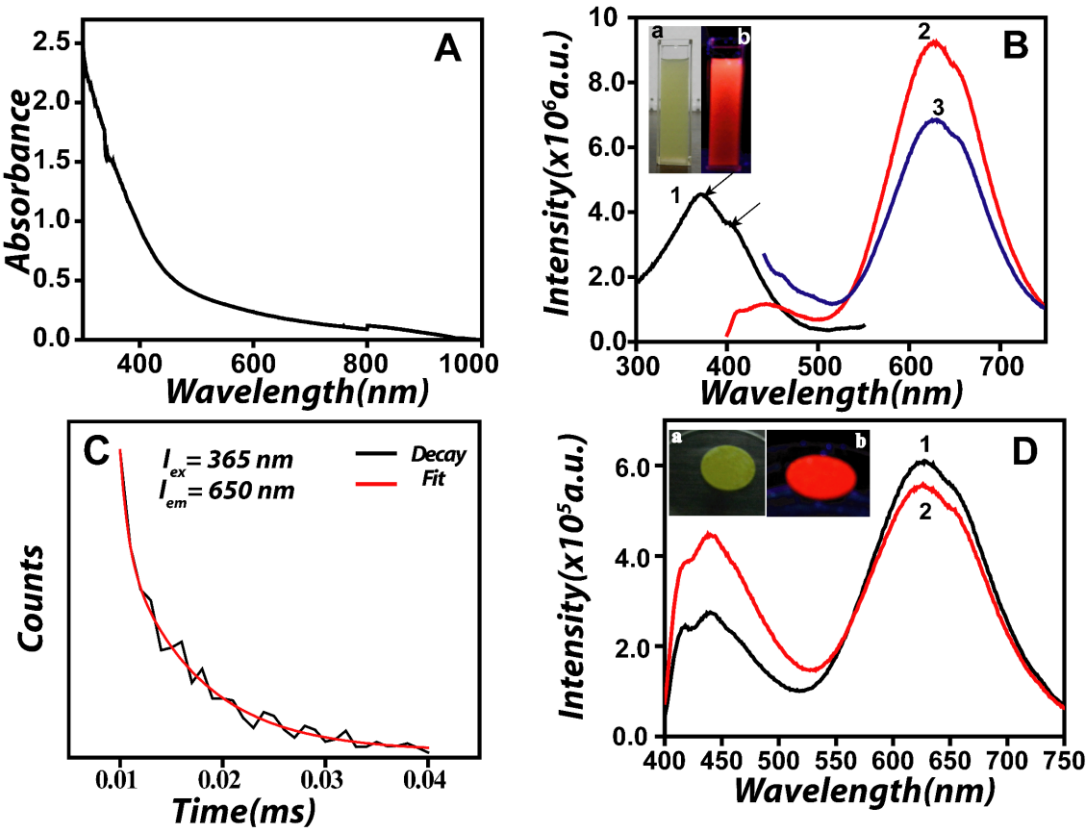

Figure 5.1 (**A**) UV-visible spectrum of as synthesized Cu NCs formed by the reaction of Cu^{2+} with dihydrolipoic acid in presence of PVP. (**B**) Excitation spectrum of Cu NCs (Curve 1) with emission maximum at 640 nm. Emission spectra of Cu NCs with λ_{ex} = 365 nm (Curve 2) and λ_{ex} = 400 nm (Curve 3). Arrows in curve 1 shows the excitation maxima at 365 nm and 400 nm, respectively. Inset: photographs of dispersions of Cu NCs under (a) daylight and (b) UV light. (**C**) Time- dependent change in emission of Cu NCs, during their synthesis, as probed by emission spectra with λ_{ex} =365 nm. (**D**) Fluorescence spectrum of as-prepared Cu NCs in solid form (1) and the same after one month (2). Inset: photographs of Cu NCs in solid form under (**a**) daylight and (**b**) UV light.

Importantly, the emission spectrum was similar to that reported in the literature for Cu NCs, thus indicating the formation of Cu NCs. That the fluorescent spectrum did not change after 20 min of formation of Cu NCs suggests that their formation was complete within a few min (**Figure 5.2**). Interestingly, as-prepared Cu NCs could be stored for a long time in solid form. Centrifugation of the product resulted in the precipitate that was dried and stored in the form of a pellet, which appeared bright fluorescent red under an UV lamp. Fluorescence spectrum of the pellet with a peak at 635 nm was nearly the same as that of the product from the medium (**Figure 5.1D**). In addition, fluorescence spectrum of the solid recorded after one month showed almost no change, thus indicating the superior stability of the solid Cu NCs (**Figure 5.1D**, inset). Importantly, solid Cu NCs also appeared bright fluorescent red under the UV lamp. The prime challenge while working with Cu NCs is their instability under

ambient conditions, due to the ease of oxidization of Cu(0) to Cu^{2+} (E_0 = 0.34 V) in contrast to Ag (E_0= 0.80 V) or Au (E_0 = 1.50 V). Thus, by this method not only were fluorescent Cu NCs formed but also were easy to store in the solid form without using any inert atmosphere. To analyze the role of all reagents in formation and stability of Cu NCs in aqueous medium, several control experiments were performed (**Figure 5.3A**).

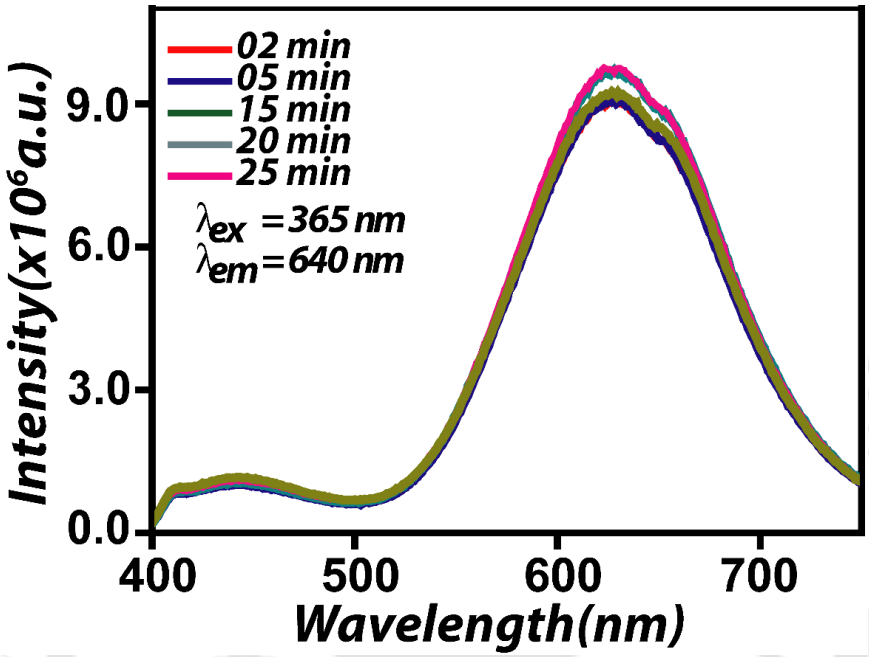

Figure 5.2 Time dependent change in emission of Cu NCs, during their synthesis, as probed by emission spectra with λ_{ex} =365 nm.

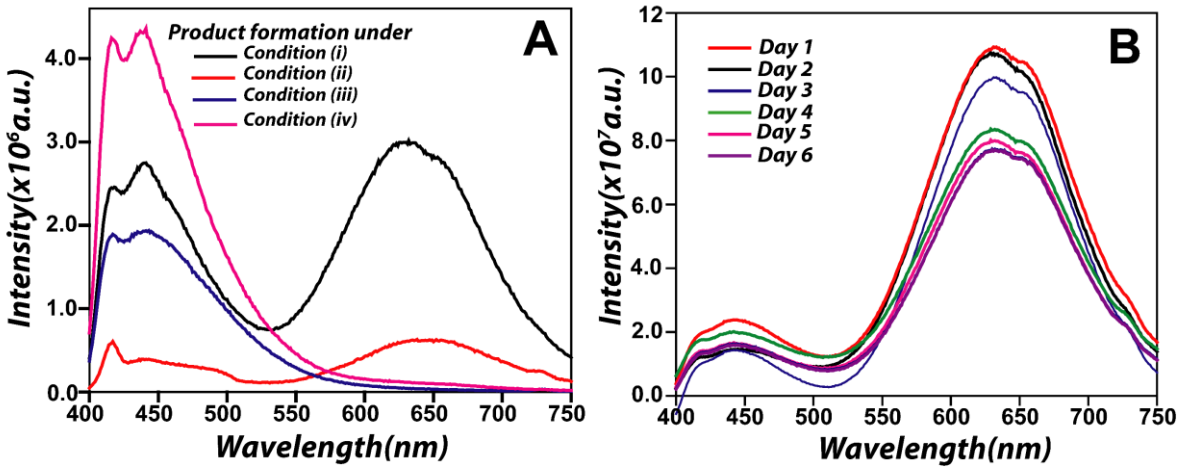

Figure 5.3 (**A**) Optimization of reaction condition for the synthesis of Cu NCs, formed from the reaction between Cu^{2+} and dihydrolipoic acid (DHLA), in presence of PVP. Fluorescence spectra of the product synthesised (i) from $CuCl_2$, PVP, NaCl, ascorbic acid and DHLA; (ii) from $CuCl_2$, NaCl, ascorbic acid and DHLA; (iii) from $CuCl_2$, PVP, ascorbic acid and DHLA and (iv) from $CuCl_2$, PVP, NaCl and DHLA. (**B**) Stability of synthesized Cu NCs in the presence of PVP as studied by fluorescence spectroscopy. The change in the fluorescence emission intensity indicated the instability of Cu NCs beyond 3 d.

The emission results in **Figure 5.3A** indicate that in presence of PVP, not only were the NCs stable but also had higher emission intensity. It is reported that PVP stabilizes NCs through weak coordination bonds.[32] The excess chloride ion present in saturated solution of NaCl helped in forming Cu(I) chloride, which is then easily reduced to Cu(0) in presence of ascorbic acid.[29] It was also observed that Cu NCs synthesized in aqueous medium using PVP as a stabilizer were stable as long as 3 d; the fluorescent intensity decreased quickly with time, indicating that the Cu NCs became unstable in the long run (**Figure 5.3B**).

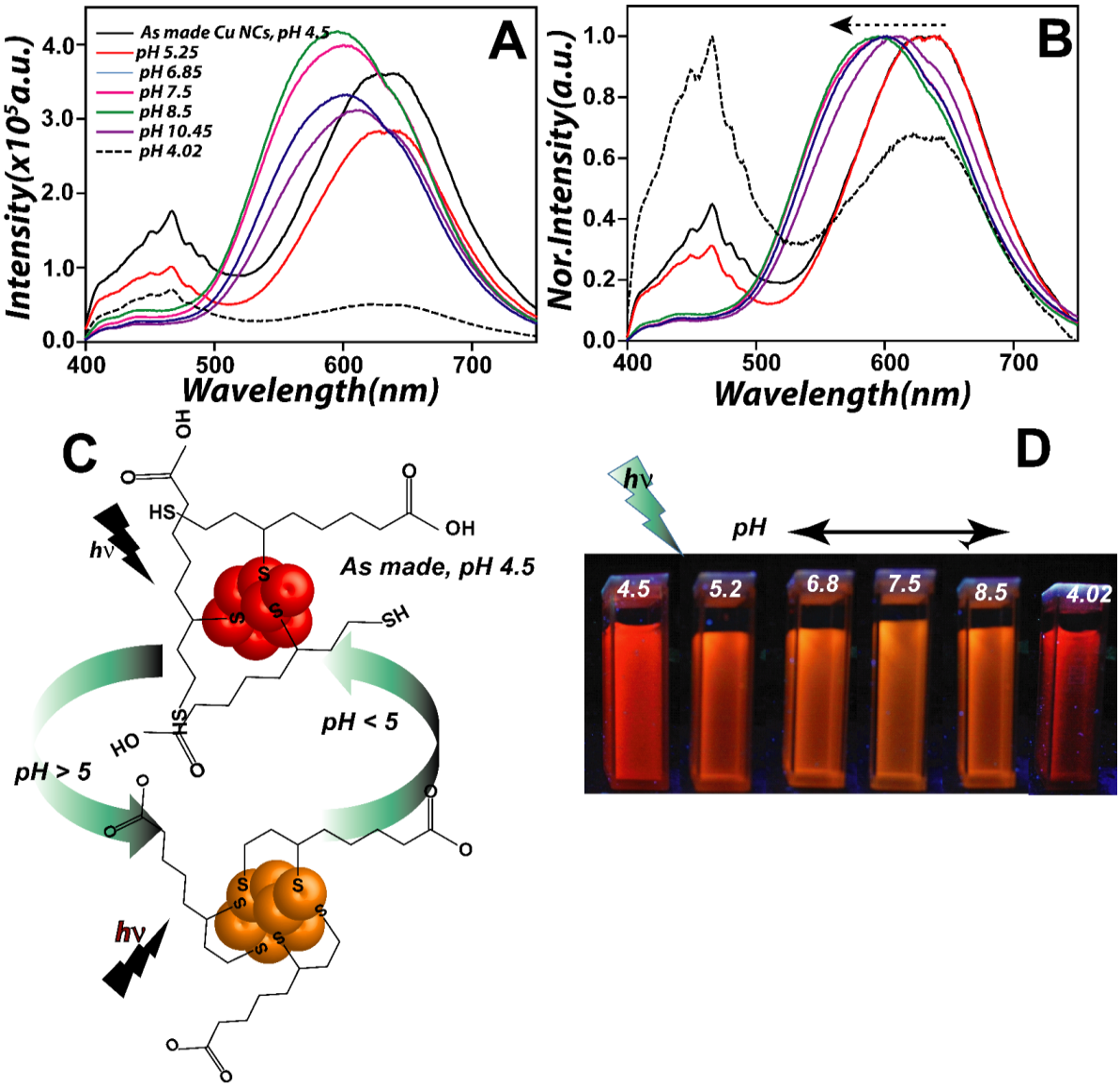

Figure 5.4 (A) Fluorescence spectra of as-synthesized Cu NC dispersions in the pH range 4.5–11. (**B**) Normalized fluorescence spectra of as-synthesized Cu NCs in the pH range 4.5–11. The arrows indicate the shift of wavelength in the pH range 4.5–11. (**C**) Schematic representation of the chemistry of the reversibility of fluorescence color from red to orange (and emission) with the change in pH. (**D**) Photographs of Cu NCs under UV lamp (λ_{ex}= 365 nm) in the pH range of 4.5 to 8.5.

Further investigation indicated that the emission spectrum (and thus the fluorescent color) of the dispersion of as-synthesized Cu NCs in water could be tuned reversibly by changing the pH of the medium. Cu NCs synthesized at pH 4.5 emitted a red fluorescence at

650 nm (λ_{ex} = 365 nm). It is important to mention here that there was slight precipitation from the dispersion when kept at pH 4.5. This could be due to the protonation of carboxylic acid (−COOH) group and one of the thiol (−SH) groups of DHLA, while the second −SH group in the deprotonated state could be bonded to the NC. When the pH was increased clear dispersion was observed (at pH 6.5) and it remained as such up to a pH of 11.0. The change in pH from 4.5 to 11.0 was accompanied by an increase in fluorescence intensity (**Figure 5.4A**), which could be attributed to the deprotonation of the –COOH as well as the remaining –SH group of DHLA. Accompanying the increase in fluorescence intensity, emission maximum had also shifted from 650 to 590 nm (at pH 6.5 and beyond, **Figure 5.4B**), while the color of the dispersion changed from fluorescent red to orange (**Figure 5.4C, D**). The change in color and emission maximum of Cu NCs depend on the surface anchoring groups of NCs. This could be attributed to the charge transfer from the ligand-to-metal core of NCs (Cu atoms) through Cu–S bonds.[30,31,33] Importantly, the fluorescence emission spectrum could be reversibly switched between pH 4.5 and 11.0 (**Figure 5.4C,D**).

The fluorescence QY at different pH values of the medium was determined using quinine sulfate (having QY of 54%) as the standard. The QY was found to be 7.2% at pH 4.5, whereas it was 10.8% at pH 8.5 (**Figure 5.5**). The results indicated not only the brightly emissive nature of Cu NCs but also the pH tuneability of emission, which may be useful for practical applications such as biomarker signal probes in diagnostic applications for cancer and other diseases and codelivery of nucleic acid and therapeutic for real time tracking.

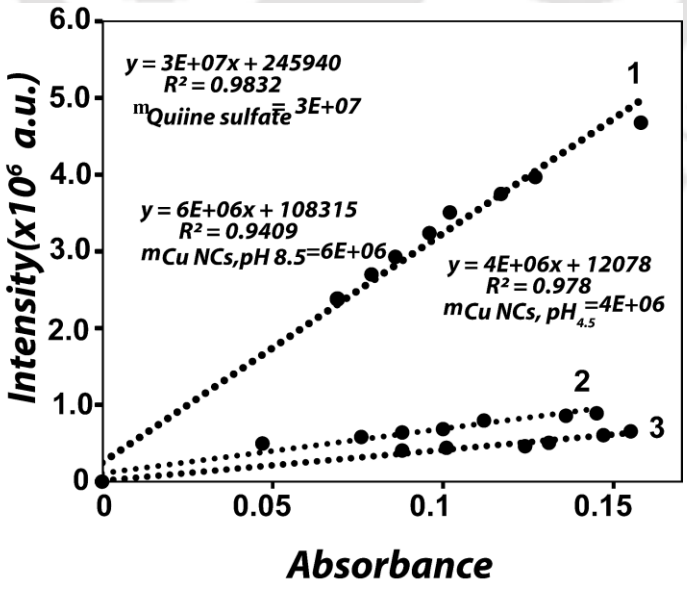

Figure 5.5 Quantum yield determination of as-synthesized Cu NCs with respect to quinine sulfate as the reference. Line 1 represents the data for quinine sulfate, Line 2 represents the data for as-synthesized Cu NCs at pH 8.5 and Line 3 represents the data for Cu NCs at pH 4.5.

TEM analysis of as-synthesized Cu NCs revealed the presence of small particles with diameter 1.9 ± 0.6 nm (**Figure 5.6B**). Agglomerated structures of NCs (diameter >2 nm) were also observed. Literature reports suggest the enhancement of fluorescence QY due to agglomeration,[22] which may well be the case herein. Further, high-resolution TEM (HRTEM) analysis did not reveal the clear lattice fringes for smaller particles; however, for some of the bigger particles (diameter >2 nm) fringes with lattice spacing of 0.28 nm, corresponding to the (110) plane of CuO [**Figure 5.6A**, inset (i) and (ii)] could be observed. It could be that some nanoscale particles with larger sizes were formed in the medium; however, their concentration was sufficiently low in the medium to give rise to any SPR band. Additionally, a single band obtained in 1.2% agarose gel electrophoresis suggested monodispersed nature of the synthesized Cu NCs (**Figure 5.7**).

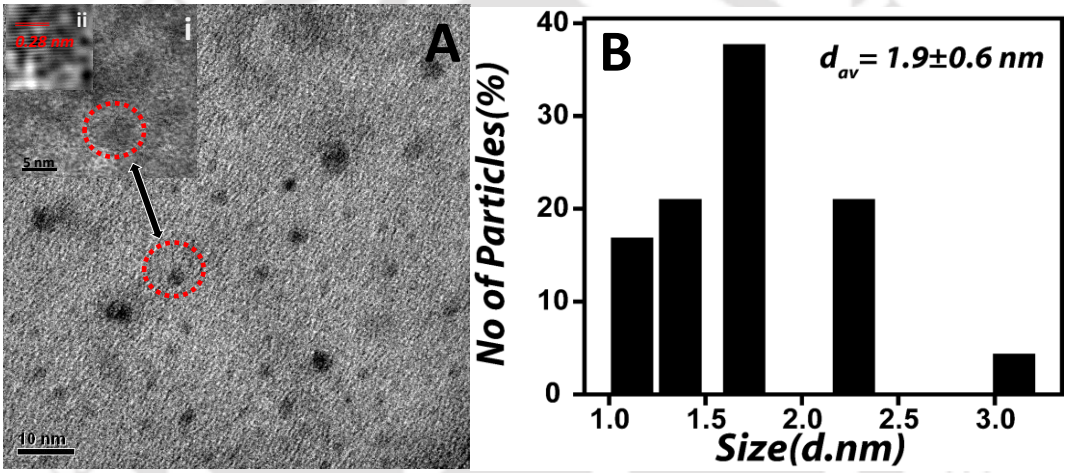

Figure 5.6 (**A**) TEM image of as synthesized Cu NCs (Scale bar is 10 nm). Inset (i) is the HRTEM images of a large Cu nanoparticle with a lattice spacing of 0.28 nm, which matches with (110) plane of CuO. (**B**) Particle size distribution histogram of Cu NCs as obtained from TEM measurement (**Figure 5.6A**).

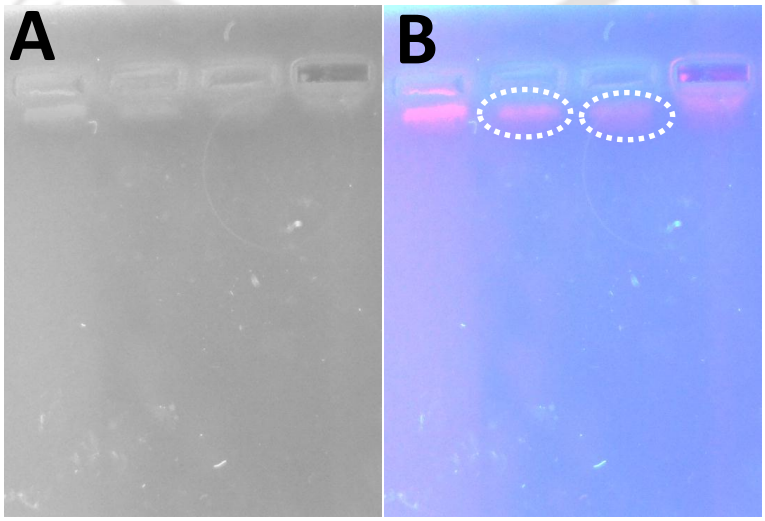

Figure 5.7 1.2 % agarose gel electrophoresis to confirm the sizes of Cu NCs (**A**) Day light (**B**) under UV light. The dotted white circles confirmed the presence of single band.

FTIR spectral measurement (**Figure 5.8**) revealed that the characteristic peak of S–H stretch of DHLA at 2585 cm^{-1} was absent in the composite containing Cu NCs following their formation. The results indicated the possibility of stabilization of NCs *via* Cu–S–R bonding.

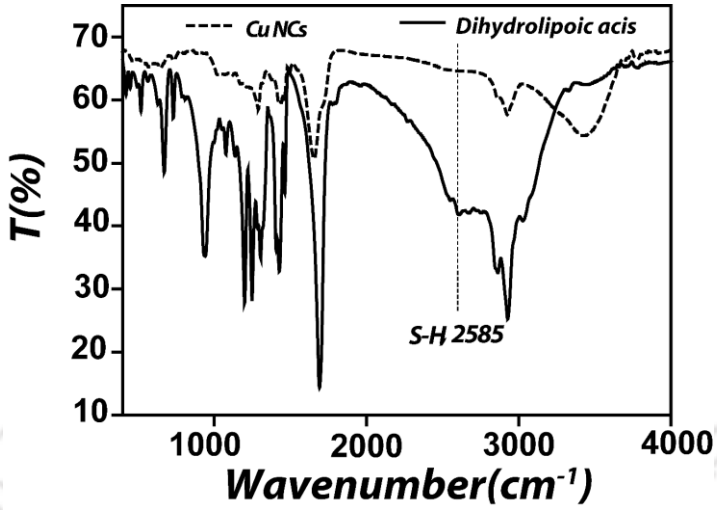

Figure 5.8 FTIR spectra of dihydrolipoic avid (solid line) and the product containing Cu NCs and other components (dotted line).

Among the noble metals, Cu has the highest oxidation tendency owing to its lowest reduction potential, and this is an important challenge in synthesizing stable NCs. It is therefore imperative to determine the oxidation state of Cu in the composite. XPS measurements were thus carried out to probe the oxidation state of Cu in NCs (**Figure 5.9**). XPS spectrum revealed two peaks at 932.0 and 951.8 eV, which were assigned to Cu $2p_{3/2}$ and Cu $2p_{1/2}$ states of Cu(0), as consistent with the literature values.[19,20] Importantly, the absence of any peak at 942.0 eV indicated the absence of Cu^{2+} in Cu NCs. Further XPS probe of Cu NCs indicated the presence of C, N, O, and S (**Figure 5.10**). Notably, a small difference (~0.1 eV) in binding energy of Cu(0) and Cu(I) is difficult to distinguish in the XPS spectrum. Therefore, the valence state of Cu in our NCs may be 0 or +1, and possibly some of the surface Cu atoms are partially oxidized. The binding energy of S 2p was found to be 163.0 eV, which indicated the possible adsorption of S on the surface of Cu NCs by Cu–S bonding.[34] The result is also consistent with the FTIR spectrum (**Figure 5.8**).

The atomic composition of Cu NCs was determined by MALDI-TOF MS spectrometric analysis in negative mode, using α-cyano-4-hydroxycinnamic acid as a matrix. Four prominent peaks (**Figure 5.11A**) appeared at *m*/*z* 1080, 1103, 1126, and 1148, which can be attributed to $[Cu_4L_4 - 6H^+]^{6-}$, $[Cu_4L_4 - 6H^+ + Na^+]^{5-}$, $[Cu_4L_4 - 6H^+ + 2Na^+]^{4-}$ and $[Cu_4L_4 - 6H^+ + 3Na^+]^{3-}$, respectively, where L is $C_8H_{16}O_2S_2$. The results indicated the formation of monodispersed Cu NCs with molecular formula of Cu_4. In addition, MALDI-

TOF MS analysis of Cu NCs were carried out at different pH (i.e., 6.5, 8.5, and 10.5), which confirmed that the size of Cu NCs remained same from pH acidic to highly basic medium (**Figure 5.11B–D**). Also, the reversible nature of the observation suggests that the sizes of the emitting particles were not altered.

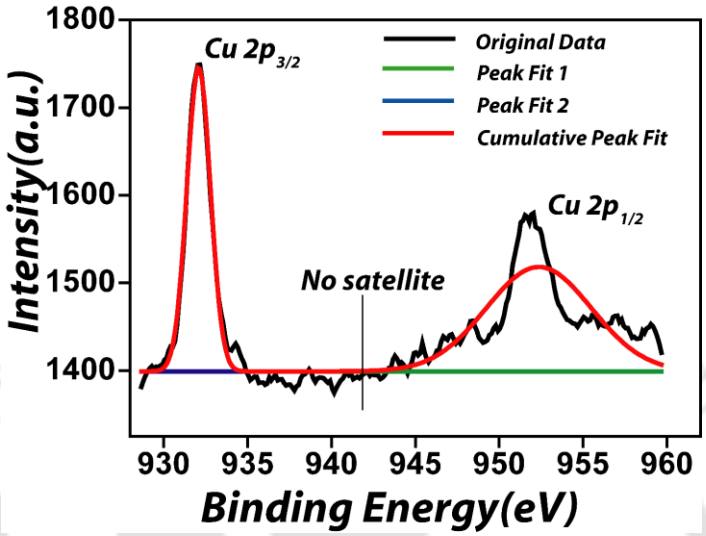

Figure 5.9 X-ray photoelectron spectrum representing the Cu 2p signal of as prepared Cu NCs. The absence of satellite peak at 942 eV indicated the absence of Cu^{2+} in Cu NCs samples.

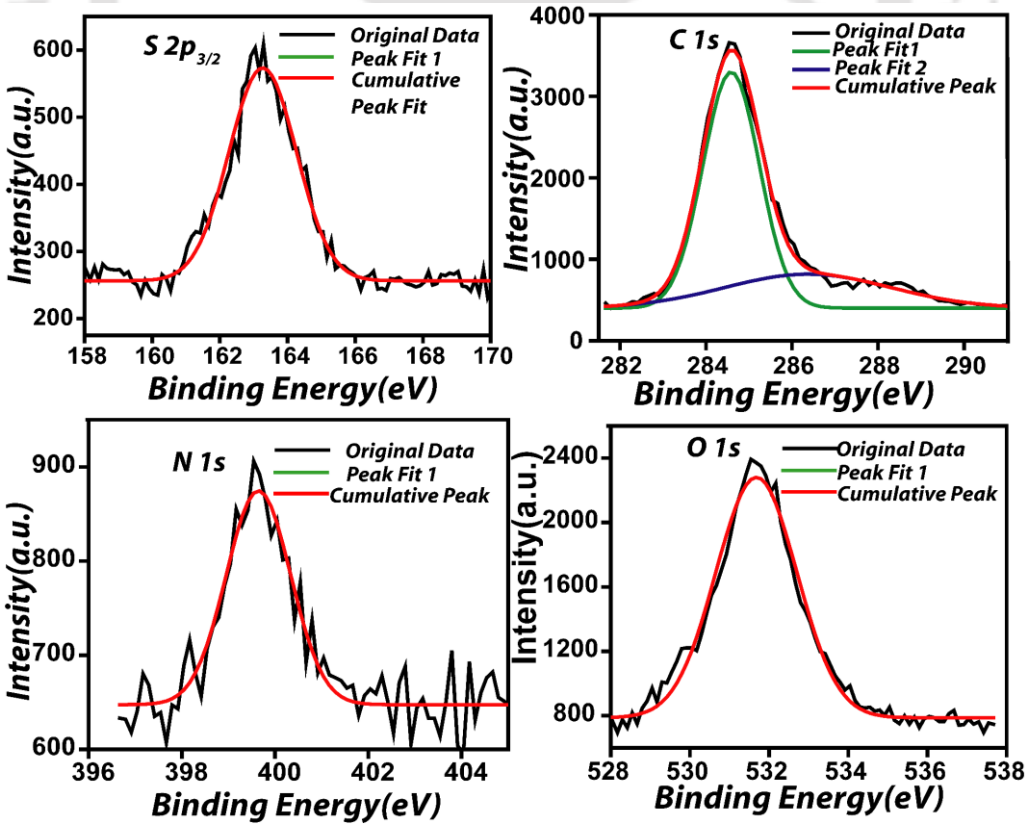

Figure 5.10 X-ray photoelectron spectroscopy analysis for the detection of elements present in the product containing Cu NCs: (i) Sulfur (**S**), (ii) carbon (**C**), (iii) nitrogen (**N**) and (iv) oxygen (**O**).

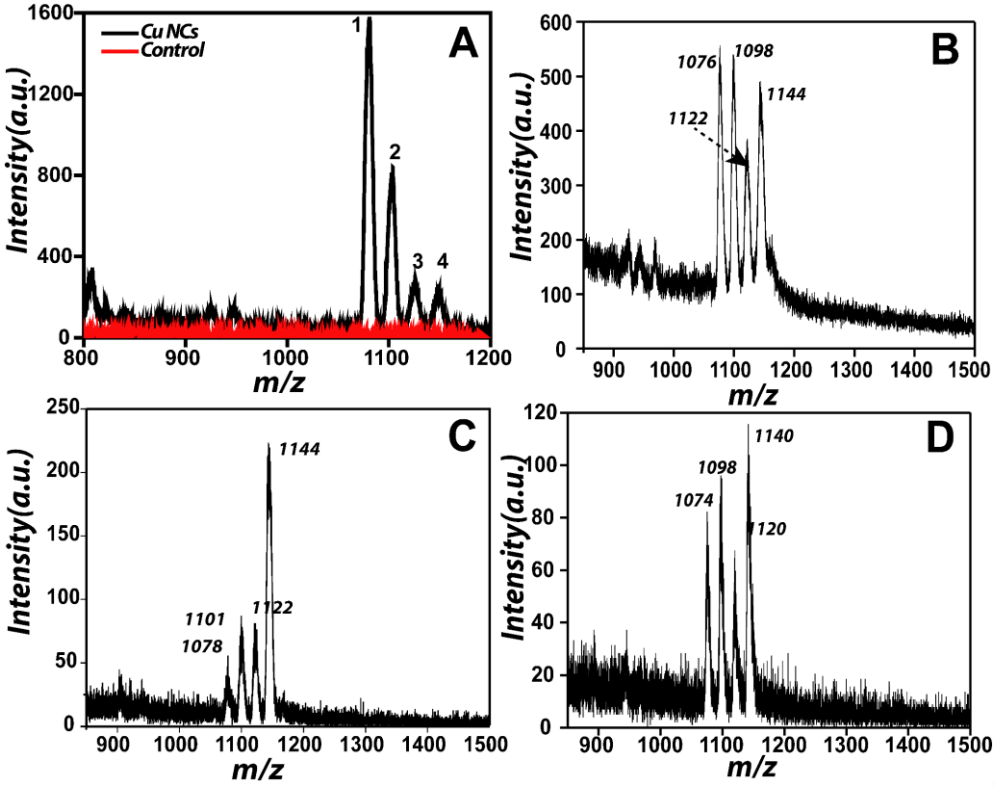

Figure 5.11 MALDI-TOF MS spectra of (**A**) Cu NCs (in black) and control containing DHLA and PVP (in red) with the assignment of characteristics peaks due to $[Cu_4L_4 - 6H^+]^{6-}$, $[Cu_4L_4 - 6H^+ + Na^+]^{5-}$, $[Cu_4L_4 - 6H^+ + 2Na^+]^{4-}$ and $[Cu_4L_4 - 6H^+ + 3Na^+]^{3-}$, and of Cu NCs at different pH values : (**B**) 6.5, (**C**) 8.5 and (**D**) 10.5 with the assignment of the characteristics peaks in the range of m/z 1070-1145

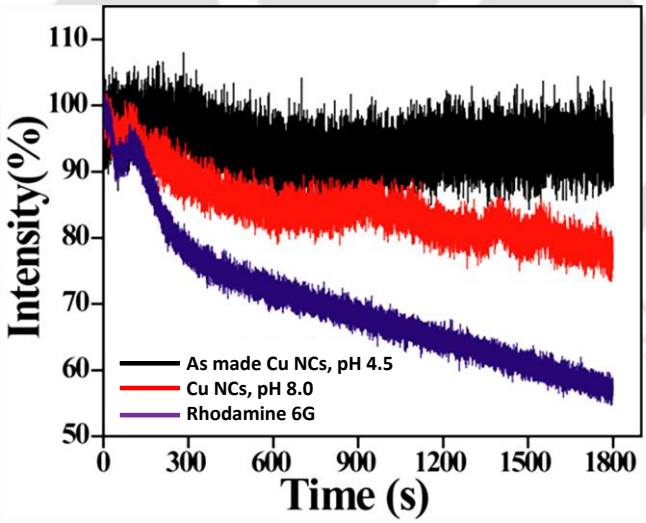

Figure 5.12 Representative time trace of fluorescence intensity decrease of product containing Cu NCs recorded at two different pH values of the medium (black and red traces), in comparison to organic dye (Rhodamine 6G) recorded under same conditions.

Furthermore, the photostability of Cu NCs revealed the importance of NCs for bioimaging and cell labeling applications. The fluorescence intensity of Cu NCs in acidic pH remained unaltered under continuous irradiation of UV light in the time interval of 0.1 s, whereas in basic pH the intensity decreased slightly; however under both conditions the decrease was

much less in comparison to organic dye rhodamine 6G (**Figure 5.12**). The fluorescence intensity decrease rate (F/F_0) of Cu NCs measured at the maxima in acidic pH (pH 4.5) and basic pH (pH 8) were found to be 0.037% and 0.24%, respectively, whereas in case of rhodamine 6G, the rate was found to be 0.43%. The resistance to photobleaching and their stability in solid form make the Cu NCs strong candidates for biological applications.

Additionally, zeta potential measurements were performed at different pH of the medium to find out the surface charge of Cu NCs. As-prepared Cu NCs stabilized by PVP were found to have a zeta potential of −4.09 mV (at pH 4.5), the value changed to −15.8 mV at pH 9.0 (**Table 5.1**). It is plausible that at acidic pH, the NCs were stabilized by the $-NH_3^+$ of PVP and −COOH group of DHLA, whereas in basic medium the stabilizing groups are $-NH_2$ and −COO–, thus changing the emission behaviour of the NCs.

Table 5.1 Zeta potential determination of Cu NCs at different pH values of the medium.

Sample	pH	Zeta Potential (mV)
As synthesized product Cu NCs	4.2	−4.02±0.02
Cu NCs	6.5	−7.72±0.01
Cu NCs	7.4	−12.5±0.30
Cu NCs	8.5	−15.8±0.08
Cu NC-hydrogel composite	7.4	−12.5±0.28
Cisplatin loaded Cu NC-hydrogel composite	7.4	−10.5±0.35

The bright fluorescence, highly photostable and small size of Cu NCs could make them ideal candidates for biological application such as cellular labeling and bioimaging. For example, their fluorescence properties could be used for tracking the drug delivery in cells, which could have a competitive edge over the popular but toxic semiconductor quantum dots. To test the feasibility of their use, Cu NCs were synthesized in PVP/PVA hydrogel, and the composite was used as a nanocarrier for drug delivery in HeLa cells. PVP and PVA are hydrophilic and biodegradable polymers approved by the Food and Drug Administration (FDA) for medical applications. These polymers have been extensively used for synthesizing hydrogels for drug delivery and other pharmaceutical applications.[35,36] Hydrogels are three-dimensional network structures with high amount of water content, which are ideal for loading water-soluble drugs/molecules. Here, PVP/PVA hydrogel was synthesized by a method based on freeze–thaw cycle and such formation was confirmed by TEM and FTIR analyses. TEM measurement indicated the spherical nature of the hydrogel particles with average diameter of 155 ± 32 nm (**Figure 5.13A**). FTIR spectra of PVA, PVP, and hydrogel

are shown in **Figure 5.13B**. Broad band at 3420 cm^{-1} represents the presence of hydrogen-bonded structures and thus hydrophilic nature of hydrogel. PVA showed bands at 3429 and 1088 cm^{-1} corresponding to O–H group and crystalline structure of PVA, respectively; whereas PVP showed a sharp band at 1657 cm^{-1}, which is due to −C═O stretching vibration. The formation of the hydrogel through physical cross-linking was indicated by the shift of −C═O stretching frequency to 1643 cm^{-1}; whereas the peak due to the crystalline structure of PVA shifted to 1099 cm^{-1}, indicating the change in the structure.[37] The transition temperature of polymer hydrogel was analysed using differential scanning calorimetry (DSC). DSC thermogram of the hydrogel showed a single glass transition temperature (**Figure 5.13C**) at 80 °C, which indicated the interaction between two constituent polymers.[38]

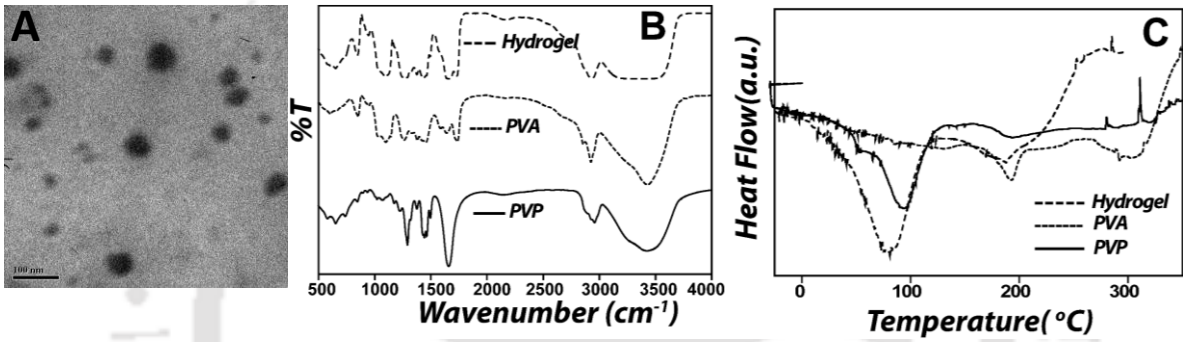

Figure 5.13 (**A**) TEM image of hydrogel indicating the formation of PVP/PVA hydrogel nanoparticle (Scale bar is 50 nm). (**B**) FTIR spectra and (**C**) DSC thermogram of hydrogel, PVP and PVA.

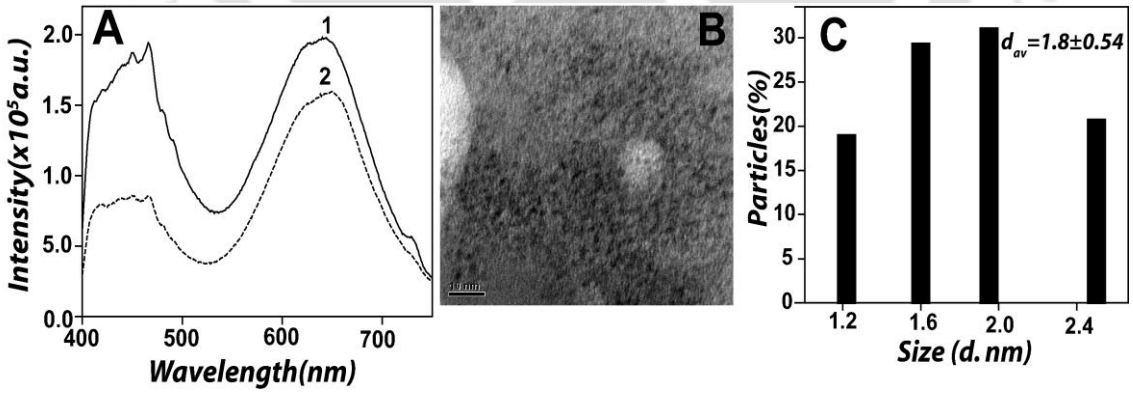

Figure 5.14 (**A**) Fluorescence spectra of Cu NCs (**1**) and Cu NC-hydrogel composite (**2**). (**B**) TEM image of Cu NCs in the hydrogel. Scale bar is 10 nm. (**C**) Size distribution histogram of Cu NCs in hydrogel shown in (**B**).

An important challenge is the synthesis of Cu NCs with intact property (as in the above) in the hydrogel. Interestingly, Cu NCs could be synthesized in hydrogels without much change of the reaction condition. The optical properties of the NCs in the hydrogel were nearly the same as those in PVP. For example, the emission spectrum of Cu NC–

hydrogel composite comprised of a peak at 640 nm with an excitation maximum at 365 nm (**Figure 5.14A**). Importantly, the average size of the NCs in PVP/PVA hydrogel was found to be 1.8 ± 0.5 nm, which is close to the size of the particles generated in PVP polymer (**Figure 5.14B, C**).

The brightly fluorescent Cu NCs in the hydrogel were further used to investigate the therapeutic and imaging potential of the composite. The composite was used to probe CP delivery to cancer cells and to find the synergy of action of the two (Cu NCs and CP), if any. In addition to optical properties for imaging application, the size of composite particle is important for cellular uptake. Hydrodynamic diameter of hydrogel (only) probed by dynamic light scattering (DLS) study was found to be 220 nm; while for Cu NC–hydrogel composite it was found to be 284 nm (**Table 5.2**). On addition of CP, the average hydrodynamic diameter of Cu NC–hydrogel composite was found to increase up to 345 nm (**Figure 5.15**). The size, although appears to be on the higher side of permissible limit for *in vivo* applications, still it is known to be effective for drug delivery to cancer cells. It is well established that in tumor tissue the presence of leaky vasculature of blood vessels, which have larger pores in contrast to healthy tissue permits enhanced permeation and retention (EPR) of larger particles. The permeability of nanoscale particles of sizes up to 400 nm has been reported. Therefore, CP-loaded Cu NC–hydrogel with higher in size could be internalized by cancer tissues.[39]

The encapsulation of CP into the Cu NC–hydrogel composite was confirmed by FTIR and fluorescence spectroscopy. The sharp N–H and Pt–N stretching bands for CP were present at 3444 and 519 cm^{-1}, respectively, along with the bands of hydrogel at 1647 cm^{-1} and 1076 cm^{-1} (**Figure 5.16A**). Fluorescence spectroscopic investigation supported the interaction between the composite and CP. For example, when CP was added to the composite, the fluorescence intensity of Cu NCs decreased, confirming interaction between them (**Figure 5.16B**). Interaction between the Cu NCs and CP inside the hydrogel was further confirmed by ^{1}H NMR spectroscopy (**Figure 5.17)**. The characteristic peaks of –COOH of the ligand-stabilized Cu NCs was found at 11.8 ppm, whereas the peak vanished when the NCs interacted with CP along with the appearance of the peak at 4.137 ppm due to $–NH_3$ group. This indicated that Cu NCs were bound to CP through carboxylic groups,[40,41] leading to loss of its luminescence. The results also indicated that CP effectively diffused through the hydrogel containing NCs. Also, interaction through the $–NH_3$ group of CP suggest the stability of the clusters and preservation of activity of the drug in the medium. The loading of CP to the composite was further supported by zeta potential measurements. The zeta potentials of Cu NC–hydrogel composite and CP-loaded Cu NC–hydrogel composite, both measured at pH 7.4, were found to be −12.5 and −10.5 mV, respectively.

The change of zeta potential indicated the loading of drug into the Cu NC–hydrogel composite. Additionally, stability of the composite is also important for its practical usages. The stability of the composite was investigated by the fluorescence spectroscopy. The results, shown in **Figure 5.18**, indicated that with time the composite remained reasonably stable, with 50% decrease in fluorescence intensity in 48 h, at physiological pH of 7.4.

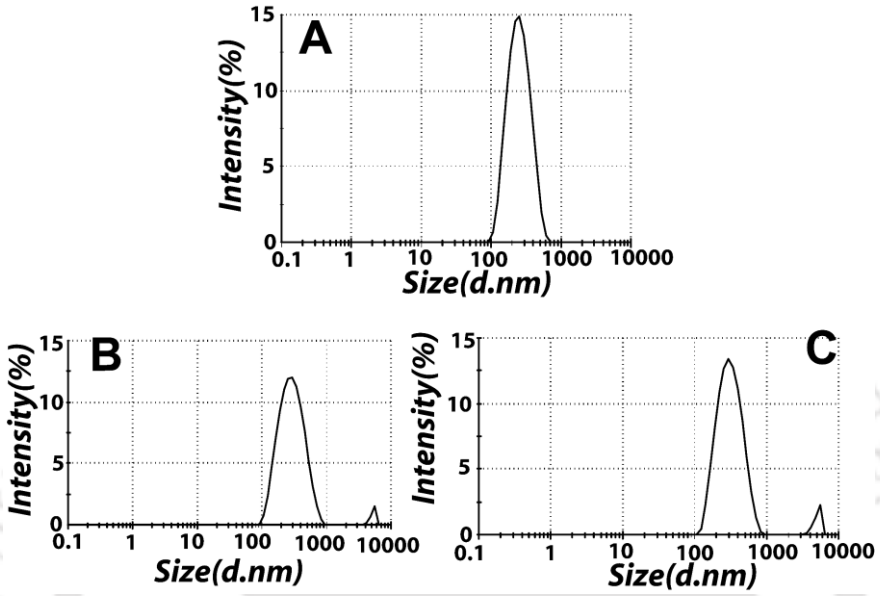

Figure 5.15 DLS-based particle size distribution curves of (**A**) hydrogel, (**B**) Cu NC – hydrogel composite and (**C**) cisplatin loaded Cu NC –hydrogel composite.

Table 5.2 DLS-based particle size determination.

Sample	Size (nm)
Hydrogel	220
Cu NC–hydrogel composite	284
Cisplatin loaded Cu NC–hydrogel composite	345

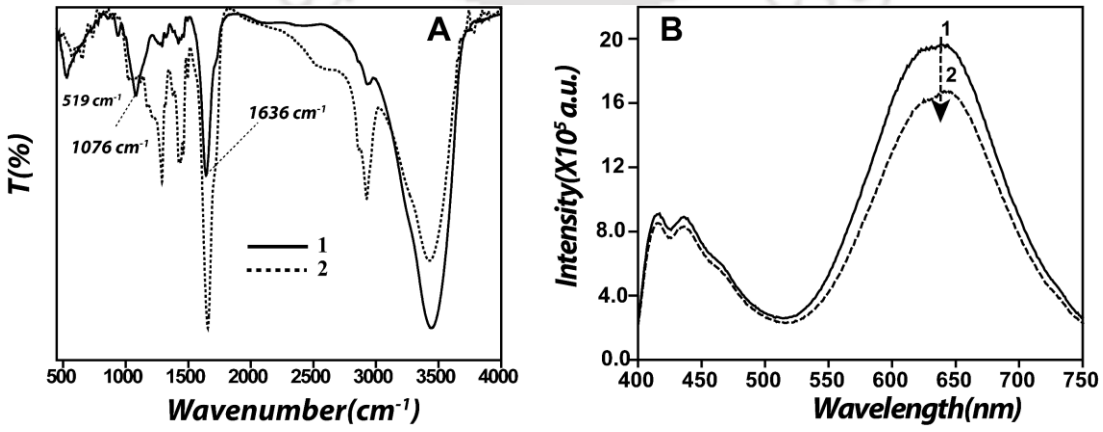

Figure 5.16 (**A**) FTIR spectra of (1) Cu NC-hydrogel composite and (2) cisplatin loaded Cu NC-hydrogel composite. (**B**) Fluorescence spectra of (1) Cu NC-hydrogel composite and (2) cisplatin loaded Cu NC-hydrogel composite. The excitation wavelength was kept at 365 nm.

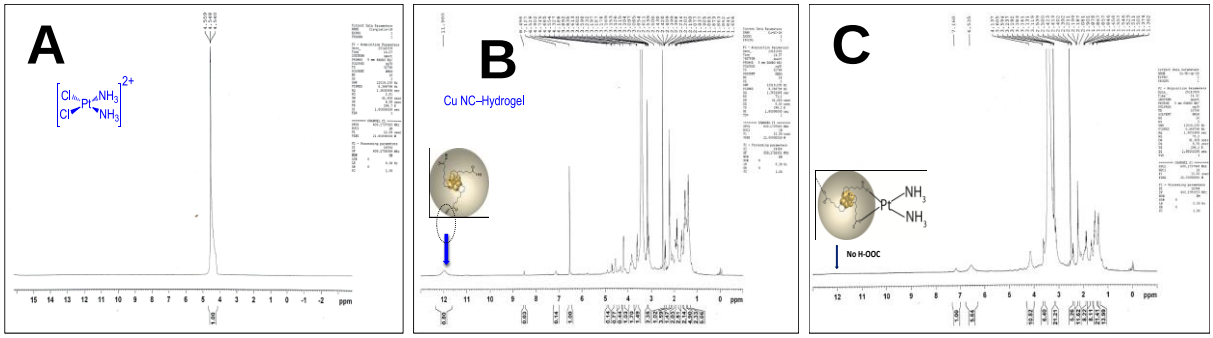

Figure 5.17 ^{1}H-NMR spectra of (A) cisplatin (B) hydrogel-Cu NC composite and (C) cisplatin loaded hydrogel-Cu NC composite.

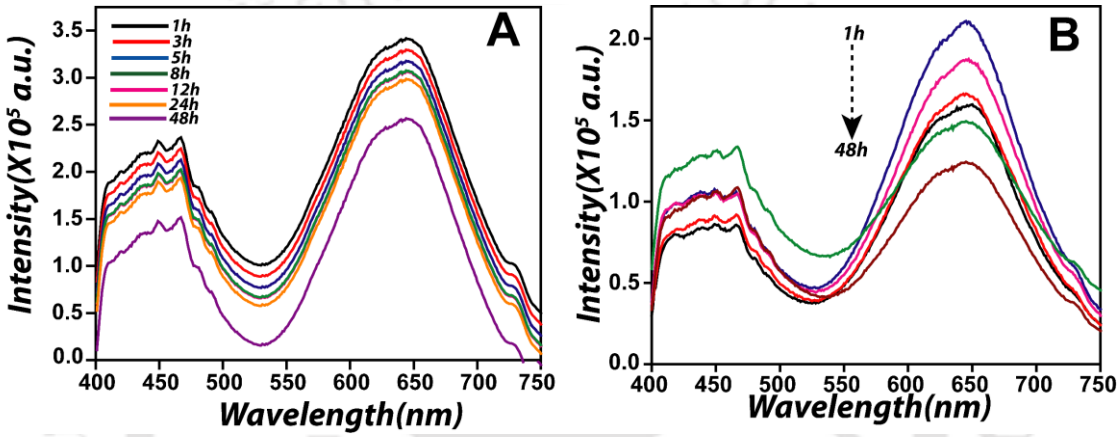

Figure 5.18 Stability test by fluorescence spectroscopy. Time dependent fluorescence spectra of (**A**) Cu NC-hydrogel composite and (**B**) cisplatin loaded Cu NC-hydrogel composite, measured for 48 h.

For microscopic imaging, HeLa cells were incubated with Cu NC–hydrogel composite (2 h) in Dulbecco's Modified Eagle's Medium (DMEM). Following this, the medium was removed; cells were washed with PBS and finally observed under fluorescence microscope. As shown in **Figure 5.19**, brightly fluorescent cells with yellow and red colors could be observed. The colors correspond to emission from Cu NCs viewed using two different filters (red and green respectively). The results indicated that the composite hydrogel could potentially be used for imaging of cells, in conjunction with the delivery of drugs.

One of the important criteria of an efficient nanocarrier is its ability to encapsulate high concentration of drug molecules in each carrier, essentially determining the loading efficiency. The loading efficiency of CP in Cu NC–hydrogel composite was determined using UV–vis spectroscopy by following absorption at 230 nm (due to the drug). The results indicated that Cu NC–hydrogel composite could be loaded with a maximum of ~78% of CP (with 19.6 μg/mL concentration in the solution containing 1.0 mL of Cu NC–hydrogel composite). CP is highly soluble in water. It is plausible that the apparent high efficiency

could be due to the loading of the molecules on the surface as well as inside the hydrogel particle and the strong bonding between −COOH of Cu NCs (being embedded in the polymer) and CP. This could be due to the hydrophilic nature of the hydrogel with extensive presence of hydrogen bonded interpenetrating network.[42] Before checking the anticancer activity of the drug-loaded composite, *in vitro* release kinetics was pursued using UV–vis spectroscopy. The time-dependent cumulative release profiles are shown in **Figure 5.20**, which revealed that 75% of CP was released at pH 4.5 within 24 h, whereas 52% was released at pH 7.4 in the same time. The results indicated that the release of CP was slower at physiological pH than under acidic condition. This could be due to stronger bonding between the drug molecule and hydrogel, which could be disrupted at acidic pH than at nearly neural condition. Other parameters like hydration capacity of the hydrogel and pore sizes may also contribute to pH-dependent differential release kinetics of the drug.[43]Similarly, the release of Cu from Cu NC–hydrogel composite was investigated by AAS (**Figure 5.21**). Briefly, it was found that after 24 h of incubation at 37 °C, ~8.8 ppm of Cu was released from 21.08 μg/mL of Cu being present in Cu NC–hydrogel composite in acetate buffer of pH 4.5.

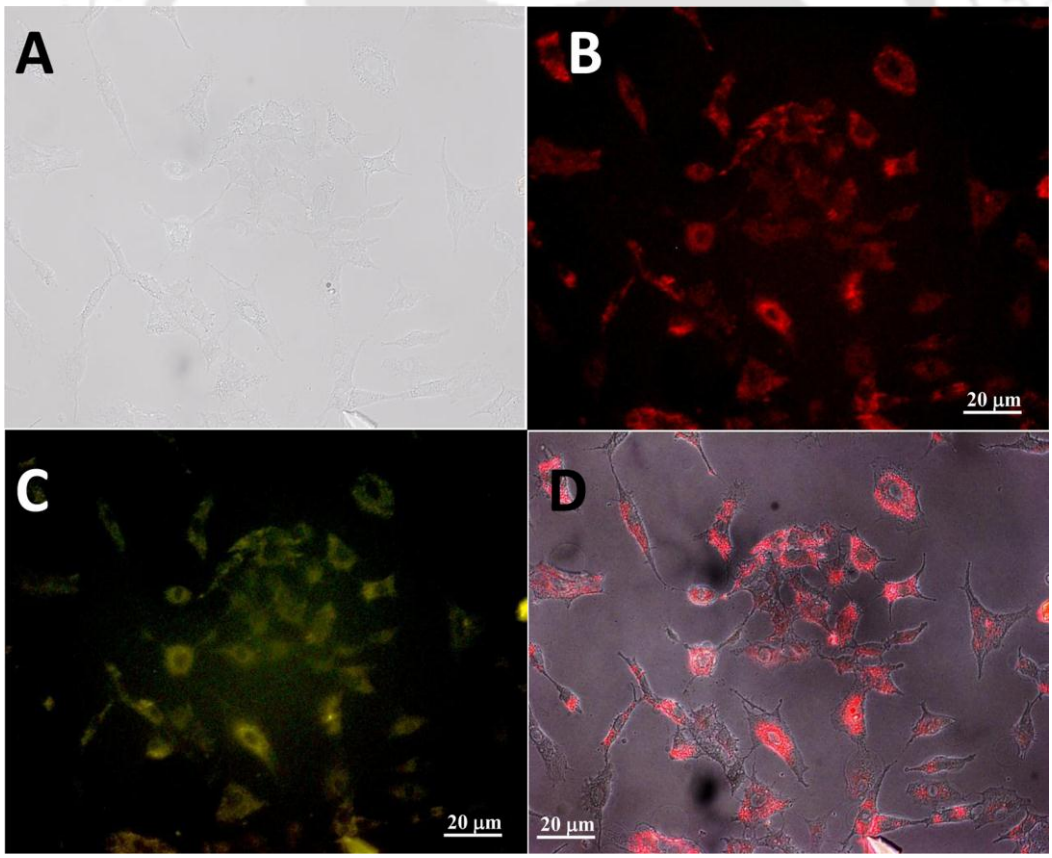

Figure 5.19 Epifluorescence microscopy images of HeLa cells incubated with Cu NC−hydrogel composite after 2 h. (**A**) Image under bright field; (**B,C**) fluorescence images of HeLa cells under excitation filter of blue (465−495 nm) and green (540/25 nm) with emission band-pass filters green (515−555 nm), and red (605/55 nm), respectively. (**D**) Microscopic merged image with bright field under same green excitation light of the same cells. Scale bar is 20 μm.

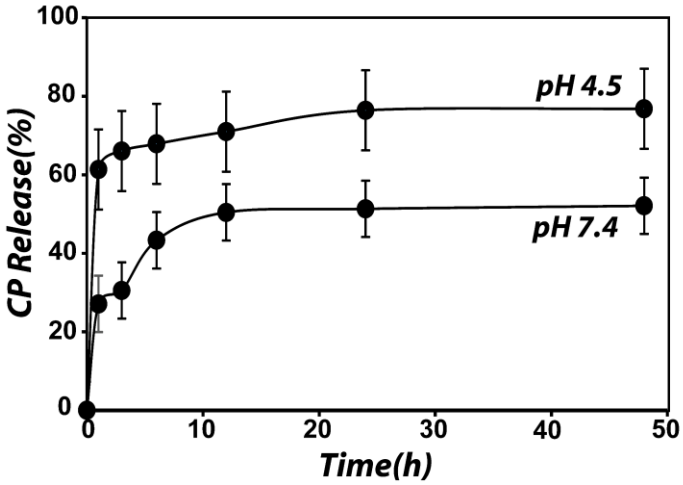

Figure 5.20 *In vitro* CP release profile (in %) from CP-loaded Cu NC−hydrogel composite over 48 h at pH 4.5 in acetate buffer (black circle) and at pH 7.4 in phosphate buffer saline (red circle), both performed at 37 °C.

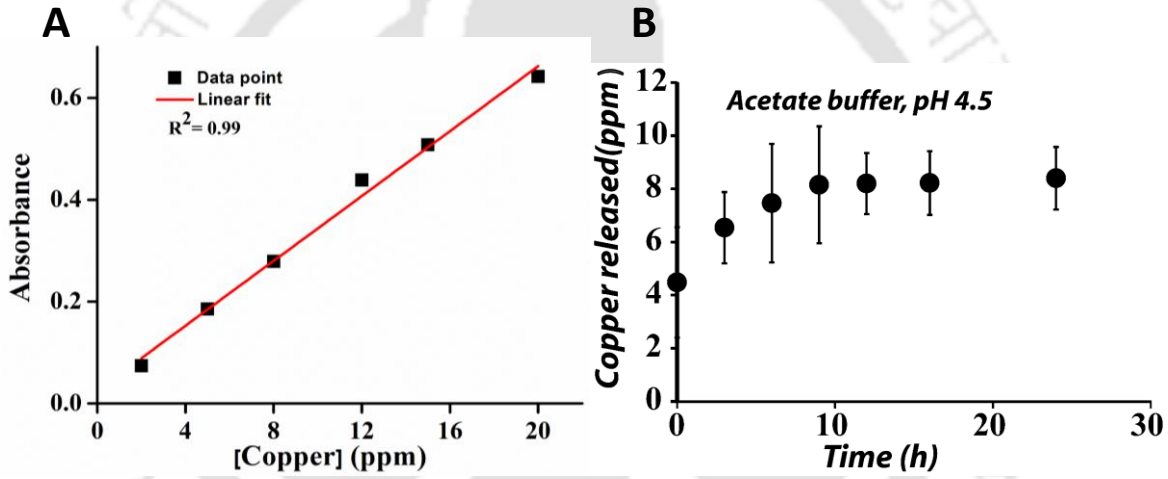

Figure 5.21 Study of release of Cu from Cu NC-hydrogel composite by atomic absorption spectroscopy: (**A**) standard curve of Cu with linear fit and (**B**) Cu release in acetate buffer.

Finally, the utility of the drug-loaded nanocarrier was measured by its ability to work effectively against cancer cells at least *in vitro*. In the current case, the uptake and release of CP-loaded Cu NC–hydrogel composite was studied *in vitro* following treatment with HeLa cells for 3 h in DIMEM. The cells were then analyzed by fluorescence microscopy, flow cytometry, and fluorescence spectroscopy. Fluorescence microscopic images of the cells (**Figure 5.22A, B**) could easily discern the uptake of the drug loaded composite as seen by the emission due to red color under blue light excitations, respectively. In drug delivery, cellular images constitute an important indicator of the consequences of delivery. The results reported herein indicated that the NC containing drug loaded composite could be a potential candidate for real time application. In addition, the fluorescence due to the NCs could be used to follow the cellular uptake of the loaded carrier using flow cytometry. For this, HeLa

cells were independently incubated with Cu NC–hydrogel composite (8.9 µg/mL) and CP-loaded Cu NC–hydrogel composite (4.3 µg/mL of CP was loaded to 8.9 µg/mL of Cu NC–hydrogel composite) for 3 h and analyzed by FACS without using any commercial dye. Cu NC–hydrogel composite and CP-loaded Cu NC–hydrogel composite showed prominent shifts in the fluorescent intensity in FL3-H (low pass/670 nm) channel in comparison to untreated cells, which correspond to red fluorescence due to the NCs (**Figure 5.22C**). The fluorescence intensity was maximum in FL3-H channel in contrast to FL1-H channel, which might be due to the Stokes shifted emission from Cu NCs with the 488 nm laser excitation that was used in FACS Calibur instrument. Additionally, Cu NC–hydrogel composite and CP–loaded Cu NC–hydrogel composite showed almost same shift in the FL3-H channel, which indicated the interaction between the NCs and cells. As a result, NCs could be used for cellular tracking agent instead of commercial dyes. The cytometry results further confirmed the uptake of the free as well as drug-loaded composite by the cells. Furthermore, the TEM image (**Figure 5.23**) of treated HeLa cells confirmed the uptake of Cu NC–hydrogel composite. A magnified image (**Figure 5.23B, C**) evidenced the presence of Cu NCs inside the cells.

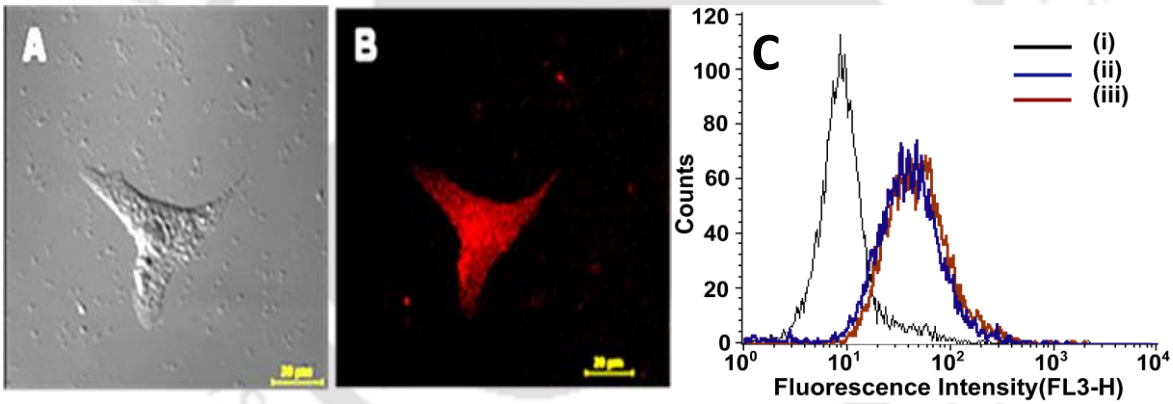

Figure 5.22 Confocal microscopic images of HeLa cells treated with cisplatin loaded Cu NC-hydrogel composite, recorded after 4 h of incubation. (**A**) Image under bright field and **(B**) fluorescence image of HeLa cells under green light. Scale bar is 20 µm. (**C**) FACS analysis confirming the uptake of the composite by cells as observed by shifting fluorescence intensity in FL3-H channel: (i) untreated HeLa cells, (ii) hydrogel-Cu NC (8.9 µg/mL) and (iii) cisplatin loaded Cu NC-hydrogel composite treated HeLa cells.

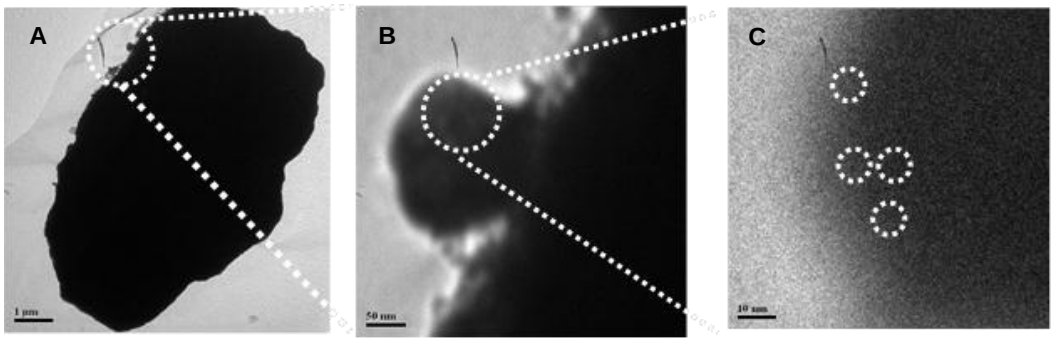

Figure 5.23 (**A**) TEM image of HeLa cell treated with cisplatin loaded Cu NC-hydrogel composite. (**B, C**) Magnified TEM images of the treated cell indicating the presence of Cu NCs inside the cell.

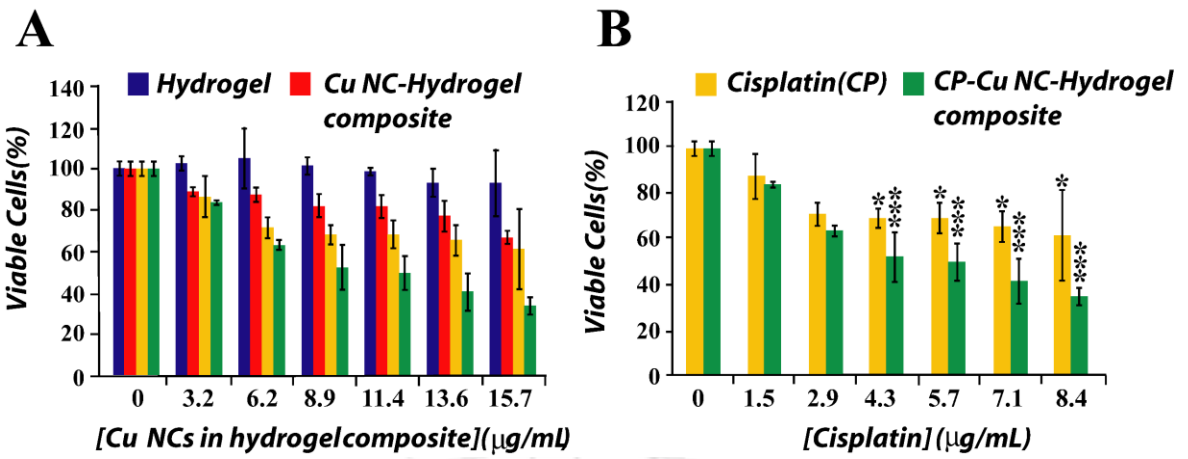

Figure 5.24 Viability of HeLa cells followed by MTT assay after 24 h treatment with (**A**) hydrogel, Cu NC–hydrogel composite and CP-loaded Cu NC-hydrogel composite with varying concentrations of the composite, free CP and CP loaded Cu NC-hydrogel composite at varying cisplatin concentrations; (**B**) CP only and CP-loaded Cu NC–hydrogel composite (shown separately from (A) for ease of comparison). Experiments were carried out in triplicate. Statistical significance was found between CP loaded Cu NC-hydrogel composite (green line) and free CP (yellow line). Statistical significance is denoted by *($p< 0.05$), **($p< 0.005$),and ***($p< 0.001$).

The significance of released drug from the CP-loaded Cu NC–hydrogel composite inside the HeLa cells was explored by cell viability assay and FESEM. For cell viability studies based on [3-(4,5-dimethylthiazol-2-yl)-2,5-diphenyltetrazolium bromide] (MTT) assay, cells were incubated with Cu NC–hydrogel composite, CP only, and CP-loaded Cu NC–hydrogel composite for 24 h at 37 °C. The concentration of the CP was kept in the range of 1.5–8.4 μg/mL in the composite, whereas Cu NC–hydrogel composite was used in varying concentrations from 3.2–15.7 μg/mL. **Figure 5.24A** clearly depicts that 100% of cells were viable upon incubation with hydrogel, indicating the affordable biocompatibility for the drug delivery by the hydrogel nanocomposites. Similarly, 75% of the cells were viable upon incubation with 15.7 μg/mL of the Cu NC–hydrogel composite. When the cells were treated with CP-loaded Cu NC–hydrogel composite, the cell viability decreased to 52% at 8.9 μg/mL of Cu NC–hydrogel composite, where the concentration of CP was 4.3 μg/mL. **Figure 5.24B** also shows the comparative effect of CP on cancer cells when incubated in the form of free drug molecules versus when loaded in the composite. It was found that at a concentration of 8.4 μg/mL of free CP, the cell viability was reduced to 68%, whereas at the same concentration of the drug when loaded in the composite, the viable cells were reduced to 34%. The MTT assay confirmed the potential synergistic effect of anti-cell proliferative Cu NC–hydrogel composite with CP on apoptosis of HeLa cells, which increased the efficacy of CP on HeLa cells. It was observed that addition of Cu NC–hydrogel composite decreased IC_{50} value of CP in HeLa cells. **Figure 5.24B** clearly shows that 70% of the cells were viable

upon incubation with 4.3 μg/mL of CP only for 24 h. Addition of 8.9 μg/mL composite with 4.3 μg/mL of the CP resulted an increase in the cell death by 18%. This indicated that Cu NC–hydrogel composite could enhance the drug efficacy of the composite and can decrease the IC_{50} value of CP. The IC_{50} value of CP when loaded in the hydrogel was calculated to be 5.5 μg/mL. On the other hand, at 8.4 μg/mL of free CP cell viability was reduced to 68% only. The significant decrease of cell viability in the presence of drug-loaded carrier as opposed to free drug molecule evidenced the importance of suitable carrier for increasing the therapeutic efficacy. The result demonstrated that the combination of Cu NC–hydrogel composite and CP can be used as a potential applicant to design new chemotherapeutic agent.

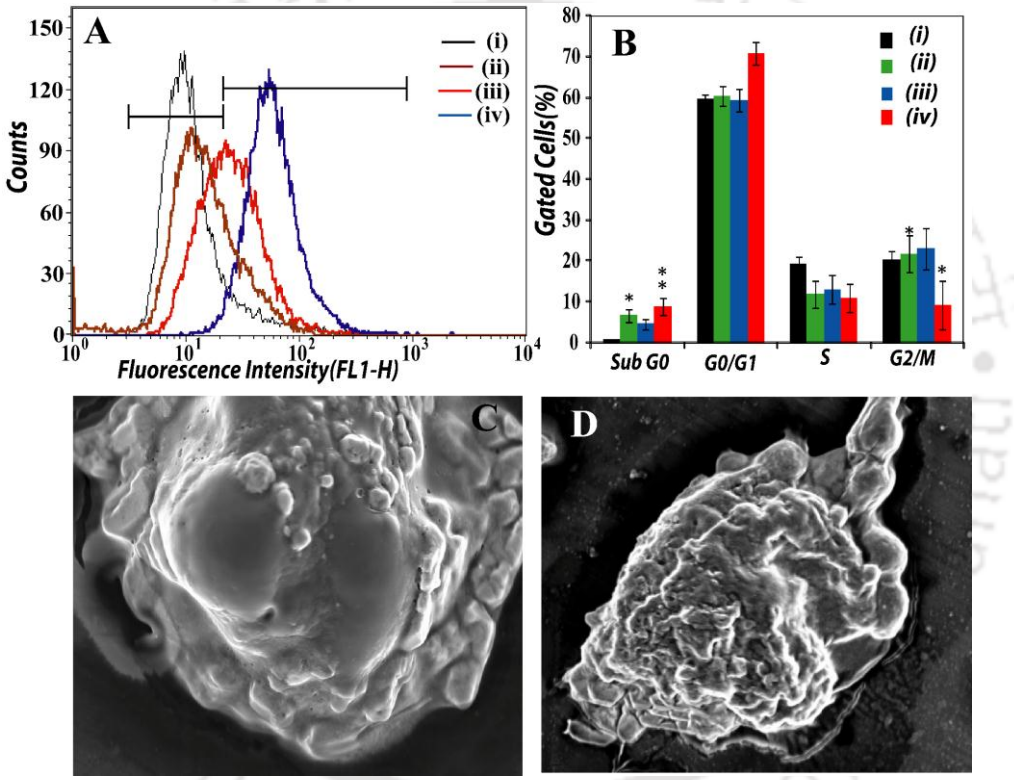

Figure 5.25 (**A**) Flow cytometric analysis of ROS production in HeLa cells: (i) untreated cells, (ii) cells treated with Cu NC–hydrogel composite, (iii) cells treated with CP only, and (iv) cells treated with CP loaded Cu NC–hydrogel composite. (**B**) Effect of Cu NCs and CP in HeLa cells analyzed by FACS in each phase of cell cycle: (i) untreated cells, (ii) cells treated with CP only, (iii) cells treated with Cu NC–hydrogel composite, and (iv)Cells treated with CP loaded Cu NC–hydrogel composite. (**C, D**) FESEM images of a HeLa cells, treated with Cu NC–hydrogel composite and CP loaded Cu NC–hydrogel composite for 24 h revealing apoptotic cell deaths. Experiments were carried out in triplicate. Statistical significance was found between free CP (green line) and CP loaded Cu NC–hydrogel composite (red line). Statistical significance is denoted by *($p< 0.05$), **($p< 0.005$),and ***($p< 0.001$).

Biological utility of composites depends on the size, shape, chemical composition, solubility, and surface structures of the NPs. Metal NPs can induce oxidative stress, due to the ROS generation, governed by the pro-oxidant functional groups present on the surface of NPs as well as owing to the redox properties of transition metal NPs. It has been reported that

Cu NPs could generate ROS in so-treated cells.[44] However, the size of the Cu particles is the key determinant of toxicity. In case of NCs, the particle size is <2 nm. This shrinkage in size increases the surface-to-volume ratio and alters the electronic and chemical properties. This might create specific surface groups, which can function as reactive sites, with electron donor/acceptor properties that interact with molecular O_2 to form $O_2^{-\bullet}$. Apart from surface properties of NCs, Cu can induce oxidative stress *via* Fenton-type reactions, where Cu^{2+} reacts with H_2O_2 to yield $OH^{\bullet}$ and $O_2^{-\bullet}$.[45] It is also plausible that Cu^{+} species present on the surface of the NC induces oxidative stress. Importantly, the rate of Cu fraction release is higher when the NP is smaller in size.[46] ROS generation by Cu NC–hydrogel composite makes it not only an interesting candidate for induction of apoptosis but also provides an important potential for synergistic activity in the presence of a second drug. Interestingly, oxidative stress is associated with apoptotic cell death, which is caused by any chemotherapeutic agent.[47] Thus, flow cytometric studies of the HeLa cells treated with loaded and unloaded composite indicated induction of oxidative stress by the Cu NCs present in the composite. From **Figure 5.25A**, it is evident that Cu NC encapsulated hydrogel generated ROS. Thus, while the cells themselves had the lowest emission intensity (FL1-H), the Cu NC–hydrogel composite-treated cells showed higher emission, which was lower than that due to the only CP-treated cells. However, CP containing composite induced highest emission intensity indicating the synergy of action of Cu NCs and CP. The percentage of ROS generation by hydrogel–Cu NC composite and CP-loaded hydrogel–Cu NC composite are shown in **Figure 5.26**, as compared to the untreated HeLa cells and CP only. It was found that more than 20% of ROS were generated by Cu NC–hydrogel composite in comparison to untreated HeLa cells.

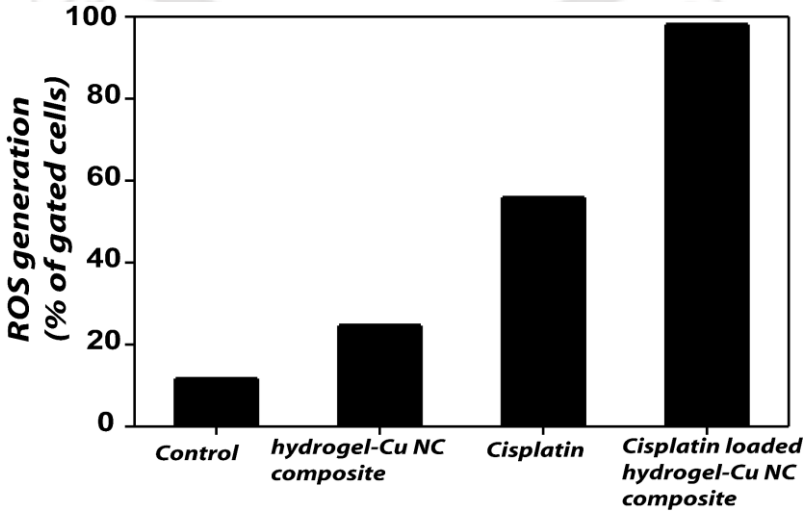

Figure 5.26 Flow cytometric analysis of reactive oxygen species generation in HeLa cells.

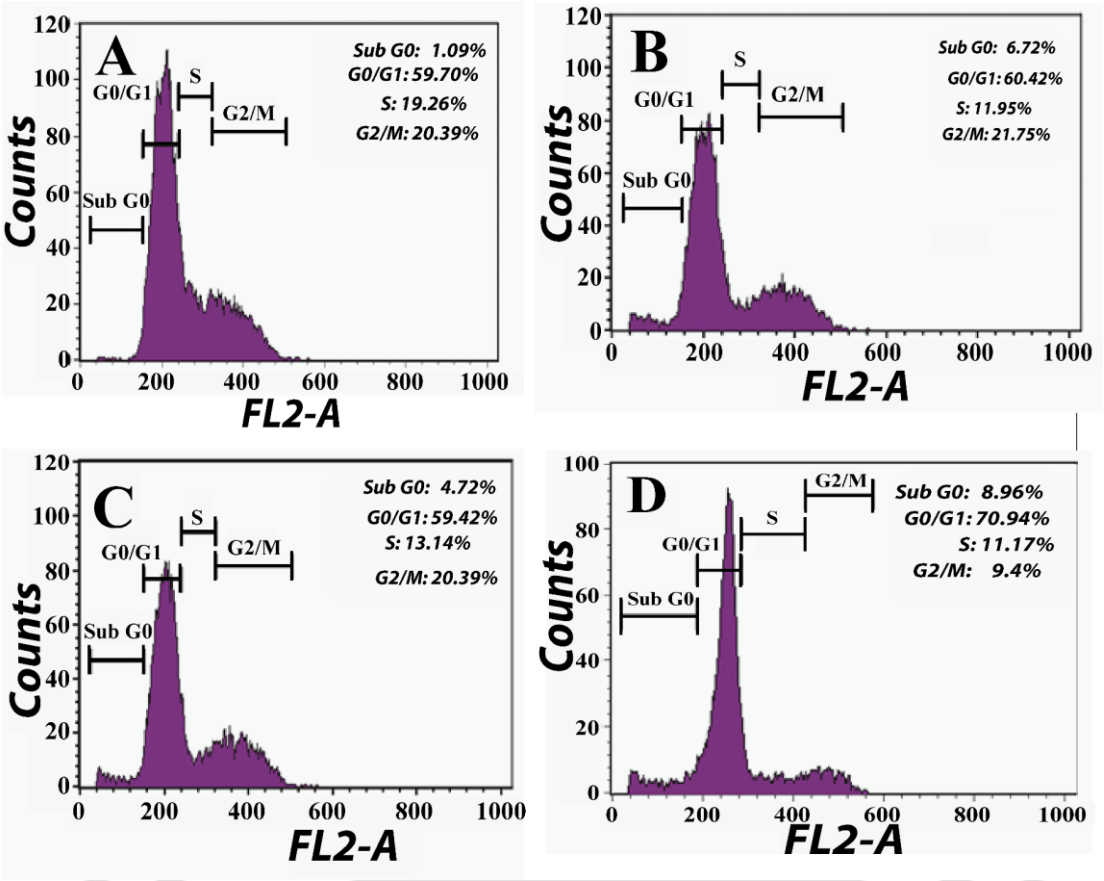

Figure 5.27 Cell cycle analyses by FACS. The data are for (**A**) control cells, (**B**) cells treated with cisplatin, (**C**) cells treated with Cu NC-hydrogel composite and (**D**) cells treated with CP-loaded Cu NC-hydrogel composite.

To pursue the synergistic effect of Cu NC–hydrogel composite and CP, cell cycle analysis was performed by propidium iodide (PI) staining to confirm the apoptotic mode of cell death due to the oxidative stress induced by Cu NC–hydrogel composite and CP-loaded Cu NC–hydrogel composite treated cells. Flow cytometric study showed that the populations of cells in different stages of cell cycle like G0/G1, S and G2/M were affected following the treatment with Cu NC–hydrogel composite and CP-loaded Cu NC–hydrogel composite in contrast to the control cells (**Figure 5.25B**). Increased percentage of population of sub G0/G1 phase of Cu NC–hydrogel composite treated cells (4.72%) and CP-loaded Cu NC−hydrogel composite treated cells (8.96%) provided primary evidence for apoptotic cell death. Cell cycle analysis for control cells, CP, Cu NC–hydrogel composite and CP-loaded Cu NC–hydrogel composites are shown in **Figure 5.27**.

Further, FESEM analysis were performed on the cells treated with Cu NC–hydrogel composite and CP-loaded composite to follow the typical morphological changes of the cells following the treatment with drugs. For this, cells were incubated with Cu NC–hydrogel composite and CP-loaded Cu NC–hydrogel composite for 24 h, which was followed by

imaging using FESEM (**Figure 5.25 C, D**). Generally, CP binds with the guanine bases of DNA leading to cross-linking of DNA, which interferes with mitotic cell division and results in apoptotic cell death.[48] The morphological changes of the treated cells (**Figure 5.25 C, D**) revealed apoptotic cell death caused by Cu NCs only and Cu NCs and CP combined, being present in the composite. FESEM image of control HeLa cells revealed no sign of apoptosis (**Figure 5.28**), which was in good agreement with the cell viability assay. Further, apoptosis mode of cell death was confirmed by Caspase 3 assay in HeLa cells. Apoptotic cell death is primarily governed by the Caspase 3, which is a cysteine-aspartic acid protease.[49] Caspase 3 assay results (**Figure 5.29**) confirm that about 97.7% control HeLa cells were found to be nonapoptotic corresponding to M1 in the histogram of **Figure 5.29A**, while 10.1% cells show apoptosis corresponding to M2 in the histogram (**Figure 5.29C**), when treated with only Cu NC–hydrogel composite. Similarly, when the cells were treated with only CP, 30.9% cells had shown apoptosis while 38.9% cells had shown apoptosis after the treatment with CP-loaded Cu NC–hydrogel composite (**Figure 5.29B,D**).

Calculation of Combination index (CI) with different drug dose concentrations.

CI values can be calculated by using the following equation [50, 51]

$$CI = \frac{D_a^m}{D_a} + \frac{D_b^m}{D_b}$$

Where median effect doses (D_a, D_b) of each drug alone and the median effect doses ($D_m{}^a$, $D_m{}^b$) of each drug in the combination.

Table 5.3 Combination Index (CI) from viable cells at IC_{40}.

Cisplatin loaded Cu NC-hydrogel composite	Combination Index (CI)
IC_{40}	0.607 < 1, synergism of cisplatin and Cu NCs

The overall results indicated that Cu NC encapsulated CP-loaded hydrogel composite was more effective for apoptotic mode of cell death, which also confirmed the synergistic effect of Cu NCs and CP present in the composite. Additionally, synergy of action of CP and Cu NCs was further quantified by the combination index (CI).[50,51] The CI was determined by dose–effect profile of the drugs. The extent of interaction between the drugs was evaluated from the CI plot and such a plot gives the quantitative information about the interactions with the values of CI >1, CI <1, and CI = 0, indicating the antagonism, synergism and additivity, respectively. From **Table 5.3**, it is clear that synergistic effect was present at two cell viable points, namely, at $IC_{20}$and IC_{40}, in comparison to free CP and hydrogel–Cu NC composite.

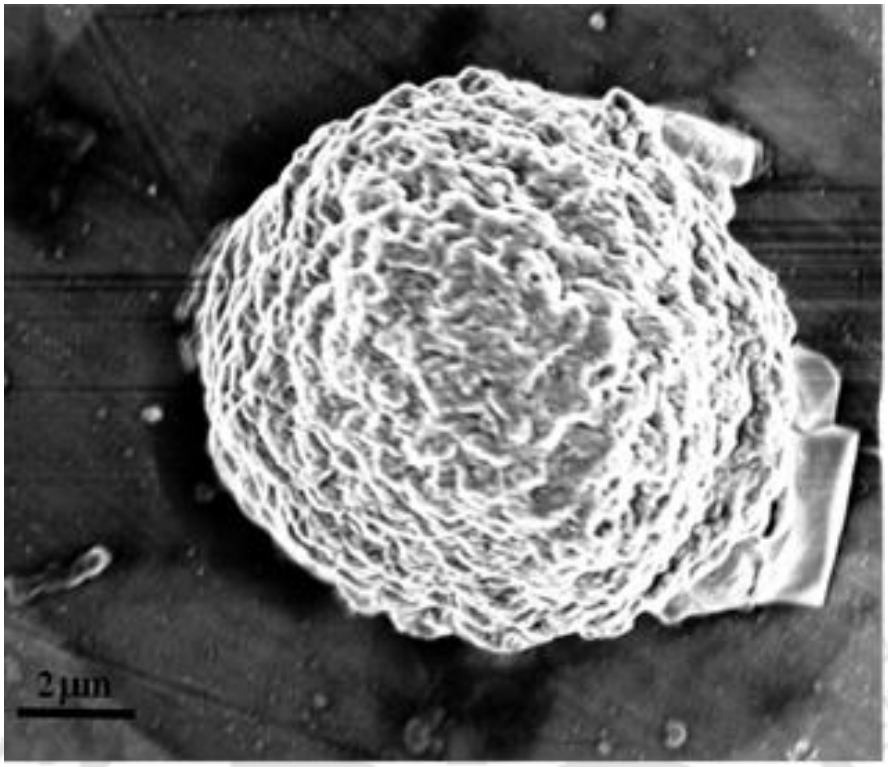

Figure 5.28 Field emission scanning electron microscopy image of HeLa cell.

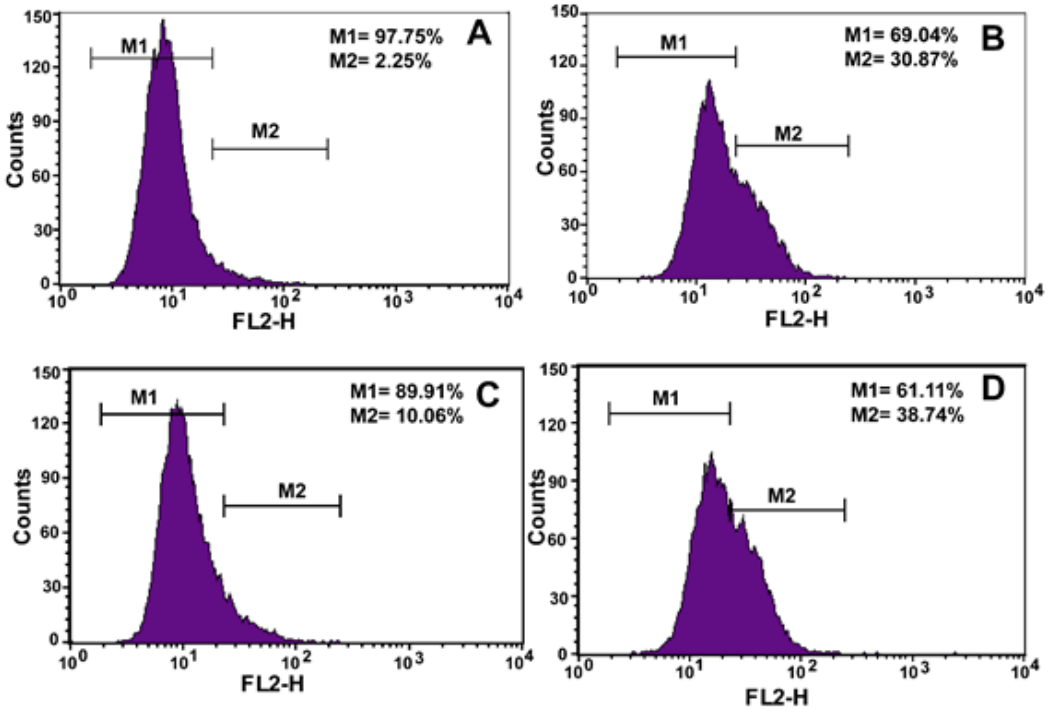

Figure 5.29 Caspase 3 assay of HeLa cells following 24 h incubation with reagents (as specified below) at 37 ºC. The data are for (**A**) control HeLa cells, (**B**) cisplatin treated HeLa cells, (**C**) Cu NC-hydrogel treated HeLa cells and (**D**) cisplatin loaded Cu NC-hydrogel treated cells.

5.4. CONCLUSION

In summary, we have reported the synthesis of stable and brightly fluorescent Cu NCs using a one-step process in aqueous medium. The NCs could be stabilized in the solid form, where they retained their fluorescence for more than a month. The emission property of the NCs in the aqueous medium could be tuned with pH of the medium. This is the first time that the pH tuneability of Cu NC emission is being reported. These Cu NCs, when embedded into PVP, could easily be converted to hydrogel and be used further to deliver anticancer drug CP to HeLa cells, with enhanced efficiency of killing the cells. The synergy of action of ROS generation due to Cu NCs and anticancer drug action of CP makes the composite valuable for practical application. In addition, optical imaging of the uptake of stable red fluorescent Cu NCs may find use in theranostic applications, owing to their high luminescence.

5.5. REFERENCES

1. Shiang, Y.-C.; Huang, C.-C.; Chang, H.-T. *Chem. Commun*. **2009**, 3437–3439.
2. Wei, H.; Wang, Z.; Yang, L.; Tian, S.; Hou, H.; Lu, Y. *Analyst* **2010**, *135*, 1406–1410.
3. Liu, B. Y.; Ai, K.; Cheng, X.; Huo, L.; Lu, L. *Adv. Funct. Mater*. **2010**, *20*, 951–956.
4. Wu, X.; He, X.; Wang, K.; Xie, C.; Zhou, B.; Qing, Z. *Nanoscale* **2010**, *2*, 2244–2249.
5. Lin, C.-A. J.; Yang, T.-Y.; Lee, C.-H.; Huang, S. H.; Sperling, R. A.; Zanella, M.; Li, J. K.; Shen, J.-L. ; Wang, H.-H. ; Yeh, H.-I.; Parak, W. J.; Chang, W. H. *ACS Nano* **2009**, *3*, 395–401.
6. Yu, J.; Choi, S.; Dickson, R. M. *Angew. Chem., Int. Ed*. **2009**, *48,* 318–320.
7. Tanaka, S.-I.; Miyazaki, J.; Tiwari, D. K.; Jin, T.; Inouye. Y. *Angew. Chem., Int. Ed.* **2011**, *50*, 431–435.
8. Kauffman, D. R.; Alfonso, D.; Matranga, C.; Qian, H.; Jin. R *J. Am. Chem. Soc*. **2012**, *134*, 10237−10243.
9. Chen. W.; Chen, S. *Angew. Chem., Int. Ed.* **2009**, *48*, 4386–4389.
10. Zhu, Y.; Qian, H.; Drake, B. A.; Jin. R. *Angew. Chem., Int. Ed*. **2010**, *49*, 1295–1298.
11. Sahoo, A. K.; Banerjee, S.; Ghosh, S. S.; Chattopadhyay, A. *ACS Appl. Mater. Interfaces* **2014**, *6*, 712−724.
12. Shen, Z.; Duan, H.; Frey, H. *Adv. Mater*. **2007**, *19*, 349−352.
13. Petty, J. T.; Zheng, J.; Hud, N. V.; Dickson, R. M. *J. Am. Chem. Soc*. **2004**, *126*, 5207−5212.
14. Richards, C. I.; Choi, S.; Hsiang, J.-C.; Antoku, Y.; Vosch, T.; Bongiorno, A.; Tzeng, Y.-L.; Dickson, R. M. *J. Am. Chem. Soc*. **2008**, *130*, 5038−5039.
15. Xie, J.; Zheng, Y.; Ying, J. Y. *J. Am. Chem. Soc*. **2009**, *131*, 888−889.
16. Liu, C.-L.; Wu, H.-T.; Hsiao, Y.-H.; Lai, C.-W.; Shih, C.-W.; Peng, Y.-K.; Tang, K.-C.; Chang, H.-W.; Chien, Y.-C.; Hsiao, J.-K.; Cheng, J.-T.; Chou, P.-T. *Angew. Chem., Int. Ed*. **2011**, *50*, 7056−7060.
17. Kawasaki, H.; Hamaguchi, K.; Osaka, I.; Arakawa, R. *Adv. Funct. Mater*. **2011**, *21*, 3508−3515.
18. Martin, M. N.; Li, D.; Dass, A.; Eah, S-K. *Nanoscale* **2012**, *4*, 4091–4094.
19. Ghosh, R.; Sahoo, A. K.; Ghosh, S. S.; Paul, A.; Chattopadhyay, A. *ACS Appl. Mater. Interfaces* **2014**, *6*, 3822–3828.
20. Wei, W.; Lu, Y.; Chen, W.; Chen, S. *J. Am. Chem. Soc*. **2011**, *133*, 2060–2063.
21. Jia, X.; Yang, X.; Li, J.; Lia, D.; Wang, E. *Chem. Commun*. **2014**, *50*, 237−239.
22. Jia, X.; Li, Li.; Wang, E. *Small* **2013**, *9*, 3873–3879.
23. Jia, X.; Li, J.; Han, L.; Ren, J.; Yang, X.; Wang, E. *ACS Nano* **2012**, *6*, 3311−3317.
24. Wang, C.; Wang, C.; Xu, L.; Cheng, H.; Lin, Q.; Zhang, C. *Nanoscale* **2014**, *6*, 1775–1781.
25. Gaggelli, E.; Kozlowski, H.; Valensin, D.; Valensin, G. *Chem. Rev*. **2006**, *106*, 1995−2044.
26. Cater, M. A.; Fontaine, S. L.; Shield, K.; Deal, Y.; Mercer, J. F. *Gastroenterology* **2006**, *130*, 493−506.
27. Banerjee, S.; Sahoo, A. K.; Chattopadhyay, A.; Ghosh, S. S. *RSC Adv*. **2013**, *3*, 14123–14131.

28. Lakowicz, J. R. Principles of Fluorescence Spectroscopy, 2nd Ed., Kluwer Academic/Plenum Publishers, New York, **1999**.
29. Xiong, J.; Wang, Y.; Xue, Q.; Wu, X. *Green Chem*. **2011**, *13*, 900–904.
30. Yam, V. W.-W.; Cheng, E. C.-C.; Zhou, Z.-Y. *Angew. Chem., Int. Ed.* **2000**, *39*, 1683–1685.
31. Yam, V. W.-W.; Cheng, E. C.-C.; Cheung, K.-K. *Angew. Chem., Int. Ed*. **1999**, *38*, 197–199.
32. Mathew, A.; Sajanlal, P. R.; Pradeep, T. *J. Mater. Chem.* **2011**, *21*, 11205–11212.
33. Wu, Z.; Jin, R. *Nano Lett.* **2010**, *10*, 2568–2573.
34. Bensebaa, F.; Ellis, T. H.; Kruus, E.; Voicu, R.; Zhou, Y. *Langmuir* **1998**, *14*, 6579−6587.
35. Peppas, B. N. A.; Hilt, J. Z.; Khademhosseini, A.; Robert Langer, R. *Adv. Mater*. **2006**, *18*, 1345–1360.
36. Bharali, D. J.; Sahoo1, S. K.; Mozumdar, S.; Maitra, A. *J. Colloid Interface Sci.* **2003**, *258*, 415–423.
37. Gong, M.; Zhang, L.; Zuo, Y.; Zou, Q.; Wang, Y.; Wang, L.; Li. Y. *J. Appl. Polym. Sci.* **2011,** DOI 10.1002/app.
38. Razzak, M. T.; Zainuddin; Erizal; Dewi, S. P.; Lely, H.; Taty, E.; Sukirno. *Radiat. Phys. Chem.* **1999**, *55*, 153–165.
39. Yuan, F.; Dellian, M.; Fukumura, D.; Leunig, M.; Berk, D. A.; Torchilin, V. P.; Jain, R. K. *Cancer Res.* **1995**, *55*, 3752–3756.
40. Xu, C. J.; Wang, B. D.; Sun, S. H. *J. Am. Chem. Soc*. **2009**, *131*, 4216−4217.
41. Haxtona, K. J.; Burt, H. M. *Dalton Trans*. **2008**, 5872−5875.
42. Chen, J.-P.; Leu, Y.-L.; Fang, C.-L.; Chen, C.-H.; Fang, J.-Y. *J. Pharm. Sci.* **2011**, *100*, 655–666.
43. Hamidi, M.; Azadi, A.; Rafiei, P. *Adv. Drug Delivery Rev.* **2008**, *60*, 1638–1649.
44. Jose, G. P.; Santra, S.; Mandal, S. K.; Sengupta, T. K. *J. Nanobiotechnol.* **2011**, *9*, 1–8.
45. Nel, A.; Xia, T.; Mädler, L.; Li, N. *Science*, **2006**, *311*, 622–627.
46. Midander, K.; Cronholm, P.; Karlsson, H. L.; Elihn, K.; Möller, L.; Leygraf, C.; Wallinder, I. O. *Small* **2009**, 5, 389–399.
47. Peng, K.-W.; Wang, H.; Qin, Z.; Wijewickrama, G. T.; Lu, M.; Wang, Z.; Bolton, J. L.; Thatcher, G. J. *ACS Chem. Biol.* **2009**, *4*, 1039−1049.
48. Guo, S.; Wang, Y.; Miao, L.; Xu, Z.; Lin, C. M.; Zhang, Y.; Huang, L. *ACS Nano* **2013,** *7*, 9896–9904.
49. Sanpui, P.; Chattopadhyay, A.; Ghosh, S. S. *ACS Appl. Mater. Interfaces* **2011**, *3*, 218−228.
50. Zhao, L.; Wientjes, M. G.; Au, J. L.-S. *Clin. Cancer Res*. **2004**, *10*, 7994–8004.
51. Chou, T.-C. *Cancer Res.* **2010**, *70*, 440−446.

Chapter 6

Conclusion and Future Outlook

This chapter describes the summary of the present study and scope for future studies.

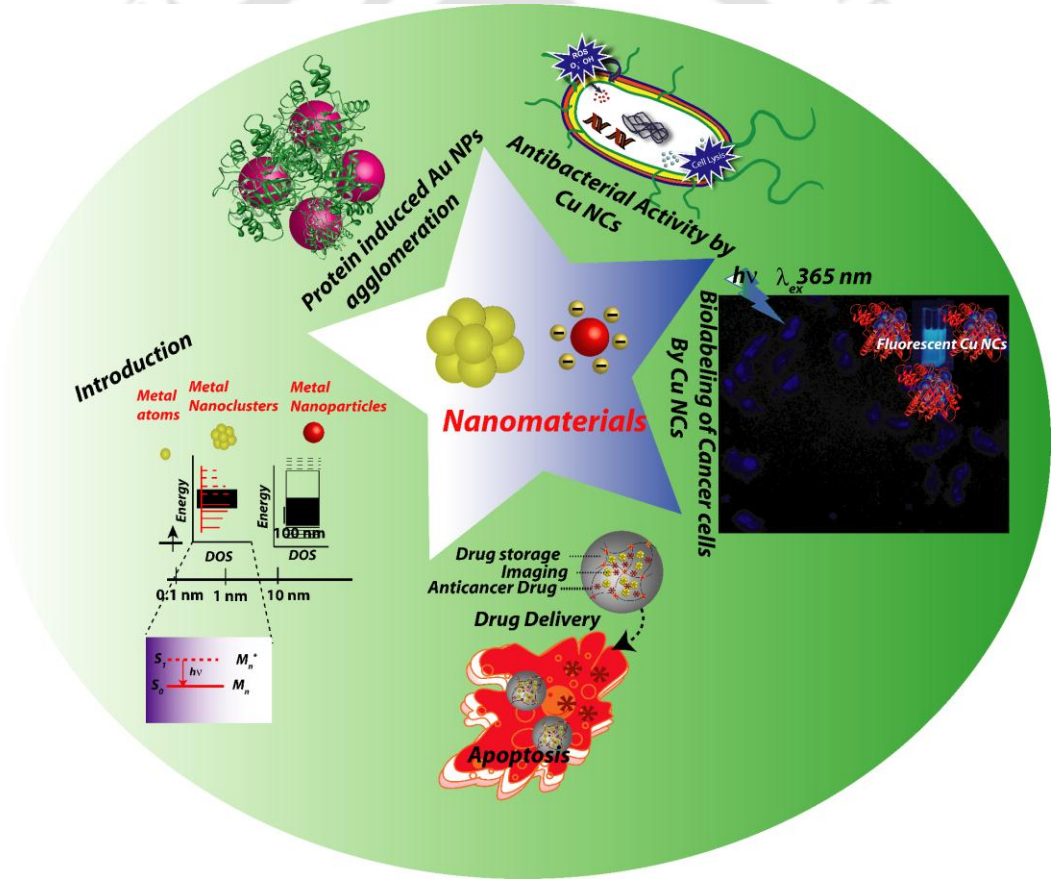

6.1. Summary of the Present Work

An increasing demand and a commensurate advancement of nanotechnology have witnessed the advent of nanomaterials as the emerging candidates for diverse biomedical applications. The extensive utility of nanomaterials, particularly in therapeutic and theranostic, is primarily governed by the tuneability of their intrinsic physical and chemical properties based on size, shape and surface functionalization.

In this thesis, first, the effect of a chemical denaturant on the agglomeration behavior of a citrate stabilized Au NP–protein composite has been demonstrated. UV–Vis and Fourier transform infrared (FTIR) spectroscopy, circular dichroism (CD), dynamic light scattering (DLS) based particle size analyses, fluorescence studies, zeta potential measurements, and transmission electron microscopy (TEM) has been used to determine the agglomeration behaviour of Au NPs in presence of protein. Our studies indicated that when α-amylase was added to a cit–Au NP dispersion, agglomerated structures were formed whose sizes increased with time. On the other hand, when urea was also added, the agglomerated structures did not grow further indicating that the agglomeration process was arrested. In addition, urea was found to permeate to the surface of Au NPs in the agglomerated units, as seen by changes in UV–Vis spectra, zeta potential measurements, FTIR and fluorescence measurements. The results of CD and FTIR spectroscopic studies reveal the cit–Au NP induced conformational change of α-amylase, leading to its agglomeration. The activity of proteins present in the agglomerated structures was still retained. Interestingly, addition of chemically denatured protein (urea treated α-amylase) to the cit–Au NP–protein composite did not result in further agglomeration of the composite. The observations reported herein indicated that the interaction between the cit–Au NP and protein leading to agglomeration is dependent on the conformation of protein. Urea induced unfolding of free proteins and the presence of ions in the medium stopped the growth of agglomerated structures.

Next, water soluble copper nanoclusters (Cu NCs) with an average diameter of 2.6 nm and a bright red luminescence under UV light were synthesized by biomolecule bovine serum albumin (BSA) as a stabilizing agent. The NCs showed absorption and emission spectra having an absorption at 405 nm and emission maxima at 640 nm. We have then reported the antibacterial activity of Cu NCs using green fluorescent protein (GFP) expressing recombinant *E. coli* as a model bacterium. The minimum inhibitory concentrations (MIC) and minimum bactericidal concentration (MBC) of Cu NCs were found to be 13.2 ± 0.46 μg/mL and 16.1 ± 0.8 μg/mL, respectively, in terms of Cu concentration in

the medium. Electron microscopy (EDS-FESEM) and zeta potential measurement revealed the attachment of Cu NCs to the bacterial membrane, leading to a change in bacterial morphology. It was observed that the NCs induced oxidative stress in the treated bacteria, ultimately resulting in bacterial death. The ultra-small size of BSA stabilized NCs enables them to easily cross through the bacterial membrane and subsequently generate reactive oxygen species (ROS), inducing oxidative stress within the bacterial cell. Atomic absorption spectroscopy (AAS) and growth curves conformed that the antibacterial activity was governed by the Cu NCs rather than Cu^{2+} leached out from the Cu NCs.

We have then synthesized blue fluorescent Cu NCs using single step reduction of $CuSO_4$ by hydrazine in presence of lysozyme as a stabilizing agent. The emission from the NCs was found to be dependent on the excitation wavelength. The fluorescence quantum yield (QY) of Cu NCs was found to be as high as 18%. MALDI-TOF mass spectroscopic analysis indicated the presence of species corresponding to Cu_2 to Cu_9. The Cu NCs formed agglomerated structures with an average size of 2.3 nm, which were constituted of smaller particles of average diameter of 0.96 nm, as confirmed by TEM analysis. The NCs were found to be stable in pH range 4–10. The Cu NCs showed wavelength-tunable emission, photostability, high QY and stability in an aqueous medium under ambient conditions; they could easily be isolated and used for labeling cervical cancer HeLa cells. Cell viability studies indicated their noncytotoxic nature, making the NCs ideal for biological applications. The Cu NCs were found to be hemocompatible at the concentrations used for bioimaging and cell viability assay (0.6–4.5 μg/mL). Thus, blood compatibility assay supported the potential of composites (thus Cu NCs) for applications *in vivo*.

Finally, we have tried to develop a nanocarrier using red fluorescent Cu NCs that have been synthesized using dihydrolipoic acid in presence of biocompatible polymer polyvinylpyrrolidone in aqueous medium. Mass spectroscopic analysis indicated the presence of species of Cu_4. TEM analysis indicated an average size of 1.9 nm for the individual Cu NCs. The emission property of as synthesized Cu NCs could be tuned reversibly according to the pH. The PVP stabilized Cu NCs were then converted into hydrogel composite by freeze thaw method by polyvinyl alcohol (PVA). The composites were stable for long time more than one month in solid form with intake fluorescence property. Further, the emission due to the NCs was useful for imaging mammalian cells by optical microscopy and more importantly to probe the cells by commercial flow cytometer, without using any other dye. Cisplatin was then loaded into the Cu NCs containing hydrogel composite for effective

delivery to cancer cells, which was probed by the emission property of Cu NCs. Fascinatingly, Cu NCs were found to generate ROS in cancer cells which increased the efficacy of cisplatin in killing the cancer cells by providing the synergy of action.

6.2. Future Outlook

We hope, through the work presented in this thesis, to be able to establish the interactions of nanoparticles (NPs) with proteins. The interaction gives a better understanding of the application of metal NPs/protein in theranostic and therapeutic use. Therefore, there is a scope to design nanomaterials on the basis of safety issue *via* predetermination of the nature and conformation of the protein that is adsorbed onto the surface of NPs for different biomedical applications. As biotechnology is taken as the application, this study can help to understand protein corona formation on NPs *in vivo*. Future studies may be proposed on whole serum protein for better understanding of mixed protein surface functionality in theranostics.

On the other hand, protein and polymer stabilized Cu NCs could be used as an imaging modality in theranostic uses. The surface functionalization of Cu NCs could be readily clutched with silica, graphene oxide, carbon nanotube, *etc.* for the use in gene as well as protein delivery. Interestingly, Cu NCs have the ability to generate ROS which could be used for the detection of cancer cells. In addition, the pH tunable emission property of Cu NCs could be an ideal pathway to track cancer cells without using any organic dye. Besides theranostic applications, Cu NCs could be used in optoelectronic devices like transistor, solar cell *etc*. Additionally, Cu NCs could be used as an effective catalyst for organic conversions due to their nano size.

Appendix

Appendix

Chapter 2

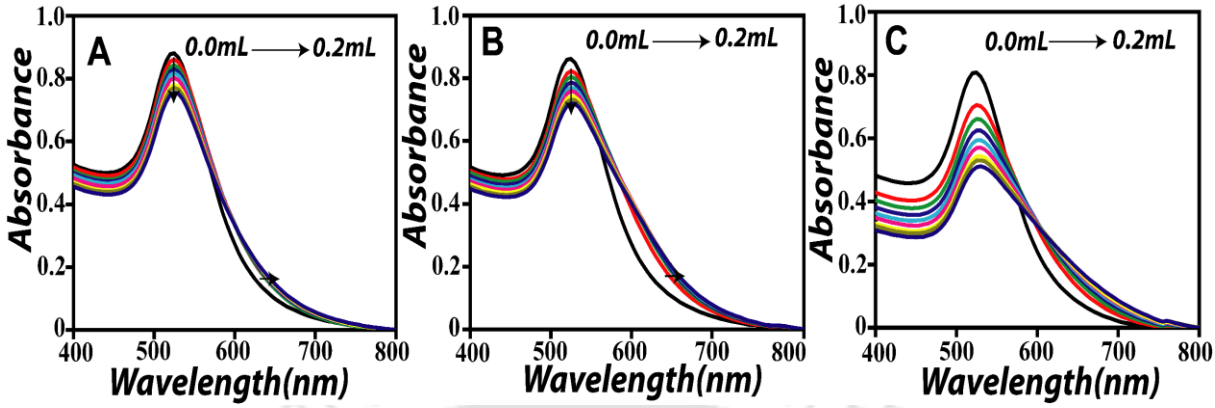

Figure. 2A.1 UV–Vis spectra of 3.0 mL of cit–Au NPs solution on successive addition (from 0.01 mL to 0.2 mL) of 4 M stock urea solution, already containing (A) 0.02 mL (B) 0.04 mL α–amylase and (C) 0.06 mL of α–amylase. The stock concentration of α–amylase was 127 nM. All the UV–Vis spectra were recorded after 5 min incubation. Cit -Au NPs mixture with α–amylase was kept for 5 min, urea added to the composite, kept further for 5 min and then the spectra recorded.

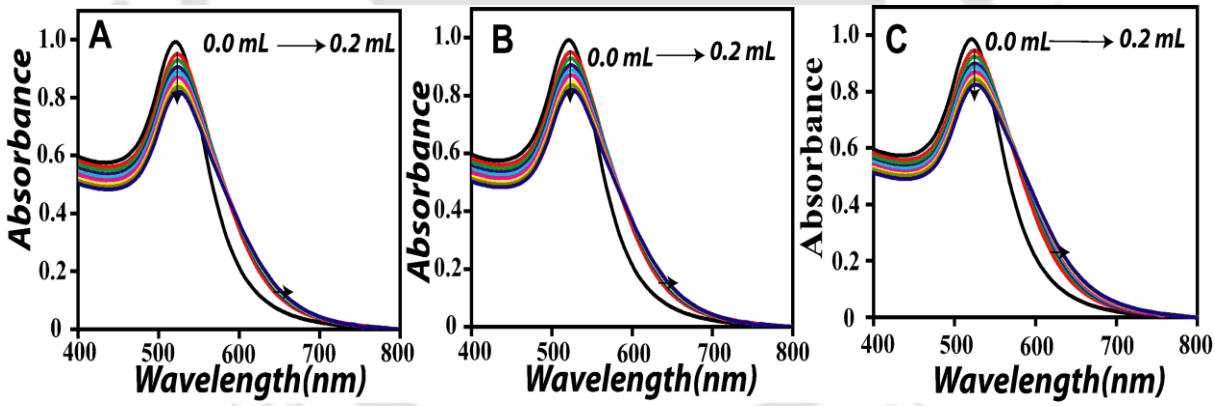

Figure. 2A.2 UV–Vis spectra of 3.0 mL of cit–Au NPs solution on successive addition (from 0.01 mL to 0.2 mL) of 6 M stock urea solution, already containing (A) 0.02 mL (B) 0.04 mL α–amylase and (C) 0.06 mL of α–amylase. The stock concentration of α–amylase was 127 nM. All the UV–Vis spectra were recorded after 5 min incubation. cit -Au NPs mixture with α–amylase was kept for 5 min, urea added to the composite, kept further for 5 min and then the spectra recorded.

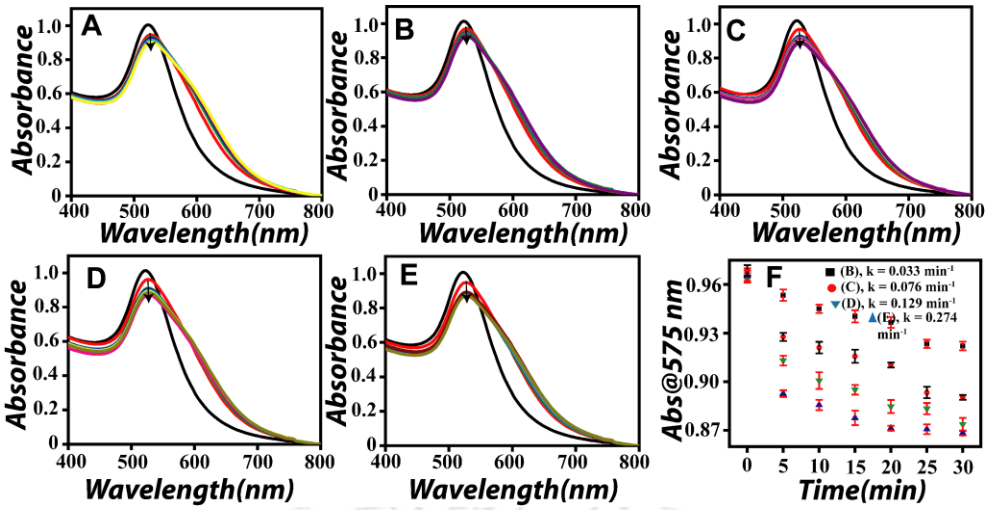

Figure 2A.3 Time dependent UV–Vis spectra for cit–Au NPs with 0.06 mL α–amylase in presence of **(A)** 0.00 mL **(B)** 0.05 mL **(C)** 0.10 mL **(D)** 0.15 mL **(E)** 0.20 mL of urea solution. All samples were kept for 5 min before recording the spectra**.** The stock concentration of α–amylase and urea were 127 nM and 8 M, respectively**. (F)** Absorbance at 575 nm of (**B**), (**C**), (**D**) and (**E**) with time interval of 5 min. The error bar were calculated from three sets of experiments.

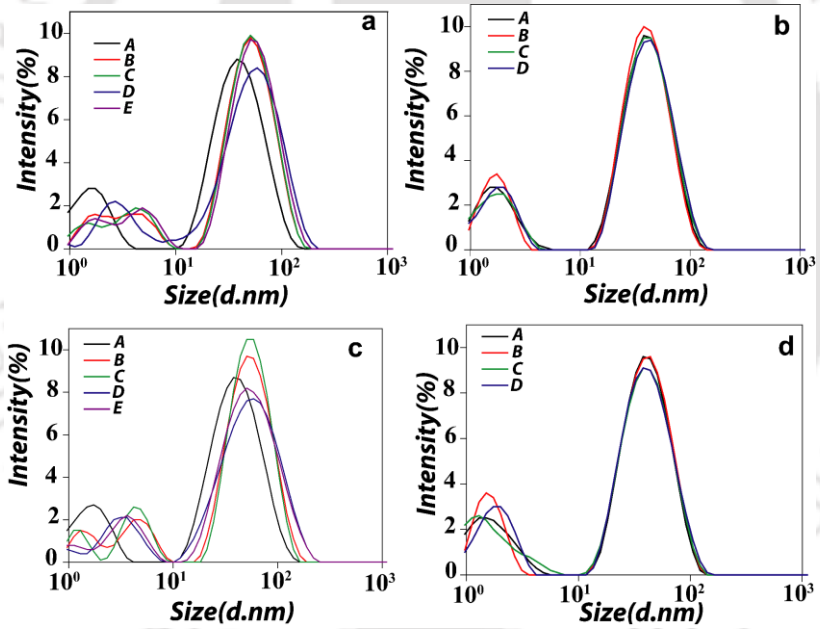

Figure 2A.4 Particle size distribution curves of (a): (**A**) 3.0 mL cit–Au NPs dispersion (B) 3.0 mL cit–Au NPs + 0.06 mL α–amylase solution (**C**) 3.0 cit–Au NPs + 0.06 mL α–amylase solution + 0.05 mL urea solution (**D**) 3.0 mL cit–Au NPs + 0.06 mL α–amylase solution + 0.150 mL urea solution (**E**) 3.0 mL cit–Au NPs + 0.06 mL α–amylase solution + 0.250 mL urea solution (stock concentration of α–amylase and urea are 127 nM and 4 M, respectively)
(**b**): (**A**) 3.0 mL of cit–Au NPs dispersion (**B**) 3.0 mL cit–Au NPs + 0.50 mL urea solution (**C**) 3.0 mL cit–Au NPs + 0.15 mL urea solution (**D**) 3.0 mL cit–Au NPs + 0.25 mL urea solution (stock concentration of urea solution is 4 M)
(**c**): (**A**) 3.0 mL of cit–Au NPs dispersion (**B**) 3.0 mL cit–Au NPs + 0.06 mL α–amylase solution (**C**) 3.0 mL cit–Au NPs + 0.06 mL α–amylase solution + 0.05 mL urea solution (**D**) 3.0 mL cit–Au NPs + 0.06 mL α–amylase solution + 0.150 mL urea solution (**E**) 3.0 mL cit–Au NPs + 0.06 mL α–amylase solution + 0.250 mL urea solution (stock concentration of α–amylase and urea are 127 nM and 6 M, respectively). (**d**): (**A**) 3.0 mL cit–Au NPs dispersion (**B**) 3.0 mL cit–Au NPs + 0.50 mL urea solution (**C**) 3.0 mL cit–Au NPs + 0.15 mL urea solution (**D**) 3.0 mL cit–Au NPs + 0.25 mL urea solution (stock concentration of urea solution is 6 M).

Table 2A.1: Particle size distribution from DLS measurements using 4 M urea stock solution. All the samples were kept for 5 min before recording the size. Urea was added to cit–Au NPs–α amylase composite every 5 min interval**.**

Sample	Size (d.nm)	Peak 1 size (d.nm)	Peak 1 area (%)	Peak 2 size (d.nm)	Peak 2 area (%)
3.0 mL cit–Au NPs	12.4	43.9	78.8	1.5	21.2
3.0 mL cit–Au NPs + 0.06 mL of α–amylase	20.6	56	80	4.4	10.5
3.0 mL cit–Au NPs + 0.06 mL of α–amylase + 0.05 mL of 4 M urea solution	21	57	80	4.2	13.6
3.0 mL cit–Au NPs + 0.06 mL of α–amylase + 0.15 mL of 4 M urea solution	21.7	60	83	3.1	15
3.0 mL cit–Au NPs + 0.06 mL of α–amylase + 0.25 mL of 4 M urea solution	23	60	80	4.8	11.3

Table 2A.2: DLS measurements of cit-Au NPs in presence of 4 M of urea solution only. All the samples were kept for 5 min before recording the size. Urea was added to cit–Au NPs–α amylase composite every 5 min interval.

Sample	Size (d.nm)	Peak 1 size (d.nm)	Peak 1 area (%)	Peak 2 size (d.nm)	Peak 2 area (%)
3.0mL cit–Au NPs	12.54	47	79	1.7	21
3.0ml cit–Au NPs + 0.01mL of 8M urea solution	12.17	43	80	1.7	20
3.0ml cit–Au NPs + 0.05 mL of 8 M urea solution	12.39	46	79	1.7	21
3.0ml cit–Au NPs + 0.120 mL of 8 M urea solution	12.54	47	79	1.7	20.9

Table 2A.3: Particle size distribution from DLS measurements using 6 M urea stock solution. All the samples were kept for 5 min before recording the size. Urea was added to cit–Au NPs–α amylase composite every 5 min interval.

Sample	Size (d.nm)	Peak 1 size (d.nm)	Peak 1 area (%)	Peak 2 size (d.nm)	Peak 2 area (%)
3.0 mL cit–Au NPs	12.54	43.6	77.6	2	17.9
3.0 mL cit–Au NPs + 0.06 mL of α–amylase	21.4	59.4	80	4.6	12.3
3.0 mL cit–Au NPs + 0.06 mL of α–amylase + 0.05 mL of 6 M urea solution	21.7	59	80	4.5	13.6
3.0 mL cit–Au NPs + 0.06 mL of α–amylase + 0.15 mL of 6 M urea solution	23.4	63	82.5	3.3	14.6
3.0 mL cit–Au NPs + 0.06 mL of α–amylase + 0.25 mL of 6 M urea solution	23.7	63.2	82	3.6	14.3

Table 2A.4: DLS measurements of cit-Au NPs in presence of 6 M of urea solution only. All the samples were kept for 5 min before recording the size. Urea was added to cit–Au NPs every 5 min interval**.**

Sample	Size (d.nm)	Peak 1 size (d.nm)	Peak 1 area (%)	Peak 2 size (d.nm)	Peak 2 area (%)
3.0ml cit–Au NPs	12.17	44	78	1.7	21
3.0ml cit–Au NPs + 0.01mL of 8M urea solution	12.04	45	80	1.6	19
3.0ml cit–Au NPs + 0.05 mL of 8 M urea solution	12.12	45	78	1.7	22
3.0ml cit–Au NPs + 0.120 mL of 8 M urea solution	12.05	45	78	1.8	20

Table 2A.5: Measurement of zeta potentials of cit–Au NPs in presence of 8M urea only. All the samples were kept for 5 min before recording the zeta potential. Urea was added to cit–Au NPs every 5 min interval**.**

Sample	Zeta potential (mV)	Size (d.nm)
3.0 mL cit–Au NPs	-49.7	12.48
3.0 mL cit–Au NPs + 0.01 mL of 8 M urea solution.	-47.9	12.48
3.0 mL cit–Au NPs + 0.05 mL of 8 M urea solution.	-45.8	12.56
3.0 mL cit–Au NPs + 0.12 mL of 8 M urea solution.	-44.1	12.66

Table 2A.6: DLS measurement of cit–Au NPs in presence of 8M of urea solution. All the samples were kept for 5 min before recording the particle size distribution. Urea was added to cit–Au NPs every 5 min interval.

Sample	Size (d.nm)	Peak 1 size (d.nm)	Peak 1 area (%)	Peak 2 size (d.nm)	Peak 2 area (%)
3.0mL cit–Au NPs	19	45.84	78	1.69	21
3.0ml cit–Au NPs + 0.01mL of 8M urea solution	19.05	45	78.6	1.7	22
3.0ml cit–Au NPs + 0.05 mL of 8 M urea solution	19	46	77	2.2	14
3.0ml cit–Au NPs + 0.120 mL of 8 M urea solution	19	48	79	2.04	21

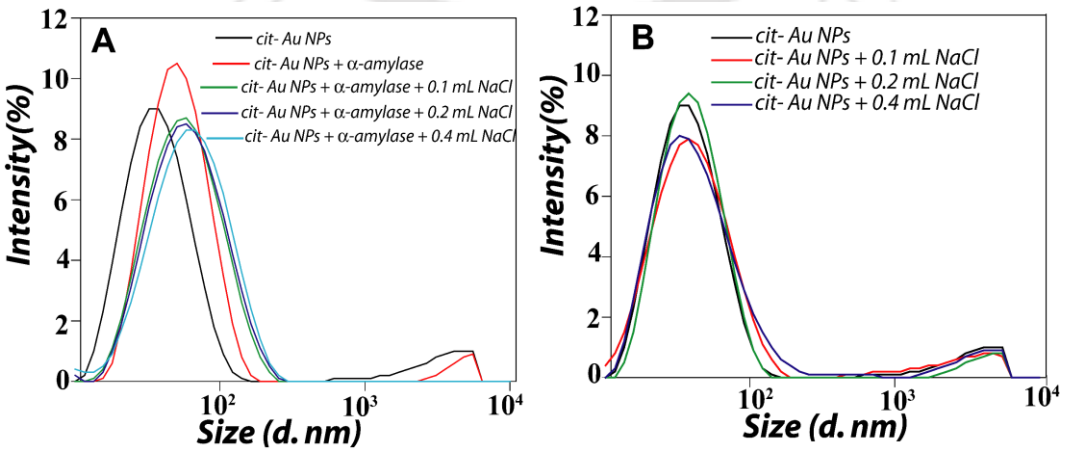

Figure 2A.5 Particle size distribution curves of 3.0 mL cit–Au NPs in presence of 50 mM NaCl and: **(A)** 0.06 mL **(B)** 0.0 mL of α–amylase solution. All the samples were kept for 5 min before recording the particle size distribution. NaCl was added to cit–Au NPs-amylase composite every 5 min interval.

Table 2A.7: Particle size distribution of 3.0 mL cit–Au NPs in presence of 50 mM NaCl. All the samples were kept for 5 min before recording the size. NaCl was added to cit–Au NPs every 5 min interval.

Sl No.	Sample	Size (d.nm)
1	3.0 mL of ci–Au NPs	16
2	3.0 mL of cit–Au NPs + 0.1 mL of 50 mM NaCl	18
3	3.0 mL of cit–Au NPs + 0.2 mL of 50 mM NaCl	19.8
4	3.0 mL of cit–Au NPs + 0.4 mL of 50 mM NaCl	20.7

Table 2A.8: Particle size distribution of 3.0 mL cit–Au NPs in presence of 0.06 mL of 127 nM α–amylase solution and 50 mM NaCl. All the samples were kept for 5 min before recording the size. NaCl was added to cit–Au NPs–α amylase composite every 5 min interval.

Sl No.	Sample	Size (d.nm)
1	3.0 mL of cit–Au NPs	16
2	3.0 mL of cit–Au NPs + 0.06 mL α–amylase	29
3	3.0 mL of cit–Au NPs + 0.06 mL α–amylase + 0.1 mL 50 mM NaCl	30
4	3.0 mL of cit–Au NPs + 0.06 mL α–amylase + 0.2 mL 50 mM NaCl	31
5	3.0 mL of cit–Au NPs + 0.06 mL α–amylase + 0.4 mL 50 mM NaCl	32

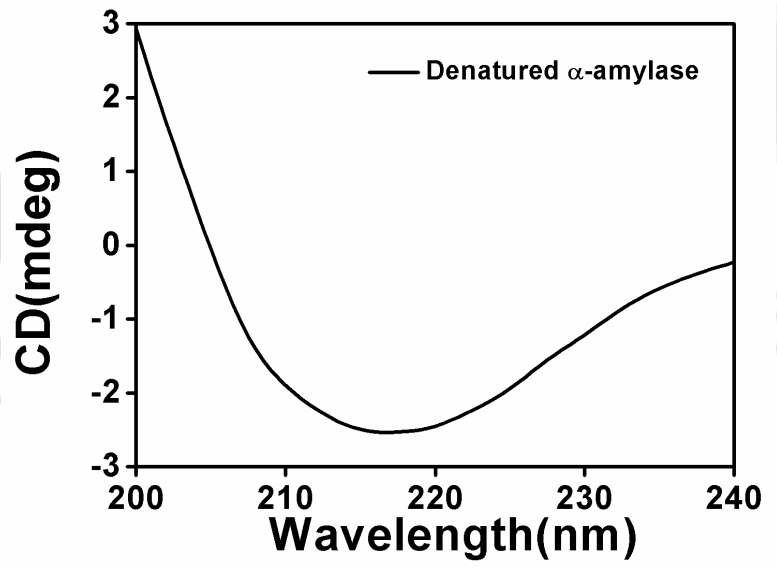

Figure 2A.6 CD spectra of 0.06 mL of α–amylase+ 0.4 mL of 8 M urea solution. Spectra were recorded in the wavelength region 200–250 nm. The concentration of α–amylase in solution was found to be 24.9 nM. The α–amylase and urea mixture was kept for 3 hours at 4°C.

TABLE 2A.9: Determination of helicity of α–amylase from UV- CD spectroscopy

Sample	α– helix (%)	β– sheet (%)
Native α–amylase	82	6
0.06 mL of α–amylase+ 0.4 mL of 8 M urea solution	10	73

Enzymatic activity of α–amylase was measured by following the digestion of starch in absence of, and in presence of the α–amylase–Au NP composite, as well as urea treated α–amylase–Au NP composite. The amount of starch left was followed by the iodine test method by an earlier adopted procedure.[1] When iodine is added to the mixture of Au NP–protein and starch, a new UV–vis band emerged at 565 nm, which is the characteristics peak for the starch–iodine complex (**Figure 2A.7**). UV–Vis spectra were recorded at regular intervals of time and the area under the curves were determined and plotted as a function of time as shown in **Figure 2A.7**. In all cases the digestion of starch was found to follow first order kinetics (**Figure 2A.7**). Previous studies have shown that the enzyme activity of the extensively agglomerated cit–Au NPs composites is reduced while the activity of mildly agglomerated cit–Au NPs composites is enhanced.[2]The marginal reduction in the enzymatic activity of cit–Au NPs protein composite from the native protein in this study.

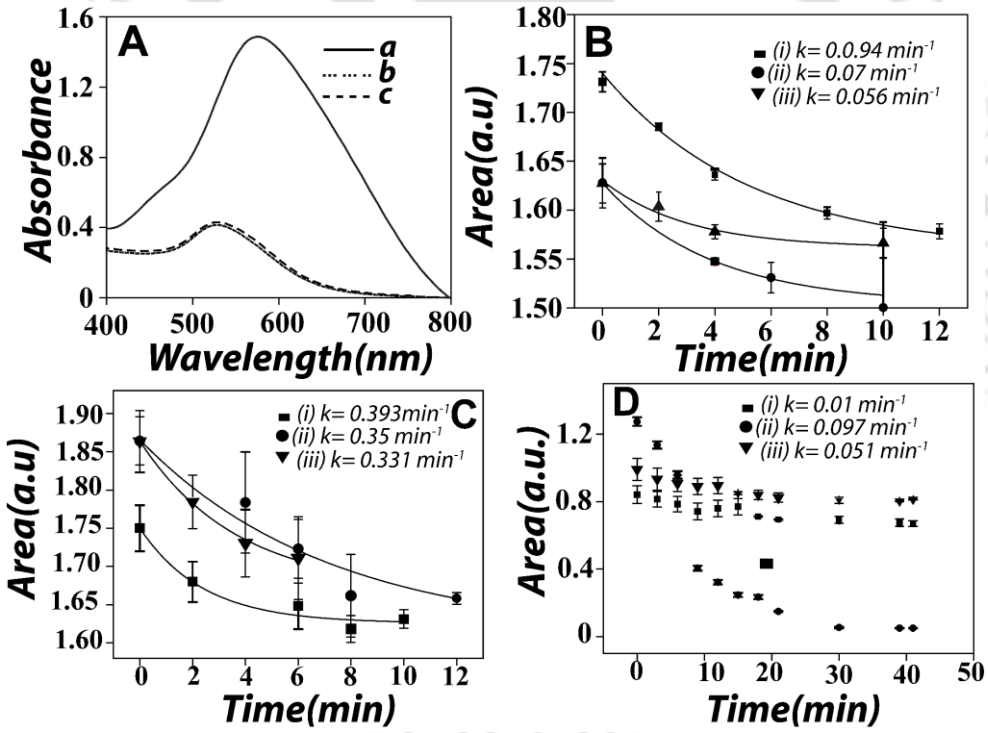

Figure 2A.7 (**A**) UV–Vis spectra of the starch-Au NPs composite (solid line, **a**), starch–Au NPs–urea composite (small dotted line, **b**) compared to the starch–Au NPs–urea in the presence of iodine (big dotted line, **c**). Comparative kinetic studies of starch digestion in the starch-Au NPs in absence and presence of (**i**) 3.0 mL of cit–Au NPs+0.06mL of α–amylase (**ii**) 3.0 mL of cit–Au NPs+0.06mL of α–amylase+0.5mL of urea and (**iii**) 3.0 mL of cit–Au NPs+0.06mL of α–amylase+1.5mL of urea (**B**) 4 M. (**C**) 6 M and (**D**) 8 M of urea solution. The stock concentration of α–amylase was 1270 nM. The error bar were calculated from three set of experiments.

REFERENCE

1. Deka, J.; Paul, A.; Ramesh, A.; Chattopadhyay, A. *Langmuir*, **2008**, *24*, 9945–9951.
2. Deka, J.; Paul, A.; Chattopadhyay, A. *RSC Advances*, **2012**, ***2***, 4736–4745.

Publication

JOURNAL(S).

1. **Ghosh, R.**; Goswami, U.; Ghosh, S. S.; Paul, A.; Chattopadhyay, A. "Synergistic anticancer activity of fluorescent copper nanoclusters and cisplatin delivered through a hydrogel nanocarrier" ***ACS Appl. Mater. Interfaces***, *7*, 209–222 (**2015**).DOI: 10.1021/acsami.5b08088.

2. **Ghosh, R.**; Sahoo, S. K.; Ghosh, S. S.; Paul, A.; Chattopadhyay, A. "Blue-emitting copper nanoclusters synthesized in the presence of lysozyme as candidates for cell labeling" ***ACS Appl. Mater. Interfaces***, *6*, 3822–3828 (**2014**).

3. **Ghosh, R.**; Deka, J.; Chattopadhyay, A.; Paul, A. "Conformation aspect in the α-amylase induced agglomeration of citrate-stabilized gold nanoparticles" ***RSC Adv.*** *3*, 23015–23027 (**2013**).

4. **Ghosh, R.**; Goswami, U.; Sanpui, Pallab.; Ghosh, S. S.; Paul, A.; Chattopadhyay, A. "Superior Antibacterial Activity of Fluorescent Copper Nanoclusters via Reactive Oxygen Species (ROS)" **2015** (Manuscript to submit)

ORAL PRESENTATION(S)).

1. Fluorescent copper nanoclusters and their theranostic applications.
   ***NanoSci*-2014**" at the Institute of Advanced Study in Science and Technology (IASST), Guwahati, Assam, India (**2014**).

POSTERS IN CONFERENCE(S).

1. Metal nanoclusters and their biological applications.
   International Conference on Nano Science and Technology–ICONSAT at Department of Chemistry, Punjab University, Chandigarh, India (**2014**).

2. Is protein denaturation the origin of citrate stabilized gold nanoparticles agglomeration?
   Frontiers in Chemical Sciences–FICS at Department of Chemistry, Indian Institute of Technology Guwahati, Guwahati, Assam, and India (**2012**).

3. Protein denaturation induced agglomeration of citrate stabilized gold nanoparticles.
   Conference on Photochemistry and Luminescence–CPL at Department of Chemistry, Indian Institute of Technology Guwahati, Guwahati, Assam, India (**2012**).

RSC Advances

RSC Publishing

PAPER

View Article Online
View Journal | View Issue

Conformation aspect in the α-amylase induced agglomeration of citrate-stabilized gold nanoparticles†

Cite this: *RSC Adv.*, 2013, **3**, 23015

Rama Ghosh,[a] Jashmini Deka,[a] Arun Chattopadhyay*[ab] and Anumita Paul*[a]

In this article we report the effect of a chemical denaturant on the agglomeration behaviour of a citrate stabilized Au NP–protein composite. We have used α-amylase as a model protein and urea as the chemical denaturant. The agglomeration behaviour has been studied by UV-Visible and Fourier transform infrared (FTIR) spectroscopy, circular dichroism (CD), dynamic light scattering (DLS) based particle size analyses, fluorescence studies, zeta potential measurements and transmission electron microscopy (TEM). Our studies indicate that when α-amylase was added to a cit–Au NP dispersion, agglomerated structures were formed whose sizes increased with time. On the other hand, when urea was also added, the agglomerated structures did not grow further indicating that the agglomeration process was arrested. In addition, urea was found to permeate to the surface of Au NPs in the agglomerated units, as seen by changes in the UV-Vis spectra, zeta potential measurements, FTIR and fluorescence measurements. Results of CD and FTIR studies are indicative of the α-helix of the protein being stabilized in the cit–Au NP induced conformational changes of α-amylase leading to its agglomeration. The activity of the proteins present in the agglomerated structures was still retained. Interestingly, addition of chemically denatured protein (urea treated α-amylase) to the cit–Au NP–protein composite did not result in further agglomeration of the composite. The observations reported herein indicate that the interaction between the cit–Au NP and the protein leading to agglomeration is dependent on the conformation of the protein, and that while native protein was involved in the agglomeration process, denatured protein was not involved in agglomeration process. Urea induced unfolding of the free proteins as well as the presence of ions in the medium stopped or stalled the growth of the agglomerated structures.

Received 15th July 2013
Accepted 20th September 2013

DOI: 10.1039/c3ra43623c

www.rsc.org/advances

Introduction

Rapid progress in nanoscale science and technology is increasingly finding nanomaterials being used for a wide range of applications starting from food and clothing to diagnostics and therapeutics.[1–5] Interactions of nanoparticles with proteins have been found to alter the conformation of proteins, which in turn could potentially activate unwanted biochemical reactions that may lead to toxicity and disease.[6] Among the nanomaterials, gold nanoparticles (Au NPs) and nanorods (NRs) have been proposed to have large-scale applications especially in healthcare. For example, functionalized Au NPs have been used, among others, for hyperthermia treatment of cancer cells,[7] for estimation of pathogens,[8] for assay of proteins,[9–15] for DNA sensing,[16–18] for enzymatic activity assays[19,20] and for probing selective cellular functions.[21] Further, Au NPs, when functionalized with proteins, have been used for immunoassays,[22,23] light controlled released of drug[24] and for glucose sensing.[25] Recently protein functionalized Au NPs have been used for killing cancer cells.[26] Also, interactions of Au NP with enzymes have led to activity enhancement.[27,28] Anticipating an increasing role of properties of Au NPs and their interactions with proteins in applications related to nanobiotechnology, it deserves attention on a more fundamental level, especially understanding the factors which lead to property modifications of either one or both of them.

Recent investigations of interactions of Au NP dispersions and proteins indicate that when the NPs are stabilized through electrostatic interaction with the stabilizing molecules they tend to form agglomerates in the presence of proteins.[13] The nature and extent of agglomeration depends on the protein and its conformation and also on its concentration in the medium.[29] For example, when citrate-stabilized Au NPs were treated with proteins, the extinction spectrum of the NPs changed systematically with the concentration of the proteins and their conformations.[30] These changes have been associated with

[a]*Department of Chemistry, Indian Institute of Technology, Guwahati, Assam, India – 781039. E-mail: anumita@iitg.ernet.in; arun@iitg.ernet.in*

[b]*Centre for Nanotechnology, Indian Institute of Technology, Guwahati, Assam, India – 781039*

† Electronic supplementary information (ESI) available: Additional UV-Vis spectra, time dependent UV-Vis studies, TEM images, DLS based particle size analyses, zeta potential measurements, FTIR, UV-CD spectra, and enzyme activity measurements. See DOI: 10.1039/c3ra43623c

agglomeration of the NPs and proteins, the extent of which depended on the above mentioned parameters. Studies also indicated specificity of interactions involving a binary mixture of proteins and Au NPs.[31] Interestingly, although the agglomeration behaviours have been studied with substantial details along with the consequences on the properties of the NPs, there is still a lack of systematic studies on the fate of the proteins, especially in regard to their conformation and activity. Our laboratory has recently demonstrated that the agglomeration is associated with the modulation of activity of the enzyme (in this case α-amylase). Further, the modulation has been proposed to be due to oriented attachment of the proteins on the NPs at lower concentrations giving rise to enhanced activity.[28] At higher concentrations of protein, the agglomeration leads to non-availability of the protein for enhanced catalysis. However, there are still many questions about the fate of the conformation of the attached protein. Recent studies indicated possible partial unfolding of the protein upon attachment to the NP.[13,31] In addition, a pertinent question could be raised on the origin of agglomeration. In this respect, it would be important to probe the fate of the agglomerates in the presence of a chemical denaturant of protein, as this may provide at least some answers on the mechanism of agglomeration of a mixture of protein and cit–Au NP. Further, it can be anticipated that knowledge arising out of these studies would facilitate further understanding of the consequences of introducing Au NPs in living systems.

Herein we report the agglomeration behaviour of a mixture of citrate-stabilized Au NPs and a protein (α-amylase) in the presence of urea, which is a chemical denaturant of the protein. The protein α-amylase is an *endo* acting enzyme, which belongs to the glycosidic hydrolase 13 (GH13) family. The molecular weight of α-amylase is 55 kDa, which consists of three domains (Scheme 1). The larger, the N-terminal part, consists of 330 amino acid residues. The central domain has the typical parallel-stranded α/β barrel structure. The C-terminal domain forms a distinct globular unit where the chain folds into an eight-stranded antiparallel β-barrel. The amino acid sequence contains 12 cysteines, 5 disulfide bonds and two exposed free thiol groups (cys 103, cys 119), which are spatially close to each other.[32] The attachment of an Au NP to one free thiol group would facilitate binding with the neighbouring –SH group. It is possible that many α-amylase molecules could bind simultaneously with Au NPs forming an aggregate.[33] Earlier investigations from our laboratory indicated both concentration and conformation dependent changes occurring in a mixture of native or denatured protein and Au NPs.[29,30] However, what we have probed here is the influence of a denaturing agent on the agglomeration of a mixture of protein and Au NPs. UV-Visible spectroscopy, transmission electron microscopy (TEM), dynamic light scattering (DLS) based particle size analysis, zeta potential measurement, UV-circular dichroism (CD) measurement, fluorescence spectroscopy and Fourier transform infrared (FTIR) spectroscopy have been used to establish the potential origin of agglomeration of Au NPs in the presence of the protein. The results indicated that the interaction between the NPs and the native protein in aqueous medium is conformation dependent and this interaction led to the agglomeration of Au NPs and the protein molecules. Initially, smaller agglomerated structures formed between the NPs and protein. However, the sizes of these structures grew with time by incorporating additional proteins and NPs. On the other hand, in the presence of urea further growth of the structures was arrested. Urea not only denatured the proteins in the medium and partly those present on the surface of the agglomerates, but also stabilized the structures. Interestingly, the proteins present in the agglomerates retained enzymatic activity in the presence of urea, in comparison to those present freely in the medium.

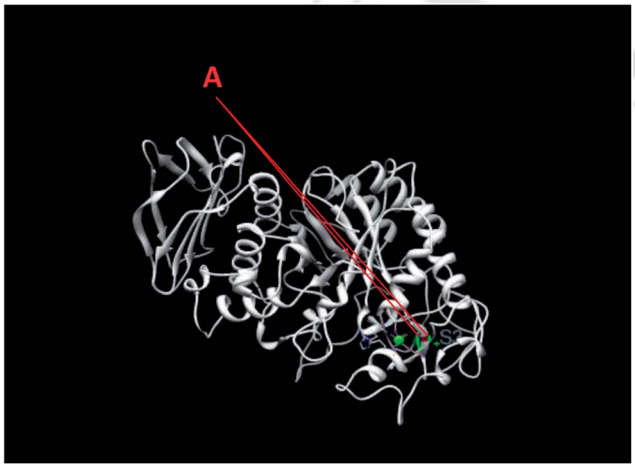

Scheme 1 Three-dimensional structure of α-amylase showing the location of (A) Au NP binding site containing free thiol groups. The protein database (PDB) number is 1SMD.

Experimental section

Materials

α-Amylase from hog pancreas (43.6 U mg^{-1} activity) and hydrogen tetrachloroaurate trihydrate were purchased from Sigma Aldrich Chemical Co., trisodium citrate 2-hydrate (purified) and urea (extra-pure) were purchased from Merck Specialities Private Limited, India. Milli-Q grade water (18.2 MΩ cm) was used for all the experiments. The isoelectric point of α-amylase is 6.5.

Preparation of cit–Au NP dispersion

Citrate stabilized Au NPs were synthesized by the following procedure: a mixture of 0.750 mL of 1.73×10^{-2} M $HAuCl_4$ and 30.0 mL of Milli-Q grade water was taken in a round bottom flask and then heated to boiling under reflux conditions. When the mixture started to boil, 1.0 mL of 0.857 M trisodium citrate 2-hydrate solution was added to the above solution all at once, under constant stirring. The solution first turned faint blue and then changed to deep wine red, indicating the formation of a cit–Au NP dispersion. The solution was boiled and stirred continuously for another 30 min to ensure the complete reduction of $HAuCl_4$. The formation of cit–Au NPs was confirmed by UV-Vis spectroscopy and TEM analysis. The pH of cit–Au NP was 5.5. The dispersion of cit–Au NPs was diluted 2

times with phosphate buffer (0.01 M, pH = 7.0) with overall pH of 6.9, before performing experiments. The concentration of cit–Au NP was found to be 44.6 nM from the particle size from TEM analysis.

Preparation of protein

1.0 mg mL^{-1} α-amylase was used in these experiments. 1.0 mg mL^{-1} of α-amylase was prepared by dissolving α-amylase protein in 0.01 M phosphate buffer. It was found that α-amylase was sparingly soluble in buffer, and hence it was stirred for 15 min in a magnetic stirrer at room temperature to mix it properly. Then, it was centrifuged at 5000 rpm for another 15 minutes. The supernatant was collected and used for further experiments. The actual protein content was determined using the Bradford test for 1.0 mg mL^{-1} solution. The concentration of stock α-amylase solution is 1270 nM. α-Amylase solution was diluted 10 times with phosphate buffer solution to obtain 127 nM. The calibration and actual concentration of α-amylase was calculated by our group.[29] The molar concentrations of protein used in UV-Visible experiments, DLS and zeta potential measurements, TEM analysis and FTIR spectroscopy measurements were from 0.84 nM to 2.5 nM. But for CD analysis and enzymatic activity studies the concentration of protein used was 24.9 nM. The ratios of protein and cit–Au NP used in different experiments were varied from 1 : 0.19 to 1 : 0.56.

Preparation of urea solutions

4 M, 6 M and 8 M urea stock solutions were prepared by dissolving the appropriate amounts of urea in phosphate buffer.

Preparation of denatured α-amylase solution

8 M urea solution was added to a 1.5 mL portion of 1270 nM α-amylase solution and kept for 4 h at 4 °C in a refrigerator. This was then brought to room temperature for further experiments.

Analytical measurements

UV-Vis spectroscopic measurements were carried out using a Hitachi U-2900 spectrophotometer in the range 400–800 nm. FT-IR spectroscopic measurements were performed by using a Spectrum One, Perkin Elmer spectrophotometer in the range 400–4000 cm^{-1}. TEM measurements were made using a JEOL JEM 2100 TEM operating at a maximum accelerating voltage of 200 kV. CD spectra were recorded by using a JASCO J-815 machine. The instrument was calibrated with camphor sulfonic acid. All CD spectra were recorded at 25 °C using a thermostatically controlled cell holder with the path length of cell being 10 mm. DLS and zeta potential measurements for samples were carried out by using a Malvern zeta size Nano-ZS90 instrument at an instrument temperature of 25 °C and viscosity of 0.8872 mPa s. Fluorescence spectroscopic measurements were performed using a Fluromax 4-spectroflurometer with a Xe lamp. Excitation wavelength was set at 280 nm. The excitation and emission slit widths were fixed at 5 nm.

UV-Vis measurements

Successive addition of urea to the cit–Au NP–protein composite. These experiments were performed in three sets. For set I, a mixture of cit–Au NPs, protein and urea, the following procedure was followed: 3.0 mL of cit–Au NP dispersion was taken in a plastic cuvette and its UV-Vis spectrum was recorded. 0.02 mL of 127 nM α-amylase solution was added to it, shaken well for 5 min and the UV-Vis spectrum was recorded thereafter. The final concentration of α-amylase in the mixture was found to be 0.84 nM. 0.01 mL of 8 M stock urea solution was added dropwise to the Au NP–protein composite, shaken well, kept for another 5 min and the UV-Vis spectrum was recorded. The final concentration of urea in the mixture was found to be 0.026 M. This was followed by the addition of 0.02 mL of 8 M stock urea solution to the mixture and the UV-Vis spectrum was recorded. In this manner, successive addition of urea solution was performed, followed by the UV-Vis spectra recording. The addition of urea and recording of spectra was continued till there was no change in the UV-Vis spectra. For every set of experiments the protein concentration was kept constant in the plastic cuvette before adding the urea solution to it. Similar experiments were carried out for 0.04 mL and 0.06 mL α-amylase with 8 M stock urea solution. The final concentration of α-amylase for 0.04 mL and 0.06 mL was found to be 1.7 nM and 2.5 nM, respectively. This completes the set I experiments. For set II, identical experiments were carried out with 4 M of stock urea solution and for set III, similar experiments were carried out with 6 M stock urea solution. The UV-Vis spectra are reported in Fig. S2 and S3 (ESI†).

Calculation of the average area under the UV-Vis spectrum. The area under the UV-Vis extinction curve was determined by using the software which is automatically associated with the operating software of the spectrophotometer. The average area under the extinction curve was calculated by selecting two wavelengths under the extinction spectrum. For calculating the average area, the extreme wavelengths were set at 405 nm and 650 nm.

Sample preparation for TEM analysis

Eight sample solutions were prepared for TEM analysis. They were a solution containing cit–Au NPs (without α-amylase), a solution containing 0.04 mL α-amylase of 127 nM with 3.0 mL of cit–Au NPs dispersion, a mixture of 3.0 mL of cit–Au NPs containing 0.04 mL of 127 nM α-amylase with 0.01 mL of 8 M urea, a mixture of 3.0 mL of cit–Au NPs containing 0.04 mL 127 nM α-amylase with 0.05 mL of urea, and a mixture of 3.0 mL of cit–Au NPs containing 0.04 mL of 127 nM α-amylase with 0.12 mL of 8 M urea. The final concentration of α-amylase in the mixture was found to be 1.7 nM. Similarly, the final concentrations of urea in the mixtures were found to be 0.026 M, 0.129 M and 0.304 M, respectively. The TEM samples for control experiments were made from 3.0 mL of cit–Au NPs in the presence of the corresponding volume of 8 M stock urea solution as mentioned above. The above solutions were drop cast on carbon-coated copper TEM grids (5 min after addition of protein/urea to the cit–Au NP dispersions) and then kept for drying overnight at room

temperature. These grids were analyzed by a Jeol JEM 2100 TEM operating at a maximum accelerating voltage of 200 kV.

Sample preparation for FT-IR measurements

The solutions of cit–Au NPs containing 2.5 nM α-amylase and 0.2 mL of urea (8 M) stock solutions were centrifuged at 25 000 rpm and 4 °C for 30 min and dried at room temperature for recording the FT-IR spectra. FT-IR spectra of native α-amylase, urea, and the above centrifuged pellets were recorded by forming a disc with KBr. The scan was performed in the range of 400–4000 cm^{-1} in transmittance mode.

Particle size analysis by DLS method

3.0 mL of cit–Au NPs dispersion was taken in a quartz cuvette for which the particle size distribution was measured using a Malvern zeta size instrument. 0.04 mL of 127 nM α-amylase solution was added to the above solution of cit–Au NPs and shaken well before recording the particle size distribution. To this solution 0.01 mL of 8 M urea solution was added, shaken well and its particle size distribution was recorded. The final concentration of urea solutions in the mixture was found to be 0.026 M. In this way urea was continually added till addition of 0.05 mL and then 0.120 mL with final concentration of urea of 0.129 M and 0.304 M were achieved. The mixtures were shaken well and particle size distributions were recorded. All the samples were kept for 5 min before recording the particle size distribution.

Zeta potential determination by DLS method

3.0 mL of cit–Au NP dispersion was taken in a quartz cuvette for which the zeta potential was measured using a Malvern zeta size instrument. To this, 0.04 mL of 127 nM α-amylase solution was added and shaken well before recording the zeta potential distribution. The final concentration of α-amylase in the mixture was found to be 1.7 nM. To this 0.01 mL of 8 M urea solution was added and shaken well before recording the zeta potential. The final concentration of urea in the mixture was found to be 0.026 M. This analysis continued till addition of 0.05 mL and then 0.12 mL of 8 M urea to the above solution was attained, in which the final concentrations of urea were found to be 0.129 M and 0.304 M respectively. All the samples were kept for 5 min before recording the zeta potential. Zeta potential was also recorded for mixtures containing 3.0 mL cit–Au NPs with 0.01 mL, 0.05 mL and 0.120 mL of 8 M stock urea solution with final concentrations 0.027 M, 0.131 M and 0.307 M, respectively, by following the above mentioned procedure.

Sample preparation for circular dichroism

For CD measurements, we have used 24.5 nM α-amylase which was 10 times more than other studies. This was necessary to achieve sufficient sensitivity for the measurements. 0.06 mL of 1270 nM α-amylase was added to 3.0 mL of cit–Au NPs and incubated for 5 min and the CD spectrum was then recorded. The final concentration of α-amylase in the mixture was found to be 24.5 nM. Similarly, 0.4 mL of 8 M urea solution was added to the above protein NP composite and kept for another 5 min and the spectrum was monitored. The final concentration of urea in the mixture was found to be 0.92 M. UV-CD spectra were also recorded after 30 min incubation of the samples.

Sample preparation for fluorescence measurements

Fluorescence measurements were carried out in three different modes of addition: in set I, 3.0 mL of sodium phosphate buffer was taken in a fluorescence cuvette and 0.06 mL of 1270 nM α-amylase was added and its emission spectra was recorded by using a Fluromax 4-spectrometer with a Xe lamp. The concentration of α-amylase in solution was found to be 24.9 nM. 0.4 mL of 8 M urea solution was added dropwise to the above solution and mixed well and kept for 5 min before recording the emission spectra. Similarly, the emission spectrum of the maintained mixture of α-amylase and urea in the presence of 3.0 mL of cit–Au NPs was recorded, the protein and urea mixture was added dropwise to cit–Au NPs. Before recording the spectrum, the sample was mixed well and kept for another 5 min.

In set II, 3.0 mL of cit–Au NPs was taken in a fluorescence cuvette and 0.06 mL of 1270 nM α-amylase was added and its emission spectrum was recorded. The above-mentioned protein was added dropwise to 3.0 mL of cit–Au NP dispersion and the time-dependent fluorescence measurements were made. Spectra were recorded after 5, 10, 15, 20, 25 and 30 min from the time of addition of proteins to cit–Au NP dispersion. After 30 min, 0.4 mL of 8 M urea solution was added to the maintained mixture, mixed well and kept for 5 min and the emission spectrum was recorded. The concentration of urea in the solution was found to be 0.92 M.

In set III, 3.0 mL of cit–Au NPs was taken in a fluorescence cuvette and to it 0.06 mL of 1270 nM α-amylase was added and the emission spectrum was recorded. Similarly, 0.4 mL of 8 M urea solution was added simultaneously the above mixture and shaken well, and the emission spectrum of α-amylase was recorded. Before recording the spectra, the samples were kept for 5 min.

Results and discussion

Cit–Au NP dispersions, prepared by the trisodium citrate 2-hydrate reduction of $HAuCl_4$, appeared wine red in colour. When 0.02–0.06 mL of 127 nM α-amylase was added to 3.0 mL of cit–Au NP dispersion, the wine red colour slowly changed to deep purple. This is in accordance with the observations made earlier.[29] Further, when urea was added to this dispersion, the intensity of the purple colour increased marginally. The above observations of colour changes were corroborated by detailed UV-Vis spectroscopic studies described below.

The UV-Vis spectrum of the cit–Au NP dispersion showed a single band with a peak at 521 nm (Fig. 1A) due to the surface plasmon resonance (SPR) peak of the Au NPs. When urea was added to the dispersion, there was a small yet systematic decrease in peak intensity at 521 nm accompanied by slight broadening of the peak, with increasing volume (from 0.01 mL to 0.250 mL) of 8 M solution of urea. On the other hand, the

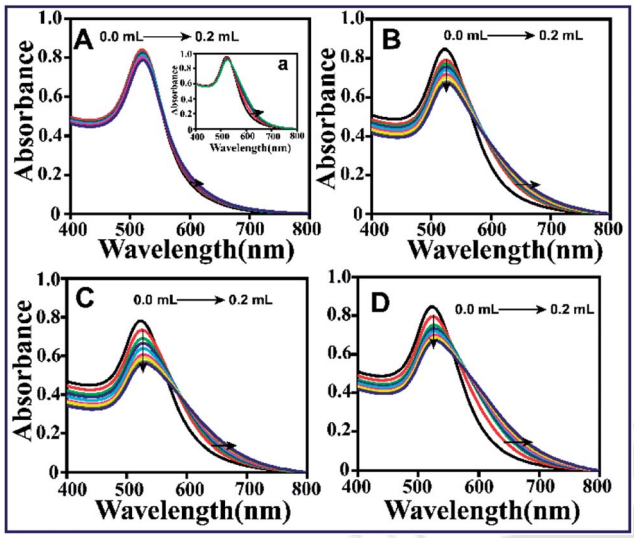

Fig. 1 UV-Vis spectra of 3.0 mL of cit–Au NP solution on successive addition (from 0.01 mL to 0.2 mL) of 8 M stock urea solution, already containing (A) 0.00 mL, (B) 0.02 mL, (C) 0.04 mL and (D) 0.06 mL of α-amylase. The stock concentration of α-amylase was 127 nM. All the UV-Vis spectra were recorded after 5 min incubation. Cit–Au NP mixture with α-amylase was kept for 5 min, urea was added to the composite, kept further for 5 min and then the spectra were recorded. Inset: (a) UV-Vis spectra of 3.0 mL of cit–Au NP solution on addition of 0.02–0.06 mL of 127 nM α-amylase.

effect of addition of α-amylase to cit–Au NPs is known to broaden the SPR band due to the agglomeration of the Au NPs upon adsorption of the native protein to the surface of the NPs.[29,30] In this study too we observed that increasing amounts of α-amylase (0.02–0.06 mL of 127 nM) to cit–Au NPs (3.0 mL) led to considerable broadening of the SPR peak accompanied by a small but consistent red shift (521 to 524 nm) in the peak maximum (Fig. 1A inset, and Fig. 3B). More importantly though, it was observed that increasing amounts of α-amylase did not cause significant decrease in the SPR peak intensity at 521 nm (Fig. 1A inset), an observation which differed from that obtained by the addition of urea to cit–Au NPs (*i.e.* Fig. 1A) where the peak intensity at 521 nm decreased with increasing urea concentration. Thus the slight decrease in peak intensity at 521 nm in the case of urea addition to cit–Au NPs, in Fig. 1A, is probably related to dilution of the sample.

Urea is known to denature free protein.[34] However, when α-amylase is bound to cit–Au NPs, the effect of added urea showed some interesting behaviour, both as a function of concentration and as a function of time. Fig. 1(B–D) shows the effect of added urea concentration on the SPR band of cit–Au NP dispersion containing α-amylase. To delineate the time effects from concentration effects, the concentration spectra in Fig. 1(B–D) were recorded with a constant delay of 5 min between additions of any reagent. It was found that when 0.01 mL of 8 M urea solution was added to 3.0 mL of cit–Au NP solution containing a specific amount of α-amylase (in the range 0.02–0.06 mL of 127 nM), the absorption maximum shifted from 523 nm to 525 nm with increasing amount of urea. In other words, successive additions of urea (up to 0.2 mL) led to increasing broadening of the SPR peak towards longer wavelengths. But additions beyond 0.150 mL of 8 M stock urea solution resulted in no further change in the UV-Vis spectrum (Fig. 1B–D) indicating that a saturation concentration of urea was reached. The final concentration ranges of urea and α-amylase in these solutions were 0.026–0.378 M and 1.7–2.5 nM respectively corresponding to Fig. 1B–D, respectively. Similar UV-Vis results for studies carried out with 4 M and 6 M stock solutions of urea are given in the ESI (Fig. S2 and S3†), which demonstrate reproducibility of the results even at lower concentrations of urea.

A better representation of the twin effects of peak broadening and SPR peak intensity changes in Fig. 1A–D is obtained by plotting the area under these spectra (between 405 and 650 nm) against the concentration of urea for each α-amylase containing cit–Au NP solution as shown in Fig. S1A.† It was found that in the presence of α-amylase, the SPR peak area decreased exponentially with increasing concentration of urea and the effect was more pronounced for cit–Au NPs containing larger amounts of α-amylase (Fig. S1A†). It may be noted that a similar plot of area under the SPR peak of cit–Au NPs plotted against concentration of α-amylase in the absence of urea (Fig. S1B†) yielded a graph whose area increased linearly with the concentration of the protein and then reached saturation level, consistent with our earlier findings.[30] Thus while the addition of α-amylase increased the area under the curve as well as broadened the SPR peak, addition of urea in the presence of the protein had the effect of more broadening but accompanied with a systematic decrease in peak area. The latter was due to a significant decrease in SPR peak intensity. The combined results in Fig. 1 and S1† suggest that the agglomeration process of cit–Au NPs with α-amylase is not necessarily driven by denaturation of the protein.

Previous time-dependent UV-Vis spectroscopic studies of cit–Au NP in the presence of α-amylase indicated that the broadening of SPR peak in the presence of α-amylase gradually increased with time and reached a saturation level, beyond which further broadening was not observed.[29] In the present study, when 0.06 mL of 127 nM α-amylase was added to 3 mL of cit–Au NP solution the UV-Vis spectrum recorded at 5 min intervals was found to evolve slowly with time (Fig. 2A). Further, with time the changes became less and less apparent and after about 40 min the changes were hardly noticeable. In other words, the spectrum reached a 'saturation point' in time. Thereafter, 0.01–0.2 mL of 8 M stock urea was added and the evolution of the UV-Vis spectrum was recorded at increasing concentrations of urea, the results of which are displayed in Fig. 2B. The addition of urea to the 'time saturated' cit–Au NP–protein composite resulted in a slight decrease in the peak absorbance at 522 nm accompanied by a slight red shift to 524 nm. Apart from this, the 'time saturated' spectrum of cit–Au NP protein composite was not much affected upon addition of urea. Small changes that are observed in Fig. 2B are similar to the control experiments of addition of urea to cit–Au NP (Fig. 1A) and may be attributed to dilution effects. We conclude from here that once protein agglomeration with cit–Au NP is complete, urea had a minimal effect on the UV-Vis spectrum.

In another experiment, 0.06 mL of 127 nM α-amylase was added to 3.0 mL of cit–Au NP dispersion. After 5 min, 0.12 mL of

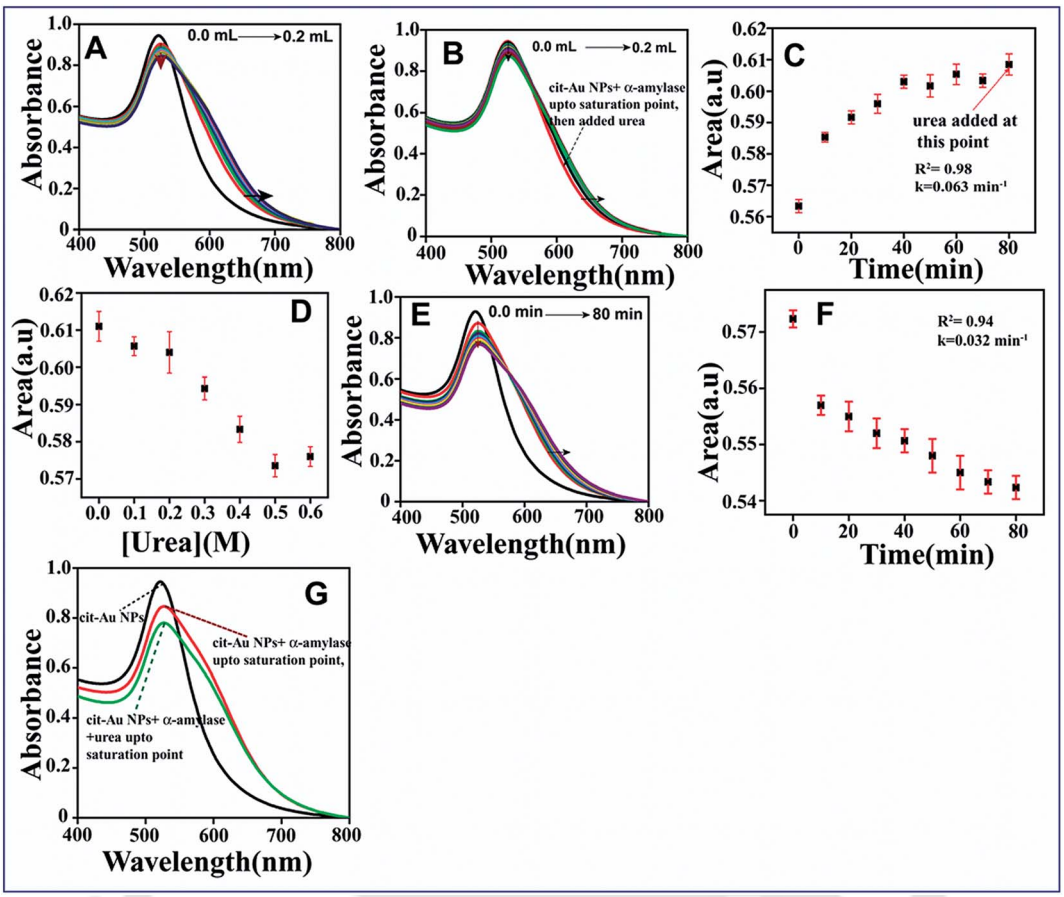

Fig. 2 (A) Time dependent UV-Vis spectra of 3.0 mL of cit–Au NPs in the presence of 0.06 mL of α-amylase (0–80 min). (B) Time dependent UV-Vis extinction spectra of 3.0 mL of cit–Au NPs in the presence of 0.06 mL of α-amylase after reaching saturation point and addition of successive amounts of 8 M urea solution (0.01–0.2 mL). (C) Area under the curves in (A) *versus* corresponding time. (D) Area under the curves in the presence of 0.06 mL of α-amylase after reaching saturation point and then adding successive amounts of 8 M stock urea solution. (E) Time dependent UV-Vis extinction spectra of 3.0 mL of cit–Au NPs in the presence of 0.06 mL of α-amylase and 0.12 mL urea solutions (0–80 min). Cit–Au NP–protein composites were kept for 5 min and then urea solution was added to it and the extinction spectra were recorded. (F) Area under the curves in (E) *versus* corresponding time. (G) Comparative broadening up to saturation point of 3.0 mL cit–Au NPs in the presence of 0.06 mL of α-amylase, and of 3.0 mL of cit–Au NPs in the presence of 0.06 mL of α-amylase and 0.12 mL urea solution. The stock concentrations of α-amylase and urea were 127 nM and 8 M, respectively. The error bars were calculated from three set of experiments.

8 M urea solution was added and the UV-Vis spectra were recorded at 5 min intervals. In the presence of urea, the UV-Vis spectrum of a cit–Au NP and α-amylase mixture was found to evolve with time accompanied by a substantial decrease in peak absorbance at 522 nm. Further, a shoulder at 600 nm became prominent and there appeared to be an isosbestic point at 575 nm (Fig. 2E). Interestingly, we found that the isosbestic point was sharper when the concentration of urea was higher for the same concentration of protein (Fig. S4†). Since the agglomeration of cit–Au NPs in the presence of protein does not lead to an isosbestic point (Fig. 2A), the origin of the isosbestic point must be attributed to the presence of urea in the system during the agglomeration process of α-amylase and cit–Au NP seen in Fig. 2E. Further, this system also reached a saturation point in time beyond which no further change in the spectrum was observed (Fig. 2E). A comparison of the time saturated spectra in Fig. 1A and 2E is given in Fig. 2G, which shows that in the presence of urea, the extinction spectrum of the cit–Au NP–protein composite broadened more with time than in the absence of urea. The combined results in Fig. 2A, E and G suggest that the conformations of proteins around cit–Au NP in the two agglomerated systems, *i.e.* α-amylase in the presence of urea and α-amylase in the absence of urea, are different.

A comparison of plots of area under the UV-Vis spectra with time and concentration of urea for the two cases: Fig. 2C for cit–Au NPs in the presence of only α-amylase up to the saturation point and Fig. 2D for cit–Au NPs in the presence of α-amylase after reaching the saturation point and then addition of urea, shows that in the absence of urea the peak area increased up to the saturation point. Further, addition of increasing amounts of urea to the cit–Au NP–protein composite at 'saturation point' caused the area to decrease (Fig. 2D). Similarly the area under the SPR band of cit–Au NPs in the presence of freshly added α-amylase and a constant amount of urea also decreased with time (Fig. 2F). Thus here again we find the spectral behaviour of cit–Au NP is different in the presence of α-amylase only, on one hand, and in the presence α-amylase plus urea, on the other hand.

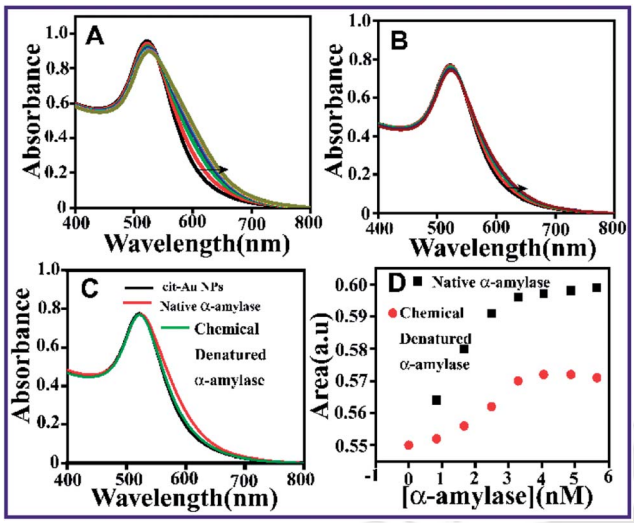

Fig. 3 UV-Vis spectra of 3.0 mL of cit–Au NPs in the presence of: (A) various amounts of native α-amylase of 127 nM with final concentration from 0.84–5.66 nM added successively, (B) various amounts of chemically denatured α-amylase (0.02–0.08 mL of 127 nM with final concentration from 0.84–5.66 nM added successively, (C) comparative analysis of native α-amylase (0.04 mL as final concentration 1.7 nM) and denatured α-amylase (0.04 mL as final concentration 1.7 nM), (D) comparison of normalised area under the extinction curves of native α-amylase (0.84–5.66 nM) and denatured α-amylase 0.84–5.66 nM).

An estimate of the rates of the two processes can be obtained from Fig. 2C and F. Both the processes are first order but the former showed an exponential growth while the latter showed an exponential decay in the area under their respective extinction spectra with time. The rate constant for the growth in the peak area of the cit–Au NP spectrum in the presence of α-amylase was 0.064 min^{-1}, while the first order decay in the peak area of the cit–Au NP spectrum in the presence of urea and α-amylase occurred with a rate constant of 0.032 min^{-1}. Thus the conformation changes of α-amylase in the presence of urea (leading possibly to denaturation) proceeded more slowly than the conformational changes occurring in the absence of urea when cit–Au NPs was present in the system. As a result, at higher concentrations of urea the rate of denaturation of protein can effectively compete with the agglomeration process possibly explaining the more pronounced isosbestic point in the UV-Vis spectra of cit–Au NPs (ESI and Fig. S4†). Also, the difference in rates of the two processes suggests that the conformational changes of α-amylase associated with cit–Au NPs are probably distinct and different from those which occur in the presence of denaturant urea. The overall observations, so far thus, seem to suggest that the changes in the optical behaviour of cit–Au NPs in the presence of a denaturant added after the addition of α-amylase are distinctly different from the optical behaviour of cit–Au NPs containing only α-amylase.

The large drop in the area under the extinction spectrum of the cit–Au NP–protein composite on addition of urea (Fig. 2F) probably reflects conformational changes in α-amylase, which affect the next stage of interaction of the protein with Au NPs. It is obvious that the UV-Vis spectrum of cit–Au NPs broadened in the presence of protein only (Fig. 2A) till the 'saturation point'. Further, when urea was added after the saturation point, the spectrum changed marginally (Fig. 2B). It is reported that the denatured form of α-amylase broadens the extinction curve of cit–Au NPs less than the native form of protein α-amylase.[29] Therefore the marginal changes in Fig. 2B suggest that urea is unable to affect the conformation of the protein once it is agglomerated in the protein–cit–Au NPs composite. However, if urea is added early on, during the course of the agglomeration process of α-amylase with cit–Au NPs, the denaturation process may effectively compete and change the course of the agglomeration process. The large changes in the spectral characteristics shown in Fig. 2E and the drastic drop in area under the SPR band in Fig. 2F, are indicative of an interplay of such competing processes. Therefore, when urea is present while the agglomeration process is taking place, simultaneous changes in the conformation of α-amylase[30] must be responsible for the greater broadening of the SPR peak of Au NPs. Moreover, when time dependent UV-Vis spectra were recorded for cit–Au NPs containing constant amount of α-amylase, but different concentrations of urea, it was found that for higher concentrations of urea the SPR peak broadened more (Fig. S4, ESI†). The first order rate constants extracted from the exponential decay in the peak area under these SPR bands showed that peak broadening was faster for higher concentrations of urea (Fig. S4F†). This is consistent with the more pronounced isosbestic point in the UV-Vis spectra of the cit–Au NP α-amylase system at higher concentrations of urea (ESI, Fig. S4†). This indicated that in the presence of α-amylase only, cit–Au NPs agglomerated more easily whereas in the presence of urea the extent of agglomeration was less.

We have observed that when 0.02 mL of native α-amylase was added to 3.0 mL of cit–Au NPs, the absorption maximum shifted from 521 nm to 523 nm (Fig. 3A and inset to Fig. 1A). The changes in spectral characteristics continued to occur with more addition of protein till a volume of 0.08 mL was reached when the protein concentration was 3.29 nM, indicating a saturation of the process (Fig. 3D). Similar experiments carried out in the presence of 0.08

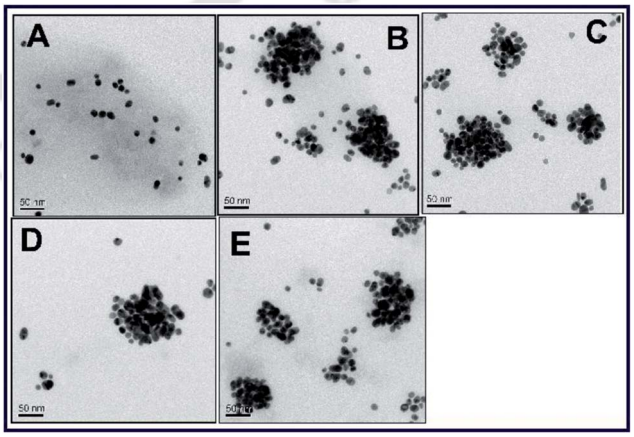

Fig. 4 TEM images (scale bar 50 nm) of 3.0 mL of cit–Au NPs dispersions in the presence of (A) 0.00 mL α-amylase, (B) 0.04 mL of α-amylase, (C) 0.04 mL α-amylase + 0.01 mL urea solution, (D) 0.04 mL of α-amylase + 0.05 mL urea solution, (E) 0.04 mL α-amylase + 0.12 mL urea solution. The stock concentrations of α-amylase and urea were 127 nM and 8 M, respectively.

mL of 127 nM chemically denatured α-amylase showed nominal changes in the spectral characteristics (Fig. 3B) which saturated at a concentration of 4.09 nM as seen on a plot of area *vs.* concentration (Fig. 3D). A clear comparison of the two saturated spectra, seen in Fig. 3C, shows greater SPR peak broadening of cit–Au NPs in the presence of native α-amylase than in the presence of chemically denatured α-amylase. A comparison of plots of area under the UV-Vis spectra with the concentrations of the native and denatured protein in Fig. 3D show that the area increases in both cases, it does so less in the presence of denatured protein than in the case of native protein. The above results indicate that the agglomeration of cit–Au NPs and protein depended not only on the concentration of protein but also on its conformational state.

To ascertain the origin of broadening in the UV-Vis spectra, further investigations were carried out with TEM measurements. Fig. 4A shows the image of cit–Au NP dispersion produced by the present method in the absence of protein. The average size of cit–Au NPs was found to be 10.0 ± 2.2 nm. The Au NPs produced were nearly monodispersed and spherical in shape. Addition of 0.04 mL of α-amylase to 3.0 mL of cit–Au NP dispersion led to the agglomeration without affecting the individual size of the NPs (Fig. 4B). When 0.01 mL of 8 M urea solution was added to the above solution (Fig. 4C), the size of the agglomerates was similar to the cit–Au NP–protein composite in Fig. 4B. It is noteworthy that Fig. 4C also shows the presence of a significant number of Au NPs that were not aggregated. Further addition of increasing amounts of 0.05–0.12 mL 8 M urea to the cit–Au NP–protein composite did not result in significant increase in the extent of agglomeration of the NPs as is evident from Fig. 4(C–E). Thus, the TEM results showed that cit–Au NPs in the presence of the native form of α-amylase were agglomerated. Further agglomeration was not observed when urea was added to the composite. The slight increase in extent of agglomeration that was seen could be induced by evaporation of the samples on the TEM grid.

The agglomeration of cit–Au NPs in the presence of proteins has been studied earlier by our laboratory.[29] It was found that cit–Au NPs underwent agglomeration with increasing concentration of α-amylase.[29] Such agglomeration behaviour of NPs in the presence of proteins has helped in deciphering its conformation also. Our findings here suggest that when a solution of urea was added to a cit–Au NP dispersion in the presence of α-amylase the on-going agglomeration process was affected. This indicates that adding a chemical denaturant does not necessarily promote agglomeration of the cit–Au NP–α-amylase composite. Similarly, TEM images of samples consisting of 3.0 mL of cit–Au NPs in the presence of either 0.01 mL, 0.05 mL or 0.12 mL of 8 M stock urea solutions were also recorded and the results are reported in Fig. S5 (ESI†). These images also indicate negligible agglomeration in the absence of protein. This is consistent with our observations that upon addition of urea to the Au NP dispersions in the absence of α-amylase, little change was observed in the absorption spectra of cit–Au NPs (Fig. 1A).

Further investigations on agglomeration of NPs were carried out by DLS-based measurement of particle size distribution (Fig. 5). These DLS studies also substantiated the formation of agglomerated NPs in the presence of protein, consistent with TEM and UV-Vis spectroscopic results. The agglomerated state was found to remain unchanged upon addition of urea to a solution of cit–Au NPs containing α-amylase. DLS based particle size analysis indicated that for cit–Au NPs only, the hydrodynamic diameter of the particles was 19 nm and the maximum of the particle size distribution was found to be at 37 nm. The hydrodynamic diameter and the maximum distribution of particle sizes are shown in Table 1. In the presence of 0.04 mL of 127 nM α-amylase the hydrodynamic diameter was found to increase to 38 nm and the maximum was found to shift to 77 nm. To this solution (3.0 mL cit–Au NPs containing 0.04 mL of

Table 1 Particle size distribution from DLS measurements using 8 M urea stock solution. All the samples were kept for 5 min before recording the particle size distribution. Urea was added to cit–Au NP α-amylase composite at 5 min intervals

		Peak 1		Peak 2	
Sample	Size (*d* nm)	Size (*d* nm)	Area (%)	Size (*d* nm)	Area (%)
3.0 mL cit–Au NPs	19	37	82.4	1.7	9.7
3.0 mL cit–Au NPs + 0.04 mL of 127 nM α-amylase	38	77	90.4	4.7	9.6
3.0 mL cit–Au NPs + 0.04 mL of 127 nM α-amylase + 0.01 mL of 8 M urea solution	40	80	87.3	8.2	6.8
3.0 mL cit–Au NPs + 0.04 mL of 127 nM α-amylase + 0.05 mL of 8 M urea solution	41	85	89.1	4.6	10.9
3.0 mL cit–Au NPs + 0.04 mL of 127 nM α-amylase + 0.120 mL of 8 M urea solution	41	86	88.4	4.4	8.9
3.0 mL cit–Au NPs + of 127 nM α-amylase + 0.2 mL of 8 M urea solution	41	86	87	7.7	8.8

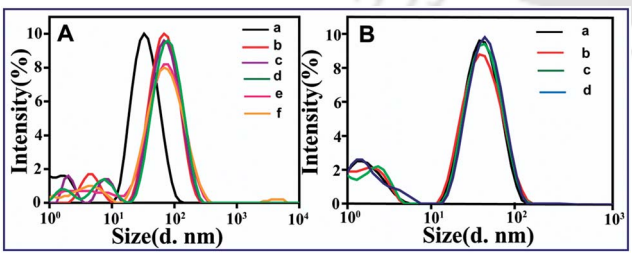

Fig. 5 Particle size distribution curves of (A) 3.0 mL of cit–Au NPs dispersion in the presence of (a) 0.00 mL α-amylase, (b) 0.04 mL α-amylase, (c) 0.04 mL of α-amylase + 0.01 mL of urea solution, (d) 0.04 mL α-amylase + 0.05 mL urea solution, (e) 0.04 mL α-amylase + 0.12 mL urea solution, (f) 0.04 mL α-amylase + 0.2 mL urea solution (the stock concentrations of α-amylase and urea were 127 nM and 8 M, respectively); (B) 3.0 mL of cit–Au NPs dispersion in the presence of (a) 0.00 mL, (b) 0.01 mL, (c) 0.05 mL, (d) 0.12 mL urea solution (the stock concentration of urea was 8 M). All the samples were kept for 5 min before recording the particle size distribution.

Table 2 Results of zeta potentials of cit–Au NPs in the presence of 127 nM of α-amylase and 8 M urea solutions

Samples	Zeta potential (mV)
3.0 mL cit–Au NPs	−50.6
3.0 mL cit–Au NPs + 0.04 mL of 127 nM α-amylase	−47.7
3.0 mL cit–Au NPs + 0.04 mL of 127 nM α-amylase + 0.01 mL of 8 M urea solution	−47.0
3.0 mL cit–Au NPs + 0.04 mL of 127 nM α-amylase + 0.05 mL of 8 M urea solution	−46.6
3.0 mL cit–Au NPs + 0.04 mL of 127 nM α-amylase + 0.120 mL of 8 M urea solution	−44.4

127 nM α-amylase) when increasing amounts of urea (0.01 mL to 0.12 mL of 8 M) were added, the hydrodynamic diameter was found to increase slightly from 40 to 41 nm and the maximum of distribution shifted from 80 to 86 nm (Table 1 and Fig. 5A). Any further addition of urea (see 0.2 mL of 8 M, Table 1) did not affect the distribution of the agglomerated state.

However, our UV-Vis data showed increased broadening upon addition of urea. To reconcile our DLS and TEM findings with UV-Vis results, it is proposed that the size of the agglomerated units remained the same upon addition of urea, and changes in dielectric constant of the local environment resulted in the observed broadening of UV-Vis spectra. DLS studies with 4 M and 6 M stock urea solutions were also carried out resulting in similar observations (Fig. S6, Table S1 and S2, ESI†). It is noteworthy that in the absence of α-amylase there was no significant change in the size distribution of cit–Au NPs upon addition of urea (Fig. 5B).

Collective observations made from UV-Vis studies, DLS measurements and TEM analysis suggested the likelihood that the presence of α-amylase led to the agglomeration of Au NPs, which remains unchanged by the further addition of urea, and that the broadening of the SPR peak on adding urea to the Au NP–protein composite might be due to other effects such as changes in dielectric constant of the medium.[35] The peptide chain of α-amylase contains 12 cysteine groups of which two –SH groups are exposed to the aqueous medium.[33] These –SH groups have a strong affinity to bind with the surface of Au NPs. That the α-amylase was adsorbed on cit–Au NPs was confirmed by zeta-potential measurements, where addition of 0.04 mL of 127 nM α-amylase to 3.0 mL cit–Au NPs caused the negative surface charge to drop from −50.6 to −47.7 mV. If we correlate the findings, the addition of α-amylase to a solution of cit–Au NPs showed a red-shift in the SPR band (Fig. 1) together with an increase in the hydrodynamic diameter (Table 1) and a drop in the negative surface charge (Table 2), they indicate a substantial coverage of the protein on the surface of the cit–Au NP.[15]

At pH ∼ 7, α-amylase is slightly negatively charged/nearly neutral (isoelectric point = 6.5), whereas the Au NPs, synthesised in the presence of excess citrate ions and fully deprotonated at pH 7.0, are stable due to the electrostatic repulsion between the negatively charged citrate capped Au NPs. Upon addition of α-amylase to cit–Au NPs, the surface charge of −47.7 mV is still sufficiently negative to stabilize the Au NPs. Thus the origin of the agglomeration of Au NPs in the presence of α-amylase is unlikely to be electrostatically driven. It is probable that at the initial stages, the nearly neutral α-amylase is driven towards the negatively charged cit–Au NPs by local electrostatic interactions involving functional groups such as the quaternary amine groups with the citrate capping agent of the Au NPs. Once the proteins and the NPs are close enough –SH groups interact with Au to form Au–S bonds. This could happen at the expense of some of the citrate molecules which are replaced from the surface of the Au NPs to make room for the incoming protein molecules. This could explain the reduced negative surface charge density observed in zeta potential measurements. Further, the adsorption of the α-amylase may lead to conformational changes in the protein which then could drive the observed agglomeration process. Also, the presence of excess proteins may lead to larger-scale agglomeration where additional proteins may remain as such without being directly attached to the Au NPs. Addition of 0.01 mL of 8 M stock urea solution to the Au NP–α-amylase dispersion showed a red shift in the SPR band from 523 nm to 525 nm (Fig. 1) accompanied by an increase in size from 38 nm to 40 nm and a slight decrease in the negative surface charge from −47.7 mV to −47.0 mV. Addition of increasing amounts of 8 M stock urea (from 0.01 mL to 0.12 mL) to the Au NP–α-amylase dispersion showed decreasing peak intensity at 523 nm accompanied by increasing broadening of the SPR band (Fig. 1) together with marginal increase in size from 40 nm to 41 nm and a decrease in the surface charge from −47.0 mV to −44.4 mV (Table 2). This means that the presence of urea did not destabilize the Au NPs by changing the overall electrostatic interactions in any major way. The above observations suggest that while electrostatic effects have a minor role to play in agglomeration of Au NPs in proteins, urea still is able to affect the surface charge of Au NPs, which presumably are embedded inside the agglomerated unit. Thus urea can possibly permeate inside the agglomerated structure. These trends in zeta potential measurements and sizes are consistent with the negligible enhancement in agglomeration of the protein conjugated Au NPs in the presence

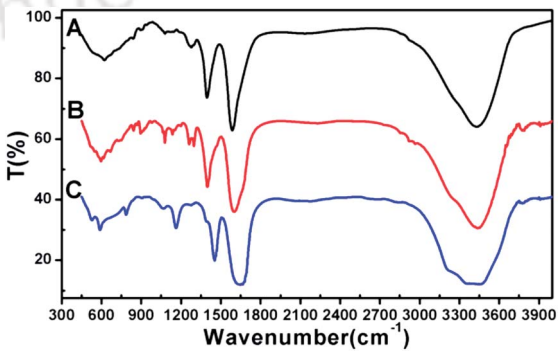

Fig. 6 FTIR spectra of cit–Au NPs in the presence of (A) 0.00 mL of α-amylase, (B) 0.04 mL of α-amylase and (C) 0.04 mL of α-amylase + 0.2 mL of 8 M urea. The FTIR spectra of α-amylase and urea are shown in Fig. S7 (ESI†).

of urea, which were also substantiated by the TEM and UV-Vis measurements that were shown in Fig. 4 and 1, respectively. Further increase in the added volume of 8 M stock urea (0.05 mL and 0.12 mL) to cit–Au NPs resulted in further decrease in measured zeta potential (−45.8 mV and −44.1 mV) without any accompanying change in the hydrodynamic diameter (Table S3, ESI†). The decreasing trend of zeta potential indicated that the overall negative charge on Au NPs decreased which may be due the direct interaction of urea with the cit–Au NPs. It is noteworthy that the addition of 0.01 mL of 8 M urea stock solution to cit–Au NPs resulted in decrease in the negative surface charge from −49.7 mV to −47.9 mV without the concomitant increase in the hydrodynamic diameter. The latter was also substantiated from UV-Vis results (Fig. 1D) where no significant agglomeration of cit–Au NPs was detected upon addition of urea.

IR spectroscopy is also an important technique to study the interaction between biomolecules and NPs.[36] Conformational changes of protein adsorbed on Au NPs have been studied by IR spectroscopy.[37] In IR spectra, proteins show three different amide bands: amide I, amide II and amide III, which provide important characteristic information for different type of secondary structures of protein. Among all the amide bands, the amide I band is found in the region of 1700–1600 cm^{-1} and is the most important in exploring the secondary structure of proteins.[38] We have recorded the FTIR spectra of native α-amylase and its conjugates with cit–Au NPs in the presence and absence of urea at pH 7.0. Pure native α-amylase showed an FTIR band in the 1625–1700 cm^{-1} region corresponding to the amide I linkage (Fig. S7, ESI†), whereas cit–Au NP showed a sharp FTIR band at around 1589 cm^{-1} which is due to ν(C═O) vibration of citrate on its surface (Fig. 6A).[39] When 1.7 nM of α-amylase was added to 3.0 mL of cit–Au NPs the FTIR spectrum showed a broad band at 1598 cm^{-1} corresponding to the cit–Au NP–protein composite (Fig. 6B). Further, several sharp peaks became prominent (Fig. 6B) such as the one at 1327 cm^{-1} which corresponds to the $\nu(COO^-)$ vibration and at 920 cm^{-1} corresponding to $\gamma(CH_2)$ of citrate group (ESI, Fig. S7†). Since these features were not prominent in the FTIR spectrum of citrate capped Au NPs (Fig. 6A), we conclude that upon addition of α-amylase a change in the environment around citrate ions occurs. It is possible that some of the Au NP surface bound citrate ions are released into polar regions of the protein which is consistent from our zeta potential measurements. When 0.301 M urea solution was added to the Au NP–α-amylase composite, the FTIR band of amide I red shifted indicating possible deformation of the protein structure in the presence of urea (Fig. 6C). FTIR studies support that the conformational changes in α-amylase by cit–Au NPs are distinct from the conformational changes induced by urea. Hence, while the former leads to agglomeration in the cit–Au NP–α-amylase system the introduction of the latter (urea) in the system stalls the agglomeration process.

The stability of the NPs was further investigated by studying agglomeration of the Au NP–protein composite in an aqueous solution over a range of NaCl concentrations. It is well known that electrolyte induced agglomeration occurs when the equilibrium between electrostatic repulsion forces and van der Waals attractive forces is disturbed due to changes in the thickness of the double layer.[40] Thus, for example, it is reported that cit–Au NPs undergo agglomeration in the presence of an electrolyte such as NaCl at high concentrations.[41] We have found that addition of increasing amounts (0.05–0.5 mL) of 50 mM NaCl to the cit–Au NP–protein composite at pH 7.0 broadens the 522 nm SPR band towards longer wavelengths (Fig. 7A). This broadening is similar to that observed in the case of addition of urea to cit–Au NP–protein composite (Fig. 2B). As the SPR broadening is not

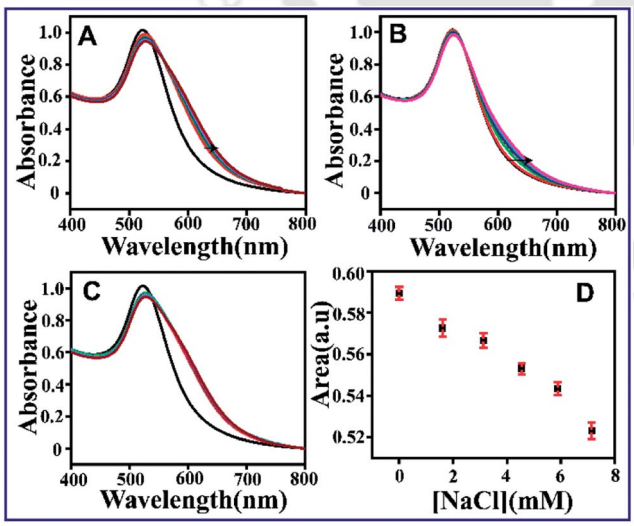

Fig. 7 UV-Vis spectra of 3.0 mL cit–Au NPs in the presence of (A) 0.06 mL α-amylase + 0.05–0.5 mL of 50 mM NaCl at pH 7.0. All the samples were kept for 5 min before recording the spectra; (B) 0.05–0.5 mL of 50 mM NaCl. (C) Time dependent UV-Vis spectra of 3.0 mL of cit–Au NPs in the presence of 0.06 mL of 127 nM α-amylase and 0.2 mL of 50 mM NaCl. NaCl was added after reaching the saturation point of Au NP–protein composite (0–60 min). (D) Area under the curve of (A) between 405 and 650 nm. The error bars were calculated from three individual experiments.

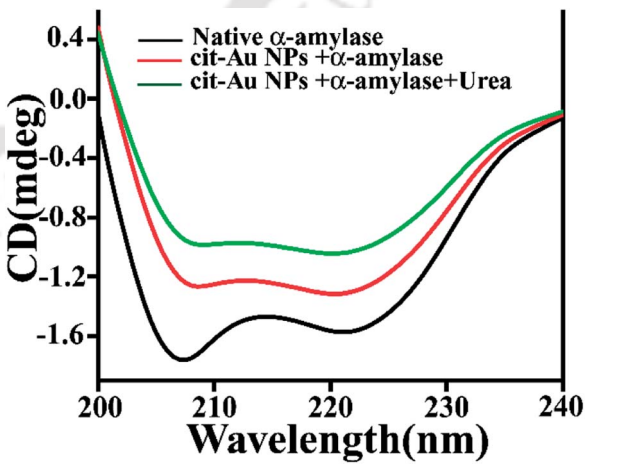

Fig. 8 CD spectra of 0.06 mL of α-amylase (black line), 3.0 mL of cit–Au NPs and 0.06 mL of α-amylase (red line) and 3.0 mL of cit–Au NPs and 0.06 mL of α-amylase with 0.4 mL of urea (green line). Spectra were recorded in the wavelength region 200–240 nm. Stock concentrations of 24.9 nM and 8 M were used for α-amylase and urea, respectively, in each set of experiments and the samples were kept for 5 minutes.

Table 3 Helicity of protein α-amylase obtained from UV-CD spectroscopy

Samples	α-Helix (%)	β-Sheet (%)
3.0 mL α-amylase	82	6
3.0 mL cit–Au NPs + 0.06 mL of 1270 nM α-amylase	74	26
3.0 mL cit–Au NPs + 0.06 mL of 1270 nM α-amylase + 0.4 mL of 8 M stock urea solution	70	29

accompanied by agglomeration as corroborated by DLS measurements, it is probably a result of changes in dielectric constant of the medium surrounding the protein layer on the surface of Au NPs, in both the cases. This is consistent with control experiments in the absence of α-amylase, which showed that when 50 mM of NaCl was added to cit–Au NPs, the UV-Vis spectra broadened slightly (Fig. 7B); which was similar to the results obtained upon addition of urea to cit–Au NPs (Fig. 1A). In this regard it is interesting to note from plots of area under the UV-Vis spectra and particle size distribution (Fig. 7D and Fig. S9, Tables S5 and S6 in ESI†) that the area under the UV-Vis spectra of protein–Au NP composites containing NaCl decreased with increasing electrolyte concentration.

CD spectroscopy is a powerful tool for studying protein conformations either when in solution or when adsorbed on a surface.[42] Fig. 8 shows far-UV CD spectra of native α-amylase, Au NP–α-amylase and Au NP–α-amylase in the presence of urea at pH 7.0. The CD spectrum of native α-amylase at pH 7.0 showed two negative minima in the ultraviolet region occurring at 208 nm and 222 nm, which are the significant peaks for α-helical conformations of protein.[42] Tabulated results obtained from the UV-CD spectra are given in Table 3, which show that the conformation of native α-amylase consists of 86% α-helix and 6% β-sheets. In the presence of cit–Au NPs after 5 min, conformational changes occur in the protein wherein some α-helix structures are converted to β-sheets, but 74% α-helix content is still retained (Table 3). These conformational changes in adsorbed α-amylase presumably result in agglomeration of the cit–Au NP–protein composites. Further when urea was added, conformational changes proceeded slowly, so that after 5 min 70% α-helix and after 30 min about 30% α-helix content still remained (Fig. S10 and Table S7 in ESI†). Interestingly though, control experiments upon addition of urea to α-amylase show that conformational changes are faster such that after 30 min only 10% α-helix content remains (Fig. S11 and Table S8 in ESI†). This suggests that cit–Au NP–protein agglomerates are more resistant to chemical unfolding of the protein by urea than free protein.[34] It is plausible that in the presence of cit–Au NPs the conformational changes directly increase the stability of the α-helix structures of the adsorbed protein molecules making them less susceptible to attack by urea than the free protein molecules. The results of CD, FTIR and DLS all are consistent with this view. The reduced enzyme activity of the cit–Au NP–protein composite and further reduction of this activity by urea (Fig. S8, ESI†) is also consistent with this model.

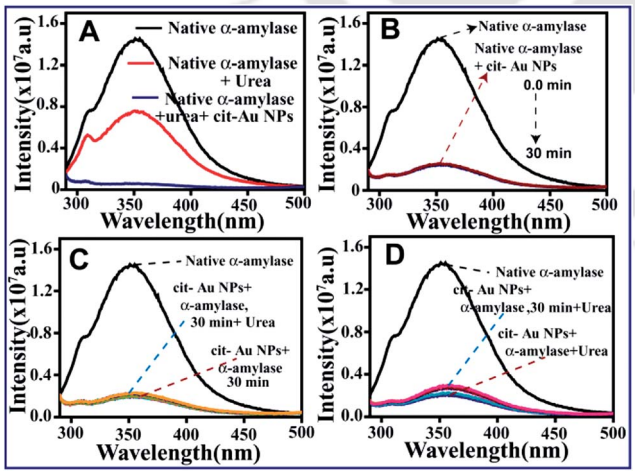

Fig. 9 Fluorescence spectra of native α-amylase, in the presence of 0.4 mL of urea, and α-amylase in the presence of 0.4 mL urea and 3.0 mL of cit–Au NPs (A). Time dependent fluorescence spectra of α-amylase (B) in the presence of 3.0 mL cit–Au NPs (0–30 min). (C) Addition of 0.4 mL of urea to the mixture containing 0.06 mL of α-amylase and 3.0 mL of cit–Au NPs after 30 min. (D) Simultaneous addition of 0.06 mL α-amylase and 0.4 mL of urea to 3.0 mL of cit–Au NPs. Spectra were recorded after 5 min. The stock concentrations of urea and α-amylase were 8 M and 127 nM, respectively.

Fluorescence studies are used to monitor the environment around the tryptophan units in a protein, shedding light on its conformation state.[43] In α-amylase at pH 7, the tryptophan units which are close to the surface of the protein and exposed to the aqueous medium fluoresce with a peak at 350 nm (Fig. 9A). When urea (0.92 M) was added to native amylase the fluorescence yield went down by ~50% but the peak position remained unchanged (Fig. 9A). This shows that unfolding was not significant at these concentrations of urea, as complete unfolding would have exposed the hydrophobic pockets, decreasing the effective dielectric constant of the medium around tryptophan, and hence blue shifting the fluorescence. Probably the small changes associated with urea addition (such as polarity) are responsible for decreased fluorescence in α-amylase in Fig. 9A. When to 0.46 mL of this solution 3.0 mL of cit–Au NP dispersion was added the fluorescence was found to be completely quenched (Fig. 9A). This indicates that urea treated protein binds to the surface of cit–Au NPs, probably close to the tryptophan units, such that their fluorescence is completely quenched.

Interestingly when the order of addition of reagents is changed the results observed are different. When native α-amylase is added to cit–Au NPs, the fluorescence yield goes down by 95% rapidly (within 5 min) and does not change further with time (Fig. 9B). This indicates that α-amylase is bound to cit–Au NPs and probably close to tryptophan groups, such that it reduces the fluorescence nearly completely. The slight red shift (about 4 nm in 30 min) could be due to salt/electrostatic effect of citrate ions. We conclude that unfolding of α-amylase did not occur as a blue shift was not observed in this case. After 30 min when urea was added to this solution a small fluorescence yield (about 2%) was recovered, however more red

shift was observed (by about 4 nm in additional 30 min) (Fig. 9C). This means urea has some effect on fluorescence, meaning that the cit–Au NP–amylase aggregate is not completely impenetrable by urea and that the red shift could be associated with electrostatic effects induced by urea. This fact was also substantiated from our FTIR studies and zeta potential measurements.

In another experiment, to cit–Au NPs when native α-amylase and urea were added in quick sequence, the fluorescence yield also dropped by ~95% almost immediately and then regained about 5% after ~30 min (Fig. 9D). There was a constant red shift (while the fluorescence yield dropped by ~95%), which red shifted further when the fluorescence was partly recovered (about 5%) after 30 min. Note that the 5% regain is greater than the 2% regain in the above experiments of Fig. 9C. So urea penetrates more into the aggregated structure in this case (Fig. 9D) than that in the above case (Fig. 9C), as would be expected, because the aggregated structures grow slowly (in min) with time.

All experimental evidences indicated that the conformational changes accompanying the addition of urea to cit–Au NP treated α-amylase are certainly different than when added to free α-amylase. This was also substantiated from detailed enzymatic activity studies of the digestion of starch in the absence and presence of α-amylase–Au NP composite, as well as urea treated α-amylase–Au NP composite (Fig. S8, ESI†). We found that the rate was highest when native α-amylase was used ($k = 0.099$ min^{-1}) and that rate dropped marginally for cit–Au NP–α-amylase composite ($k = 0.097$ min^{-1}). However, in the presence of 1.5 mL of 8 M urea the rate constant of the cit–Au NPs−α-amylase composite lowered drastically ($k = 0.05$ min^{-1} *vs.* 0.097 min^{-1}, respectively). Similar experiments were carried out in the presence of 6 M and 4 M urea stock solutions containing α-amylase and Au NPs, and from these we conclude that in the presence of 8 M urea stock solution the rate for the digestion of starch was lower than for 6 M or 4 M urea stock solutions (Fig. S8, ESI†) The marginal reduction in the enzymatic activity of cit–Au NP–protein composite from the native protein in this study could be a reflection of the agglomerated state of some of the protein, whereby the embedded protein molecules are inaccessible for catalytic activity. The presence of a large number of free proteins accounts for a considerable enzyme activity in the system ($k = 0.0973$ min^{-1}). Upon addition of urea, however, enzyme activity is reduced considerably as free protein molecules are readily denatured.

Overall, from the results reported herein it is clear that when α-amylase was added to cit–Au NP dispersion, agglomeration took place leading to the formation of a composite between the NPs and the protein. With time the size of the composite increased, which was reflected in the UV-Vis spectral broadening and supported by DLS and TEM studies. However, the agglomeration reached a limit with time beyond which their sizes did not increase. Moreover, addition of urea to the cit–Au NP–protein composite did not lead to further agglomeration of the composite. Rather agglomeration of cit–Au NP–α-amylase stalled upon addition of urea. Further, FITR, zeta potential and fluorescence results indicated that the cit–Au NP–protein agglomerated structures are relatively permeable to urea.

In essence, the conformational changes in α-amylase induced by cit–Au NPs are slow and the NPs appear to stabilize the α-helix of the protein. Thus if urea is added early to the system, the cit–Au NPs do not have enough time to change the conformation of the α-amylase, making it more susceptible to attack by urea, whereby it undergoes conformational changes associated with denaturation of the protein which halt the agglomeration process. However, if urea is added much later, then cit–Au NPs have enough time to change and lock the conformation of the α-amylase which leads to formation of agglomerated structures, as well as making them less susceptible to attack by urea. A schematic representation of the process of agglomeration between cit–Au NPs and α-amylase with time and its fate upon addition of urea is shown in Scheme 2. The rate of conformational changes induced by cit–Au NPs appears to be slightly faster than the rate at which urea induces conformational changes, under the present experimental conditions. The origin of agglomeration between cit–Au NPs and α-amylase is due to conformation changes that occur upon adsorption of the protein on the surface of Au NPs. These conformation changes are distinct from those induced by the chemical denaturing agent, which is a new finding of this study.

Conclusions

In conclusion, we have been able to establish a better understanding of the agglomeration process of Au NPs and a protein. It has been observed that conformation changes in the protein upon adsorption on the surface of cit–Au NPs dominated the agglomeration process, which occurs in time-scales of minutes. When urea was added to this system, unfolding of free protein molecules in the solution took place. On the other hand, although urea permeates the cit–Au NP protein agglomerated structures, the protein molecules embedded deep within these structures are more resistant to attack by urea. However we cannot rule out some partial unfolding of the proteins attached on the periphery of the agglomerates. Unfolding of free protein molecules by urea appears to prevent further agglomeration in the system. The activity of the protein is retained partially even in the presence of urea, which indicates the retention of native structures for at least some of the proteins in the system.

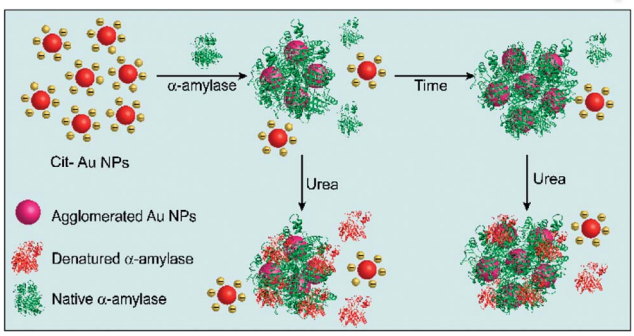

Scheme 2 A schematic representation of the agglomeration process of Au NPs in the presence of α-amylase and urea.

Overall, our results suggest that agglomeration of NPs takes place in the presence of a protein due to specific conformation changes, however these changes neither lead to unfolding of the protein towards denaturation nor does denaturation of protein favour agglomeration of Au NPs. The evidence put forth in this study indicates newer, and more specific interactions between biomolecules and NPs, which are relevant for future applications and understanding in nano-biotechnology.

Acknowledgements

We acknowledge Department of Science and Technology (DST SR/S1/PC-30/2008), India for financial support.

Notes and references

1 J. Panyam and V. Labhasetwar, *Adv. Drug Delivery Rev.*, 2003, **55**, 329–347.
2 X. Michalet, F. F. Pinaud, L. A. Bentolila, J. M. Tsay, S. Doose, J. J. Li, G. Sundaresan, A. M. Wu, S. S. Gambhir and S. Weiss, *Science*, 2005, **307**, 538–544.
3 M. Mahmoudi, H. R. Kalhor, S. Laurent and I. Lynch, *Nanoscale*, 2013, **5**, 2570–2588.
4 M. P. Sk, A. Jaiswal, A. Paul, S. S Ghosh and A. Chattopadhyay, *Sci. Rep.*, 2012, **2**, 383–387.
5 I. Perelshtein, G. Applerot, N. Perkas, G. Guibert, S. Mikhailov and A. Gedanken, *Nanotechnology*, 2008, **19**, 245705–245710.
6 E. Lavik and H. V. Recum, *ACS Nano*, 2011, **5**, 3419–3424.
7 Y. Su, X. Wei, F. Peng, Y. Zhong, Y. Lu, S. Su, T. Xu, S.-T. Lee and Y. He, *Nano Lett.*, 2012, **12**, 1845–1850.
8 A. T. Gates, S. O. Fakayode, M. Lowry, G. M. Ganea, A. Murugeshu, J. W. Robinson, R. M. Strongin and I. M. Warner, *Langmuir*, 2008, **24**, 4107–4113.
9 D.-H. Tsai, F. W. DelRio, A. M. Keene, K. M. Tyner, R. I. MacCuspie, T. J. Cho, M. R. Zachariah and V. A. Hackley, *Langmuir*, 2011, **27**, 2464–2477.
10 Y.-M. Chen, C.-J. Yu, T.-L. Cheng and W.-L. Tseng, *Langmuir*, 2008, **24**, 3654–3660.
11 D. Zhang, O. Neumann, H. Wang, V. M. Yuwono, A. Barhoumi, M. Perham, J. D. Hartgerink, P. Wittung-Stafshede and N. J. Halas, *Nano Lett.*, 2009, **9**, 666–671.
12 T. Sen, S. Mandal, S. Haldar, K. Chattopadhyay and A. Patra, *J. Phys. Chem. C*, 2011, **115**, 24037–24044.
13 S. H. Brewer, W. R. Glomm, M. C. Johnson, M. K. Knag and S. Franzen, *Langmuir*, 2005, **21**, 9303–9307.
14 P. M. Tessier, J. Jinkoji, Y.-C. Cheng, J. L. Prentice and A. M. Lenhoff, *J. Am. Chem. Soc.*, 2008, **130**, 3106–3112.
15 C.-S. Tsai, T.-B. Yu and C.-T. Chen, *Chem. Commun.*, 2005, 4273–4275.
16 G. P. Goodrich, M. R. Helfrich, J. J. Overberg and C. D. Keating, *Langmuir*, 2004, **20**, 10246–10251.
17 S. A. Claridge, H. W. Liang, S. R. Basu, J. M. J. Fréchet and A. P. Alivisatos, *Nano Lett.*, 2008, **8**, 1202–1206.
18 J.-Y. Kim and J.-S. Lee, *Nano Lett.*, 2009, **9**, 4564–4569.
19 C.-C. You, S. S. Agasti, M. De, M. J. Knapp and V. M. Rotello, *J. Am. Chem. Soc.*, 2006, **128**, 14612–14618.
20 R. Hong, N. O. Fischer, A. Verma, C. M. Goodman, T. Emrick and V. M. Rotello, *J. Am. Chem. Soc.*, 2004, **126**, 739–743.
21 L. A. Dykman and N. G. Khlebtsov, *Acta Naturae*, 2011, **2**, 34–53.
22 A. Neely, C. Perry, B. Varisli, A. K. Singh, T. Arbneshi, D. Senapati, J. R. Kalluri and P. C. Ray, *ACS Nano*, 2009, **3**, 2834–2840.
23 G. Zhou, Y. Liu, M. Luo, Q. Xu, X. Ji and Z. He, *ACS Appl. Mater. Interfaces*, 2012, **4**, 5010–5015.
24 J. C. Y. Kah, J. Chen, A. Zubieta and K. Hamad-Schifferli, *ACS Nano*, 2012, **6**, 6730–6740.
25 K. Aslan, J. R. Lakowicz and C. D. Geddes, *Anal. Chem.*, 2005, **77**, 2007–2014.
26 I.-H. Lee, H.-K. Kwon, S. An, D. Kim, S. Kim, M. K. Yu, J.-H. Lee, T.-S. Lee, S.-H. Im and S. Jon, *Angew. Chem., Int. Ed.*, 2012, **51**, 8800–8805.
27 C.-S. Wu, C.-C. Lee, C.-T. Wu, Y.-S. Yang and F.-H. Ko, *Chem. Commun.*, 2011, **47**, 7446–7448.
28 J. Deka, A. Paul and A. Chattopadhyay, *RSC Adv.*, 2012, **2**, 4736–4745.
29 J. Deka, A. Paul and A. Chattopadhyay, *J. Phys. Chem. C*, 2009, **113**, 6936–6947.
30 J. Deka, A. Paul and A. Chattopadhyay, *Nanoscale*, 2010, **2**, 1405–1412.
31 R. Khandelia, J. Deka, A. Paul and A. Chattopadhyay, *RSC Adv.*, 2012, **2**, 5617–5628.
32 G. Buisson, E. Duee, R. Haser and F. Payan, *EMBO J.*, 1987, **6**, 3909–3916.
33 A. Rangnekar, T. K. Sarma, A. K. Singh, J. Deka, A. Ramesh and A. Chattopadhyay, *Langmuir*, 2007, **23**, 5700–5706.
34 X. L. Qi, C. Holt, D. Mcnulty, D. T. Clarke, S. Brownlow and G. R. Jones, *Biochem. J.*, 1997, **324**, 341–361.
35 M. A. Mahmoud, M. Chamanzar, A. Adibi and M. A. El-Sayed, *J. Am. Chem. Soc.*, 2012, **134**, 6434–6442.
36 L. Shang, Y. Wang, J. Jiang and S. Dong, *Langmuir*, 2007, **23**, 2714–2721.
37 J. Deka, A. Paul, A. Ramesh and A. Chattopadhyay, *Langmuir*, 2008, **24**, 9945–9951.
38 W. K. Surewicz, J. H. Mantsch and D. Chapman, *Biochemistry*, 1993, **32**, 389–394.
39 I. Ojea-Jimeńez, M. F. Romero, G. N. Bastús and V. Puntes, *J. Phys. Chem. C*, 2010, **114**, 1800–1804.
40 R. J. Hunter, *Foundations of Colloid Science*, Clarendon Press, Oxford, UK, 1992.
41 G. Wang and W. Sun, *J. Phys. Chem. B*, 2006, **110**, 20901–20905.
42 N. J. Greenfield, *Nat. Protoc.*, 2006, **1**(6), 2876–2890.
43 M. Iosin, F. Toderas, P. L. Baldeck and S. Astilean, *J. Mol. Struct.*, 2009, **924–926**, 196–200.

ACS APPLIED MATERIALS & INTERFACES

Research Article

www.acsami.org

Blue-Emitting Copper Nanoclusters Synthesized in the Presence of Lysozyme as Candidates for Cell Labeling

Rama Ghosh,[†] Amaresh Kumar Sahoo,[‡] Siddhartha Sankar Ghosh,[‡,§] Anumita Paul,*[,†] and Arun Chattopadhyay*[,†,‡]

[†]Department of Chemistry, [‡]Centre for Nanotechnology, and [§]Department of Biotechnology, Indian Institute of Technology Guwahati, Guwahati-781039, India

Supporting Information

ABSTRACT: Highly fluorescent copper nanoclusters (Cu NCs) have been synthesized using single-step reduction of copper sulfate by hydrazine in the presence of lysozyme. The fluorescence quantum yield was measured to be as high as 18%. The emission was also found to be dependent on the excitation wavelength. Mass spectrometric analyses indicated the presence of species corresponding to Cu_2 to Cu_9. Transmission electron microscopic analyses indicated the formation of agglomerated particles of average diameter of 2.3 nm, which were constituted of smaller particles of average diameter of 0.96 nm. They were found to be stable between pH 4 and 10 and in addition having excellent chemical and photostability. The noncytotoxic NCs were used to successfully label cervical cancer HeLa cells.

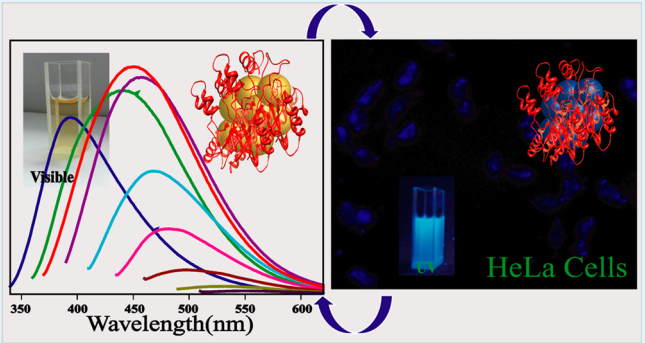

KEYWORDS: *copper nanoclusters, fluorescence, HeLa cells, photostability, cytotoxicity*

INTRODUCTION

Stabilizing nanoclusters (NCs) of noble metal remains the primary challenge in their syntheses and applications. It has been proposed that these highly luminescent and photostable NCs could substitute toxic quantum dots in bioimaging and biolabeling.[1,2] In this regard, owing to their redox properties, NCs of gold (Au), and to some extent those of silver (Ag), have been stabilized with considerable success in comparison to those of copper (Cu). For example, recently, syntheses of luminescent Au and Ag NCs have been reported using dendrimers,[3] poly(acrylic acid) polymer,[4,5] DNA,[6,7] and protein[8] as stabilizers. Among the proteins, bovine serum albumin,[8−10] lacto transferrin,[11] lysozyme,[12,13] insulin,[14] horseradish peroxidase,[15] and pepsin[16] have been preferred as stabilizers. It is important to mention here that the proposed use of these clusters in a biological environment demands their stability in an aqueous medium. This has remained a challenge for the synthesis of NCs of Cu. The ease of oxidation of Cu (E^0, 0.34 V), in comparison to that of Ag (E^0, 0.80 V) and Au (E^0, 1.50 V), has limited progress in the development of synthetic methods, especially in an aqueous medium. A recent report indicates that Cu NCs of less than 3 nm, synthesized using a polyol method under a N_2 atmosphere, were stable following their redispersion in an aqueous medium.[17] On the other hand, the possibility of the synthesis of small Cu NCs in an aqueous medium electrochemically has also been demonstrated.[18] Interestingly, DNA-hosted Cu NCs, synthesized in the presence of ascorbic acid, have been used for the identification of single nucleotide polymorphism.[19] However, there is a need for the development of aqueous-based synthetic methods for versatile use, especially in biological applications. Cu is an important trace element, being present in the human body as an essential catalytic cofactor in redox-active enzymes such as cytochrome *c* oxidase and lysyl oxidase. The permissible intake of Cu for an adult is 0.6−1.6 mg/day.[20] The ease of sequestration of Cu by a natural bodily mechanism and the availability of commercial chelating agents also make its use relatively friendly in human subjects over those of Au and Ag, especially at low concentrations.[21,22]

Herein we report the synthesis of highly fluorescent, blue-emitting Cu NCs by chemical reduction of $CuSO_4$ in an aqueous medium, in the presence of lysozyme. Lysozyme, a 14.3 kDa protein, has 129 amino acid residues including 8 cysteine residues. The antimicrobial protein is biocompatible and has been a favorite as a stabilizer of Au NCs.[13] The so-synthesized protein-stabilized Cu NCs, with wavelength-tunable emission, were stable in an aqueous medium under ambient conditions; they could easily be isolated and used for labeling cervical cancer HeLa cells. Cell viability studies indicated their noncytotoxic nature, making the NCs ideal for biological applications. The essential steps of the synthesis are depicted in Scheme 1.

Received: September 23, 2013
Accepted: February 26, 2014
Published: February 26, 2014

dx.doi.org/10.1021/am500040t | ACS Appl. Mater. Interfaces 2014, 6, 3822−3828

Scheme 1. Reaction Scheme for the Synthesis of Cu NCs in the Presence of Lysozyme[a]

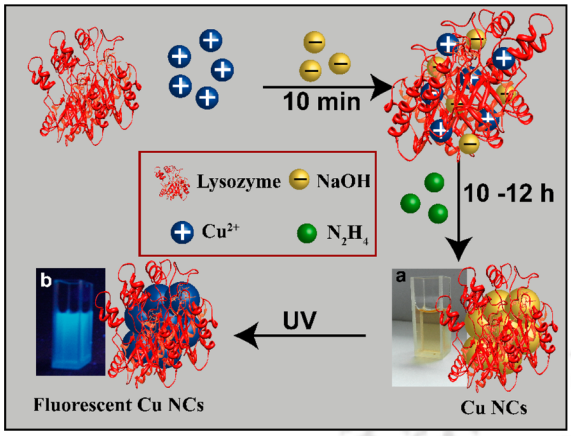

[a]Also included are the photographs of the products under (a) daylight and (b) UV light at 365 nm.

EXPERIMENTAL SECTION

Materials. Copper sulfate ($CuSO_4$), sodium hydroxide (NaOH), and hydrazine hydride (80%) were purchased from Merck Specialities Private Ltd., India. Lysozyme was purchased from Sisco Research Laboratories Pvt. Ltd. (SRL). 2,3-Bis(2-methoxy-4-nitro-5-sulfophenyl)-2*H*-tetrazolium 5-carboxanilide (XTT) and sinapinic acid for matrix-assisted laser desorption ionization (MALDI) analysis were purchased from Sigma-Aldrich USA. Milli-Q-grade water (18.2 MΩ·cm) was used for all of the experiments.

Synthesis of Cu NCs. $CuSO_4$ and lysozyme were mixed in water in a weight ratio of 2:1. The solution was stirred for 10 min at 45 °C, and then 0.04 mL of 1.0 M NaOH was added to adjust the pH to ∼10−11 when the color changed from blue to purple. To this was added 0.01 mM 80% N_2H_4, and the resulting solution was stirred for 6−12 h. The final color change of the solution was from purple to pale yellow. The same process for the synthesis was followed for different ratios of metal-to-protein concentration such as 2:1, 4:1, 6:1, and 8:1. For cell labeling and viability assay, Cu NCs were synthesized in a phosphate buffer at pH 7.4.

Characterization. Transmission electron microscopy (TEM) measurements were made using a JEOL JEM 2100 transmission electron microscope operating at a maximum accelerating voltage of 200 kV. The Cu NC dispersion was drop-cast onto carbon-coated Cu TEM grids and then kept for drying overnight at room temperature. UV−visible and fluorescence spectra were recorded with a Hitachi U-2900 or Perkin Elmer Lamda 25 and a Fluoromax-4 spectrophotometer instrument, respectively. Circular dichroism (CD) spectra were recorded using a Jasco J-815 machine. The instrument was calibrated with camphorsulfonic acid. All CD spectra were recorded at 25 °C, using a thermostatically controlled cell holder with a path length of 10 mm. ζ-potential measurements for samples were carried out using a Malvern zeta size Nano-ZS90 instrument at a temperature of 25 °C and a sample viscosity of 0.8872 mPa·s. Fourier transform infrared (FTIR) spectroscopic measurements were performed using a Perkin-Elmer Spectrum One spectrophotometer in the range 400−4000 cm^{-1}. X-ray diffraction (XRD) measurements were made using a Bruker AXS D8 Advance X-ray diffractometer fitted with a Cu $K\alpha_1$ source. Cellular labeling studies were carried out using a epifluorescence microscope (Nikon eclipse). For MALDI-time-of-flight (TOF) mass spectrometry (MS) analysis, an Applied Bio systems 4800 Plus MALDI TOF/TOF analyzer was used with sinapinic acid as the matrix. X-ray photoelectron spectroscopy (XPS) measurements for Cu NCs were performed by using a PHI 5000 VersaProbeII scanning XPS microprobe. Samples were prepared as pellets and introduced into the XPS prechamber under ultrahigh-vacuum conditions. Time-resolved fluorescence intensity decay of the NCs was recorded using a Life Spec II spectrofluorimeter. The sample was excited by a 375 nm laser light source. The decay curves were analyzed by *FAST* software, provided by Edinburgh Instruments along with the fluorimeter. The curves were fitted into the function

$$I(t) = \sum \alpha_i \exp(-t/\tau_i) \quad (1)$$

where α_i is the initial intensity of the decay component i, having a lifetime of τ_i.

The average lifetime of Cu NCs was calculated using the equation

$$\langle \tau \rangle = \frac{\sum_i \alpha_i \tau_i^2}{\sum_i \alpha_i \tau_i} \quad (2)$$

Quantum Yield Measurement of Cu NCs. Quantum yield measurement was carried out by dissolving quinine sulfate in 0.1 M H_2SO_4 (used as the reference) according to the standard protocol.[23] The Cu NC dispersion was used as such. The absorbance of the respective sample was measured on a Perkin-Elmer LS 55 UV−visible spectrophotometer. The quantum yield was calculated from the equation

$$Q = Q_R \frac{m_s}{m_r} \frac{n_s^2}{n_r^2} \quad (3)$$

where Q is the quantum yield of Cu NCs, Q_R is the quantum yield of quinine sulfate, m_s is the slope of the plot of integrated fluorescence intensity versus absorbance of Cu NCs, m_r is the slope of the plot of integrated fluorescence intensity verses absorbance of reference quinine sulfate, and n_s and n_r are the refractive indices of the sample and reference, respectively, in distilled water, which are assumed to be equal to that of water (1.33). The emission spectra for the samples were recorded at the excitation wavelength of 360 nm, keeping the slit width at 2 nm.

Sample Preparation for MALDI-TOF MS Measurement. For MALDI-TOF MS analysis, an Applied Bio systems 4800 Plus MALDI TOF/TOF analyzer was used with sinapinic acid as the matrix. Spectra were collected in the linear positive mode with mid-mass. The matrix was prepared by dissolving 10 mg of sinapinic acid in a 1:3 mixture of acetonitrile and 0.1% trifluoroacetic acid, and water was used to make up the volume to 1.0 mL (i.e., 0.2 mL of acetonitrile, 0.6 mL of 0.1% trifluoroacetic acid, and 0.2 mL of water). The samples were prepared at 1:1, 1:2, and 1:3 ratios with samples and a matrix. The cluster dispersion, without dilution, was mixed thoroughly with the matrix mixture, and from it, 0.8 μL of the resulting mixture was used for spotting.

Agarose Gel Electrophoresis. The electrophoretic stability of a lysozyme and Cu NC mixture was pursued by an agarose gel electrophoresis study. This was performed in 0.8% agarose at 5 v/cm and was visualized under a UV transilluminator (with excitation at 305 nm).

Cell Culture. HeLa cells (human cervical carcinoma) were acquired from the National Centre for Cell Sciences, Pune, India, and cultured in Dulbecco's modified Eagle's medium (DMEM) supplemented with 10% (v/v) fetal bovine serum obtained from PAA Laboratories, Austria, in a 5% CO_2 humidified incubator at 37 °C.

Cell Viability Assay. Cell viability assays were carried out as per the following. Cells (1×10^4 cells/well) were seeded in a 96-well microplate and grown in DMEM for 24 h in the presence of 5% CO_2 at 37 °C. Then various concentrations of Cu NCs (2.3−34.5 μg/mL) were added to the cells and kept for 24 h in similar conditions, which was followed by XTT assay as per standard manufacturer protocol. For the reaction, 7.0 μL of XTT was added to each well of the microplate and kept for 2 h for the formation of formazan. The control experiment was carried out in a similar way with various amounts of lysozyme. All of the experiments were carried out in triplicate. The percentage of cell viability of the control was taken as 100%. The cell viability was calculated based on the following formula:

$$\%\ \text{viable cells} = \frac{(A_{450} - A_{650})\ \text{of NC treated cells}}{(A_{450} - A_{650})\ \text{of control cells}} \times 100$$

The absorbances at 450 and 650 nm (A_{450} and A_{650}) correspond to the formation of formazan and the control medium, respectively.

Epifluorescence Microscopy. For cell imaging, 1×10^4 HeLa cells were seeded in a 35 mm cell culture plate and grown for 24 h. Cu NCs were added to the plate and incubated for another 2 h. Then, the medium was removed, and the cells were washed with phosphate-buffered saline (PBS) several times. Finally, 1 mL of PBS was added to the plate, and the cells were observed under an epifluorescence microscope (Nikon ECLIPSE TS100, Tokyo). An excitation band-pass filter for UV (340−380 nm) and an emission band-pass filter (435−485 nm) were used for cellular imaging.

Hemolysis Assay in Vitro. A total of 2.0 mL of human blood was centrifuged at 3000 rpm for 10 min to obtain human red blood cells (HRBCs). After removal of the supernatant, the HRBCs were washed with physiological buffer (PBS), which was followed by centrifugation. HRBCs so collected were suspended in deionized water. Portions of 0.1 mL of the HRBC suspension were added to 0.9 mL each of deionized water and PBS buffer, considered as positive and negative controls, respectively. Then experiments were performed in five different concentrations of a Cu NC composite. For each experiment, 0.1 mL of a stock HRBC suspension was added to 0.9 mL of a Cu NC composite with different concentrations (which varied from 0.6 to 4.5 μg/mL). All samples were incubated at 37 °C in a water bath for 3 h. After 3 h, the samples were centrifuged at 3000 rpm for 10 min, and the absorbance of the supernatants at 541 nm was recorded. The percentage of hemolysis of the Cu NC suspension was calculated by using the equation

$$\%\ \text{of hemolysis} = \frac{\text{O.D. of Cu NCs} - \text{O.D. of negative control}}{\text{O.D. of positive control} - \text{O.D. of negative control}} \times 100$$

where O.D. corresponds to the absorbance values of HRBCs at 541 nm. The hemolysis assay was performed in triplicate.

RESULTS AND DISCUSSION

Cu NCs were synthesized by treating a mixture containing a 2:1 molar ratio of $CuSO_4$ and lysozyme with N_2H_4 (0.01 mM) at pH 10−11 at 45 °C with constant stirring for 10−12 h. The medium, after reaction, appeared intense blue under a UV lamp, indicating the formation of Cu NCs (Scheme 1). The UV−visible spectrum (Figure 1A) of the reaction mixture recorded after 12 h did not exhibit the presence of any discernible peak. However, a gradual increase in extinction below 475 nm could be observed. An identical experiment in the absence of N_2H_4 did not result in such a bright-blue coloration, evidencing the role of N_2H_4 in the synthesis (Figure S1 in the Supporting Information, SI). Cu NCs, as evidenced from a strong fluorescence intensity, formed readily in the presence of hydrazine with high yield, as observed from fluorescence spectra (Figure S1 in the SI). They were reasonably stable in the presence of hydrazine after preparation at ambient conditions. In the absence of hydrazine, the fluorescence intensity decreased quickly with time (Figure S2 in the SI), thus indicating the additional role of hydrazine in stabilizing the NCs.

On the other hand, when the concentration ratio of $CuSO_4$/lysozyme was increased to 4:1 and beyond, a clear surface plasmon resonance (SPR) peak due to Cu NPs could be observed, occurring at 550 nm (Figure S3 in the SI). Thus, the studies reported in the present work were limited to products formed from a mixture of 2:1 molar ratio of $CuSO_4$ and the protein. The fluorescence spectrum of the product consisted of a single peak with a maximum at 450 nm, when excited by 360 nm light (Figure 1B). The excitation spectrum consisted of a single peak with a maximum at 360 nm (Figure 1B). The

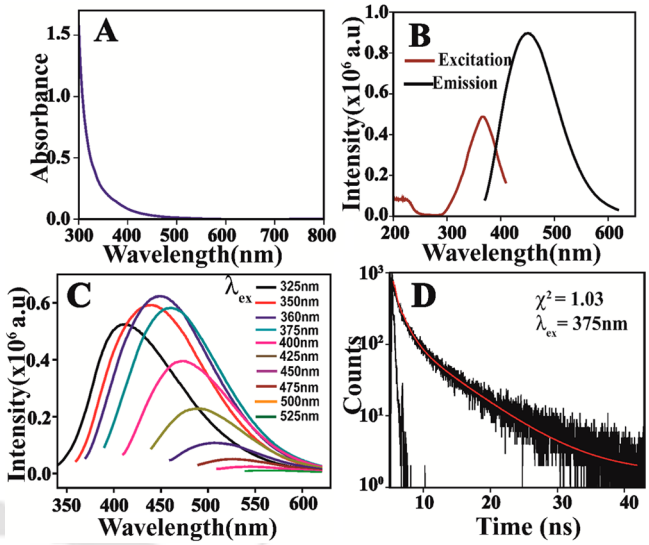

Figure 1. (A) Absorption spectrum of the product of the reaction of $CuSO_4$ and N_2H_4 in the presence of lysozyme. (B) Excitation and emission spectra of the product. (C) Excitation-dependent emission spectra of the product. (D) Fluorescence decay profile (λ_{ex} = 375 nm and λ_{em} = 450 nm) of the product.

fluorescence quantum yield was measured as 18% (λ_{ex} = 360 nm) with reference to quinine sulfate (54%) as the standard (Figure S4A in the SI).

Interestingly, the emission spectrum was found to be wavelength-tunable, with the emission maximum shifting from 410 to 575 nm, when the excitation wavelength was changed from 325 to 525 nm (Figures 1C and S4B in the SI). In the absence of N_2H_4, a similar product might have been formed; however, the fluorescence intensity of the product was less than that synthesized in the presence of N_2H_4 (Figure S5A in the SI). Also, the emission spectrum of the product formed in the absence of N_2H_4 did not exhibit clear wavelength-tunable properties like that formed in the presence of N_2H_4 (Figures S5A and S5B in the SI). The control experiment in the absence of $CuSO_4$ also indicated the presence of fluorescent species (Figure S6 in the SI); however, the intensity of fluorescence was either small or the peak occurred at shorter wavelength (Figure S6 in the SI). Also, the wavelength-tunable emission was not observed. Additionally, time-resolved fluorescence measurements indicated a clear difference between the products formed in the presence and absence of $CuSO_4$. For example, the average lifetime of emission of the product obtained from $CuSO_4$ and lysozyme was measured to be 6.5 ns (Figure 1D), whereas that in the absence of $CuSO_4$ was found to be 1.8 ns (Figure S7 and Table S2 in the SI). The emission characteristics of the product formed from the reaction match those reported for Cu NCs.[24] Thus, in the medium, Cu NCs were likely formed in the presence of the protein. Hydrazine acted as the reducing agent, producing Cu^0 from Cu^{2+} present in the medium. It was also observed that Cu NCs so produced (in the presence of hydrazine) were stable as the fluorescence emission did not change even after 15 days under ambient conditions (Figure S8 in the SI).

TEM measurements indicated the presence of small Cu NCs forming aggregates of average size of 2.3 ± 0.7 nm (Figure 2A,B). It is important to note here that the average particle size in Figure 2B appears to be higher than that of typical NCs. However, it is also known that when metallic NCs are

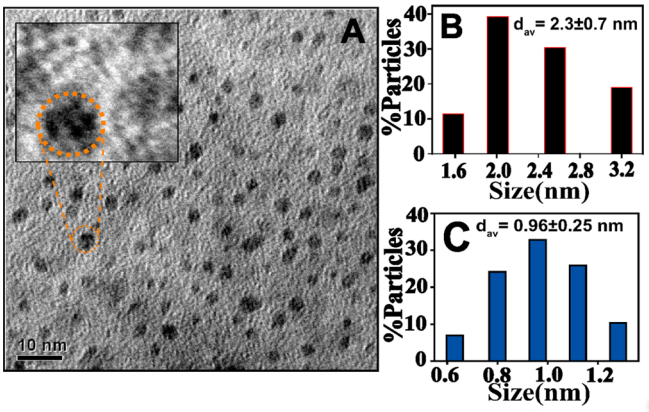

Figure 2. (A) TEM images of the product containing agglomerates of different sizes (scale bar 10 nm). The inset is the enlarged image of one of agglomerated particles. (B) Size histogram of different sizes of the particles (agglomerates). (C) Size histogram of individual clusters present inside the agglomerated product.

generated in the absence or presence of additional capping agents, agglomerated structures are formed, leading to an apparent higher particle size and even increased luminescence.[18,24,25] In the case of lysozyme, Au NCs formed agglomerated nanosized structures larger than individual NCs.[25,26] The average size of individual Cu NCs inside the aggregates (inset in Figure 2A and Figure 2C) was calculated as 0.96 ± 0.25 nm. Further probing of the sample using high-resolution TEM (HRTEM) showed the presence of crystalline particles with a lattice spacing of 0.207 nm, corresponding to the (111) plane of Cu^0.[27] The image is included in the SI (Figure S9). However, it may be stressed here that crystalline particles so observed might have been nonemissive and may represent larger SPR-active Cu nanoparticles. On the other hand, a crystalline lattice of ultrasmall atomic clusters of Cu may not be observed in HRTEM. Additionally, the population of larger crystalline Cu nanoparticles might have been rather small in the medium and thus not to have exhibited a clear SPR peak in the UV−visible spectrum.

The powder XRD pattern of the composite showed a broad peak at around 22° and the absence of characteristic peaks due to Cu (Figure S10 in the SI). The results also support a lack of crystallinity of the Cu NCs so formed and the absence of a significant population of crystalline Cu nanoparticles in the sample (consistent with a larger population of small-sized NCs).

FTIR spectra of lysozyme and lysozyme-stabilized Cu NCs are presented in Figure S11 in the SI. Three amide bands (amides I, II and III) due to the protein and occurring at 1600−1700, 1480−1575, and 1229−1301 cm^{-1}, respectively,[28,29] were present in the spectra. In addition, the peaks at 3400−3000 cm^{-1} due to −NH and −OH stretching vibrations were prominent in the spectra. The presence of functional groups such as $-NH_2$, −COOH, and −SH in the protein lysozyme may provide stability to the NCs. In a strongly alkaline medium, the protein might have been partially unfolded, thereby exposing a sufficient number of such groups that would facilitate attachment of the NCs to the protein.[30] It may also be true that the three-dimensional structure of the protein, with its functional groups separated spatially, provides enough room for attachment of more than one cluster to the same protein.

Among the three coinage metals, Cu is easily oxidized because of its low reduction potential. Therefore, it was deemed important to establish the oxidation state of Cu in the composite. For this, XPS analysis was performed for confirmation of the oxidation state of Cu in the Cu NC samples (Figure 3). Two prominent peaks, observed at 952.1

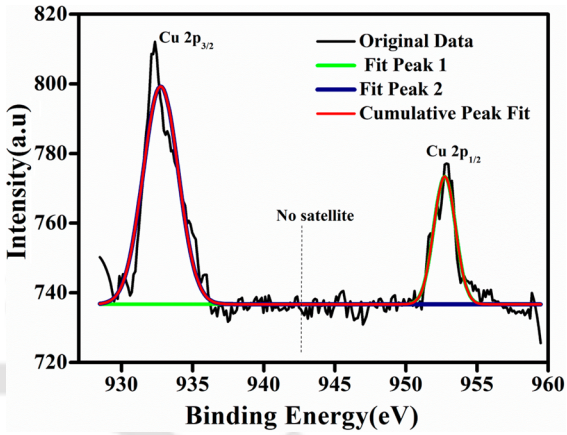

Figure 3. XPS spectrum of Cu 2p electrons in Cu NCs. The absence of satellite peaks indicated the absence of Cu^{2+}.

and 932.2 eV, were assigned to Cu $2p_{1/2}$ and Cu $2p_{3/2}$, which were characteristic peaks due to Cu^0. The absence of peak due to Cu^{2+} at 942 eV indicated that the Cu NCs did not contain Cu^{2+}. However, because the peak due to Cu^+ (932.3 eV) occurs at 0.1 eV apart from Cu^0, its presence cannot be ruled out. Further, the binding energy of sulfur (S) 2p observed at 162.8 eV (Figure S12 in the SI) indicated the presence of chemisorbed S on the surface of Cu NCs, which is supportive of the presence of Cu and S on the sample.[31,32]

Further analysis was carried out using MALDI-TOF MS to determine the core size of the Cu NCs. The spectrum was recorded in the linear positive mode, using a sinapinic acid matrix. The peak due to lysozyme appeared at 14300 Da (Figures 4 and S13 in the SI) because of its monocation form. It is expected that the molecular weight of a lysozyme/Cu NC composite will have peaks at masses higher than 14300 Da. A series of peaks in the region of 14300−14900 Da were observed. However, four peaks were prominent, which appeared at m/z 14300, 14434, 14564, and 14874 Da, as in

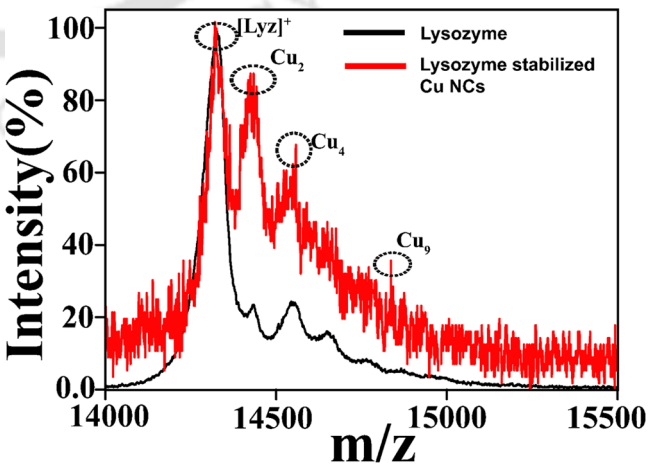

Figure 4. MALDI-TOF MS spectra of lysozyme (black line) and lysozyme-stabilized product (red line) with assignment of the characteristic peaks due to Cu NCs (dotted circles).

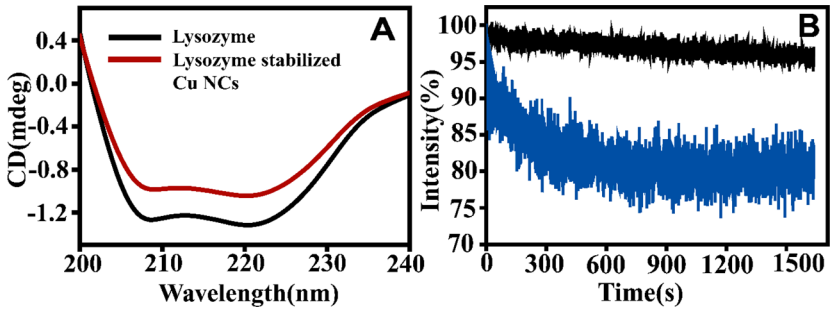

Figure 5. (A) CD spectra of lysozyme (black line) and as-synthesized Cu NCs (wine red) in the presence of lysozyme, exhibiting changes in the helicity of the α-helical structure following synthesis. (B) Representative time trace of fluorescence emission of Cu NCs (black line) showing slower decay in comparison to organic fluorophore, rhodamine 6G (blue line), under the same conditions.

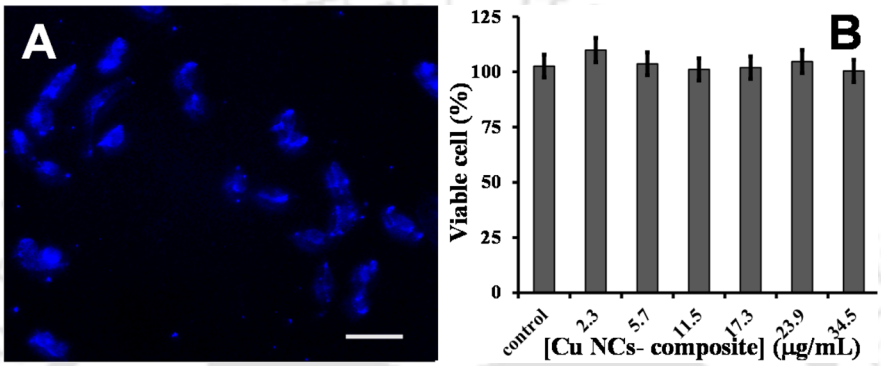

Figure 6. (A) Epifluorescence microscopic images of HeLa cells under UV light. Cells were incubated with Cu NCs for 2 h (scale bar 50 μm). (B) Cell viability for measuring the cytotoxicity of the Cu NCs on HeLa cells as measured by XTT assay after 24 h of incubation.

Figure 4. They can be attributed to $[Lyz]^+$, $[Lyz + Cu_2]^+$, $[Lyz + Cu_4]^+$, and $[Lyz + Cu_9]^+$, respectively. The results thus indicated the formation of Cu_2, Cu_4, and Cu_9 NCs, which were the same as those reported.[17,24,33] It is plausible that other clusters were also formed; however, they were not clearly detected in the MALDI-TOF MS spectrum.

CD measurements indicated a decrease in the α-helix content of the proteins present in the product medium from 52 to 45% following cluster formation (Figure 5A and Table S3 in the SI). Denaturation of the protein (even partially) consequent upon possible breakage of disulfide bonds,[26] or otherwise, might have led to agglomeration, accompanying the formation of Cu NCs at 45 °C. Additionally, the photostability of NCs is one of the properties that finds use in bioimaging and biolabeling applications. As shown in Figure 5B, fluorescence of the present Cu NCs remained nearly constant under continuous irradiation, with a fluorescence decrease rate of only 0.04%/min. In comparison, fluorescence of an organic fluorophore, rhodamine 6G, decreased at a rate of 0.23%/min with the photoirradiation time. The excellent resistance to photobleaching exhibited by the present Cu NCs, along with a considerable Stokes shift in the emission wavelength, makes a strong case for their use for cellular labeling and imaging. Additionally, an agarose gel electrophoresis study revealed the electrophoretic stability of NCs stabilized by the protein (Figure S14 in the SI).

In order to probe the surface charge of the synthesized Cu NCs, ζ-potential measurements were performed (Table S4 in the SI). The as-synthesized composite had a ζ-potential value of −28.1 mV, indicating an overall negative charge of the composite. Further, the potentials measured at the medium pH values of 9.0 and 4.5 were found to be −32.4 and −19.3 mV, respectively. The pH dependence of the ζ potential could be due to contribution from the protein, in addition to that of the clusters.

Further, it was deemed important to probe the effect of the pH on the fluorescence of the NCs. The NCs were synthesized at pH 11; the emission peak (at 450 nm) was found to be stable for 2 weeks. On the other hand, when the pH was made acidic, there was no change in the fluorescence, as was observed until an acidic pH of 4.3. The results are presented in the SI (Figure S15). The observation of pH-independent emission of Cu NCs indicates their importance for applications over a large pH range.

Cell Imaging and Cell Viability Test by XTT Analysis. An in vitro toxicity study of the NCs was examined by the XTT-based cell viability assay. XTT assay was performed to probe the cytotoxicity of the Cu NC composite by incubation in HeLa cells. The concentration of the composite used was 2.3−34.5 μg/mL. It should be mentioned here that the amount of Cu present in the composite, i.e., excluding lysozyme and hydrazine, was found to be 0.3−4.5 μg/mL. The Cu concentration is calculated based on the initial Cu salt taken for the reaction and assuming full conversion of the salt to Cu NCs. This means that the metal concentration reported here is the upper limit. The results indicated that Cu NCs had little or no cytotoxicity even at considerably higher concentration. HeLa cells (cervical cancer) in DMEM were incubated with different concentrations of Cu NCs in standard cell culture conditions. Following 24 h of incubation, the viability of the cells was determined, and the results are shown in Figure 6B. From XTT assay, it was found that more than 98% cells were viable upon incubation with 34.5 μg/mL of the Cu NC composite. The results indicated that the Cu NCs had no toxic

effect even at a considerably higher starting concentration of Cu.

The noncytotoxicity and high fluorescence quantum yield and photostability of the Cu NCs made it possible to test their suitability for cell labeling. This was pursued by incubating HeLa cells with Cu NCs for 2 h in DMEM. After removal of the medium, the cells were washed thoroughly with PBS (pH 7.4) to remove free unbound Cu NCs and finally were observed under a fluorescence microscope. The cells in the image (Figure 6A) could easily be observed under UV light (340−380 nm) because they appeared bright blue, which is the characteristic color of the Cu NCs. The corresponding image under a bright field and merged images are shown in Figure S16 in the SI. In comparison, control cells and cells treated with lysozyme did not exhibit any such fluorescence (Figures S17 and S18 in the SI). This clearly demonstrated the utility of the so-synthesized Cu NCs in live cell labeling.

Blood compatibility assay is an essential and initial requirement for the administration of any material in vivo such as hemolysis.[34] For that, preliminary investigations were performed using blood serum treated with Cu NCs. There was no loss of fluorescence (Figure S19 in the SI). On the other hand, there was an increase in fluorescence, which could be due to reducing the nature of the environment in the serum. The hemocompatibility of various concentrations of Cu NCs were performed by hemolysis assay. The results (Figures S20 and Figure S21 in the SI) demonstrated that Cu NCs did not cause significant hemolysis; i.e., they were hemocompatible at the concentrations used for the bioimaging and cell viability assay (0.6−4.5 μg/mL), which is comparable to previous studies.[35] Thus, blood compatibility assay supported the potential of the composites (and thus Cu NCs) for applications in vivo.

CONCLUSION

In conclusion, bright-blue fluorescent Cu NCs have been synthesized through a simple one-step reduction of $CuSO_4$ by N_2H_4, using lysozyme as the stabilizer. The NCs showed high photoluminescence quantum yield, excitation-tunable fluorescence, high photostability, and colloidal stability. They could be used for labeling HeLa cells. In conjunction with the photoluminescence properties, their low cytotoxicity would make them an ideal choice for biological and biomedical applications. The composite is comprised of Cu and lysozyme, where Cu is an essential trace element present in the body and lysozyme, an antimicrobial enzyme, is substantially present in a number of secretions, such as tears, saliva, etc. Thus, the composite might be considered to be biocompatible. The observed stability of the composite, coupled with the retention of fluorescence at physiological pH, is important for applications in vitro as well as in vivo.

ASSOCIATED CONTENT

Supporting Information

Additional fluorescence spectra, quantum yield calculations, MALDI-TOF MS analysis, XPS spectra, time-resolved fluorescence spectra, agarose gel electrophoresis analysis, bioimaging of cells with lysozyme, and blood compatibility studies in vitro. This material is available free of charge via the Internet at http://pubs.acs.org.

AUTHOR INFORMATION

Corresponding Authors

*E-mail: anumita@iitg.ernet.in.

*E-mail: arun@iitg.ernent.in.

Notes

The authors declare no competing financial interest.

ACKNOWLEDGMENTS

We acknowledge the Department of Science and Technology (DST Grant SR/S1/PC-30/2008), and Department of Biotechnology, Government of India, for financial support. We thank Subhamoy Banerjee and Upashi Goswami for help with the cell culture. We acknowledge help from the Department of Physics and Meteorology, IIT Kharagpur, with XPS analysis.

REFERENCES

(1) Wu, X.; He, X.; Wang, K.; Xie, C.; Zhou, B.; Qing, Z. Ultra Small Near-Infrared Gold Nanoclusters for Tumor Fluorescence Imaging in Vivo. *Nanoscale* **2010**, *2*, 2244−2249.

(2) Lin, C.-A. J.; Yang, T.-Y.; Lee, C.-H.; Huang, S. H.; Sperling, R. A.; Zanella, M.; Li, J. K.; Shen, J.-L.; Wang, H.-H.; Yeh, H.-I.; Parak, W. J.; Chang, W. H. Synthesis, Characterization, and Bioconjugation of Fluorescent Gold Nanoclusters Toward Biological Labeling Applications. *ACS Nano* **2009**, *3*, 395−401.

(3) Thompson, D.; Hermes, J. P.; Quinn, A. J.; Mayor, M. Scanning the Potential Energy Surface for Synthesis of Dendrimer-Wrapped Gold Clusters: Design Rules for True Single-Molecule Nanostructures. *ACS Nano* **2012**, *6*, 3007−3012.

(4) Sahoo, A. K.; Banerjee, S.; Ghosh, S. S.; Chattopadhyay, A. Simultaneous RGB Emitting Au Nanoclusters in Chitosan Nanoparticles for Anticancer Gene Theranostics. *ACS Appl. Mater. Interfaces* **2014**, *6*, 712−724.

(5) Shen, Z.; Duan, H.; Frey, H. Water-Soluble Fluorescent Ag Nanoclusters Obtained From Multiarm Star Poly(acrylic acid) as "Molecular Hydrogel" Templates. *Adv. Mater.* **2007**, *19*, 349−352.

(6) Petty, J. T.; Zheng, J.; Hud, N. V.; Dickson, R. M. DNA-Templated Ag Nanocluster Formation. *J. Am. Chem. Soc.* **2004**, *126*, 5207−5212.

(7) Richards, C. I.; Choi, S.; Hsiang, J.-C.; Antoku, Y.; Vosch, T.; Bongiorno, A.; Tzeng, Y.-L.; Dickson, R. M. Oligonucleotide-Stabilized Ag Nanocluster Fluorophores. *J. Am. Chem. Soc.* **2008**, *130*, 5038−5039.

(8) Xie, J.; Zheng, Y.; Ying, J. Y. Protein-Directed Synthesis of Highly Fluorescent Gold Nanoclusters. *J. Am. Chem. Soc.* **2009**, *131*, 888−889.

(9) Guével, X. L.; Hötzer, B.; Jung, G.; Hollemeyer, K.; Trouillet, V.; Schneider, M. Formation of Fluorescent Metal (Au, Ag) Nanoclusters Capped in Bovine Serum Albumin Followed by Fluorescence and Spectroscopy. *J. Phys. Chem. C* **2011**, *115*, 10955−10963.

(10) Mathew, A.; Sajanlal, P. R.; Pradeep, T. A Fifteen Atom Silver Cluster Confined in Bovine Serum Albumin. *J. Mater. Chem.* **2011**, *21*, 11205−11212.

(11) Chaudhari, K.; Xavier, P. L.; Pradeep, T. Understanding the Evolution of Luminescent Gold Quantum Clusters in Protein Templates. *ACS Nano* **2011**, *5*, 8816−882.

(12) Lin, Y.-H.; Tseng, W.-L. Ultrasensitive Sensing of Hg^{2+} and CH_3Hg^+ Based on the Fluorescence Quenching of Lysozyme Type VI-Stabilized Gold Nanoclusters. *Anal. Chem.* **2010**, *82*, 9194−9200.

(13) Zhou, T.; Haunq, Y.; Li, W.; Cai, Z.; Luo, F.; Yanq, J. C.; Chen, X. Facile Synthesis of Red-Emitting Lysozyme-Stabilized Ag Nanoclusters. *Nanoscale* **2012**, *4*, 5312−5315.

(14) Liu, C.-L.; Wu, H.-T.; Hsiao, Y.-H.; Lai, C.-W.; Shih, C.-W.; Peng, Y.-K.; Tang, K.-C.; Chang, H.-W.; Chien, Y.-C.; Hsiao, J.-K.; Cheng, J.-T.; Chou, P.-T. Insulin-Directed Synthesis of Fluorescent Gold Nanoclusters: Preservation of Insulin Bioactivity and Versatility in Cell Imaging. *Angew. Chem., Int. Ed.* **2011**, *50*, 7056−7060.

(15) Wen, F.; Dong, Y.; Feng, L.; Wang, S.; Zhang, S.; Zhang, X. Horseradish Peroxidase Functionalized Fluorescent Gold Nanoclusters for Hydrogen Peroxide Sensing. *Anal. Chem.* **2011**, *83*, 1193−1196.

(16) Kawasaki, H.; Hamaguchi, K.; Osaka, I.; Arakawa, R. pH-Dependent Synthesis of Pepsin-Mediated Gold Nanoclusters with Blue Green and Red Fluorescent Emission. *Adv. Funct. Mater.* **2011**, *21*, 3508−3515.
(17) Kawasaki, H.; Kosaka, Y.; Myoujin, Y.; Narushima, T.; Yonezawa, T.; Arakawa, R. Microwave-Assisted Polyol Synthesis of Copper Nanocrystals without Using Additional Protective Agents. *Chem. Commun.* **2011**, *47*, 7740−7742.
(18) Vilar-Vidal, N.; Blanco, M. C.; López-Quintela, M. A.; Rivas, J.; Serra, C. Electrochemical Synthesis of Very Stable Photoluminescent Copper Clusters. *J. Phys. Chem. C* **2010**, *114*, 15924−15930.
(19) Jia, X.; Li, J.; Han, L.; Ren, J.; Yang, X.; Wang, E. DNA-Hosted Copper Nanoclusters for Fluorescent Identification of Single Nucleotide Polymorphisms. *ACS Nano* **2012**, *6*, 3311−3317.
(20) Tapiero, H.; Townsend, D. M.; Tew, K. D. Trace Elements in Human Physiology and Pathology. Copper. *Biomed. Pharmacother.* **2003**, *57*, 386−398.
(21) Gaggelli, E.; Kozlowski, H.; Valensin, D.; Valensin, G. Copper Homeostasis and Neurodegenerative Disorders (Alzheimer's, Prion, and Parkinson's Diseases and Amyotrophic Lateral Sclerosis). *Chem. Rev.* **2006**, *106*, 1995−2044.
(22) Cater, M. A.; Fontaine, S. L.; Shield, K.; Deal, Y.; Mercer, J. F. ATP7B Mediates Vesicular Sequestration of Copper: Insight Into Biliary Copper Excretion. *Gastroenterology* **2006**, *130*, 493−506.
(23) Lakowicz, J. R. *Principles of Fluorescence Spectroscopy*, 2nd ed.; Kluwer Academic/Plenum Publishers: New York, 1999.
(24) Jia, Z.; Li, J.; Wang, E. Cu Nanoclusters with Aggregation Induced Emission Enhancement. *Small* **2013**, *9*, 3873−3879.
(25) Xu, H.; Suslick, K.S. Water-Soluble Fluorescent Silver Nanoclusters. *Adv. Mater.* **2010**, *22*, 1078−1082.
(26) Baksi, A.; Xavier, P. L.; Chaudhari, K.; Goswami, N.; Pal, S. K.; Pradeep, T. Protein-Encapsulated Gold Cluster Aggregates: The Case of Lysozyme. *Nanoscale* **2013**, *5*, 2009−2016.
(27) Qing, Z.; He, X.; He, D.; Wang, K.; Xu, F.; Qing, T.; Yang, X. Poly(thymine)-Templated Selective Formation of Fluorescent Copper Nanoparticles. *Angew. Chem., Int. Ed.* **2013**, *52*, 9719−9722.
(28) Shang, L.; Wang, Y.; Jiang, J.; Dong, S. pH-Dependent Protein Conformational Changes in Albumin: Gold Nanoparticle Bioconjugates: A Spectroscopic Study. *Langmuir* **2007**, *23*, 2714−2721.
(29) Surewicz, W. K.; Mantsch, J. H.; Chapman, D. Determination of Protein Secondary Structure by Fourier Transform Infrared Spectroscopy: A Critical Assessment. *Biochemistry* **1993**, *32*, 389−394.
(30) Chen, T.-H.; Tseng, W.-L. (Lysozyme Type VI)-Stabilized Au_8 Clusters: Synthesis Mechanism and Application for Sensing of Glutathione in a Single Drop of Blood. *Small* **2012**, *8*, 1912−1919.
(31) Wei, W.; Lu, Y.; Chen, W.; Chen, S. One-Pot Synthesis, Photoluminescence, and Electrocatalytic Properties of Subnanometer-Sized Copper Clusters. *J. Am. Chem. Soc.* **2011**, *133*, 2060−2063.
(32) Bensebaa, F.; Ellis, T. H.; Kruus, E.; Voicu, R.; Zhou, Y. Characterization of Self-Assembled Bilayers: Silver−Alkanethiolates. *Langmuir* **1998**, *14*, 6579−6587.
(33) Jia, X.; Yang, X.; Li, J.; Li, D.; Wang, E. Stable Cu Nanoclusters: From an Aggregation-Induced Emission Mechanism to Biosensing and Catalytic Applications. *Chem. Commun.* **2014**, *50*, 237−239.
(34) Wu, H. X.; Zhang, S. J.; Zhang, J. M.; Liu, G.; Shi, J. L.; Zhang, L. X.; Cui, X. Z.; Ruan, M. L.; He, Q. J.; Bu, W. B. A Hollow-Core, Magnetic, and Mesoporous Double-Shell Nanostructure: In Situ Decomposition/Reduction Synthesis, Bioimaging, and Drug-Delivery Properties. *Adv. Funct. Mater.* **2011**, *21*, 1850−1862.
(35) Chandra, V. S.; Baskar, G.; Suganthi, R. V.; Elayaraja, K.; Joshy, M. I.; Beaula, W. S.; Mythili, R.; Venkatraman, G.; Kalkura, S. N. Blood Compatibility of Iron-Doped Nanosize Hydroxyapatite and Its Drug Release. *ACS Appl. Mater. Interfaces* **2012**, *4*, 1200−1210.

ACS APPLIED MATERIALS & INTERFACES

Research Article

www.acsami.org

Synergistic Anticancer Activity of Fluorescent Copper Nanoclusters and Cisplatin Delivered through a Hydrogel Nanocarrier

Rama Ghosh,[†] Upashi Goswami,[‡] Siddhartha Sankar Ghosh,[‡,§] Anumita Paul,*[,†] and Arun Chattopadhyay*[,†,‡]

[†]Department of Chemistry, [‡]Centre for Nanotechnology, and [§]Department of Biotechnology, Indian Institute of Technology Guwahati, Guwahati-781039, Assam, India

Supporting Information

ABSTRACT: Highly fluorescent red copper nanoclusters (Cu NCs) were synthesized in aqueous medium in the presence of dihydrolipoic acid and poly(vinylpyrrolidone) (PVP). The Cu NCs, in solid form, were stable, retained their optical properties for a month, and could be redispersed for use when required. The NCs in aqueous medium exhibited pH-tunable reversible optical properties. The PVP stabilized NCs, when converted into hydrogel by cross-linking with poly(vinyl alcohol), delivered anticancer drug to cervical cancer (HeLa) cells, thereby inducing apoptotic cell death. The red emission properties of the Cu NCs in the hydrogel were used for optical imaging as well as for flow cytometric probe of cellular uptake. Cell viability assay, Caspase3 assay, and cell cycle analyses demonstrated that the Cu NCs present in the hydrogel composite exhibited synergy of action, along with the drug, cisplatin, against HeLa cells.

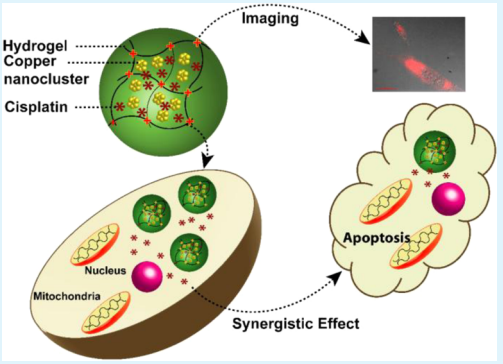

KEYWORDS: *copper nanoclusters, biolabeling, cisplatin, hydrogel, drug delivery*

INTRODUCTION

Metal nanoclusters (NC) bridge the materials gap between atom and nanoparticle (NP). The inherent quantum behavior of the NCs makes them a promising material endowed with size, tunable optical, and the other physical properties. Smaller size, reasonable chemical stability, excellent photostability, low cytotoxicity, and high luminescence quantum yield (QY) collectively provide a better prospect for using the noble metal NCs (especially Au NCs) in biological applications, instead of semiconductor quantum dots, which are generally cytotoxic. Recent surge of reports on their use for sensing,[1−3] biolabeling, bioimaging,[4−7] and chemical catalysis[8−10] is a testimony to their growing importance.

An important parameter that decides the utility of the NCs is their stability in liquid media, especially in the milieu of chemically and biochemically active moieties. This is where the development of new methods play important role in generating physically and environmentally responsive NCs. Among the noble metals, NCs of Au and Ag have been synthesized using templates such as polymer,[11,12] DNA,[13,14] protein,[15−17] and thiol-containing smaller molecular entities.[18] The inherent chemical stability of Au and Ag favors the synthesis of their NCs with comparative ease as opposed to those of Cu. The case of Cu NC is particularly difficult because of its instability even in mildly oxidizing condition. However, recent experiments from our laboratory[19] and others suggest that it is possible to synthesize stable Cu NCs. For example, Cu NCs have been synthesized using 2-mercapto-5-*n*-propylpyrimidine[20] and D-penicillamine[21] as protecting ligands. Also, etching of Cu NPs along with the use of glutathione (GSH) as a stabilizing ligand resulted into monodispersed fluorescent Cu NCs.[22] On the other hand, Cu NCs synthesized in the presence of DNA have been used to identify single nucleotide polymorphism.[23] Further, blue and red-emitting Cu NCs, synthesized in the presence of protein such as lysozyme[19] and BSA,[24] have been used in cell labeling applications. As mentioned above, while there are a few methods available for the synthesis of Cu NCs, there are still demands for Cu NCs with high stability and having application-specific stabilizing molecules or structures. For example, there is a need for obtaining stable red-emitting Cu NCs. In addition, if the NCs could be stabilized in the form of solid composites it would be better for storage, transport, and further use. That copper is an important and essential trace element in human, that there are sequestering agents for copper,[25,26] and that excess copper could be removed from the human body—in comparison to gold and silver—make it an important noble metal, which could be of paramount importance for superior biomedical applications.

Herein we report the synthesis of red fluorescent monodispersed Cu NCs in aqueous medium by using dihydrolipoic acid, in combination with biocompatible polymer poly(vinylpyrrolidone) (PVP) as a stabilizer. The fluorescence of the composite was found to be sensitive to the pH of the

Received: August 27, 2014
Accepted: December 5, 2014
Published: December 5, 2014

DOI: 10.1021/am505799q
ACS Appl. Mater. Interfaces 2015, 7, 209−222

Scheme 1. Schematic Representation of (A) Synthesis of Cu NCs Having pH-Dependent Fluorescence; (B) Synthesis of Cu NC−Hydrogel Composite by Crosslinking PVP and PVA, and (C) Cisplatin-Loaded Cu NC-Hydrogel Composite Leading to Apoptotic Cell Death as Probed by Cellular Imaging

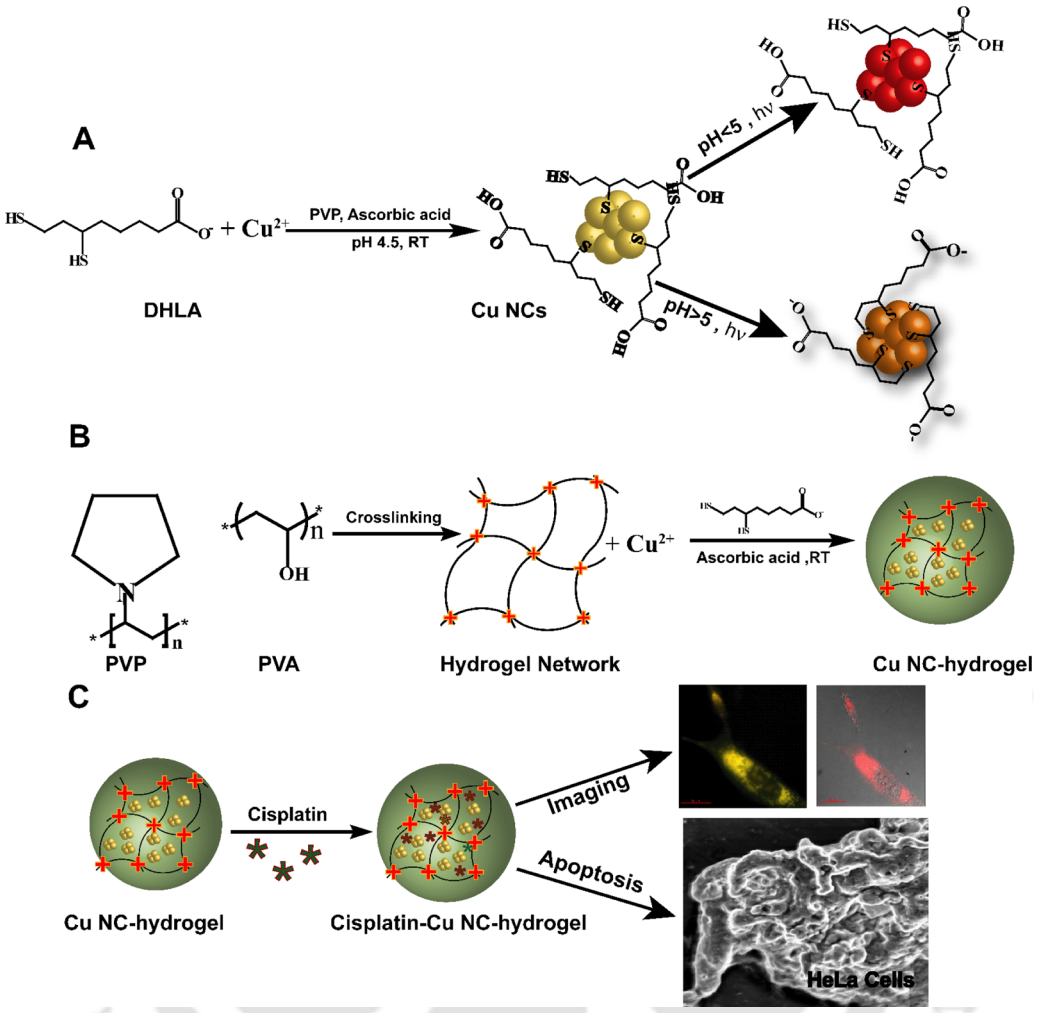

medium, and the emission could be tuned reversibly according to the pH. Also, the polymer NC composite could easily be synthesized in the form of hydrogel nanocarrier, by using poly(vinyl alcohol), PVA, as the cross-linker, which is favorable for cellular uptake.[27] The hydrogel could be then turned into a powder, which showed stable fluorescence, owing to the NCs, for more than a month. Further, the emission due to the NCs was useful for imaging mammalian cells by optical microscopy and more importantly to probe the cells by commercial flow cytometer, without having to use any other dye. Cu NC-containing hydrogel could encapsulate cisplatin (CP) for effective delivery to cancer cells, which was probed by using the emission properties of the NCs. Interestingly, it was found that Cu NCs generated reactive oxygen species in the cancer cells and hence enhanced the efficacy of CP in killing the cells, thus providing a synergy of action. The essential concept involving reaction scheme for the formation of composite of Cu NCs and PVP and its application in drug delivery as well as imaging of cells is depicted in Scheme 1.

EXPERIMENTAL SECTION

Materials. Copper chloride ($CuCl_2$), sodium hydroxide, sodium chloride, hydrochloric acid, and sodium bromide were purchased from Merck Specialties Private Limited, India. PVP, average molecular weight: 15 kDa, PVA, average molecular weight: 30 kDa, α-lipoic acid, (3-(4, 5-dimethylthiazolyl-2)-2,5-diphenyltetrazolium bromide) (MTT), and α-cyano-4-hydroxycinnamic acid were purchased from Sigma-Aldrich, U.S.A. Cisplatin was purchased from a commercial source. Milli-Q grade water (18.2 MΩ cm) was used for all experiments.

Synthesis of Copper Nanoclusters (Cu NCs). To synthesize fluorescent Cu NCs, 10.3 mg (10 mM) of α-lipoic acid was added to 5.0 mL of milli-Q water. To this insoluble mixture, 0.92 mg (5 mM) of $NaBH_4$ was added, and the mixture was stirred until the color of the medium changed from yellow to colorless, indicating the reduction of lipoic acid to dihydrolipoic acid (DHLA). Separately, 10 mg/mL of PVP was added to 3.8 mL of saturated solution of NaCl in a 15 mL culture tube, and the mixture was stirred for 2 min. To this, 0.2 mL (25 mM) of $CuCl_2$ and 3.5 mg (4 mM) of ascorbic acid were added to reduce the Cu(II) chloride to colorless Cu(I) chloride solution. This was followed by the addition of 1.0 mL (10 mM) of dihydrolipoic acid (DHLA), and the mixture was stirred for another 5 min. The final color of the mixture changed from colorless to pale yellow. The color change took place immediately after the addition of dihydrolipoic acid. The product was centrifuged at 10 000 rpm for 10 min (at 4 °C), and the precipitate was redispersed in milli-Q water and phosphate-buffered saline (PBS) (pH ≈ 7.4) for further use.

Preparation of PVP/PVA Hydrogel. Hydrogel was prepared by cross-linking of PVA and PVP (70:30 w/w) using freeze−thaw method. For this, PVP and PVA powders were mixed together containing 7.0 mL of PVA (10 mg/mL) and 3.0 mL of PVP (10 mg/

DOI: 10.1021/am505799q
ACS Appl. Mater. Interfaces 2015, 7, 209−222

mL), and the mixture was stirred while being kept at 90 °C for 24 h. Then, the mixture was kept at −20 °C for 12 h, and the frozen mixture was then allowed to melt at room temperature. The freeze−thaw step was repeated several times to induce formation of hydrogel.

Synthesis of Cu NCs in Hydrogel. Cu NCs were synthesized inside the hydrogel via in situ precipitation method. For this, 1.0 mM of $CuCl_2$ solution was added to 5.0 mL of hydrogel, then 2.6 mL of saturated solution of NaCl was added, and the mixture stirred for 10 min. After this, 4.0 mM of ascorbic acid was added, and the mixture was stirred for another 5 min. Finally, 2 mM of dihydrolipoic acid was added to it, leading to the formation of fluorescent red color inside the hydrogels. From atomic absorption spectrophotometric (AAS) analysis, it was found that 168.5 μg mL^{-1} of copper was present in the clusters synthesized with 1.0 mM of copper salt precursor.

Loading Efficiency of the Cu NC−Hydrogel Composite for Cisplatin. To determine the amount of CP loaded into the carrier Cu NC−hydrogel composite (2.0 mL, 0.5 mg of particles, corresponding to particle loading of 21.08 μg/mL) was taken in a 15 mL beaker; CP (0.1 mL of 19.6 μg/mL) was added to it, and the mixture was incubated for 24 h in the dark. The mixture was then centrifuged at 10 000 rpm for 10 min and at 4 °C. The supernatant was collected, and UV−visible spectrum was recorded for CP at 230 nm. To quantify the amount of the CP loaded in the Cu NC−hydrogel composite, the UV−visible spectrum was recorded for free CP present in the supernatant (CP_f). This was determined by measuring the absorbance at 230 nm, and the concentration so obtained was subtracted from the amount of cisplatin initially used for encapsulation (CP_i).

$$\text{loading efficiency}(\%) = \frac{CP_i - CP_f}{CP_i} \times 100$$

Analysis of Cisplatin Release from Cu Nc−Hydrogel Composite. To quantify the in vitro release of CP from Cu NC−hydrogel composite, the release profile was studied in acetate buffer (0.01 mM, pH 4.5) and PBS (0.01 mM, pH 7.4) at constant time intervals. For this, 0.5 mL of CP-loaded Cu NC−hydrogel composite was added to 1.5 mL of acetate or PBS buffer and was incubated for 48 h at 37 °C. After each time interval, that is, at 1, 3, 6, 12, 24, 36, and 48 h, the sample was centrifuged, supernatant was collected, and the amount of CP released from Cu NC−hydrogel composite was determined. The absorbance of supernatant was recorded at 230 nm, and the released CP from Cu NC−hydrogel composite in the supernatant was calculated by using the following equation.

$$\text{cumulative release}(\%) = \frac{\text{cisplatin released in the supernatant}}{\text{cisplatin loaded in the Cu NC hydrogel composite}} \times 100$$

CHARACTERIZATION

UV−visible Spectroscopic Measurements. UV−visible spectra were recoded with a Hitachi-U2900 or a PerkinElmer Lamda 25 spectrophotometer.

Fluorescence Measurements. Fluorescence spectra were recorded by using a spectrophotometer (Fluorolog −3, Horiba Jobin Edison, NY, USA). Photostability analyses of Cu NCs were carried out in the presence of continuous irradiation of ultraviolet light in the interval of time from 0.1 s to 30 min, under the excitation wavelength at 365 nm, with emission wavelength maximum being 650 nm.

Transmission Electron Microscopy (TEM). JEOL JAM 2100 TEM with maximum operating voltage of 200 kV was used for TEM measurements to analyze the size of Cu NCs. Diluted Cu NC dispersion (6.0 μL) was drop-cast on to carbon-coated copper grid and was kept for drying overnight at room temperature in the air, before making measurements.

Dynamic Light Scattering Measurements. Zeta potential and hydrodynamic diameter measurements of samples were performed by using Malvern Zeta Size Nano ZS-90 instrument at a temperature of 25 °C and using a sample viscosity of 0.8872 mPa·s.

Fourier Transform Infrared Spectroscopy. FTIR spectroscopic measurements were carried out by using PerkinElmer Spectrum One model in the range of 400−4000 cm^{-1}. For FTIR measurements, samples were prepared by drying in vacuum and then making the pellets with KBr, before recording the spectra.

Matrix-Assisted Laser Desorption Ionization Time-of−Flight mass spectrometric (MALDI-TOF-MS) Measurements. Applied Bio systems 4800 Plus MALDI TOF/TOF Analyzer was used with α-cyano-4-hydroxycinnamic acid as the matrix for MALDI-TOF-MS analysis. Mass spectra were collected in the linear negative mode with low mass. The matrix was prepared as follows. α-Cyano-4-hydroxycinnamic acid (10 mg) was dissolved in mixture of solvents of acetonitrile and trifluoroacetic acid in the ratio of 1:3, and water was used to make the volume equal to 1.0 mL. The samples were prepared by mixing Cu NCs with matrix in different ratios such as 1:1, 1:2, and 1:3; the mixtures were mixed thoroughly, and from this 0.8 μL of each sample was used for spotting.

Field-Emission Scanning Electron Microscopy (FESEM). FESEM analyses of the samples were carried out in a Carl Zeiss, SIGMA VP instrument. FESEM samples were prepared by drop-casting on a glass slide that was covered with aluminum foil and left standing overnight in the air for drying. Those samples were sputter-coated with a gold film using a sputter coater (SC 7620 "Mini", Polaron Q Sputter Coater Quorun Technologies, Newhaven, England), before analyzing under FESEM.

X-ray Photoelectron Spectroscopy (XPS). PHI 5000 VersaProbeII scanning XPS microprobe was used for X-ray photoelectron spectroscopy (XPS) measurements for Cu NCs. Samples were prepared as pellets and were introduced into the XPS prechamber under ultrahigh vacuum conditions before final measurement.

Quantum Yield Measurements of Cu NCs. Quantum yield measurement of Cu NCs was carried out by using quinine sulfate (dissolved in 0.1 M H_2SO_4) as a reference, following standard protocol.[28] The Cu NCs were used as such after synthesis. The quantum yield was calculated by using the following equation.

$$Q_{CuNC} = Q_{ref} \frac{m_{CuNC}}{m_{ref}} \frac{n_{CuNC}^2}{n_{ref}^2}$$

where $Q_{Cu\ NCs}$ and Q_{ref} are the quantum yield of Cu NCs and quinine sulfate, respectively; $m_{Cu\ NCs}$ and m_{ref} are the slopes of the plot of integrated fluorescence intensity versus absorbance of Cu NCs and quinine sulfate, respectively; and $n_{Cu\ NCs}$ and n_{ref} are the refractive indices of Cu NCs and the reference, respectively, in distilled water (assumed to be equal to that of water, that is, 1.33). The emission spectra for the samples were recorded at the excitation wavelength of 365 nm, keeping the slit width at 2 nm.

Cell Culture. HeLa cells (human cervical carcinoma) were obtained from National Centre for Cell Sciences (NCCS) Pune, India, and cultured in Dulbecco's Modified Eagle's Medium (DMEM) complemented with L-glutamine (4 mM), penicillin (50 units/mL), streptomycin (50 mg/mL)—which were purchased from sigma Aldrich—and 10% (v/v) fetal

DOI: 10.1021/am505799q
ACS Appl. Mater. Interfaces 2015, 7, 209−222

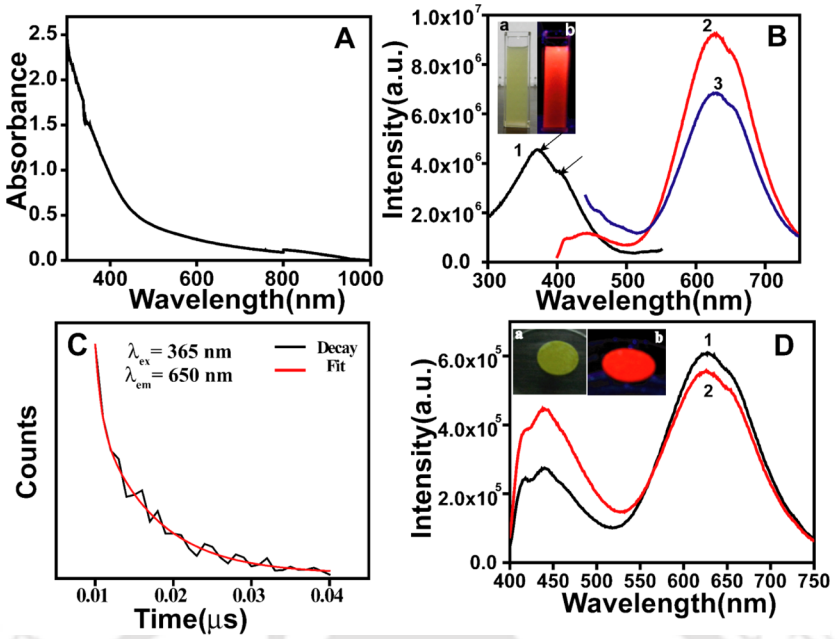

Figure 1. (A) UV−visible spectrum of as-synthesized Cu NCs formed by the reaction of Cu^{2+} with dihydrolipoic acid in the presence of PVP. (B) Excitation spectrum of Cu NCs (curve 1) with emission maximum at 650 nm. Emission spectra of Cu NCs with λ_{ex} = 365 nm (curve 2) and λ_{ex} = 405 nm (curve 3). Arrows in curve 1 show the excitation maxima at 365 and 405 nm, respectively. (inset) Photographs of dispersions of Cu NCs under (a) daylight and (b) UV light. (C) Fluorescence decay profile of Cu NCs excited at λ_{ex} = 365 nm, with emission peak being set at 650 nm. (D) Fluorescence spectrum of as-prepared Cu NCs in solid form (curve 1) and the same after one month (curve 2). (inset) Photographs of Cu NCs in solid form under (a) daylight and (b) UV light.

bovine serum (FBS, purchased from PAA Laboratories, Austria), being kept in a 5% CO_2 incubator at 37 °C.

FESEM and TEM Analysis for Untreated and Treated Cells. For TEM and FESEM analyses, HeLa cells were seeded in a 35 mm cell culture plate and nursed for 24 h. After that the CP-loaded Cu NC−hydrogel composite was added to the cells and kept for 3 h. For control sample, cells were incubated in media without the composite. After 3 h of incubation, cells were washed with PBS a number of times. Then, the cells were trypsinized, centrifuged, and fixed in glutaraldehyde solution (2%) for 10 min. The cells were then dehydrated in chilled ethanol solution and finally dispersed in absolute ethanol. For TEM sample preparation, 10 μL of the cell dispersion was drop-cast on carbon-coated copper grid and was then kept for drying in the air. For FESEM analysis, 20 μL of samples were drop-cast onto the glass slide covered with aluminum foil and was then kept for drying in the air.

Epifluorescence Microscopy. For cell imaging, 1×10^5 HeLa cells were seeded in six-well cell culture plate and grown for 24 h. HeLa cells were incubated with Cu NC−hydrogel composite or CP-loaded Cu NC−hydrogel composite for another 2 h. After 2 h of incubation, the medium was removed and the cells were washed with PBS. Finally, 1 mL of PBS was added to the plate and the cells were analyzed under epi-fluorescence microscope (Nikon ECLIPSE TS100, Tokyo) for observing the fluorescence of NCs inside the cells. For imaging, the excitation band-pass filters used were blue (340−380 nm) and green (540/25 nm) and emission band-pass filters used were green (515−555 nm) and red (655/55 nm).

Cell Viability Assay. Cell viability assay was carried out to quantify the viable cells after treatment with Cu NC−hydrogel composite and CP-loaded Cu NCs−hydrogel composite. About 1×10^4 cells/well were seeded in 96-well micro plate and were incubated in DMEM media for 24 h in the presence of 5% CO_2 at 37 °C. Then, CP-loaded Cu NC−hydrogel composite—with various concentrations (3.2−15.7 μg/mL)—was added to the cells and kept for 24 h under similar conditions. After 24 h of incubation, cell viability assay was performed which was followed by MTT assay in which tetrazolium salt, MTT [3-(4,5-dimethylthiazol-2-yl)-2,5-diphenyltetrazolium bromide] was reduced into purple colored formazan by respiring mitochondria present in the live cells. For the reaction, 7.0 μL of MTT was added to each well of the microplate and kept for 2 h in 5% CO_2 at 37 °C for the formation of formazan. After 2 h of incubation, the medium was removed and 60 μL of DMSO was added to each well for the development of purple color due to the formation of formazan, which absorbs at 550 nm. The control experiments were carried out in similar ways with various amounts of CP (1.5−8.4 μg/mL) and Cu NC−hydrogel composite (3.2−15.7 μg/mL). All the experiments were carried out in triplicate. The percentage of cell viability of control was taken as 100%. The cell viability was calculated by using the standard formula.

$$\%\text{viable cells} = \frac{(A_{550} - A_{690})\text{treated cells}}{(A_{550} - A_{690})\text{control cells}} \times 100$$

A_{550} and A_{690} are the absorbance at 550 and 690 nm corresponding to the formation of formazan and control medium, respectively.

Fluorescence-Activated Cell Sorting Analysis for Uptake of Cu NC−Hydrogel Composite. The cellular uptake of Cu NC−hydrogel composite was studied by using a flow cytometer. For this, 1×10^5 cells were seeded in 60 mm tissue culture plate for 24 h at 37 °C. Then, Cu NC−hydrogel composite (8.9 μg/mL) or CP-loaded Cu NC−hydrogel composite (8.9 μg/mL) was added to the plate and incubated for 3 h under the same condition. After incubation, the residual

DOI: 10.1021/am505799q
ACS Appl. Mater. Interfaces 2015, 7, 209−222

media were removed, and the plate was washed with PBS and trypsinized. Finally, the cells were centrifuged at 650 rcf for 5 min, and the cells were redispersed in PBS. The samples were analyzed by fluorescence-activated cell sorting (FACS) calibur (BD Biosciences), and the fluorescence of Cu NCs in the composite was recorded with the Cell Quest pro in different channels such as FL2 (band-pass filter 585/42 nm) and FL3 (low pass filter, 670 nm). For each run 15 000 cells were used.

FACS Analysis for Reactive Oxygen Species Generation. To analyze the generation of reactive oxygen species (ROS) inside the cells by Cu NC−hydrogel composite and CP-loaded Cu NC−hydrogel composite, 2′,7′-dichlorofluorecein-diacetate (DCFH-DA) staining was performed, followed by measurement using FACS calibur instrument. DCFH-DA is a nonfluorescent dye, and it diffuses into the cell through plasma membrane and is converted to DCFH by cellular esterase activity. The nonfluorescent DCFH is converted to green fluorescent 2′,7′-dichlorofluorecein (DCF) by intracellular oxidation, which absorbs at 488 nm and emits at 530 nm. For this, 2×10^5 HeLa cells were seeded in a six-well plate for 24 h. After 24 h of incubation, CP-loaded Cu NC−hydrogel composite (8.9 μg/mL) was added and kept for 3 h. After 3 h of incubation, the residual medium was removed, and the cells were washed with PBS several times. Finally, the cells were trypsinized, redispersed in 1.0 mL of fresh DMEM in which 5.0 μL of 1.0 mM of DCFH-DA was present, and incubated for 10 min at 37 °C. After incubation, the samples were analyzed for the fluorescence of DCF by flow cytometer using Cell Quest pro in fluorescence channel for 15 000 cells for each sample. The same procedure was repeated with HeLa cells treated with CP (4.5 μg/mL) and Cu NC−hydrogel composite (8.9 μg/mL). Experiments were carried out in triplicate.

RESULTS AND DISCUSSION

Red fluorescent Cu NCs were synthesized in aqueous medium at room temperature, by a simple and fast process, involving the reduction of Cu^{2+} ions by ascorbic acid and DHLA in the presence of PVP as the stabilizer. Ascorbic acid reduced Cu^{2+} to Cu^{+} ions in the presence of saturated solution of NaCl, as observed by change in the color of the medium from yellow to colorless.[29] Upon addition of DHLA the color of the solution changed from yellow to colorless accompanied by a slight precipitation. The UV−visible spectrum of the pale yellow reaction mixture, recorded after 30 min of mixing the reactants (Figure 1A), consisted of a featureless broad background and did not exhibit any peak in the region of 500−600 nm, thus excluding the formation of surface plasmon resonance (SPR) active Cu nanoparticles (NPs). The medium appeared fluorescent red under a UV lamp (Figure 1B), which indicated the formation of Cu NCs. The fluorescence spectrum of the yellow product in water exhibited two emission peaks centered at 435 and 650 nm, when excited at either 365 or 405 nm (Figure 1B). The low-energy excitation peak (at 405 nm) of the Cu NCs might be originating from the ligand-to-metal charge transfer (LMCT), whereas the high-energy excitation peak (at 365 nm) might originate from the dihydrolipoic acid ligand through intraligand as well as metal-perturbed intraligand transition.[30,31] On the other hand, the dual emission peaks of metal NCs (stabilized by the ligand) may arise either from the interband electronic transition or intraband transition.[20] However, according to Yam et al. the high-energy emission peak is due to the metal perturbed intraligand phosphorescence, whereas the low-energy emission peak may be due to LMCT.[30,31] Also, it is known that the emission properties are dependent on the size of clusters.[19] The dual emission of Cu NCs originated either from the same-sized clusters as described above or from different sizes of clusters. As our results indicate that two emissions are independent of the excitation wavelength, the emissions may be coming from the same-sized cluster. To examine whether LMCT from the triplet excited state of Cu NCs was occurring in our system, we carried out time-correlated single photon counting fluorescent experiments. A long radiative lifetime of 0.8 μs in these experiments (Figure 1C) supported that the emission had its origin in the excited triplet state of a ligand and through charge transfer to metal.[20,23,30,31] Importantly, the emission spectrum was similar to that reported in the literature for Cu NCs, thus indicating the formation of Cu NCs. That the fluorescent spectrum did not change after 20 min of formation of Cu NCs suggests that their formation was complete within a few minutes (Figure S1, Supporting Information). Interestingly, the so-prepared Cu NCs could be stored for a long time in the solid form. Centrifugation of the product resulted in the precipitate that was dried and stored in the form of a pellet, which appeared bright fluorescent red under a UV lamp. The fluorescence spectrum of the pellet with a peak at 635 nm was nearly the same as that of the product from the medium (Figure 1D). Additionally, the fluorescence spectrum of the solid recorded after one month showed almost no change, thus indicating the superior stability of the solid Cu NCs (Figure 1D, inset). Importantly, solid Cu NCs also appeared bright fluorescent red under the UV lamp. The prime challenge while working with Cu NCs is their instability under ambient conditions, due to the ease of oxidization of Cu (0) to Cu^{2+} (E_0 = 0.34 V) in comparison to Ag (E_0 = 0.80 V) or Au (E_0 = 1.50 V). Thus, by this method not only were fluorescent Cu NCs formed but also were easy to store in solid form without using any inert atmosphere. For analyzing the role of all reagents for the formation and stability of Cu NCs in aqueous medium, several control experiments were performed (Figure S2, Supporting Information). The emission results in Figure S2, Supporting Information, indicate that in the presence of PVP not only were the NCs stable but also had higher emission intensity. It is reported that PVP stabilizes NCs through weak coordination bonds.[32] The excess chloride ion present in saturated solution of NaCl helped in forming Cu(I) chloride, which is then easily reduced to Cu(0) in the presence of ascorbic acid.[29] It was also observed that Cu NCs synthesized in aqueous medium by using PVP as a stabilizer were stable as long as 3 d; the fluorescent intensity decreased quickly with time, indicating that the Cu NCs became unstable in the long run (Figure S3, Supporting Information).

Further investigation indicated that the emission spectrum (and thus the fluorescent color) of the dispersion of as-synthesized Cu NCs in water could be tuned reversibly by changing the pH of the medium. The Cu NCs synthesized at pH 4.5 emitted a red fluorescence at 650 nm (λ_{ex} = 365 nm). It is important to mention here that there was slight precipitation from the dispersion when kept at pH 4.5. This could be due to protonation of the carboxylic acid (−COOH) group and one of the thiol (−SH) groups of dihydrolipoic acid, while the second thiol group in the deprotonated state could be bonded to the NC. When the pH was increased clear solution resulted (at pH 6.5) and it remained so up to a pH of 11.0. The pH change from 4.5 to 11.0 was accompanied by an increase in the fluorescence intensity (Figure 2A), which could be attributed to

DOI: 10.1021/am505799q
ACS Appl. Mater. Interfaces 2015, 7, 209−222

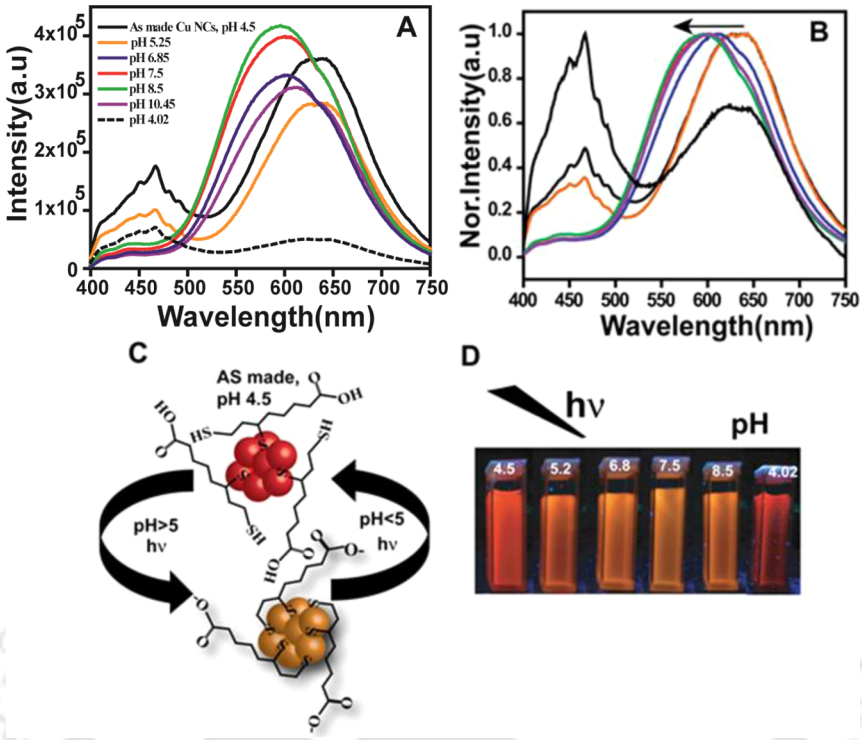

Figure 2. (A) Fluorescence spectra of as-synthesized Cu NC dispersions in the pH range of 4.5−11.0. (B) Normalized fluorescence spectra of as-synthesized Cu NCs in the pH range of 4.5−11. The arrows indicate the shift of wavelength in the pH range of 4.5−11. (C) Schematic representation of chemistry for the reversibility of fluorescence color from red to orange (and emission) by change in pH. (D) Photographs of Cu NCs under UV lamp (λ_{ex} = 365 nm) in the pH range of 4.5 to 8.5.

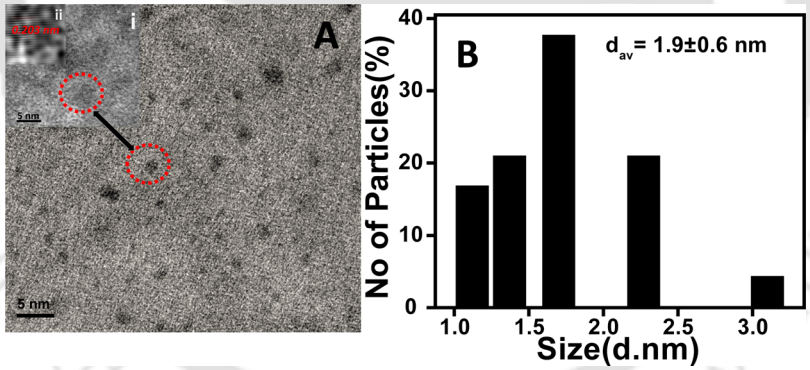

Figure 3. (A) TEM image of as-synthesized Cu NCs (with 5 nm scale bar). Inset (i) is the HRTEM images of a large Cu nanoparticle and (ii) IFFT image of the nanoparticle with lattice spacing of 0.203 nm corresponding to the (111) plane of Cu(0). (B) Particle size histogram of Cu NCs as obtained from TEM measurement (Figure 3A). The size distribution of Cu NCs was calculated from several images (from the same sample) and by considering more than 100 particles.

the deprotonation of the COOH as well as the remaining SH group of DHLA. Accompanying the increase in fluorescence intensity, the emission maximum shifted from 650 to 590 nm (at pH 6.5 and beyond, Figure 2B), while the color of the dispersion changed from fluorescent red to orange (Figure 2C, D). The change in color and emission maximum of Cu NCs depend on the surface anchoring groups of NCs. This could be attributed to the charge transfer from the ligand to metal core of NCs (Cu atoms) through Cu−S bonds.[30,31,33] Importantly, the fluorescence emission spectrum could be reversibly switched between pH 4.5 and 11.0 (Figure 2C,D).

The fluorescence quantum yield at different pH values of the medium was determined using quinine sulfate (having quantum yield of 54%) as the standard. The quantum yield was found to be 7.2% at pH 4.5, whereas it was 10.8% at pH 8.5 (Figure S4, Supporting Information). The results indicated not only the brightly emissive nature of Cu NCs but also the pH tuneability of the emission, which may be useful for practical applications.

TEM analysis of drop-cast as-synthesized sample revealed the presence of small particles with diameter 1.9 ± 0.6 nm (Figure 3). There was also the presence of agglomerated structures with diameters greater than 2 nm. Literature reports suggest enhancement of fluorescence quantum yield due to agglomeration,[22] which may well be the case herein. Further, high-resolution TEM (HRTEM) analysis did not reveal the clear lattice fringes for the smaller particles; however, for some of the bigger particles (with diameter >2 nm) fringes with lattice spacing 0.203 nm, corresponding to the (111) plane of Cu (0)

DOI: 10.1021/am505799q
ACS Appl. Mater. Interfaces 2015, 7, 209−222

(Figure 3A, inset (i) and (ii)) could be observed. It could be that some nanoscale particles with larger sizes were formed in the medium; however, their concentration was sufficiently low in the medium to give rise to any SPR band. Additionally, a single band obtained in 1.2% agarose gel electrophoresis suggested monodispersed nature of the synthesized Cu NCs (Figure S5, Supporting Information).

FTIR spectral measurement (Figure S6, Supporting Information) revealed that the characteristic peak of S−H stretch of DHLA at 2585 cm^{-1} was absent in the composite containing Cu NCs following their formation. The results indicated the possibility of stabilization of the NCs through Cu−S−R bonding.

Among the noble metals, Cu has the highest oxidation tendency owing to its lowest reduction potential, and this is an important challenge to overcome for obtaining stable NCs. In this context, it is important to determine the oxidation state of Cu in the composite. Thus, X-ray photoelectron spectroscopy (XPS) measurements were carried out to probe the oxidation state of Cu in the NCs (Figure 4). XPS spectrum indicated the

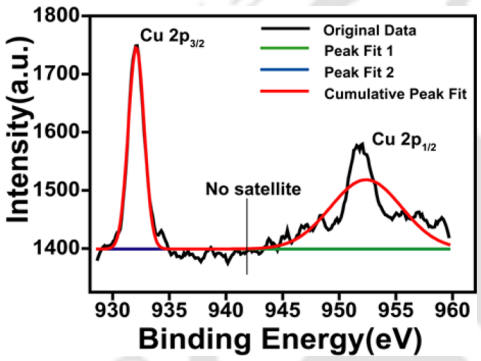

Figure 4. XPS spectrum representing the Cu 2p signal of as-prepared Cu NCs. The absence of satellite peak at 942 eV indicated the absence of Cu^{2+} in Cu NC samples.

presence of two peaks at 932.0 and 951.8 eV, which were assigned to Cu $2p_{3/2}$ and Cu $2p_{1/2}$ states of Cu(0), consistent with the literature values.[19,20] Importantly, the absence of any peak at 942.0 eV indicated the absence of Cu^{2+} in Cu NC samples. Further XPS probe of the sample indicated the presence of C, N, O, and S in the Cu NC composite sample (Figure S7, Supporting Information). It is also noteworthy that the small difference in binding energy of Cu(0) and Cu(I) (~0.1 eV) is difficult to distinguish in the XPS spectrum. Therefore, the valence state of Cu in our NCs may be 0 or +1, and possibly some of the surface Cu atoms may be partially oxidized. The binding energy of sulfur (S) 2p was found to be 163.0 eV, which indicated the possible adsorption of sulfur on the surface of Cu NCs through Cu−S bonding.[34] The result is consistent with FTIR spectrum of the NC sample (Figure S5, Supporting Information).

The atomic composition of the Cu NCs was analyzed by MALDI-TOF MS spectrometric analysis in the negative mode, using α-cyano-4- hydroxycinnamic acid as a matrix. Four prominent peaks (Figure 5) appeared at m/z 1080, 1103, 1126, and 1148, which can be attributed to $[Cu_4L_4 - 6H^+]^{6-}$, $[Cu_4L_4 - 6H^+ + Na^+]^{5-}$, $[Cu_4L_4 - 6H^+ + 2Na^+]^{4-}$ and $[Cu_4L_4 - 6H^+ + 3Na^+]^{3-}$, respectively, where L is $C_8H_{16}O_2S_2$. The results indicated the formation of monodispersed Cu NCs with molecular formula of Cu_4. In addition, MALDI-TOF MS

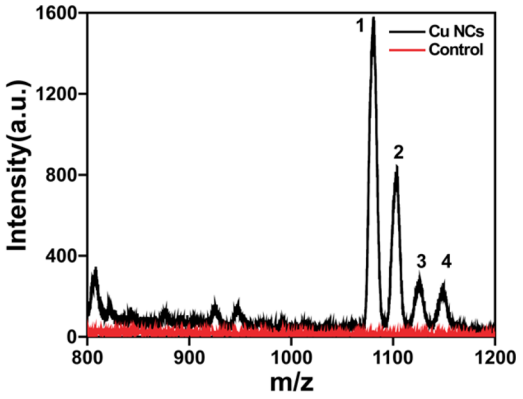

Figure 5. MALDI-TOF MS spectra of Cu NCs (in black) and control containing DHLA and PVP (in red) with the assignment of the characteristics peaks due to (1) $[Cu_4L_4 - 6H^+]^{6-}$, (2) $[Cu_4L_4 - 6H^+ + Na^+]^{5-}$, (3) $[Cu_4L_4 - 6H^+ + 2Na^+]^{4-}$ and (4) $[Cu_4L_4 - 6H^+ + 3Na]^{3-}$.

analysis of Cu NCs were carried out at different pH (i.e., 6.5, 8.5, and 10.5), which confirmed that the size of Cu NCs remained same from pH acidic to highly basic medium (Figure S8, Supporting Information). Also, the reversible nature of the observation suggests that the sizes of the emitting particles were not altered.

Furthermore, the photostability of Cu NCs revealed the importance of the NCs for bioimaging and cell labeling applications. The fluorescence intensity of Cu NCs in acidic pH remained unaltered under continuous irradiation of UV light in the time interval of 0.1 s, whereas in basic pH the intensity decreased slightly; however under both conditions the decrease was much less in comparison to organic dye rhodamine 6G (Figure S9, Supporting Information). The fluorescence intensity decrease rate (F/F_0) of Cu NCs measured at the maxima in acidic pH (pH 4.5) and basic pH (pH 8) were found to be 0.037% and 0.24%, respectively, whereas in case of rhodamine 6G, the rate was found to be 0.43%. The resistance to photobleaching and their stability in solid form make the Cu NCs strong candidates for biological applications.

Additionally, zeta potential measurements were performed at different pH of the medium to find out the surface charge of Cu NCs. The as-prepared Cu NCs stabilized by PVP was found to have zeta potential of −4.09 mV (at pH 4.5), the value changed to −15.8 mV at pH 9.0 (Table S1, Supporting Information). It is plausible that at acidic pH, the NCs were stabilized by the $-NH_3^+$ of PVP and −COOH group of DHLA, whereas in basic medium the stabilizing groups are $-NH_2$ and −COO−, thus changing the emission behavior of the NCs.

The bright fluorescence, highly photostable and small size of Cu NCs could make them ideal candidates for biological application such as cellular labeling and bioimaging. For example, their fluorescence properties could be used for tracking the drug delivery in cells, which could have competitive edge over much popularized but toxic semiconductor quantum dots. To test the feasibility of their use, Cu NCs were synthesized in PVP/PVA hydrogel, and the composite was used as a nanocarrier for drug delivery in HeLa cells. PVP and PVA are hydrophilic and biodegradable polymers approved by FDA for medical applications. These polymers have been extensively used for synthesizing hydrogels for drug delivery and other pharmaceutical applications.[35,36] Hydrogels are three-dimensional network structures with high amount of water content,

DOI: 10.1021/am505799q
ACS Appl. Mater. Interfaces 2015, 7, 209−222

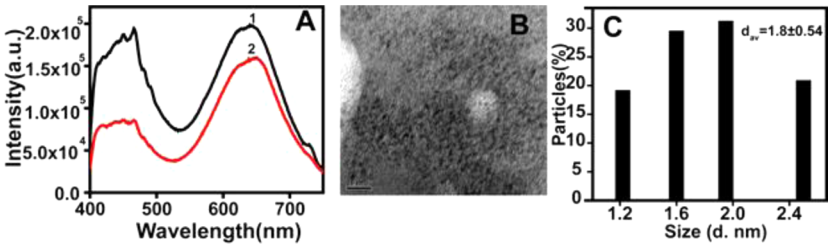

Figure 6. (A) Fluorescence spectra of Cu NCs (curve 1) and Cu NC−hydrogel composite (curve 2). (B) TEM image of Cu NCs in the hydrogel. Scale bar is 10 nm. (C) Size distribution histogram of Cu NCs in the hydrogel (as obtained from Figure 6B).

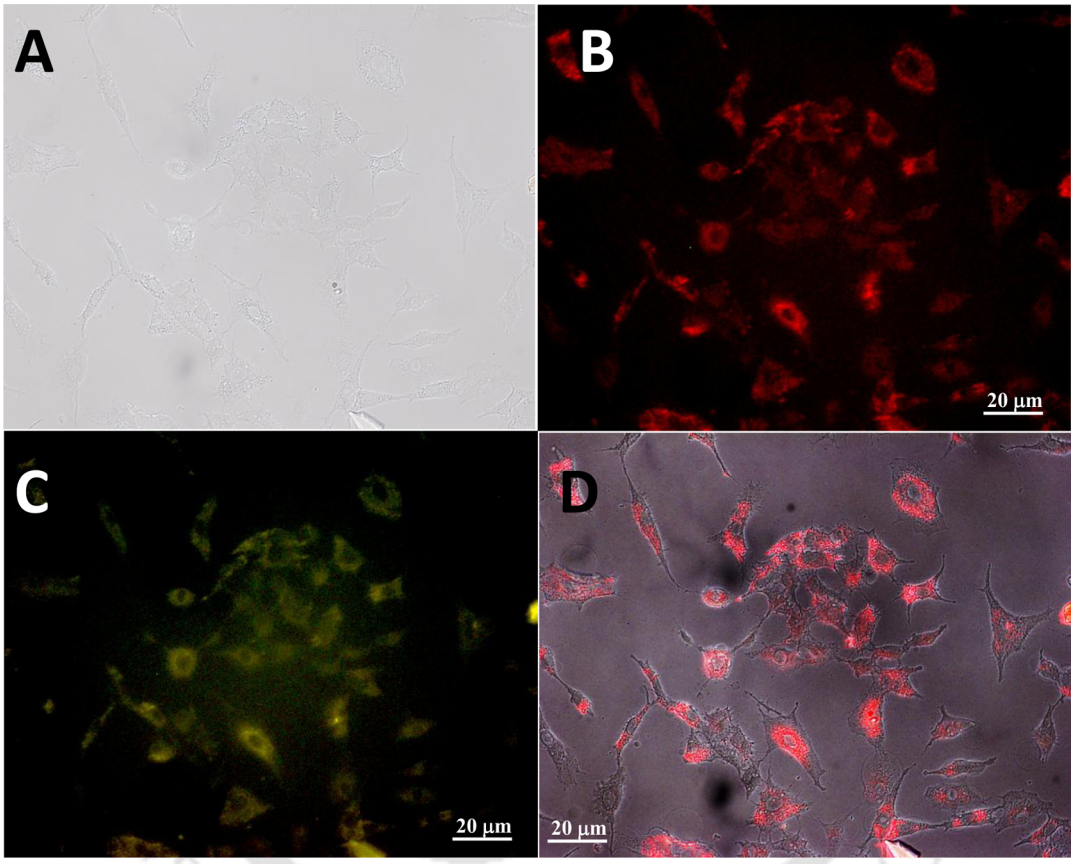

Figure 7. Epifluorescence microscopic images of HeLa cells incubated with Cu NC−hydrogel composite after 2 h. (A) Image under bright field; (B, C) fluorescence images of HeLa cells under excitation filter of blue (465−495 nm) and green (540/25 nm) with corresponding emission band-pass filters green (515−555 nm), and red (605/55 nm), respectively. (D) Microscopic merged image with bright field under same green excitation light of the same cells. Scale bar is 20 μm.

which are ideal for loading water-soluble drugs/molecules. Here, PVP/PVA hydrogel was synthesized by using a method based on freeze−thaw cycle and such formation was confirmed by TEM and FTIR analytical methods. TEM measurement indicated the spherical nature of the hydrogel particles with average diameter of 155 ± 32 nm (Figure S10A, Supporting Information). FTIR spectra of PVA, PVP, and the hydrogel are shown in Figure S10B, Supporting Information. The broad band at 3420 cm^{-1} represents the presence of hydrogen-bonded structures and thus hydrophilic nature of the hydrogel. PVA showed bands at 3429 and 1088 cm^{-1} corresponding to O−H group and crystalline structure of PVA, respectively; whereas PVP showed a sharp band at 1657 cm^{-1}, which is due to −C═O stretching vibration. The formation of the hydrogel through physical cross-linking was indicated by the shift of −C═O stretching frequency to 1643 cm^{-1}; whereas the peak due to the crystalline structure of PVA shifted to 1099 cm^{-1}, indicating the change in the structure.[37] Further, the polymer hydrogel was characterized by differential scanning calorimeter (DSC) in order to find its transition temperature. The DSC thermogram of the hydrogel showed a single glass transition temperature (Figure S11, Supporting Information) at 80 °C, which indicated the interaction between two constituent polymers.[38]

An important challenge is the synthesis of Cu NCs with intact property (as in the above) in the hydrogel. Interestingly, Cu NCs could be synthesized in hydrogels without much change of the reaction condition. The optical properties of the NCs in the hydrogel were nearly the same as those in PVP. For example, the emission spectrum of Cu NC−hydrogel composite comprised of a peak at 640 nm with an excitation maximum at 365 nm (Figure 6A). Importantly, the average size

DOI: 10.1021/am505799q
ACS Appl. Mater. Interfaces 2015, 7, 209−222

of the NCs in PVP/PVA hydrogel was found to be 1.8 ± 0.5 nm, which is close to the size of the particles generated in PVP polymer (Figure 6B, C).

The brightly fluorescent Cu NCs in the hydrogel were further used to investigate the therapeutic and imaging potential of the composite. The composite was used to probe CP delivery to cancer cells and to find the synergy of action of the two (Cu NCs and CP), if any. In addition to the optical properties for imaging application, the size of the composite particle is important for cellular uptake. The hydrodynamic diameter of hydrogel (only) probed using dynamic light scattering (DLS) measurement was found to be 220 nm; whereas the same for Cu NC−hydrogel composite was found to be 284 nm. On addition of CP to Cu NC−hydrogel composite, the size increased further. The average hydrodynamic diameter of CP-loaded Cu NC−hydrogel composite was found to be 345 nm (Figure S12, Supporting Information). The size, although appears to be on the higher side of permissible limit for in vivo applications, still it is known to be effective for drug delivery to cancer cells. It is well-established that in tumor tissues the presence of larger pores—in comparison to healthy tissues−permits enhanced permeation and retention (EPR) of larger particles. The permeability of nanoscale particles of sizes up to 400 nm has been reported. Therefore, CP-loaded Cu NC−hydrogel with higher in size could be internalized by cancer tissues.[39]

The encapsulation of CP into the Cu NC−hydrogel composite was confirmed by FTIR and fluorescence spectroscopy. The sharp N−H and Pt−N stretching bands for CP were present at 3444 and 519 cm^{-1}, respectively, along with the bands of hydrogel at 1647 cm^{-1} and 1076 cm^{-1} (Figure S13B, Supporting Information). Fluorescence spectroscopic investigation supported interaction between composite and CP. For example, when CP was added to the composite, the fluorescence intensity of Cu NCs decreased, confirming interaction between them (Figure S13A, Supporting Information). The interaction between the Cu NCs and CP inside the hydrogel was further confirmed by ^1H NMR spectroscopy (Figure S14, Supporting Information). The characteristic peaks of COOH of the ligand-stabilized Cu NCs was found at 11.8 ppm, whereas the peak vanished when the NCs interacted with CP along with the appearance of the peak at 4.137 ppm due to NH_3 group. This indicated that Cu NCs were bound to CP through carboxylic groups,[40,41] leading to loss of its luminescence. The results also indicated that CP effectively diffused through the hydrogel containing NCs. Also, interaction through NH_3 group of CP suggest the stability of the clusters and preservation of activity of the drug in the medium. The loading of CP to the composite was further supported by zeta potential measurements. The zeta potentials of Cu NC−hydrogel composite and CP-loaded Cu NC−hydrogel composite, both measured at pH 7.4, were found to be −12.5 and −10.5 mV, respectively. The change of zeta potential indicated the loading of drug into the Cu NC−hydrogel composite. Additionally, stability of the composite is also important for its practical usages. The stability of the composite was investigated by the fluorescence spectroscopy. The results, shown in Figure S15, Supporting Information, indicated that with time the composite remained reasonably stable, with 50% decrease in fluorescence intensity in 48 h, at physiological pH of 7.4.

For microscopic imaging, HeLa cells were incubated with Cu NC−hydrogel composite for 2 h in Dulbecco's Modified Eagle's Medium (DMEM). Following this, the medium was removed; cells were washed with phosphate buffer saline (PBS), and finally they were observed under fluorescence microscope. As shown in Figure 7, brightly fluorescent cells with yellow and red colors could be observed. The colors correspond to emission from Cu NCs viewed using two different filters (red and green respectively). The results indicated that the composite hydrogel could potentially be used for imaging of cells, in conjunction with the delivery of drugs.

One of the important criteria of an efficient nanocarrier is its ability to encapsulate high concentration of drug molecules in each such carrier, essentially determining the loading efficiency. The loading efficiency of CP in Cu NC−hydrogel composite was determined using UV−vis spectroscopy by following absorption at 230 nm (due to the drug). The results indicated that Cu NC−hydrogel composite could be loaded with a maximum of ∼78% of CP (with 19.6 μg/mL concentration in the solution containing 1.0 mL of Cu NC−hydrogel composite). Cisplatin is highly soluble in water. It is plausible that the apparent high efficiency could be due to the loading of the molecules on the surface as well as inside the hydrogel particle and the strong bonding between −COOH of Cu NCs (being embedded in the polymer) and CP. This could be due to the hydrophilic nature of the hydrogel with extensive presence of hydrogen bonded interpenetrating network.[42] Before checking the anticancer activity of the drug-loaded composite, in vitro release kinetics was pursued using UV−vis spectroscopy. The time-dependent cumulative release profiles are shown in Figure 8, which revealed that 75% of CP was released at pH 4.5 within 24 h, whereas 52% was released at pH 7.4 in the same time. The results indicated that the release of CP was slower at physiological pH than under acidic condition. This could be due to stronger bonding between the drug molecule and hydrogel, which could be disrupted at acidic pH than at nearly neural condition. Other parameters like hydration capacity of the hydrogel and pore sizes may also contribute to pH-dependent differential release kinetics of the drug.[43] Similarly, the release of copper from Cu NC−hydrogel composite was investigated by atomic absorption spectroscopy (AAS). The results are shown in Figure S16, Supporting Information). Briefly, it was found that after 24 h of incubation at 37 °C, ∼8.8 ppm of copper was released from 21.08 μg/mL of copper—being present in Cu NC−hydrogel composite—in acetate buffer of pH 4.5.

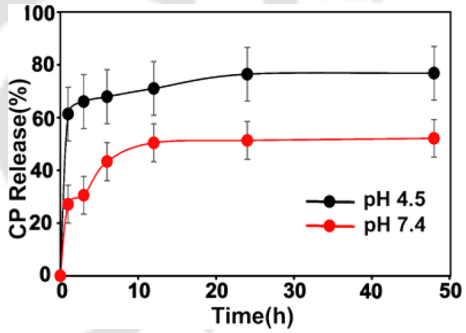

Figure 8. In vitro CP release profile (in %) from CP-loaded Cu NC−hydrogel composite over 48 h at pH 4.5 in acetate buffer (black circle) and at pH 7.4 in phosphate buffer saline (red circle). Both of the experiments were performed at 37 °C.

DOI: 10.1021/am505799q
ACS Appl. Mater. Interfaces 2015, 7, 209−222

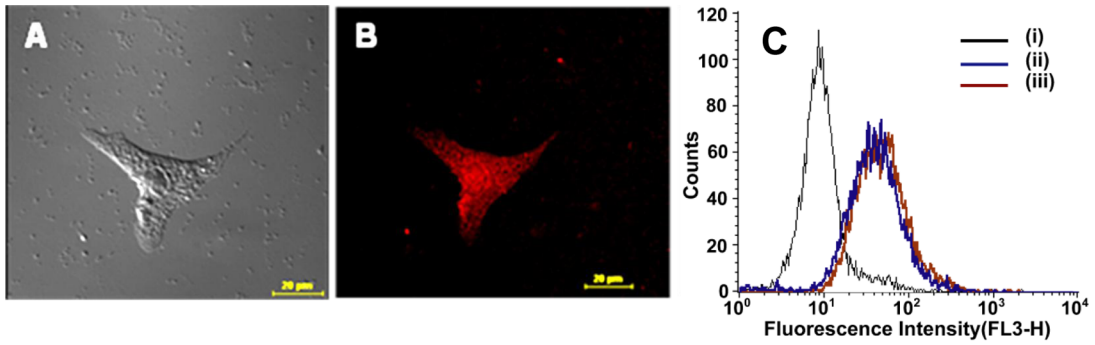

Figure 9. Confocal microscopic images of HeLa cells treated with CP-loaded Cu NC−hydrogel composite, recorded after 4 h of incubation. (A) Image under bright field and (B) fluorescence image of HeLa cells under green light. Scale bar is 20 μm. (C) FACS analysis confirming the uptake of the composite by cells as observed by shifting fluorescence intensity in FL3-H channel: (i) untreated HeLa cells, (ii) hydrogel−Cu NC (8.9 μg/mL) and (iii) CP-loaded Cu NC−hydrogel composite treated HeLa cells.

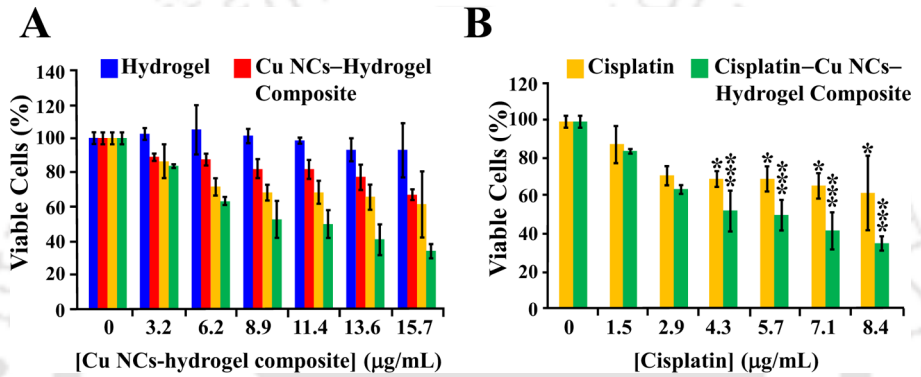

Figure 10. Viability of HeLa cells followed by MTT assay after 24 h treatment with (A) hydrogel, Cu NC−hydrogel composite and CP-loaded Cu NC−hydrogel composite with varying concentrations of the composite, free CP and CP-loaded Cu NC−hydrogel composite at varying CP concentrations; (B) CP only and CP-loaded Cu NC−hydrogel composite (shown separately from (A) for ease of comparison). Experiments were carried out in triplicate. Statistical significance was found between CP-loaded Cu NC−hydrogel composite (green line) and free CP (gray line). Statistical significance is denoted by *($p < 0.05$), **($p < 0.005$),and ***($p < 0.001$).

Finally, the utility of the drug-loaded nanocarrier is measured by its ability to work effectively against cancer cells−at least in vitro. In the current case, the uptake and release of CP-loaded Cu NC−hydrogel composite was studied in vitro following treatment with HeLa cells for 3 h in DIMEM. The cells were then analyzed by fluorescence microscopy, flow cytometry and fluorescence spectroscopy. Fluorescence microscopic images of the cells (Figure 9A,B) could easily discern the uptake of the drug loaded composite as seen by the emission due to red color under blue light excitations, respectively. In drug delivery, cellular images constitute an important indicator of the consequences of delivery. The results reported herein indicated that the NC containing drug loaded composite could be a potential candidate for real time application. Additionally, the fluorescence due to the NCs could be used to follow the cellular uptake of the loaded carrier using flow cytometry. For this, HeLa cells were independently incubated with Cu NC−hydrogel composite (8.9 μg/mL) and CP-loaded Cu NC−hydrogel composite (4.3 μg/mL of CP was loaded to 8.9 μg/mL of Cu NC−hydrogel composite) for 3 h and analyzed by fluorescence-activated cell sorting (FACS) without using any commercial dye. Cu NC−hydrogel composite and CP-loaded Cu NC−hydrogel composite showed prominent shifts in the fluorescent intensity in FL3-H (low pass/670 nm) channel in comparison to untreated cells, which correspond to red fluorescence due to the NCs (Figure 9C). The fluorescence intensity was maximum in FL3-H channel in comparison to FL1-H channel, which might be due to the Stokes shifted emission from Cu NCs with the excitation by the laser at 488 nm, which was used in the FACS Calibur instrument. Additionally, Cu NC−hydrogel composite and CP-loaded Cu NC−hydrogel composite showed almost the same shift in the FL3-H channel, which indicated the interaction between the NCs and the cells. As a result, NCs could be used for cellular tracking agent instead of commercial dyes. The cytometry results further confirmed the uptake of the free as well as drug-loaded composite by the cells. Additionally, TEM image (Figure S17, Supporting Information) of treated HeLa cells confirmed the uptake of Cu NC−hydrogel composite. A magnified image (Figure S17B,C, Supporting Information) evidenced the presence of Cu NCs inside the cells.

The significance of released drug from the CP-loaded Cu NC−hydrogel composite inside the HeLa cells was explored by cell viability assay and field-emission scanning electron microscopy (FESEM). For cell viability studies based on [3-(4,5-dimethylthiazol-2-yl)-2,5-diphenyltetrazolium bromide] (MTT) assay, cells were incubated with Cu NC−hydrogel composite, CP only, and CP-loaded Cu NC−hydrogel composite for 24 h at 37 °C. The concentration of the CP was kept in the range of 1.5−8.4 μg/mL in the composite, whereas Cu NC−hydrogel composite was used in varying concentrations from 3.2−15.7 μg/mL. Figure 10A clearly depicts that 100% of cells were viable upon incubation with hydrogel, indicating the affordable biocompatibility for the drug

DOI: 10.1021/am505799q
ACS Appl. Mater. Interfaces 2015, 7, 209−222

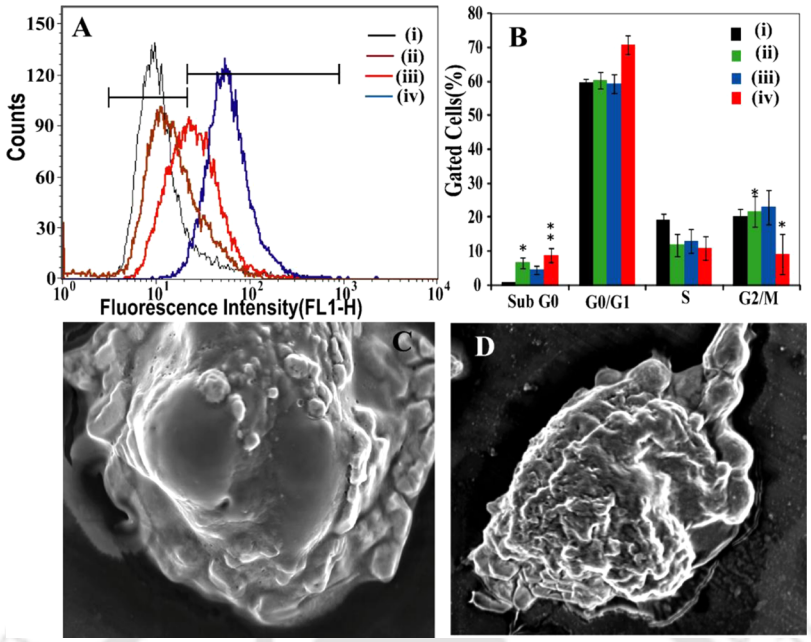

Figure 11. (A) Flow cytometric analysis of ROS production in HeLa cells: (i) untreated cells, (ii) cells treated with Cu NC−hydrogel composite, (iii) cells treated with CP only, and (iv) cells treated with CP Cu NC−hydrogel composite. (B) The effect of Cu NCs and CP in HeLa cells was analyzed by FACS in each phase of cell cycle. (i) Untreated cells, (ii) cells treated with CP only, (iii) cells treated with Cu NC−hydrogel composite, and (iv) cells treated with CP Cu NC−hydrogel composite. (C, D) FESEM images of a HeLa cells, treated with Cu NC−hydrogel composite and CP-loaded Cu NC−hydrogel composite for 24 h revealing apoptotic cell deaths. Experiments were carried out in triplicate. Statistical significance was found between free CP (green line) and CP-loaded Cu NC−hydrogel composite (red line). Statistical significance is denoted by *($p < 0.05$), **($p < 0.005$), and ***($p < 0.001$).

delivery by the hydrogel nanocomposites. Similarly, 75% of the cells were viable upon incubation with 15.7 μg/mL of the Cu NC−hydrogel composite. When the cells were treated with CP-loaded Cu NC−hydrogel composite, the cell viability decreased to 52% at 8.9 μg/mL of Cu NC−hydrogel composite, where the concentration of CP was 4.3 μg/mL. Figure 10B also shows the comparative effect of CP on cancer cells when incubated in the form of free drug molecules versus when loaded in the composite. It was found that at a concentration of 8.4 μg/mL of free CP, the cell viability was reduced to 68%, whereas at the same concentration of the drug when loaded in the composite, the viable cells were reduced to 34%. The MTT assay confirmed the potential synergistic effect of anticell proliferative Cu NC−hydrogel composite with CP on apoptosis of HeLa cells, which increased the efficacy of CP on HeLa cells. It was observed that addition of Cu NC−hydrogel composite decreased IC_{50} value of CP in HeLa cells. Figure 10B clearly shows that 70% of the cells were viable upon incubation with 4.3 μg/mL of CP only for 24 h. Addition of 8.9 μg/mL composite with 4.3 μg/mL of the CP resulted an increase in the cell death by 18%. This indicated that Cu NC−hydrogel composite could enhance the drug efficacy of the composite and can decrease the IC_{50} value of CP. The IC_{50} value of CP when loaded in the hydrogel was calculated to be 5.5 μg/mL. On the other hand, at 8.4 μg/mL of free CP cell viability was reduced to 68% only. The significant decrease of cell viability in the presence of drug-loaded carrier as opposed to free drug molecule evidenced the importance of suitable carrier for increasing the therapeutic efficacy. The result demonstrated that the combination of Cu NC−hydrogel composite and CP can be used as a potential applicant for designing new chemotherapeutic agent.

Biological utility of composites depends on the size, shape, chemical composition, solubility, and surface structures of the NPs. Metal NPs can induce oxidative stress, due to the reactive oxygen species (ROS) generation, governed by the pro-oxidant functional groups present on the surface of NPs as well as owing to the redox properties of transition metal NPs. It has been reported that Cu NPs could generate ROS in so-treated cells.[44] However, the size of the copper particles is the key determinant of toxicity. In case of NCs, the particle size is <2 nm. This shrinkage in size increases the surface-to-volume ratio and alters the electronic and chemical properties. This might create specific surface groups, which can function as reactive sites, with electron donor/acceptor properties that interact with molecular O_2 to form $O_2^{-\bullet}$. Apart from surface properties of NCs, copper can induce oxidative stress via Fenton-type reactions, where Cu ion reacts with H_2O_2 to yield $OH^\bullet$ and $O_2^{-\bullet}$.[45] It is also plausible that Cu^+ species present on the surface of the NC induces oxidative stress. Importantly, the rate of copper fraction release is higher when the NP is smaller in size.[46] ROS generation by Cu NC−hydrogel composite makes it not only an interesting candidate for induction of apoptosis but also provides an important potential for synergistic activity in the presence of a second drug. Interestingly, oxidative stress is associated with apoptotic cell death, which is caused by any chemotherapeutic agent.[47] Thus, flow cytometric studies of the HeLa cells treated with loaded and unloaded composite indicated induction of oxidative stress by the Cu NCs present in the composite. From Figure 11A, it is evident that the Cu NC encapsulated hydrogel generated ROS. Thus, while the cells themselves had the lowest emission intensity (FL1-H), the Cu NC−hydrogel composite-treated cells showed higher emission, which was lower than that due to the only CP-treated cells. However, CP containing composite induced

DOI: 10.1021/am505799q
ACS Appl. Mater. Interfaces 2015, 7, 209−222

highest emission intensity indicating the synergy of action of Cu NCs and CP. The percentage of ROS generation by hydrogel−Cu NC composite and CP-loaded hydrogel−Cu NC composite are shown in Figure S18 in the Supporting Information, as compared to the untreated HeLa cells and CP only. It was found that more than 20% of ROS were generated by Cu NC−hydrogel composite in comparison to untreated HeLa cells.

To pursue the synergistic effect of Cu NC−hydrogel composite and CP, we have performed cell cycle analysis by propidium iodide (PI) staining to confirm the apoptotic mode of cell death due to the oxidative stress induced by Cu NC−hydrogel composite and CP-loaded Cu NC−hydrogel composite treated cells. The flow cytometric analysis showed that the populations of cells in different stages of cell cycle such as G0/G1, S and G2/M were affected following the treatment with Cu NC−hydrogel composite and CP-loaded Cu NC−hydrogel composite in contrast to the control cells (Figure 11B). The increased percentage of population of sub G0/G1 phase of Cu NC−hydrogel composite treated cells (4.72%) and CP-loaded Cu NC−hydrogel composite treated cells (8.96%) provided primary evidence for the apoptotic mode of cell death. The cell cycle analysis for control cells and CP only, Cu NC−hydrogel composite and CP-loaded Cu NC−hydrogel composite are shown in Figure S19, Supporting Information. Further, FESEM analysis were performed on the cells treated with Cu NC−hydrogel composite and CP-loaded composite to follow the typical morphological changes of the cells following the treatment with drugs. For this, cells were incubated with Cu NC−hydrogel composite and CP-loaded Cu NC−hydrogel composite for 24 h, which was followed by imaging using FESEM (Figure 11C,D). Generally, CP binds with the guanine bases of DNA leading to cross-linking of DNA, which interferes with mitotic cell division and results in apoptotic cell death.[48] The morphological changes of the treated cells (Figure 11C,D) revealed apoptotic cell death caused by Cu NCs only and Cu NCs and CP combined, being present in the composite. FESEM analysis was also carried out for control HeLa cells where no sign of apoptosis was observed (Figure S20, Supporting Information), which was in good agreement with the cell viability assay. Further, apoptosis mode of the cell death was confirmed by the Caspase 3 assay in HeLa cells. The apoptotic cell death is primarily governed by the Caspase 3, which is a cysteine-aspartic acid protease.[49] As is evident from the caspase 3 assay results (Figure S21, Supporting Information) about 97.7% control HeLa cells were found to be nonapoptotic corresponding to M1 in the histogram of Figure S21A, Supporting Information, while 10.1% cells show apoptosis corresponding to M2 in the histogram (Figure S21C, Supporting Information), when treated with only Cu NC−hydrogel composite. Similarly, when the cells were treated with only CP, 30.9% cells had shown apoptosis whereas 38.9% cells had shown apoptosis after the treatment with CP-loaded Cu NC−hydrogel composite (Figure S21B, D, Supporting Information). The overall results indicated that Cu NC encapsulated CP-loaded hydrogel composite was more effective for apoptotic mode of cell death, which also confirmed the synergistic effect of Cu NCs and CP present in the composite. Additionally, synergy of action of CP and Cu NCs was further quantified by the combination index (CI).[50,51] The CI was determined by dose−effect profile of the drugs. The extent of interaction between the drugs was evaluated from the CI plot and such a plot gives the quantitative information about the interactions with the values of CI >1, CI <1, and CI = 0, indicating the antagonism, synergism and additivity, respectively. From Table S3 of Supporting Information, it is clear that synergistic effect was present at two cell viable points, namely, at IC_{20} and IC_{40}, in comparison to free CP and hydrogel−Cu NC composite.

CONCLUSION

In summary, we have reported the synthesis of stable and brightly fluorescent Cu NCs using a one-step process in aqueous medium. The NCs could be stabilized in the solid form, where they retained their fluorescence for more than a month. The emission property of the NCs in the aqueous medium could be tuned with pH of the medium. This is the first time that the pH tuneability of Cu NC emission is being reported. These Cu NCs, when embedded into PVP, could easily be converted to hydrogel and be used further to deliver anticancer drug CP to HeLa cells, with enhanced efficiency of killing the cells. The synergy of action of ROS generation due to Cu NCs and anticancer drug action of CP makes the composite valuable for practical application. In addition, optical imaging of the uptake of stable red fluorescent Cu NCs may find use in theranostic applications, owing to their high luminescence.

ASSOCIATED CONTENT

Supporting Information

Additional emission spectra, FTIR spectra, XPS analysis results, photostability, fluorescence decay results, zeta potential table, TEM and FESEM images, DLS measurement, NMR data, DSC thermogram results are included. This material is available free of charge via the Internet at http://pubs.acs.org.

AUTHOR INFORMATION

Corresponding Authors

*E-mail: arun@iitg.ernet.in. (A.C.)
*E-mail: anumita@iitg.ernet.in. (A.P.)

Notes

The authors declare no competing financial interest.

ACKNOWLEDGMENTS

We acknowledge the Department of Electronics and Information Technology (No. 5(9)/2012-NANO) and Department of Biotechnology (BT/49/NE/TBP/2010), Government of India, for financial support. We also thank D. Barpuzary and A. K. Sahoo for help. The authors thank Central Instrument Facilty, IIT Guwahati, for TEM and FESEM analyses.

REFERENCES

(1) Shiang, Y.-C.; Huang, C.-C.; Chang, H.-T. Gold Nanodot-based Luminescent Sensor for the Detection of Hydrogen Peroxide and Glucose. *Chem. Commun.* **2009**, 3437−3439.
(2) Wei, H.; Wang, Z.; Yang, L.; Tian, S.; Hou, H.; Lu, Y. Lysozyme-Stabilized Gold Fluorescent Cluster: Synthesis and Application as Hg^{2+} Sensor. *Analyst* **2010**, *135*, 1406−1410.
(3) Liu, B. Y.; Ai, K.; Cheng, X.; Huo, L.; Lu, L. Gold-Nanocluster-Based Fluorescent Sensors for Highly Sensitive and Selective Detection of Cyanide in Water. *Adv. Funct. Mater.* **2010**, *20*, 951−956.
(4) Wu, X.; He, X.; Wang, K.; Xie, C.; Zhou, B.; Qing, Z. Ultra Small Near-Infrared Gold Nanoclusters for Tumor Fluorescence Imaging in Vivo. *Nanoscale* **2010**, *2*, 2244−2249.
(5) Lin, C.-A. J.; Yang, T.-Y.; Lee, C.-H.; Huang, S. H.; Sperling, R. A.; Zanella, M.; Li, J. K.; Shen, J.-L.; Wang, H.-H.; Yeh, H.-I.; Parak, W.

DOI: 10.1021/am505799q
ACS Appl. Mater. Interfaces 2015, 7, 209−222

J.; Chang, W. H. Synthesis, Characterization, and Bioconjugation of Fluorescent Gold Nanoclusters Towards Biological Labeling Applications. *ACS Nano* **2009**, *3*, 395−401.
(6) Yu, J.; Choi, S.; Dickson, R. M. Shuttle-Based Fluorogenic Silver-Cluster Biolabels. *Angew. Chem., Int. Ed.* **2009**, *48*, 318−320.
(7) Tanaka, S.-I.; Miyazaki, J.; Tiwari, D. K.; Jin, T.; Inouye, Y. Fluorescent Platinum Nanoclusters: Synthesis, Purification, Characterization, and Application to Bioimaging. *Angew. Chem., Int. Ed.* **2011**, *50*, 431−435.
(8) Kauffman, D. R.; Alfonso, D.; Matranga, C.; Qian, H.; Jin, R. Experimental and Computational Investigation of Au_{25} Clusters and CO_2: A Unique Interaction and Enhanced Electrocatalytic Activity. *J. Am. Chem. Soc.* **2012**, *134*, 10237−10243.
(9) Chen, W.; Chen, S. Oxygen Electroreduction Catalyzed by Gold Nanoclusters: Strong Core Size Effects. *Angew. Chem., Int. Ed.* **2009**, *48*, 4386−4389.
(10) Zhu, Y.; Qian, H.; Drake, B. A.; Jin, R. Atomically Precise $Au_{25}(SR)_{18}$ Nanoparticles as Catalysts for the Selective Hydrogenation of α,β-Unsaturated Ketones and Aldehydes. *Angew. Chem., Int. Ed.* **2010**, *49*, 1295−1298.
(11) Sahoo, A. K.; Banerjee, S.; Ghosh, S. S.; Chattopadhyay, A. Simultaneous RGB Emitting Au Nanoclusters in Chitosan Nanoparticles for Anticancer Gene Theranostics. *ACS Appl. Mater. Interfaces* **2014**, *6*, 712−724.
(12) Shen, Z.; Duan, H.; Frey, H. Water-Soluble Fluorescent Ag Nanoclusters Obtained From Multiarm Star Poly(acrylic acid) as a "Molecular Hydrogel" Templates. *Adv. Mater.* **2007**, *19*, 349−352.
(13) Petty, J. T.; Zheng, J.; Hud, N. V.; Dickson, R. M. DNA-Templated Ag Nanocluster Formation. *J. Am. Chem. Soc.* **2004**, *126*, 5207−5212.
(14) Richards, C. I.; Choi, S.; Hsiang, J.-C.; Antoku, Y.; Vosch, T.; Bongiorno, A.; Tzeng, Y.-L.; Dickson, R. M. Oligonucleotide-Stabilized Ag Nanocluster Fluorophores. *J. Am. Chem. Soc.* **2008**, *130*, 5038−5039.
(15) Xie, J.; Zheng, Y.; Ying, J. Y. Protein-Directed Synthesis of Highly Fluorescent Gold Nanoclusters. *J. Am. Chem. Soc.* **2009**, *131*, 888−889.
(16) Liu, C.-L.; Wu, H.-T.; Hsiao, Y.-H.; Lai, C.-W.; Shih, C.-W.; Peng, Y.-K.; Tang, K.-C.; Chang, H.-W.; Chien, Y.-C.; Hsiao, J.-K.; Cheng, J.-T.; Chou, P.-T. Insulin-Directed Synthesis of Fluorescent Gold Nanoclusters: Preservation of Insulin Bioactivity and Versatility in Cell Imaging. *Angew. Chem., Int. Ed.* **2011**, *50*, 7056−7060.
(17) Kawasaki, H.; Hamaguchi, K.; Osaka, I.; Arakawa, R. pH-Dependent Synthesis of Pepsin-Mediated Gold Nanoclusters with Blue Green and Red Fluorescent Emission. *Adv. Funct. Mater.* **2011**, *21*, 3508−3515.
(18) Martin, M. N.; Li, D.; Dass, A.; Eah, S.-K. Ultrafast, 2 min Synthesis of Monolayer-Protected Gold Nanoclusters (d < 2 nm). *Nanoscale* **2012**, *4*, 4091−4094.
(19) Ghosh, R.; Sahoo, A. K.; Ghosh, S. S.; Paul, A.; Chattopadhyay, A. Blue-Emitting Copper Nanoclusters Synthesized in the Presence of Lysozyme as Candidates for Cell Labeling. *ACS Appl. Mater. Interfaces* **2014**, *6*, 3822−3828.
(20) Wei, W.; Lu, Y.; Chen, W.; Chen, S. One-Pot Synthesis, Photoluminescence, and Electrocatalytic Properties of Subnanometer-Sized Copper Clusters. *J. Am. Chem. Soc.* **2011**, *133*, 2060−2063.
(21) Jia, X.; Yang, X.; Li, J.; Lia, D.; Wang, E. Stable Cu Nanoclusters: From an Aggregation Induce Emission mechanism to Biosensing and Catalytic Applications. *Chem. Commun.* **2014**, *50*, 237−239.
(22) Jia, X.; Li, Li.; Wang, E. Cu Nanoclusters with Aggregation Induced Emission Enhancement. *Small* **2013**, *9*, 3873−3879.
(23) Jia, X.; Li, J.; Han, L.; Ren, J.; Yang, X.; Wang, E. DNA-Hosted Copper Nanoclusters for Fluorescent Identification of Single Nucleotide Polymorphisms. *ACS Nano* **2012**, *6*, 3311−3317.
(24) Wang, C.; Wang, C.; Xu, L.; Cheng, H.; Lin, Q.; Zhang, C. Protein-Directed Synthesis of pH-responsive Red Fluorescent Copper Nanoclusters and Their Applications in Cellular Imaging and Catalysis. *Nanoscale* **2014**, *6*, 1775−1781.
(25) Gaggelli, E.; Kozlowski, H.; Valensin, D.; Valensin, G. Copper Homeostasis and Neurodegenerative Disorders (Alzheimer's, Prion, and Parkinson's Diseases and Amyotrophic Lateral Sclerosis). *Chem. Rev.* **2006**, *106*, 1995−2044.
(26) Cater, M. A.; Fontaine, S. L.; Shield, K.; Deal, Y.; Mercer, J. F. ATP7B Mediates Vesicular Sequestration of Copper: Insight Into Biliary Copper Excretion. *Gastroenterology* **2006**, *130*, 493−506.
(27) Banerjee, S.; Sahoo, A. K.; Chattopadhyay, A.; Ghosh, S. S. Hydrogel Nanocarrier Encapsulated Recombinant IκBα as a Novel Anticancer Protein Therapeutics. *RSC Adv.* **2013**, *3*, 14123−14131.
(28) Lakowicz, J. R. *Principles of Fluorescence Spectroscopy,* 2nd ed.; Kluwer Academic/Plenum Publishers: New York, 1999.
(29) Xiong, J.; Wang, Y.; Xue, Q.; Wu, X. Synthesis of Highly stable dispersions of nanosized Copper particles using L-ascorbic acid. *Green Chem.* **2011**, *13*, 900−904.
(30) Yam, V. W.-W.; Cheng, E. C.-C.; Zhou, Z.-Y. A Highly Soluble Luminescent Decanuclear Gold (I) Complex with a Propeller- Shaped Structure. *Angew. Chem., Int. Ed.* **2000**, *39*, 1683−1685.
(31) Yam, V. W.-W.; Cheng, E. C.-C.; Cheung, K.-K. A Novel High-Nuclearity Luminescent Gold (I)−Sulfido Complex. *Angew. Chem., Int. Ed.* **1999**, *38*, 197−199.
(32) Mathew, A.; Sajanlal, P. R.; Pradeep, T. A Fifteen Atom Silver Cluster Confined in Bovine Serum Albumin. *J. Mater. Chem.* **2011**, *21*, 11205−11212.
(33) Wu, Z.; Jin, R. On the ligand's Role in the Fluorescence of Gold Nanoclusters. *Nano Lett.* **2010**, *10*, 2568−2573.
(34) Bensebaa, F.; Ellis, T. H.; Kruus, E.; Voicu, R.; Zhou, Y. Characterization of Self-Assembled Bilayers: Silver−Alkanethiolates. *Langmuir* **1998**, *14*, 6579−6587.
(35) Peppas, B. N. A.; Hilt, J. Z.; Khademhosseini, A.; Robert Langer, R. Hydrogels in Biology and Medicine: From Molecular Principles to Bionanotechnology. *Adv. Mater.* **2006**, *18*, 1345−1360.
(36) Bharali, D. J.; Sahoo1, S. K.; Mozumdar, S.; Maitra, A. Cross-linked Polyvinylpyrrolidone Nanoparticles:A Potential Carrier for Hydrophilic Drugs. *J. Colloid Interface Sci.* **2003**, *258*, 415−423.
(37) Gong, M.; Zhang, L.; Zuo, Y.; Zou, Q.; Wang, Y.; Wang, L.; Li, Y. Investigation on the Interpenetrating Polymer Networks (IPNs) of Polyvinyl Alcohol and Poly(N-vinyl pyrrolidone) Hydrogel and Its In Vitro Bioassessment. *J. Appl. Polym. Sci.* **2011**, DOI: 10.1002/app.
(38) Razzak, M. T.; Zainuddin; Erizal; Dewi, S. P.; Lely, H.; Taty, E.; Sukirno. The Characterization of Dressing Component Materials and radiation formation of PVA-PVP Hydrogel. *Radiat. Phys. Chem.* **1999**, *55*, 153−165.
(39) Yuan, F.; Dellian, M.; Fukumura, D.; Leunig, M.; Berk, D. A.; Torchilin, V. P.; Jain, R. K. Vascular Permiability in a Human Tumor Xenograft: Molecular size Dependence and Cutoff Size. *Cancer Res.* **1995**, *55*, 3752−3756.
(40) Xu, C. J.; Wang, B. D.; Sun, S. H. Dumbbell-like Au−Fe_3O_4 Nanoparticles for Target-Specific Platin Delivery. *J. Am. Chem. Soc.* **2009**, *131*, 4216−4217.
(41) Haxtona, K. J.; Burt, H. M. Hyperbranched Polymers for Controlled Release of Cisplatin. *Dalton Trans.* **2008**, 5872−5875.
(42) Chen, J.-P.; Leu, Y.-L.; Fang, C.-L.; Chen, C.-H.; Fang, J.-Y. Thermosensitive Hydrogels Composed of Hyaluronic Acid and Gelatin as Carriers for the Intravesical Administration of Cisplatin. *J. Pharm. Sci.* **2011**, *100*, 655−666.
(43) Hamidi, M.; Azadi, A.; Rafiei, P. Hydrogel Nanoparticles in Drug Delivery. *Adv. Drug Delivery Rev.* **2008**, *60*, 1638−1649.
(44) Jose, G. P.; Santra, S.; Mandal, S. K.; Sengupta, T. K. Singlet oxygen mediated DNA degradation by Copper Nanoparticles: Potential towards Cytotoxic effect on Cancer Cells. *J. Nanobiotechnol.* **2011**, *9*, 1−8.
(45) Nel, A.; Xia, T.; Mädler, L.; Li, N. Toxic Potential of Materials at the Nanolevel. *Science* **2006**, *311*, 622−627.
(46) Midander, K.; Cronholm, P.; Karlsson, H. L.; Elihn, K.; Möller, L.; Leygraf, C.; Wallinder, I. O. Surface Characteristics, Copper Release, and Toxicity of Nano- and Micrometer-Sized Copper and Copper(II) Oxide Particles: A Cross-Disciplinary Study. *Small* **2009**, *5*, 389−399.

(47) Peng, K.-W.; Wang, H.; Qin, Z.; Wijewickrama, G. T.; Lu, M.; Wang, Z.; Bolton, J. L.; Thatcher, G. J. Selective Estrogen Receptor Modulator Delivery of Quinone Warheads to DNA Triggering Apoptosis in Breast Cancer Cells. *ACS Chem. Biol.* **2009**, *4*, 1039−1049.
(48) Guo, S.; Wang, Y.; Miao, L.; Xu, Z.; Lin, C. M.; Zhang, Y.; Huang, L. Lipid-Coated Cisplatin Nanoparticles Induce Neighboring Effect and Exhibit Enhanced Anticancer Efficacy. *ACS Nano* **2013**, *7*, 9896−9904.
(49) Sanpui, P.; Chattopadhyay, A.; Ghosh, S. S. Induction of Apoptosis in Cancer Cells at Low Silver Nanoparticle Concentrations using Chitosan Nanocarrier. *ACS Appl. Mater. Interfaces* **2011**, *3*, 218−228.
(50) Zhao, L.; Wientjes, M. G.; Au, J. L.-S. Evaluation of Combination Chemotherapy: Integration of Nonlinear Regression, Curve Shift, Isobologram, and Combination Index Analyses. *Clin. Cancer Res.* **2004**, *10*, 7994−8004.
(51) Chou, T.-C. Drug Combination Studies and Their Synergy Quantification Using the Chou-Talalay Method. *Cancer Res.* **2010**, *70*, 440−446.

DOI: 10.1021/am505799q
ACS Appl. Mater. Interfaces 2015, 7, 209−222

Permissions

PERMISSION

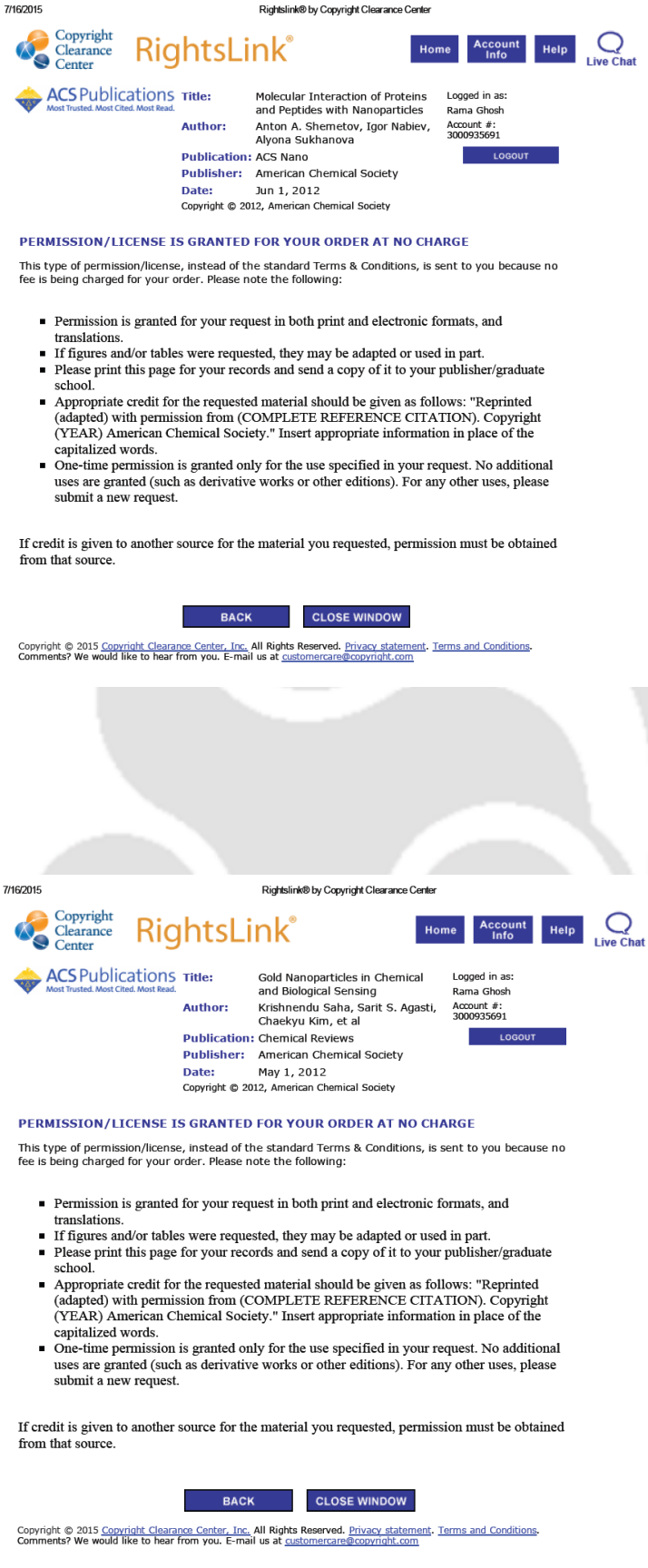

7/16/2015 Rightslink® by Copyright Clearance Center

Copyright Clearance Center RightsLink® Home Account Info Help Live Chat

ACS Publications Most Trusted. Most Cited. Most Read.

Title: Molecular Interaction of Proteins and Peptides with Nanoparticles
Author: Anton A. Shemetov, Igor Nabiev, Alyona Sukhanova
Publication: ACS Nano
Publisher: American Chemical Society
Date: Jun 1, 2012
Copyright © 2012, American Chemical Society

Logged in as: Rama Ghosh
Account #: 3000935691
LOGOUT

PERMISSION/LICENSE IS GRANTED FOR YOUR ORDER AT NO CHARGE

This type of permission/license, instead of the standard Terms & Conditions, is sent to you because no fee is being charged for your order. Please note the following:

- Permission is granted for your request in both print and electronic formats, and translations.
- If figures and/or tables were requested, they may be adapted or used in part.
- Please print this page for your records and send a copy of it to your publisher/graduate school.
- Appropriate credit for the requested material should be given as follows: "Reprinted (adapted) with permission from (COMPLETE REFERENCE CITATION). Copyright (YEAR) American Chemical Society." Insert appropriate information in place of the capitalized words.
- One-time permission is granted only for the use specified in your request. No additional uses are granted (such as derivative works or other editions). For any other uses, please submit a new request.

If credit is given to another source for the material you requested, permission must be obtained from that source.

BACK CLOSE WINDOW

Copyright © 2015 Copyright Clearance Center, Inc. All Rights Reserved. Privacy statement. Terms and Conditions.
Comments? We would like to hear from you. E-mail us at customercare@copyright.com

7/16/2015 Rightslink® by Copyright Clearance Center

Copyright Clearance Center RightsLink® Home Account Info Help Live Chat

ACS Publications Most Trusted. Most Cited. Most Read.

Title: Gold Nanoparticles in Chemical and Biological Sensing
Author: Krishnendu Saha, Sarit S. Agasti, Chaekyu Kim, et al
Publication: Chemical Reviews
Publisher: American Chemical Society
Date: May 1, 2012
Copyright © 2012, American Chemical Society

Logged in as: Rama Ghosh
Account #: 3000935691
LOGOUT

PERMISSION/LICENSE IS GRANTED FOR YOUR ORDER AT NO CHARGE

This type of permission/license, instead of the standard Terms & Conditions, is sent to you because no fee is being charged for your order. Please note the following:

- Permission is granted for your request in both print and electronic formats, and translations.
- If figures and/or tables were requested, they may be adapted or used in part.
- Please print this page for your records and send a copy of it to your publisher/graduate school.
- Appropriate credit for the requested material should be given as follows: "Reprinted (adapted) with permission from (COMPLETE REFERENCE CITATION). Copyright (YEAR) American Chemical Society." Insert appropriate information in place of the capitalized words.
- One-time permission is granted only for the use specified in your request. No additional uses are granted (such as derivative works or other editions). For any other uses, please submit a new request.

If credit is given to another source for the material you requested, permission must be obtained from that source.

BACK CLOSE WINDOW

Copyright © 2015 Copyright Clearance Center, Inc. All Rights Reserved. Privacy statement. Terms and Conditions.
Comments? We would like to hear from you. E-mail us at customercare@copyright.com

7/17/2015 Rightslink® by Copyright Clearance Center

Copyright Clearance Center RightsLink® Home Account Info Help Live Chat

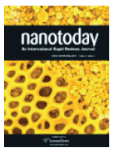

Title: Metal nanoclusters: New fluorescent probes for sensors and bioimaging
Author: Libing Zhang,Erkang Wang
Publication: Nano Today
Publisher: Elsevier
Date: February 2014
Copyright © 2014 Elsevier Ltd. All rights reserved.

Logged in as:
Rama Ghosh
Account #:
3000935691
LOGOUT

Order Completed

Thank you very much for your order.

This is a License Agreement between Rama Ghosh ("You") and Elsevier ("Elsevier"). The license consists of your order details, the terms and conditions provided by Elsevier, and the payment terms and conditions.

Get the printable license.

License Number	3671360112716
License date	Jul 17, 2015
Licensed content publisher	Elsevier
Licensed content publication	Nano Today
Licensed content title	Metal nanoclusters: New fluorescent probes for sensors and bioimaging
Licensed content author	Libing Zhang,Erkang Wang
Licensed content date	February 2014
Licensed content volume number	9
Licensed content issue number	1
Number of pages	26
Type of Use	reuse in a thesis/dissertation
Portion	figures/tables/illustrations
Number of figures/tables/illustrations	1
Format	both print and electronic
Are you the author of this Elsevier article?	No
Will you be translating?	No
Original figure numbers	figure 1
Title of your thesis/dissertation	Gold and Copper based nanomaterials for potential Theranostic applications
Expected completion date	Sep 2015
Estimated size (number of pages)	200
Elsevier VAT number	GB 494 6272 12
Permissions price	0.00 USD
VAT/Local Sales Tax	0.00 USD / 0.00 GBP
Total	0.00 USD

ORDER MORE... CLOSE WINDOW

8/3/2015 Rightslink® by Copyright Clearance Center

Copyright Clearance Center RightsLink® Home Account Info Help Live Chat

ACS Publications Most Trusted. Most Cited. Most Read.

Title: Multifunctional Gold Nanoparticles for Diagnosis and Therapy of Disease
Author: Aneta J. Mieszawska, Willem J. M. Mulder, Zahi A. Fayad, et al
Publication: Molecular Pharmaceutics
Publisher: American Chemical Society
Date: Mar 1, 2013
Copyright © 2013, American Chemical Society

Logged in as:
Rama Ghosh
Account #:
3000935691
LOGOUT

PERMISSION/LICENSE IS GRANTED FOR YOUR ORDER AT NO CHARGE

This type of permission/license, instead of the standard Terms & Conditions, is sent to you because no fee is being charged for your order. Please note the following:

- Permission is granted for your request in both print and electronic formats, and translations.
- If figures and/or tables were requested, they may be adapted or used in part.
- Please print this page for your records and send a copy of it to your publisher/graduate school.
- Appropriate credit for the requested material should be given as follows: "Reprinted (adapted) with permission from (COMPLETE REFERENCE CITATION). Copyright (YEAR) American Chemical Society." Insert appropriate information in place of the capitalized words.
- One-time permission is granted only for the use specified in your request. No additional uses are granted (such as derivative works or other editions). For any other uses, please submit a new request.

If credit is given to another source for the material you requested, permission must be obtained from that source.

BACK CLOSE WINDOW

9/21/2015 Rightslink® by Copyright Clearance Center

Copyright Clearance Center RightsLink® Home Account Info Help Live Chat

ACS Publications Most Trusted. Most Cited. Most Read.

Title: Glutathione-Protected Silver Nanoclusters as Cysteine-Selective Fluorometric and Colorimetric Probe

Author: Xun Yuan, Yuanqi Tay, Xinyue Dou, et al

Publication: Analytical Chemistry

Publisher: American Chemical Society

Date: Feb 1, 2013

Copyright © 2013, American Chemical Society

Logged in as: Rama Ghosh Account #: 3000935691 LOGOUT

PERMISSION/LICENSE IS GRANTED FOR YOUR ORDER AT NO CHARGE

This type of permission/license, instead of the standard Terms & Conditions, is sent to you because no fee is being charged for your order. Please note the following:

- Permission is granted for your request in both print and electronic formats, and translations.
- If figures and/or tables were requested, they may be adapted or used in part.
- Please print this page for your records and send a copy of it to your publisher/graduate school.
- Appropriate credit for the requested material should be given as follows: "Reprinted (adapted) with permission from (COMPLETE REFERENCE CITATION). Copyright (YEAR) American Chemical Society." Insert appropriate information in place of the capitalized words.
- One-time permission is granted only for the use specified in your request. No additional uses are granted (such as derivative works or other editions). For any other uses, please submit a new request.

If credit is given to another source for the material you requested, permission must be obtained from that source.

BACK CLOSE WINDOW

Rightslink® by Copyright Clearance Center https://s100.copyright.com/AppDispatchServle

Copyright Clearance Center RightsLink® Home Account Info Help Live Chat

ACS Publications Most Trusted. Most Cited. Most Read.

Title: Synergistic Anticancer Activity of Fluorescent Copper Nanoclusters and Cisplatin Delivered through a Hydrogel Nanocarrier

Author: Rama Ghosh, Upashi Goswami, Siddhartha Sankar Ghosh, et al

Publication: Applied Materials

Publisher: American Chemical Society

Date: Jan 1, 2015

Copyright © 2015, American Chemical Society

Logged in as: Rama Ghosh Account #: 3000935691 LOGOUT

PERMISSION/LICENSE IS GRANTED FOR YOUR ORDER AT NO CHARGE

This type of permission/license, instead of the standard Terms & Conditions, is sent to you because no fee is being charged for your order. Please note the following:

- Permission is granted for your request in both print and electronic formats, and translations.
- If figures and/or tables were requested, they may be adapted or used in part.
- Please print this page for your records and send a copy of it to your publisher/graduate school.
- Appropriate credit for the requested material should be given as follows: "Reprinted (adapted) with permission from (COMPLETE REFERENCE CITATION). Copyright (YEAR) American Chemical Society." Insert appropriate information in place of the capitalized words.
- One-time permission is granted only for the use specified in your request. No additional uses are granted (such as derivative works or other editions). For any other uses, please submit a new request.

BACK CLOSE WINDOW

9/21/2015 Rightslink® by Copyright Clearance Center

Copyright Clearance Center RightsLink® Home Account Info Help Live Chat

ACS Publications Most Trusted. Most Cited. Most Read.

Title: Nuclear Targeting Dynamics of Gold Nanoclusters for Enhanced Therapy of HER2+ Breast Cancer

Author: Yuling Wang, Jiji Chen, Joseph Irudayaraj

Publication: ACS Nano

Publisher: American Chemical Society

Date: Dec 1, 2011

Copyright © 2011, American Chemical Society

Logged in as: Rama Ghosh Account #: 3000935691 LOGOUT

PERMISSION/LICENSE IS GRANTED FOR YOUR ORDER AT NO CHARGE

This type of permission/license, instead of the standard Terms & Conditions, is sent to you because no fee is being charged for your order. Please note the following:

- Permission is granted for your request in both print and electronic formats, and translations.
- If figures and/or tables were requested, they may be adapted or used in part.
- Please print this page for your records and send a copy of it to your publisher/graduate school.
- Appropriate credit for the requested material should be given as follows: "Reprinted (adapted) with permission from (COMPLETE REFERENCE CITATION). Copyright (YEAR) American Chemical Society." Insert appropriate information in place of the capitalized words.
- One-time permission is granted only for the use specified in your request. No additional uses are granted (such as derivative works or other editions). For any other uses, please submit a new request.

If credit is given to another source for the material you requested, permission must be obtained from that source.

BACK CLOSE WINDOW

9/21/2015 Rightslink® by Copyright Clearance Center

Copyright Clearance Center RightsLink® Home Account Info Help Live Chat

ACS Publications Most Trusted. Most Cited. Most Read.

Title: Synthesis, Characterization, and Bioconjugation of Fluorescent Gold Nanoclusters toward Biological Labeling Applications

Author: Cheng-An J. Lin, Ting-Ya Yang, Chih-Hsien Lee, et al

Publication: ACS Nano

Publisher: American Chemical Society

Date: Feb 1, 2009

Copyright © 2009, American Chemical Society

Logged in as: Rama Ghosh Account #: 3000935691 LOGOUT

PERMISSION/LICENSE IS GRANTED FOR YOUR ORDER AT NO CHARGE

This type of permission/license, instead of the standard Terms & Conditions, is sent to you because no fee is being charged for your order. Please note the following:

- Permission is granted for your request in both print and electronic formats, and translations.
- If figures and/or tables were requested, they may be adapted or used in part.
- Please print this page for your records and send a copy of it to your publisher/graduate school.
- Appropriate credit for the requested material should be given as follows: "Reprinted (adapted) with permission from (COMPLETE REFERENCE CITATION). Copyright (YEAR) American Chemical Society." Insert appropriate information in place of the capitalized words.
- One-time permission is granted only for the use specified in your request. No additional uses are granted (such as derivative works or other editions). For any other uses, please submit a new request.

If credit is given to another source for the material you requested, permission must be obtained from that source.

BACK CLOSE WINDOW

9/21/2015 Rightslink® by Copyright Clearance Center

Copyright Clearance Center RightsLink® Home Account Info Help Live Chat

Title: Insulin-Directed Synthesis of Fluorescent Gold Nanoclusters: Preservation of Insulin Bioactivity and Versatility in Cell Imaging

Author: Chien-Liang Liu,Hung-Tsung Wu,Yi-Hsuan Hsiao,Chih-Wei Lai,Chun-Wei Shih,Yung-Kang Peng,Kuo-Chun Tang,Hsing-Wei Chang,Yun-Chen Chien,Jong-Kai Hsiao,Juei-Tang Cheng,Pi-Tai Chou

Publication: Angewandte Chemie International Edition

Publisher: John Wiley and Sons

Date: Jun 17, 2011

Copyright © 2011 WILEY-VCH Verlag GmbH & Co. KGaA, Weinheim

Logged in as: Rama Ghosh Account #: 3000935691 LOGOUT

Order Completed

Thank you for your order.

This Agreement between Rama Ghosh ("You") and John Wiley and Sons ("John Wiley and Sons") consists of your license details and the terms and conditions provided by John Wiley and Sons and Copyright Clearance Center.

Your confirmation email will contain your order number for future reference.

Get the printable license.

License Number	3713750892740
License date	Sep 21, 2015
Licensed Content Publisher	John Wiley and Sons
Licensed Content Publication	Angewandte Chemie International Edition
Licensed Content Title	Insulin-Directed Synthesis of Fluorescent Gold Nanoclusters: Preservation of Insulin Bioactivity and Versatility in Cell Imaging
Licensed Content Author	Chien-Liang Liu,Hung-Tsung Wu,Yi-Hsuan Hsiao,Chih-Wei Lai,Chun-Wei Shih,Yung-Kang Peng,Kuo-Chun Tang,Hsing-Wei Chang,Yun-Chen Chien,Jong-Kai Hsiao,Juei-Tang Cheng,Pi-Tai Chou
Licensed Content Date	Jun 17, 2011
Licensed Content Pages	5
Type of use	Dissertation/Thesis
Requestor type	University/Academic
Format	Print and electronic
Portion	Figure/table
Number of figures/tables	1
Original Wiley figure/table number(s)	3
Will you be translating?	No
Title of your thesis / dissertation	Gold and Copper based nanomaterials for potential Theranostic applications
Expected completion date	Sep 2015
Expected size (number of pages)	200
Requestor Location	Rama Ghosh Department of Chemistry Indian Institute of Technology Guwahati Guwahati, India 781039 Attn: Rama Ghosh

https://s100.copyright.com/AppDispatchServlet 1/2

9/21/2015 Rightslink® by Copyright Clearance Center

Copyright Clearance Center RightsLink® Home Account Info Help Live Chat

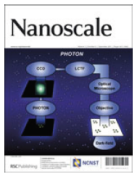

Title: Ultrasmall near-infrared gold nanoclusters for tumor fluorescence imaging in vivo

Author: Xu Wu,Xiaoxiao He,Kemin Wang,Can Xie,Bing Zhou,Zhihe Qing

Publication: Nanoscale

Publisher: Royal Society of Chemistry

Date: Sep 8, 2010

Copyright © 2010, Royal Society of Chemistry

Logged in as: Rama Ghosh Account #: 3000935691 LOGOUT

Order Completed

Thank you very much for your order.

This is a License Agreement between Rama Ghosh ("You") and Royal Society of Chemistry. The license consists of your order details, the terms and conditions provided by Royal Society of Chemistry, and the payment terms and conditions.

Get the printable license.

License Number	3713750759556
License date	Sep 21, 2015
Licensed content publisher	Royal Society of Chemistry
Licensed content publication	Nanoscale
Licensed content title	Ultrasmall near-infrared gold nanoclusters for tumor fluorescence imaging in vivo
Licensed content author	Xu Wu,Xiaoxiao He,Kemin Wang,Can Xie,Bing Zhou,Zhihe Qing
Licensed content date	Sep 8, 2010
Volume number	2
Issue number	10
Type of Use	Thesis/Dissertation
Requestor type	academic/educational
Portion	figures/tables/images
Number of figures/tables/images	1
Distribution quantity	1
Format	print and electronic
Will you be translating?	no
Order reference number	None
Title of the thesis/dissertation	Gold and Copper based nanomaterials for potential Theranostic applications
Expected completion date	Sep 2015
Estimated size	200
Total	0.00 USD

ORDER MORE... CLOSE WINDOW

7/28/2015 Rightslink® by Copyright Clearance Center

Copyright Clearance Center RightsLink® Home Account Info Help Live Chat

Title:	Noble Metal Clusters: Applications in Energy, Environment, and Biology	Logged in as: Rama Ghosh Account #: 3000935691
Author:	Ammu Mathew,Thalappil Pradeep	LOGOUT
Publication:	Particle & Particle Systems Characterization	
Publisher:	John Wiley and Sons	
Date:	May 26, 2014	

© 2014 WILEY-VCH Verlag GmbH & Co. KGaA, Weinheim

Review Order

Please review the order details and the associated terms and conditions.

No royalties will be charged for this reuse request although you are required to obtain a license and comply with the license terms and conditions. To obtain the license, click the Accept button below.

Licensed Content Publisher	John Wiley and Sons
Licensed Content Publication	Particle & Particle Systems Characterization
Licensed Content Title	Noble Metal Clusters: Applications in Energy, Environment, and Biology
Licensed Content Author	Ammu Mathew,Thalappil Pradeep
Licensed Content Date	May 26, 2014
Licensed Content Pages	37
Type of use	Dissertation/Thesis
Requestor type	University/Academic
Format	Print and electronic
Portion	Figure/table
Number of figures/tables	1
Original Wiley figure/table number(s)	Figure 2
Will you be translating?	No
Title of your thesis / dissertation	Gold and Copper based nanomaterials for potential Theranostic applications
Expected completion date	Sep 2015
Expected size (number of pages)	200
Requestor Location	Rama Ghosh Department of Chemistry Indian Institute of Technology Guwahati Guwahati, India 781039 Attn: Rama Ghosh
Total	0.00 USD

Edit Order Details

Edit Requestor Location This location may be used to determine your tax liability

☑ I agree to these terms and conditions.

☐ I understand this license is for reuse only and that no content is provided.

Customer Code (if supplied) APPLY

https://s100.copyright.com/AppDispatchServlet 1/2

9/22/2015 Rightslink® by Copyright Clearance Center

Copyright Clearance Center RightsLink® Home Account Info Help Live Chat

ACS Publications Most Trusted. Most Cited. Most Read.

Title:	Synthesis of Small Atomic Copper Clusters in Microemulsions	Logged in as: Rama Ghosh Account #: 3000935691
Author:	Carlos Vázquez-Vázquez, Manuel Bañobre-López, Atanu Mitra, et al	LOGOUT
Publication:	Langmuir	
Publisher:	American Chemical Society	
Date:	Jul 1, 2009	

Copyright © 2009, American Chemical Society

PERMISSION/LICENSE IS GRANTED FOR YOUR ORDER AT NO CHARGE

This type of permission/license, instead of the standard Terms & Conditions, is sent to you because no fee is being charged for your order. Please note the following:

- Permission is granted for your request in both print and electronic formats, and translations.
- If figures and/or tables were requested, they may be adapted or used in part.
- Please print this page for your records and send a copy of it to your publisher/graduate school.
- Appropriate credit for the requested material should be given as follows: "Reprinted (adapted) with permission from (COMPLETE REFERENCE CITATION). Copyright (YEAR) American Chemical Society." Insert appropriate information in place of the capitalized words.
- One-time permission is granted only for the use specified in your request. No additional uses are granted (such as derivative works or other editions). For any other uses, please submit a new request.

If credit is given to another source for the material you requested, permission must be obtained from that source.

BACK CLOSE WINDOW

ANNEX – I

INFORMATION TO IBSC/ RCGM FOR IMPORT/ EXCHANGE OF GMOS AND PRODUCTS THEREOF FOR RESEARCH PURPOSE

1. Name of the Applicant Arun Chattopadhyay.
Designation Professor
(a) Address (Registered Office) Department of Chemistry

Telephone No. 0361-2582304, 0361-2582333/4
Telex No.
Fax No. 0361-2582349
e-mail – arun@iitg.ernet.in

(b) Address (Research Station) Department of Chemistry, Centre for Nanotechnology.
Telephone No. 0361-2582333/4, 3071
Telex No.
Fax No. 0361-2582349
e-mail arun@iitg.ernet.in

2. Application for (to indicate the purpose):

To investigate some of the preliminary experiments with blood serum by using Nanomaterials that were developed in our laboratory.

3. Objectives of the proposal:
(Applicant should also indicate the relationships of the work plan with environmental safety issues, taking al'1o into consideration the safety to human and animal health when open field experiments are parts of objectives). The composite is Biocompatible as well as human blood compatible/biodegrade

4. Description of the GMOs/ product there of (in scientific terms):
(a) Morphology
(b) Physiology
(c) Number of copies of the genes incorporated
(d) Status of approval is country of origin.

5. Quantity of GMOs/ products there of to be

imported/exchanged:

6. Summary of the proposed work plan utilizing GMOs/ products there of:
(This should indicate schematic lab work, green house studies whenever applicable and details of open field experiments including the map of the experimental plot(s) & the planting pattern of trans gene plants! seeds)

7. Details on:
(a) Source of nucleic acid(s):
(b) Nucleic acid sequence (Please enclose the nucleic acid sequence map of the
target gene):
(c) Vector(s) (Please enclose the map of the vector gene):
(d) Sequence of the genes incorporated/ to be incorporated into the host organlsm.
(e) Host(s) that carrying the vector(s)/ target gene(s):
(f) Manipulative procedures in outline:

8. Source of GMOs/products there of:
Name of the Agency
Contact person's name
Address

Telephone No.
Telex No.
Fax No.
e-mail

9. Mode of shipment:

10. Decontamination, disposal mechanisms & risk management:

11. Any other relevant points(s)

12. Declaration:
I declare that the information provided in the above format is correct and accurate to the best of my knowledge. The "Safety Guidelines" brought out by the Department of Biotechnology, Ministry of Science & Technology, Govt. of

India will be and is being strictly followed. The imported/ exchanged material will be and is being utilized for the said purpose only. In case any untoward incident occurs, the Chairman of the IBSC and the Member-Secretary of the RCGM will be informed immediately.

Date: Signature of the Applicant 08/12/2013

Forwarded & recommended

Prof. S.S. Ghosh
03/01/2013
Member, IBSC.

Forwarded:

The proposal set out above has been considered by the "Institutional Biosafety Committee" on _____ and is forwarded to RCGM for further necessary action.

Date : Signature of the Chairman, IBSC

(Note : Please submit 20 copies of the application to the Department of Biotechnology for placing the same in the meeting of RCGM)

To be submitted in triplicate

INDIAN INSTITUTE OF TECHNOLOGY GUWAHATI

Name of the Applicant (In Block letters): MS. RAMA GHOSH

Name of the PI: Prof. Anumita Paul.

Name of the Co Investigator:

Name of the Research Proposal with Details: To investigate some of the primilinary experiments such as Haemolytic study with blood serum by using nanomaterials which were developed in our laboratory.

Funding Agency:

Term of the Project:

IBSC Clearance obtained (please tick ✓): Y ☑ N ☐

Name of Sample: Blood ✓ / Serum / Body Fluid (please tick the appropriate one)

Identified Sample: YES

If Yes, name of the Identified Donor (in block letters): Ms. RAMA GHOSH

R Ghosh.
Signature of the Identified Donor

15/12/13
Date of consent

Dipak Ranjan
Name & Signature of Sr. Lab Assistant

15/12/2013
Date

Name & Signature of Sr. Medical Officer

Date

P Barua
Name & Signature of Chief Medical Officer

15/12/13
Date

N.B.: Please submit in three copies (triplicate) with one to be retained by the Principal Investigator, one by the donor and the one for the Medical records.